7-2015

The Effects of Strain and Vacancies on the Electric and Vibrational Properties of Ferroelectric BaTiO3 from First-principles

Aldo Serge Michael Raeliarijaona
University of Arkansas, Fayetteville

Recommended Citation

Raeliarijaona, Aldo Serge Michael, "The Effects of Strain and Vacancies on the Electric and Vibrational Properties of Ferroelectric BaTiO3 from First-principles" (2015). *Theses and Dissertations*. 1207.
http://scholarworks.uark.edu/etd/1207

The Effects of Strain and Vacancies on the Electric and Vibrational Properties of Ferroelectric $BaTiO_3$ from First-principles.

The Effects of Strain and Vacancies on the Electric and Vibrational Properties of Ferroelectric $BaTiO_3$ from First-principles.

A dissertation submitted in partial fulfillment
of the requirements for the degree of
Doctor of Philosophy in Physics

By

Aldo Raeliarijaona
Abilene Christian University
Bachelor of Science in Engineering Physics, 2008

July 2015
University of Arkansas

This dissertation is approved for recommendation to the Graduate Council

Professor Huaxiang Fu
Thesis Director

Professor Laurent Bellaiche
Committee member

Professor Gregory Salamo
Committee member

Professor Hameed Naseem
Committee member

Professor Reeta Vyas
Committee member

ABSTRACT

The studies of ferroelectricity (FE) are of technological significance because of the multitude of applicable properties that ferroelectric materials exhibit. The mastery, and control of these properties necessitate the knowledge of the fundamental physics governing these insulating materials.

In this dissertation I present the results of first-principles investigations of the behavior of the fundamental ferroelectric properties under strain, and in the presence of vacancies. In the first part I introduce the important FE properties, their common behavior, and their numerous valuable applications. Following this background on FEs, a review of theoretical methods is presented with topics such as: Density Functional Theory (DFT), Pseudopotential method, Berry Phase Calculation and Density Functional Perturbation Theory (DFPT). Further, new theoretical approaches are introduced in this dissertation to enable the study of polarization for charged system.

In this work I report behaviors of polarization in rhombohedral (R3m) $BaTiO_3$ (BTO) that do not conform with intuition, or the current state of known behavior of epitaxially strained BTO. These studies reveal a polarization that increases with tensile strain, instead of compressive strain, and a polarization that is anticorrelated with an elongation of the out-of-plane axis. Additionally, the studies indicate strain-driven phase transitions to R3c and Cm upon application of moderate epitaxial compressive ($\eta = -1.75\%$) and small tensile strain ($\eta = +0.375\%$), respectively. A simple physical explanation, which can be extended to FE materials of the same symmetry, is also provided for this unusual FE behavior.

I also report the studies on the evolution of phonon modes of vibration under strain in tetragonal (P4mm) BTO, revealing that careful analyses are necessary in the assignment of vibration modes in strained system due to different mode ordering between unstrained and strained systems. The splitting between Longitudinal Optical and Transverse Optical vibration mode is rigorously defined in this work, and shown to depend on mode mixing. The evolution of important quantities such as dielectric constant is also presented in this work.

Finally, the results of investigations on the influence of vacancies on ferroelectric and ferromagnetic properties will be presented in this dissertation. First, the studies of vacancy formation energy are highlighted, which shows the type and charge character of the vacancy that are most likely to occur under any given growth conditions. Afterward, I present the effect of vacancies on polarization and polarization switching in tetragonal BTO, demonstrating the relevance of polarization change in charged polar system, and proposing a method of calculating the polarization and an new polarization-switching pathway in FE BTO in the presence of charged vacancies. Then, I reveal the possibility of vacancy-induced ferromagnetism in BTO, and the microscopic origin of this ferromagnetism.

To Erwin Michaël and Raeliarijaona Adolphe Lucien for everything you have given me,

the path you have opened and urged me to tread,

the joy, love and support.

ACKNOWLEDGEMENTS

The completion of this work wouldn't have been possible without the intervention of some extraordinary people in my life to whom the following few paragraphs are addressed. First, I would like to thank my mother for her love and all the sacrifices she made in her life to show me the joy of learning. These few words are just a glimpse of the loving sentiments of a son lucky to have such an exceptional woman as a mother. I would also like to acknowledge the strong support and encouragement that all my siblings, Rondro, Danie and Gerald, have given me; the joy, smile and sunshine that Cassandra, Mitchel, Jade, Arianne and Arielle always bring to my life. "You guys are the non-Euclidean reference frame I use in defining myself."

I would also like to express my utmost appreciation to my fiancée Sandratra for the laughter, love and understanding, which immensely helped me through the whole process. She was the anchor that kept my sanity on the docks of my mind. My next thoughts and words of appreciation go to my brothers Arisoa and Eddy for their help and advice, especially resolving issues related to Latex. Many thanks to Rajendra Adhikari for answering many questions from the novice that I was.

I am forever grateful to my adopted mother Vicki Clopton Anderson for her hospitality, kindness and for welcoming me to her family. A similar sense of gratitude to the Voss family who showed me the Southern hospitality.

I would also like to acknowledge the Malagasy support group I had during my studies here in Fayetteville: Mampionona, Hervet, the Andriamampianina family Ilo, Lira and Tahiana, Manda, Michaël. I am also indebted to Andrew Kumalo and his family for being the big brother who watched over me during these years. Special thanks to the Bellaiche family: Sheila, Mathias, Lucas and Laurent for their kindheartedness and warmth. Appreciations to Laurent Bellaiche for being a great mentor and an extraordinary teacher and for the invaluable lessons he has taught me in class and on the soccer field.

The body of work presented here wouldn't have been possible without the diligent scrutiny of a great committee: Dr. Bellaiche, Dr. Naseem, Dr. Salamo, Dr. Vyas and Dr. Fu whose perspicacious questions and insights shaped this dissertation.

Last and certainly not the least, my most sincere gratitude to my advisor Dr. Huaxiang Fu for his unwavering support and his willingness to tirelessly teach and train young, aspiring scientists. To the risk of sounding like a sycophant I would like to say: "Thanks for being a living example of what a good scientist and a great human being should be. I am thankful that you never cease to push me to become both. The excellent teacher and researcher that you are is a standard I wish to attain in the future."

TABLE OF CONTENTS

LIST OF FIGURES

LIST OF TABLES

PUBLICATIONS

“*Predicted coupling of the Electromagnetic angular momentum density with magnetic moments*”, Aldo Raeliarijaona, Surendra Singh, Huaxiang Fu, Laurent Bellaiche, Phys. Rev. Lett. 110, 137205 (2013).*Published*

“*Various evidences for the unsual polarization behaviors in epitaxially strained (111)* $BaTiO_3$”, Aldo Raeliarijaona, Huaxiang Fu, J. App. Phys. 115, (2014). *Published*

“*Unsuppressed polarization and new polarization switching mechanismin ferroelectrics with vacancies*”, Aldo Raeliarijaona, Huaxiang Fu (*Submitted Feb. 2015*).

“ *Evolution of zone-center phonon structure in epitaxially strained tetragonal* $BaTiO_3$ ”, Aldo Raeliarijaona, Huaxiang Fu (*S*ubmitted Jun. 2015).

“ *Ferromagnetism induced by vacancies in* $BaTiO_3$*: sensitive dependence on charge state, origin of ferromagnetism, and allowed temperature range.”*, Aldo Raeliarijaona, Huaxiang Fu (*T*o be submitted).

1 Introduction and background materials

The discovery of the Seignette-electricity in Rochelle salt ($KNaC_4H_4O_6$-$4H_2O$) by Valasek in 1921 [3] marks the beginning of the study of what is presently known as ferroelectricity. The cause of ferroelectricity (FE) was elusive, at first, mainly due to the system's complicated structure and experimental limitations at the time, but with the advent of a much simpler system such as $BaTiO_3$ (BTO) in 1940, the study took considerable leap forward. The computational studies of materials also evolved into an important field after the seminal papers by Kohn and Hohenberg [4], and Kohn and Sham [5]. This evolution shed light into behaviors that were theoretically intractable and experimentally inaccessible. Its ability to provide physical insights, macroscopic as well as microscopic, with results and predictions matching closely the experimental data while making minimal assumptions about the system prove to be the triumph of the computational approach. The study undertaken is within the scope of the computational approach focusing on ferroelectric materials.

1.1 Definitions and properties of ferroelectricity and related phenomena

1.1.1 Definitions of FE

The term ferroelectric (FE) describes an insulating material which exhibits a switchable spontaneous polarization **P**. A spontaneous polarization is understood to be a nonzero polarization when there is no applied electric field (**E**-field). The switching between different equivalent configurations is usually initiated by the application of an electric field (**E**-field). For a special class of material known as multiferroic, the magnetic field (**B**-field) can also be responsible for the switching via the magnetoelectric coupling. Note that the term ferroelectric, which was first used by Erwin Schrodinger in 1912, can be etymologically misleading for it is not necessary for a system to contain *ferrum* or iron to show the ferroelectric behavior, as is the case of BTO. Instead, it is dubbed accordingly because a similar behavior albeit magnetic, ferromagnetism (FM), has been well known many centuries before and Fe is among the most famous ferromagnets.

1.1.2 Origin of FE

In 1944, the discovery of the first FE perovskite oxides BTO prompted further inquiries into the ferroelectric phenomenon, most importantly the microscopic origin of FE. Before we elaborate further on the subject, let us first describe the perovskite oxide structure. These compounds have the chemical formula ABO_3 where A and B are cations and O the oxygen atom. Common A and B atoms are: {Pb, Ba, Sr, Ca, Bi} and {Ti, Zr, Fe}, respectively.

In the perovskite structure the A atom is located at the origin (0,0,0) or corner of the cube, the B atom at the center of the cube $\left(\frac{1}{2},\frac{1}{2},\frac{1}{2}\right)$, and the Oxygen atoms form an octahedron by occupying the centers of the 6 cubic faces. An equivalent way to view the structure is to consider that the A atom is surrounded by 8 O octahedra, each enclosing one B atom at their center. In the tetragonal phase, in order to differentiate between the O atom sharing a plane with Ti and the O atom at the apex of one of the half pyramids we label the O atoms as: O1 with the position $\left(\frac{1}{2},\frac{1}{2},0\right)$ in crystal unit; O2 whose position is $\left(0,\frac{1}{2},\frac{1}{2}\right)$ or equivalently $\left(\frac{1}{2},0,\frac{1}{2}\right)$. The perovskite structure is depicted in Fig1.1.

Owing to its relatively simple structure, investigations of the microscopic origin of FE became manageable. From a symmetry argument, the polarization **P** is present in system without

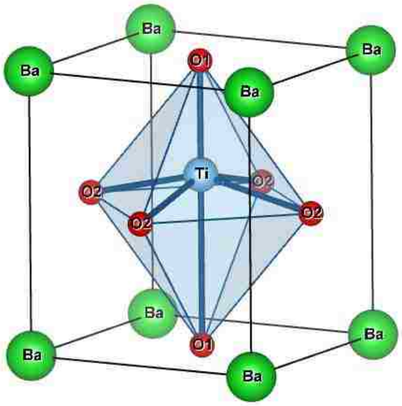

Figure 1.1: A common tetragonal perovskite ABO_3 with the A=Ba atoms occupying the corner of the cube, the B=Ti atom the body center and the face-centered O atoms forming the octahedron, O1 being the apical oxygen and O2 the O atom on the Ti-O base plane.

spatial inversion symmetry. The study of the origin of FE then focuses on what drives this symmetry breaking. In the early years, Slater [6] and Cochran [7], emphasized the importance of the long-range (LR) Coulomb interaction and the delicate balance between the long-range and a short-range (SR) interaction in driving the FE instability. The LR interaction favors ferroelectric distortion while the SR interaction favors higher symmetry. The study by R. E. Cohen [8] pinpointed the microscopic origin of FE. Cohen demonstrated that the hybridization between the Ti 3d and O 2p electrons drives the FE instability in $BaTiO_3$. In the study, when the hybridization in question was inhibited FE distortion disappeared. This lead to the conclusion that in most perovskite oxides, hybridization between the B cation and O is essential to FE. However in some cases, such as $PbTiO_3$ or $BiFeO_3$, the cation A also plays a prominent role in the FE instability. In a similar manner, the hybridization between the A-site cation's 6p electrons and the 2p electrons of the nearby O atoms can also cause FE distortion. In the case of $PbTiO_3$ for example, Cohen's study [8] reported that the hybridization of the A cation and the neighboring O atoms enhances the FE distortion already caused by the B-O hybridization.

1.1.3 Properties of FE

Hysteresis curve

Hysteretic behavior is an idiosyncrasy of systems with memories, such as ferromagnets, or ferroelastics. The so-called hysteresis curve may have various shapes according to the system, and they contain valuable information about the system's behavior upon application of the adequate input. The FE hysteresis curve describes the behavior of the electric polarization **P** as a function of the applied E-field and its past history. A common FE hysteresis curve is depicted in Fig.1.2.

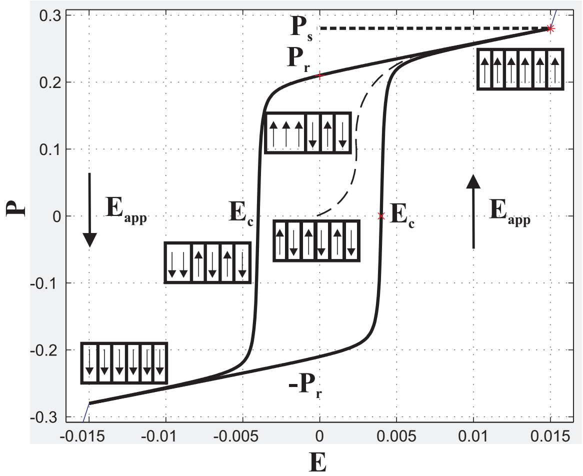

Figure 1.2: Ferroelectric hysteresis curve. The abscissa gives the applied E-field and the ordinate shows the resulting polarization P. Evolutions of FE domains are also drawn to demonstrate the macroscopic behavior of the system.

In general, the initial state of a FE material is a multidomain form, i.e the material has different domains with different polarization orientations. For sake of argument we are going to assume a zero net polarization and domain orientations as depicted in Fig.1.2.

Poling

1. Starting at the (E=0,P=0)-point with the crystal in the multidomain form, we assume that an E-field pointing up is applied as shown to the right of Fig.1.2.

2. When a small E_{up} is applied, up-domains increase at the expense of other domains. Under such magnitude the system's response is linear and the process is reversible, meaning if the field is removed the system goes back to its initial state.

3. When large enough E_{up} is applied, the size of up-domain increases, the system's response is nonlinear, and the process is irreversible. This is mainly due to defects, which are known to pin domain wall motion. [9]

4. Up-domains grow further, as larger field is applied, until the saturation point is attained, a point where all the domains are up.

At the saturation point, the system is known as a monodomain crystal because of the homogeneity of the polarization. The process of turning the multidomain system into a single crystal is called **poling**. If the E-field is removed after poling, the system retains a polarization similar to the saturation polarization but often lower, called **remnant polarization** $\mathbf{P}_r$. The remnant polarization $\mathbf{P}_r$ is the spontaneous polarization mentioned in the definition of ferroelectricity since it is the polarization of the system at zero field.

Polarization reversal: In order to reverse the system's polarization, at this stage pointing up, an electric field oppositely oriented (pointing down) needs to be applied. In the Kolmogorov-Avrami model of polarization switching (KA), [10, 11] the reversal of **P** occurs inhomogeneously and is initiated by a nucleus formation that has **P** pointing down. In such model and its variants, such as the Kolmogorov-Avrami-Ishibashi (KAI) [10, 11, 12] model, nuclei usually form around defects and they can grow sideways and in forward directions at a speed depending on the applied field until the polarization of the whole system is reversed.

Hysteresis landmarks: In the hysteresis curve, the value of the electric field $\mathbf{E}_{app}$ that makes $P = 0$ is denoted as E_c (see Fig.1.2) and is called the coercive field. In an ideal, symmetric hysteresis curve the polarization changes sign abruptly at E_c. Therefore the notion of coercive field can be understood as the value of applied electric field to switch the polarization of a FE system. The area enclosed within a given hysteresis curve is proportional to the energy lost during a switching cycle. This is known as the **loss tangent** of the device.

Let us remark that experimentally the value of the spontaneous polarization is never measured directly. It is rather the change of polarization $\Delta\mathbf{P}$ that is measured during a switching process and the value P_r is extrapolated from $\Delta\mathbf{P}$ after symmetry has been assumed.

Potential well

Another important properties of FEs is displayed by the plot of the energy of the system as a function of parameters, such as atomic displacements, strains, etc. The plot conveys information on the system's stability within a given range of the pertinent parameters. In order to plot such relationship the energy is usually written as Taylor polynomials. Such Taylor expansion is justified because the parameters in question describe small changes of the system. Ferroelectricity is particularly characterized by a double-well potential as depicted in Fig.1.3. The conventional parameter used is the off-center displacement of the Ti atom, usually denoted by u, related to $\mathbf{P}$ by $P = Z^* u$, where Z^* is the dynamical charge. The energy can be written as $E = \alpha u^2 + \beta u^4$, taking only even powers of u because of symmetry. The existence of two local minima means that there are two equivalent, degenerate ground state configurations for the system. As depicted in Fig.1.3, these minima occur at $u_{opt,1} > 0$ and $u_{opt,2} < 0$. Note that the double-well is only present in the case where α and β have opposite sign as evidenced in Fig.1.3. These two minima correspond to values of **P**'s between which the system can be switched. In this case the process of polarization switching, via application of E-field, is viewed as providing the FE system with enough energy to overcome the barrier of the double-well potential. The potential well also shows a metastable state, a state of unstable equilibrium given the negative curvature of the potential at $u = 0$.

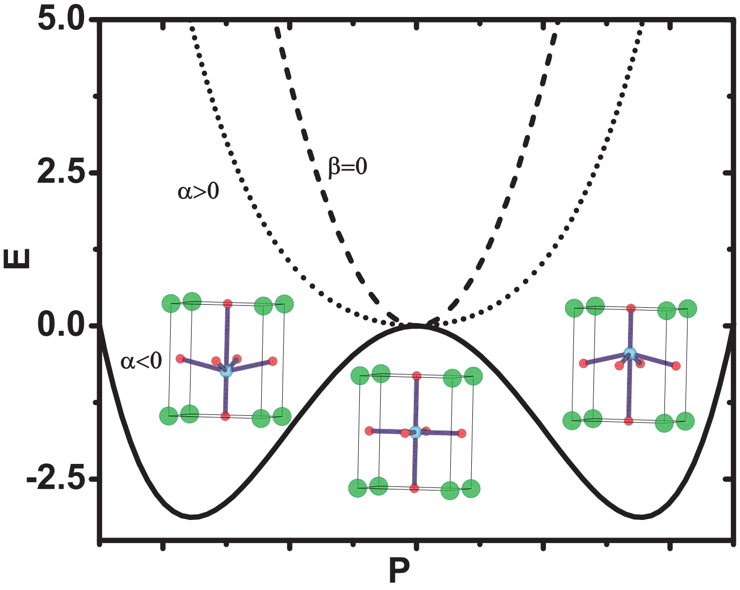

Figure 1.3: Figure of a ferroelectric double-well energy (solid curve), a paraelectric single-well quadratic potential (dashed curve), and the case for which β and α both have the same sign (dotted curve). The atomic configuration of the unit cell at the extrema of the FE double-well is shown.

Temperature dependence and Phase transitions

Matter can exist in different state known as phase. These phases can exhibit particular sets of symmetries and structures, and are stable within certain range of temperature and pressure. A system can undergo a process known as phase transition where it changes its state. Elementary, and commonplace examples of phase transitions are solidification, evaporation, or sublimation of H_2O molecule. These changes in phase of matter can be instigated by various thermodynamical parameters such as pressure, strain, temperature or chemical composition — For instance FE phase transition can be induced in paraelectric (PE) $SrTiO_3$ by substituting isotope O^{18} for O^{16}. [13] In the study of ferroelectricity, one cannot circumvent the topic of phase transition since FE itself is a phase that appears below the critical temperature T_c known as Curie temperature, named after Pierre Curie who discovered the critical point for magnetic system. For the sake of simplifying the discussion we are going to assume a temperature-driven phase transition for our system, noting that the argument can straightforwardly be extended to other parameter-driven transitions.

The important thermodynamic potential when describing a phase is the Gibbs free energy, which is given by $G = U + PV - TS$, where U, P, V, T, and S are the internal energy, pressure, volume, temperature, and entropy of the system, respectively. The Gibbs free energy is by definition the energy required to make room for the system in space, that is the mechanical work done by the system (resp. on the system) on its entourage (resp. by its entourage). Phase transitions may occur when two Gibbs free energies cross. These transitions can be classified according to the differentiability class of the free energy, or the microscopic vs macroscopic behavior of the system before and after the transition.

First-order vs second-order transition: The first categorization due to Ehrenfest stipulates that a phase transition is of nth-order when $\frac{\partial^n \mathscr{G}}{\partial \lambda^n}$, where λ is a thermodynamic parameter, is discontinuous. That is a phase transition is *first-order* or *second order* according to the continuity of the order of the Gibbs free energy derivatives. One implication of this categorization is obtained if we consider the Gibbs free energy $dG = dU + d(PV) - d(TS) = Vdp - SdT$ and assume that we have a first-order phase transition. Using the definition of first-order transition, we have:

$$\left.\frac{dG}{dT}\right|_{P,T=T_c^+} \neq \left.\frac{dG}{dT}\right|_{P,T=T_c^-}, \tag{1.1}$$

which can be evaluated to yield:

$$\Delta S = S(T_c^-) - S(T_c^+) \neq 0. \tag{1.2}$$

From Eq.1.2 we can conclude that a first-order transition is accompanied by a latent heat of transformation as heat ΔS is given off or required for the system to transition to the new phase. Another difference between the two type of transitions is related with the fact that the order parameter changes discontinuously in the first-order phase transition and continuously in the second order phase transition. This can be viewed as a consequence of the Ehrenfest characterization since the order parameter, which stabilizes a given phase, is obtained from the equilibrium condition, which in turn involves the first-order derivative of the free energy. It is for this reason that first and second-order transitions are usually referred as discontinuous and continuous transition,respectively.

Order-disorder vs displacive phase transition: This classification of phase transition is related with the macroscopic vs microscopic behavior of the system above T_c. This new classification can be described as follow:

1. **Order-disorder:** A system is said to have an order-disorder phase transition when it shows microscopic order below, and macroscopic disorder above T_c as its name “order-disorder”

suggests. Simply put:

$$\begin{cases} P_i \neq 0, \text{ but } \frac{\sum_i P_i}{\Omega} = 0 & \text{for} T > T_c \\ P_i \neq 0, \text{ and } \frac{\sum_i P_i}{\Omega} \neq 0 & \text{for} T < T_c, \end{cases}$$

where P_i is the dipole moment of cell i, Ω is the unit cell volume. In other words, when T > T$_c$ perusal of the system evidences polarization at the microscopic level but they are not macroscopically coherent enough as depicted in Fig.1.4. Thermal energy causes each site to randomly tunnel through the barrier such that the macroscopic value of the **P** is zero above T$_c$. Compounds such as $NaNO_3$, NH_4Br, NH_4Cl display order-disorder phase transitions, [14] in such compounds phase transition is first-order because the distance that the atoms in some unit cell have to move is quite considerable.

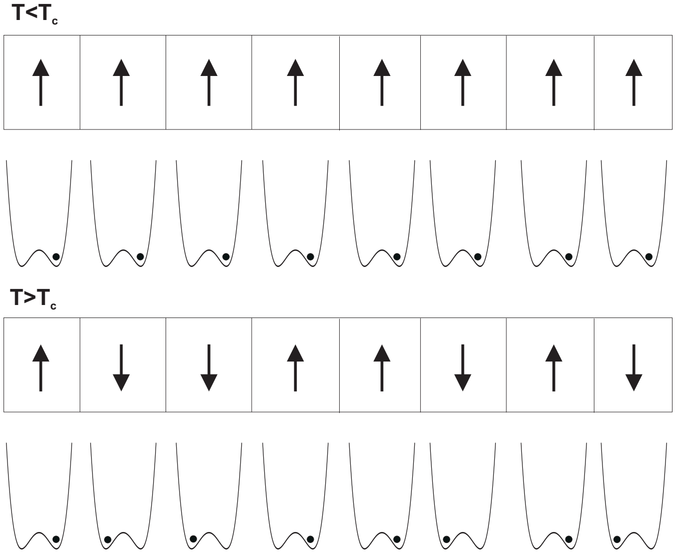

Figure 1.4: The behavior of unit cells of a given system in the order-disorder phase transition for the ordered phase, T<T$_c$, and the disordered phase, T>T$_c$.

2. **Displacive:** A phase transition is displacive when microscopic ordering goes from nonexistent to existent as the system transition below T$_c$. The displacive phase transition can be

described as follow:

$$\begin{cases} P_i = 0, \text{ and } \frac{\sum_i P_i}{\Omega} = 0 & \text{for} T > T_c \\ P_i \neq 0, \text{ and } \frac{\sum_i P_i}{\Omega} \neq 0 & \text{for} T < T_c. \end{cases}$$

Using ferroelectricity as an example, a displacive system shows no polarization microscopically above T_c, and evidences a ferroelectric distortion in each unit cell below T_c, shown in Fig.1.5. This type of phase transition often requires the notion of soft-mode, a special mode of atomic vibration that goes to zero (softens) as the temperature goes below T_c. Structural phase transitions involve the condensation of this special phonon vibration as the temperature is lowered below T_c. During the soft mode condensation, the atoms are moved to a new equilibrium from their previous equilibrium positions above T_c. This new equilibrium is in accord with the displacement pattern of the soft mode vibration. Perovskite oxides, such as $PbTiO_3$ show instance of displacive phase transition. [14]

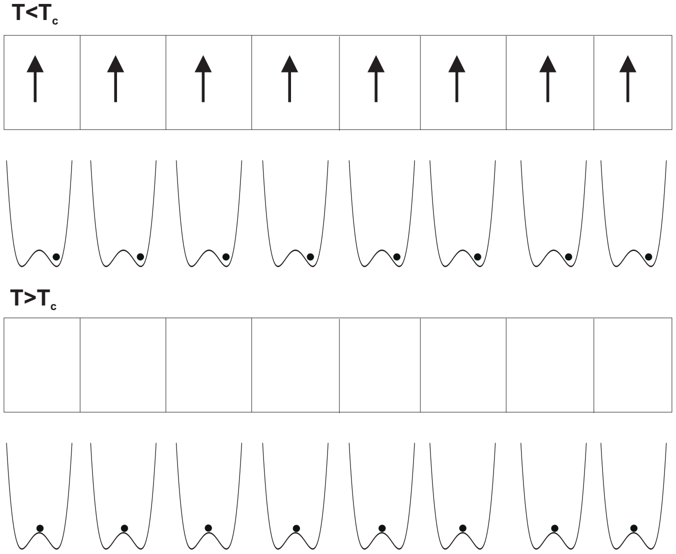

Figure 1.5: The behavior of unit cells of a given system in the displacive phase transition for the ordered phase, T<T_c, and the disordered phase, T>T_c.

Let us remark that this categorization of phase transition describes extreme situations. Some materials like $BaTiO_3$ can show a mixed behavior of displacive and order-disorder phase transition. Indeed Zhong, Vanderbilt and Rabe [15] reported that $BaTiO_3$ displays both transitions but with the order-disorder transition existing to a higher extent.

Thus far we have just taken phase transitions as a fact. Let us discuss a little bit about the theory explaining why phase transitions do happen. To do so we revisit the fluctuation theory of statistical mechanism. Thermodynamic quantities such as energy (U) and polarization (P) can fluctuate within a small region around their average value $\langle E \rangle$, and $\langle P \rangle$, respectively. From statistical mechanics the fluctuations of E and P are given by:

$$\Delta U = k_B T^2 C_v, \tag{1.3}$$

and

$$\Delta P = k_B T V \chi, \tag{1.4}$$

where C_v and χ are the heat capacity at constant volume and electric susceptibility respectively. Normally these fluctuations are small but there are instances where they diverge. These divergences occur in the vicinity of phase transition. To explain this singular behavior we take the dielectric susceptibility for example. The susceptibility describes the system's response to an applied electric field and can be defined as $\chi = \frac{\Delta P}{\Delta E}$, but **P** spontaneously exists in FE, and with $\Delta E \to 0$, $\chi \to \infty$.

Landau phenomenology: Phase transitions can be described using the simple, yet powerful, formalism devised by Lev Landau [16, 17] in an attempt to unify the theory of phase transition. [18]

The premises of the Landau phenomenological theory are:

1. There is an onset of a thermodynamic quantity called order parameter, which can be used to describe the phase of the system, as the system's temperature is lowered below T$_c$ — This quantity gets its nomenclature from the fact that it becomes non zero as the temperature of the system is lowered below T$_c$ hence describing a state with lower entropy, therefore more order.
2. Transition occurs between two phases which are symmetrically related, i.e it involves a spontaneous symmetry breaking.
3. In the vicinity of the phase transition, the microscopic behavior of the system ceases to be of much relevance due to a long-range order.

The ansatz of the Landau theory of phase transition is the expansion of the free energy as a Taylor polynomial of the order parameter. Intuitively when the temperature is lowered the system has less kinetic energy hence the interactions involving the order parameter become more prominent. The application of the Landau theory in FE materials is known as the Landau-Ginzburg-Devonshire (LGD) theory or the Landau-Devonshire (LD) theory, and within the LD theory the free energy is expanded as a function of the FE order parameter, which is the electric polarization P.

$$\mathscr{F}(P) = a_0 + a_1 P + a_2 P^2 + a_3 P^3 + a_4 P^4 + \mathscr{O}(P^5). \tag{1.5}$$

A symmetry-based argument such as $\mathscr{F}(P) = \mathscr{F}(-P)$ implies that $a_{2n+1} = 0$, for any integer, in the expansion of the free energy Eq.1.5,

$$\mathscr{F}(P) = a_0 + a_2P^2 + a_4P^4 + \mathscr{O}(P^6). \tag{1.6}$$

With the zeroth order term viewed as a reference energy level, the free energy can be simplified further as:

$$\mathscr{F}(P) = a_2P^2 + a_4P^4 + \mathscr{O}(P^6). \tag{1.7}$$

In order to guarantee the system's preference of the ordered phase below the temperature T_0, with $T_0 \leq T_c$, a_2 is made temperature dependent; by choosing the simplest parametrization of a_2:

$$\mathscr{F}(P) = \alpha(T - T_0)P^2 + bP^4 + \mathscr{O}(P^6). \tag{1.8}$$

Note that $T_0 < T_c$ for first-order transition, and T_0=T_c for second-order transitions. From Eq.1.8 one can derive the order parameter's temperature dependence by considering the equilibrium condition, $\frac{\partial \mathscr{F}(P)}{\partial P} = 0$. The equilibrium condition leads to values of P which optimizes the free energy.

$$\frac{\partial \mathscr{F}(P)}{\partial P} = 2P\left(\alpha(T - T_0) + 2bP^2\right) = 0. \tag{1.9}$$

A simple sign study of the free energy derivative yields:

The temperature dependence of the electric susceptibility can be derived by considering: $\mathscr{F}(P) = \alpha(T - T_0)P^2 + bP^4 + PE$, where the expression of E(P), $E = 2\alpha(T - T_0)P + 4bP^3$, is derived from the equilibrium condition. The electric susceptibility χ is obtained using $\chi = \frac{\Delta P}{\Delta E}\big|_{P=0} =$

		P$_-$		0		P$_+$	
$2P$	-		-		+		+
$\alpha(T-T_0)+2bP^2$	+		-		-		+
$\mathscr{F}'$	-		+		-		+
$\mathscr{F}$	↘		↗		↘		↗

Table 1.1: Sign table of the free energy derivative with respect to polarization.

$\frac{1}{2\alpha(T-T_0)}$, which is the Curie-Weiss law for FE.

The phase transitions of many FE perovskite oxides have been extensively studied especially the material of interest, BaTiO$_3$. BaTiO$_3$ is known to exhibit 3 phase transitions, one paraelectric (PE) to ferroelectric (FE), and 2 FE to FE transitions:

1. **Cubic**($Pm\bar{3}m$) (PE)→**Tetragonal**($P4mm$) (FE) at T$_c$=393 K

   with $P = 18\ \mu Cm^{-2}$; [19]

2. **Tetragonal**($P4mm$) (FE)→**Orthorhomic**($Amm2$) (FE) at T$_c$=278 K

   with $P = 20\ \mu Cm^{-2}$; [19]

3. **Orthorhombic**($Amm2$) (FE)→**Rhombohedral**($R3m$) (FE) at T$_c$=183 K

   with $P = 22\ \mu Cm^{-2}$. [19]

Levanyuk-Ginzburg criterion: The Landau free energy expansion is taken in the neighborhood of the critical region T$_c$, therefore its region of validity should only be in the vicinity of the phase transition. The range of validity of LG theory is given by the Levanyuk-Ginzburg criterion:[20]

$$t_c = \left(\frac{k_B T_c}{\Delta F(0)\xi^d(0)}\right)^{\frac{2}{4-d}}, \tag{1.10}$$

where t_c is the relative width of the critical region, T_c is the critical temperature, ξ the correlation length of the order parameter, and d is the dimension of the problem. The L-G criterion in Eq.1.10 stresses the importance of ξ in determining the range of validity of LGD theory. Because of the long range aspect of **P** in FE transition, the L-G criterion can be satisfied within only a small region around the critical temperature.

Dielectric property

The discovery of $BaTiO_3$ is historically linked with an extensive search of high-permittivity materials for war-time technologies. [21] The sizable value of dielectric constant in FE materials can easily be shown to relate to the FE phase transition. The dielectric constant is essentially the response function of the medium to an applied electric field, and it is a function of the electric susceptibility as defined by: $\epsilon \equiv \varepsilon_0(1+\chi)$, where ε_0 is the permittivity of free space. Borrowing from the previous section, it can be concluded that the dielectric constant reaches a large value when the system is close to the FE transition.

One can also see this divergence of the dielectric constant starting from the Lyddane-Sachs-Teller (LST) relation and using the idea of soft-mode condensation during a displacive transition. The LST relation states that:

$$\frac{\epsilon_0}{\epsilon_\infty} = \frac{\omega_L^2}{\omega_T^2}, \tag{1.11}$$

where ϵ_0, ϵ_∞ are the zero-frequency and high frequency dielectric response, respectively, the ω's are phonon vibration frequencies. Knowing that displacive FE transition involves a soft phonon, meaning $\omega_T \to 0$ as $T \to T_c$, the LST relation implies that $\epsilon_0 \to \infty$.

1.1.4 Related phenomena

Pyroelectricity

In defining ferroelectricity we had to mention the switchability of the polarization. This is indeed important in distinguishing FE materials from the class of materials known as pyroelectrics. A crystal is pyroelectric if it has a spontaneous polarization with a change in temperature, in the absence of applied electric field and stress. This polarization is not necessarily switchable which makes FE materials a subclass of pyroelectric materials. Thus a FE material is by definition a pyroelectric material but a pyroelectric material is not necessarily FE. Thermodynamically, the pyroelectric coefficient is defined as: $\gamma_p^k = \frac{\partial P^k}{\partial T}\Big|_{E,\sigma}$, where E and σ are the applied electric field and stress, respectively. This is the **primary pyroelectric** coefficient. The other effects related to temperature change, such as thermal expansion and consequently piezoelectric, give rise to the **secondary pyroelectric coefficient** γ_s^p. By computing $dP(T,\eta)$, γ_s^k can be shown to yield: $\gamma_s^k = d^{k,\alpha\beta} C_{\alpha\beta}^{\mu\nu} \alpha_{\mu\nu}$, where Einstein notation has been used, and the tensors $d^{k,\alpha\beta}$, $C^{,\mu\nu}_{\alpha\beta}$, and $\alpha^{\mu\nu}$ are the piezoelectric, elastic compliance, and thermal expansion coefficients, respectively. The inverse of the pyroelectric effect is known as the electrocaloric effect and it implies a change in temperature of the system induced by change in polarization. In Table1.2 we list the pyroelectric coefficients of few materials selected from the entries of a table from [1]. It evidences the important pyroelectric effect sustained by FE materials in comparison to regular pyroelectric materials.

Pyroelectric class	Compounds	$(\gamma_p + \gamma_s)(\mu C K^{-1} m^{-2})$
Non ferroelectrics	ZnO	-9.4
	Tourmaline	-4.0
Ferroelectrics	$BaTiO_3$	-200
	$PbZr_{0.5}Ti_{0.5}O_3$ (PZT)	-268

Table 1.2: Total pyroelectric coefficient, primary and secondary, of few notable materials, excerpt of the table from [1].

Piezoelectricity

Piezoelectricity is another effect related to ferroelectricity, which links **P** to the pressure, or strain on the material. There are two different ways of expressing the piezoelectric effect at zero electric field. The first relates P$_\alpha$ to strain $\eta_{\beta\gamma}$, this coefficient is given by the tensor $e_\alpha^{\beta\gamma}$, by $P_\alpha = e_\alpha^{\beta\gamma}\eta_{\beta\gamma}$. The second coefficient known as **piezoelectric charge constant**, or the piezoelectric strain constant[22], relates P$_\alpha$ to stress σ_ν as shown by: $P_\alpha = d_\alpha^\nu \sigma_\nu$. The relationship between the d and e coefficients can be realized using the Young modulus E as shown by:

$$e_\alpha^{\beta\gamma} = \frac{\partial P_\alpha}{\partial \eta_{\beta\gamma}} = \frac{\partial P_\alpha}{\partial \sigma_\nu}\frac{\partial \sigma_\nu}{\partial \eta_{\beta\gamma}} = d_\alpha^\nu E_\nu^{\beta\gamma}. \tag{1.12}$$

Once again we note that FE materials are de facto piezoelectric but piezoelectric materials aren't necessarily ferroelectric. In Table1.3 we list some coefficients of few piezoelectric materials. The choice between the piezoelectric tensors d or e is a matter of convenience of measurement or calculations with the most commonly used in application being the piezoelectric charge constant $d_{\alpha\beta}$. Table1.3 reveals once more, the strong piezoelectric response from FEs which is an order of magnitude larger than that of regular piezoelectric materials such as tourmaline, GaN, or α-Quartz.

Piezoelectric Compounds	d$_{33}$ (pCN^{-1})	e$_{11}$ (Cm^{-2})	e$_{33}$ (Cm^{-2})
BTO	~400 [23]		6.70 [24]
PZT	200-350 [25]		3.4 [26]
GaN			0.29 [27]
α-Quartz		0.171 [28]	
Tourmaline			~0.30 [29]

Table 1.3: Piezoelectric coefficients $d_{\alpha\beta}$ and $e_{\alpha\beta}$ of a few piezoelectric materials.

Multiferroicity

Recently the study of mutliferroic materials have attracted a lot of attentions. The possibility of combining various order parameters offers a breadth of applications and a wealth of interesting and valuable science. These type of materials exhibit more than one of the so-called ferroic order parameter simultaneously. There are 4 different types of ferroic ordering with the first one, ferroelectricity, being the main subject of our studies. The other three ferroic orders are :

- Ferroelasticity for which the existence of a spontaneous strain (η), in the absence of stress, is the defining criterion.
- Ferromagnetism which exhibits a magnetization $\mathbf{M}$ in the absence of applied magnetic field.
- Ferrotoroidicity: a ferroic order which is characterized by an onset of the toroidal moment below T_c. In the literature the toroidal moment is usually assumed to be the magnetic toroidal moment although the electric toroidal moment is also a valid order parameter as first shown by Naumov, Bellaiche and Fu. [30] The reason of this assumption resides in the fact that the difference between magnetic and electric dipolar interactions is $\sim 137^2$, [31] which implies a large dissimilarity in the size of the magnetic and electric vortices and consequently the ease of its experimental realization. [32]

These ferroic orderings can coexist coincidentally, unrelated, or they can be related leading to the classification of *Type-I* and *Type-II* multiferroics. [33] In the former class the orderings are unrelated, meaning the coupling between both ordering is small, with the instance of $BiFeO_3$ and $YMnO_3$ [33]. In the latter class, one ferroic order induces the other yielding a large coupling between the order parameters, with the example of $TbMnO_3$ [34] and $TbMn_2O_5$ [35].

1.2 Applications of ferroelectric materials

The discovery of important FE materials have been closely tied to research of new materials for technological applications. Indeed FE materials with their various properties present a plethora of technological applications. Let us begin this section by first considering one of their straightforward applications that uses their dielectric properties.

1.2.1 Dielectric properties and Capacitance

From elementary physics, the capacitance of a simple parallel plate capacitor is given by $C = \frac{\epsilon A}{d}$, where ϵ, A and d are the permittivity of the filling material, plate area and the plate spacing, respectively. From this simple expression the capacitance can be drastically increased to ~ 3, or 4 orders of magnitude in comparison to an air-filled capacitors — the relative permittivity of air is ~ 1.001 — by filling the capacitor with FE materials, with Table1.2.1 comparing the dielectric constants of a few semiconductors and some perovskite oxides. A large capacitance is desirable for example in reducing the charging time of an RC circuits, or camera shutter mechanisms. It quantifies a system's ability to store more energy.

Compounds	ϵ_{11} (ϵ_0)	Measurement Temperature
$BaTiO_3$	3,600	298
$PbTiO_3$	200	Room Temperature
$SrTiO_3$	332	298
$BiFeO_3$	40	300
$Pb_3MgNb_2O_9$	10,000	297
Si	12.1	4.2
GaAs	13.13	300

Table 1.4: Table comparing the permittivity of common ferroelectric materials and some commonly used semiconductors. [2]

1.2.2 Optical properties

Dielectric constant is also an important quantity for optical properties of materials. Other quantities such as: index of refraction $n = \sqrt{\epsilon}$, transmission, reflection, and absorption coefficients all depend on the dielectric constant. The unusually large dielectric constant of FEs therefore makes for an interesting optical properties of FEs. In fact $BaTiO_3$ can be in used electro-optic applications. For example $BaTiO_3$ crystals have been used for Second Harmonic Generation (SHG),[36] or in the presence of defects such as Fe impurities or vacancies, they demonstrate photorefractive effects.[37, 38]

1.2.3 Applications of pyro/piezoelectricity properties

FE materials naturally assume all the applications of piezoelectric and pyroelectric materials because they are a subclass of both of these classes of material. Piezoelectric (resp. pyroelectric) materials can transform mechanical (resp. thermal) signal into electrical signal and vice versa. As such they find applications in contemporary technologies such as smartphones with their touch-screens or pressure sensors, which makes use of the direct piezoelectric effect; temperature sensors which relies on the pyroelectric effect, or small motors using the inverse piezoelectric effect. An example of the latter application is found in the field of Atomic Force Microscopy (AFM), which utilizes a piezoelectric material to guide the conducting tip to scan a given sample to an accuracy of μm. As an electric signal is sent to the piezoelectric material, the later expands or contracts in response to the field thereby moving the tips. Such technologies can be found in many instruments requiring motion to a pinpoint accuracy such as moving the end of an optical resonator.

Piezoelectric materials can also be used as accelerometers. The principle is simple and it requires a piezoelectric material in a housing subject to acceleration. As the housing accelerates inertia causes the piezoelectric material to experience a pressure, translated into an electric signal, which is related to acceleration of the system. One can also take advantage of the special relationship between crystallographic orientation and the polarization of some FE materials. The anisotropy of a given FE crystal can be exploited to indicate a specific orientation, signaled by the reading of a voltage resulting from a non-zero polarization. Once again, this orientation sensing is already present in contemporary technologies such as smartphones, or tablets.

FEs can also be used in an array of detectors such as, Sound Navigation and Ranging (SONAR). The acoustic waves' reflection impinging on SONAR detectors will induce pressure on the array of detectors. The resulting pressures are converted by each detector into an electric signal which is in turn translated into an image of the targeted system. The sensitivity of FE materials to phonon vibrations make them a good candidate for infrared (IR) imaging apparatus. The array of IR detectors will produce different voltage according to the source temperature detected. One of the benefits of using FEs in IR imaging resides in the fact that it can operate at room temperature hence the possibility of uncooled IR detector arrays as opposed to other IR detectors, such as InAs, requiring cooling. FEs have a main advantage over regular piezoelectric or pyroelectric materials because the responses of FEs are usually few orders of magnitude larger than the responses of piezoelectric or pyroelectric materials, leading to fine sensibility and low-energy actuation.

1.2.4 Switchable P and its applications

The application that FEs have been touted to have employs its very definition. The switchability of **P** is paramount in the application of FEs as memory devices. Because of the long-range aspect of the governing Coulomb interaction in FEs, which means small FE domains compared to magnetic memories, FE memories are high-density — A crystal of ~12 nm corresponds to approximately 1 GB of memory with each unit cell contributing to one bit — and non-volatile. This Non-Volatile Ferroelectric Memory is the ultimate application of FEs. Considering this application, a binary number is associated to a polarization direction indicates, say $0 \rightarrow |\uparrow\rangle$ and $1 \rightarrow |\downarrow\rangle$. The READ/WRITE process can be done using piezoelectric force microscopy (PFM) tips. [39] A voltage applied through the tip imprints a given electric field orientation onto the FE domain. The READ process can be done using the same piezoelectric tip where a given polarization orientation during scanning induces a motion of the PFM tip, which in turn is translated into an electric signal corresponding to the memory read.

Although FE memories have been used in various devices such as Japanese railroad fare cards, [40] or Sony Playstation 2, there are nevertheless fundamental problems hampering its full potential. Ideally, in the memory concept described above, each unit cell is considered isolated from its neighbors. This is however not possible for **P** has a long range inducing a “cross talk” between these cells thereby affecting the stored memories. [41] Another factor hindering the incorporation of FEs into electronic components is the large value of coercive E_c needed to switch polarization for bulk systems ($50kV/cm$). [40] This problem however can be remedied by using FE thin films but toward that end there is another crippling problem: the device size cannot be decreased indefinitely without the FE properties paying the price. As FE sample size gets smaller the depolarizing field becomes more and more considerable, ultimately inhibiting FE altogether. In fact Junquera and Ghosez [42] determined the critical thickness of 26 Å for FE $BaTiO_3$. So despite the experimental ability to grow materials layer by layer, there a lower limit of the order of 7 unit cells in the allowable thickness for FE-based memory devices.

In 2008, scientists at Hewlett-Packard (HP) discovered the electric component called memristor. Although this component has been theorized to exist 23 years earlier, it wasn't until recently that it became an experimental reality. Memristors relates the magnetic flux to charge according to the memristor equation: $M = \frac{d\Phi_m}{dq}$, where M, Φ_m and q are the memristance, magnetic flux and charge respectively. Essentially they are resistors that retain history of previous charge flow, and they are characterized by a pinched hysteresis. André Chanthbouala et al. [43] devised a FE memristor by sandwiching FE materials between two metal electrodes in a so-called Ferroelectric Tunnel Junction (FTJ). The FTJs used in [43] exhibited memristive behavior, evidenced by the pinched hysteresis. It is shown in [43] that a control of vacancies in the sandwiched FE material leads to control of a large tunneling electroresistance (TER), critical to the memristive behavior.

Multiferroics, more specifically the one combining electric polarization and magnetization, can be very useful since they potentially provide the possibility of low-energy memory devices using the magnetoelectric coupling. In multiferrroic devices, memories can be stored as **P** and afterward read using magnetism. This avoids large magnetic fields required for the writing of magnetic memories, permits a dense packing of memory, and also avoids problems with the destructive reading of FE memories.[44]

In this section we have listed few state of the art applications of FE materials, showing their impact in the technological realm. Nevertheless, applications of FEs are not solely bound within the "technological fences" but rather surprisingly ubiquitous. Recently, Yuanming Liu et al. [45] realized, for the first time, the presence of FE behaviors in the interior walls of porcine blood vessels. This striking discovery may have an impact in the understanding, and preventing of blood clots formation in human.

1.3 Strain: Importance and effects in FE (BTO)

1.3.1 Definition

Any consideration of FE systems usually begins with the system's equilibrium state given by the set of atomic coordinates $\{\mathbf{R}^0\}$. However there can be instances when the system might not be in equilibrium with its constituent atoms moved to new positions $\{\mathbf{R}\}$. This atomic displacement is defined by the vector $\mathbf{u}$, $u_i = R_i - R_i^0$ and the local strain is defined by:

$$\eta_{ij} \equiv \frac{1}{2}\left(\frac{du_i}{dx^j} + \frac{du_j}{dx^i}\right) = \frac{1}{2}\left(u_{i,j} + u_{j,i}\right), \tag{1.13}$$

where x^i represents a Cartesian direction. In simpler terms, the strain tensor η_{ij} quantifies the infinitesimal deformation of a given system with respect to its initial (equilibrium) state. Strains are called normal or shear if the deformation happens normal, or respectively parallel, to a given face. They can be further distinguished as tensile or compressive if the deformation results in an elongation, or shrinking of the adequate length, respectively. Using the idea of a Cauchy strain where the length of interest is the lattice constant, η is given by: $\eta = \frac{a-a_0}{a_0}$, where a_0 is the equilibrium lattice constant and a is the new lattice constant after deformation. Thus $\eta < 0$ for a compressive strain and $\eta > 0$ for a tensile strain. Finally, according to whether the deformation occurs in either 1 or 2 directions (usually perpendicular) the strain is called uniaxial or biaxial.

1.3.2 Importance of strain in the study of FE

There are several experimental techniques to produce FE materials, such as the Sol-gel process or molecular beam epitaxy (MBE) growth. All these procedures require the use of substrates upon which to deposit the materials. One material commonly used for such function is $SrTiO_3$. More often than not the lattice constant of the substrate ($a(SrTiO_3) \simeq 3.90$ Å) does not match that of the FE material on it ($a(BaTiO_3) \simeq 3.99$Å)). This lattice constant mismatch, simply known as lattice mismatch, is one well known source of strain in FE materials. One can naively see that a deformation of ionic coordinates **u** will affect ionic spacing, thus affecting **P**. Although this simplistic consideration of **P** brushes a lot of fundamental details aside, its point is still valid: *strain affect **P***. In fact, strain is one of the tools used to tune **P** in FE materials. To view the effect of strain on FE we use the recourse of the LGD theory introduced few sections earlier. Considering the coupling between strain and polarization the free energy is given by[31]:

$$\mathscr{F}_s = \frac{1}{2}K\eta^2 + Q\eta P^2 + \ldots - \eta\sigma. \tag{1.14}$$

The first term in Eq.1.14 is Hooke's law, which represents the energy stored in the deformation; the second term gives the coupling between the strain and the polarization, and the last term represent the coupling of strain with stress. Minimization of $\mathscr{F}_s$ yields, in case of zero stress, a straightforward quadratic relation between strain and electric polarization, given by:

$$\eta = -\frac{QP^2}{K}. \tag{1.15}$$

Combining Eq.1.14, Eq.1.15 and Eq.1.7 gives:

$$\mathscr{F}(P) = a_2P^2 + a_4P^4 + \frac{Q^2P^4}{2K} - \frac{Q^2}{K}P^4 + \mathscr{O}(P^6), \tag{1.16}$$

which after simplification yields:

$$\mathscr{F}(P) = a_2 P^2 + \left(a_4 - \frac{Q^2}{2K}\right) P^4 + \mathscr{O}(P^6). \tag{1.17}$$

Eq.1.17 shows that strain affect mainly the quartic term of the free energy expansion. The effect of strain in the temperature dependence of **P** can thus be obtained from $P_{\pm} = \pm\sqrt{\frac{\alpha(T_0 - T)}{2b}}$ by making an effective change to the quartic coefficient b with that of Eq.1.17 thus yielding:

$$P_{\pm} = \pm\sqrt{\frac{\alpha(T_0 - T)}{2\left(a_4 - \frac{Q^2}{2K}\right)}} \tag{1.18}$$

The effect of strain is contained within the term $\frac{Q^2}{2K}$. It can be seen from Eq.1.18 the manner in which strain can tune **P**. Furthermore the depth of the potential well, hence the stability of FE states, is also affected according to $\Delta E \propto \frac{1}{\left(a_4 - \frac{Q^2}{2K}\right)}$. Strain is also known to affect the transition temperature T_0. This dependence can be straightforwardly derived from Eq.1.18 if we consider T_0 as $\mathrm{T}_{0,\eta}$ and in lieu of T we use the old transition temperature T_0. We therefore have:

$$\Delta T_0 = \frac{2P^2}{\alpha}\left(a_4 - \frac{Q^2}{K}\right) = \frac{-2\eta K}{Q\alpha}\left(a_4 - \frac{Q^2}{K}\right), \tag{1.19}$$

evidently showing a linear dependence of the critical temperature on strain which is in agreement with the linear decay of T_c of superconducting MgB_2 with respect to tensile strain ($\eta > 0$) [46].

There exist some perovskite oxides that are not quite FE but close to being one, the example of which is $SrTiO_3$. Such materials, known as “incipient ferroelectric”, require the application of strain to stabilize the FE state. This behavior can be understood by comparing Eq.1.8 to Eq.1.17

and assuming that the coefficients $\alpha < 0$ and $b > 0$ which means the system is paraelectric. The presence of the extra term in the quartic coefficient of Eq.1.17, however can result in stable FE states provided $\frac{Q^2}{2K} > b > 0$ which makes the sign of α and b similar.

1.4 Phonons: importance, application and prospects

1.4.1 What is phonon?

Solids are made of periodically arranged ions and electrons, tied to the ions, able to roam in their neighborhood or about the solid. These ions can interact with one another and such atom-atom interaction is at the source of what is known as phonon. At $T \neq 0K$ the constituent ions of a given solid should move but the atom-atom interaction opposes this thermally-driven motion in such a way to create an oscillation around the equilibrium position. The virtual particle associated with the quantized collective ionic vibration is called phonon.

1.4.2 Importance of phonons and applications

Structural phase transitions in solids involve a deformation of the solid from one structure to another related by symmetry. In our discussion of displacive phase transition we mentioned that the soft phonon mode theory can explain structural phase transitions. We reiterate that $\omega_{soft} \to 0$ as $T \to T_c$. We can distinguish between various types of structural phase transition according to the soft mode's wave vector. A Brillouin zone-center soft mode often leads to a ferrodistortive or ferroelectric phase transition, examples of which are $PbTiO_3$, $BaTiO_3$, $KNbO_3$. A Brillouin zone boundary soft mode is related to a cell doubling and antiferrodistortive or antiferroelectric phase transition, with $SrTiO_3$ as its flagship example, which experiences a softening at the R-point

$\left(\frac{1}{2},\frac{1}{2},\frac{1}{2}\right)$ in reciprocal space units. The condensation of the zone boundary soft-mode is associated with the well known antiphase rotation of two neighboring Oxygen octahedra in $SrTiO_3$. The transition temperature T_c is also related with the soft mode frequency ω_s given by [47]:

$$\omega_s{}^2 = -\alpha T_c, \tag{1.20}$$

So the knowledge of phonon structures provides insight into possible phase transitions and eventually the transition temperature. Furthermore Ghosez, Gonze and Michenaud [48] elucidated that the vibration between the Ti-O chain in ABO_3 is critical in determining the origin of ferroelectricity.

Phonons can interact with many other particles such as photons or electrons thereby affecting the optical and electronic properties of the solid. For example they are known to act as scattering centers for conducting electrons in metals hindering electronic conduction and resulting in the resistivity of the material. On the other hand at low enough temperature they can act as an intermediary for the attractive interaction between two electrons forming a Cooper pair in the theory of superconductivity. We see from this the multiple effect of phonons and the underlying importance of their study in solids in general. In dielectrics and polar materials, longitudinal optic (LO) and transverse optic (TO) vibrations interact with electromagnetic waves differently, the latter is responsible for the optical properties of matters while the former is responsible for the dielectric properties. The splitting between LO and TO phonons by electromagnetic waves evidences the interplay between the long-range Coulomb and the lattice dynamics.

1.4.3 The emerging field of phononics and its prospects.

The resistance to electronic motion introduced by the friction between conducting electrons and phonons in solids often heats the material. This means part of the electronic energy is wasted in the form of phonon vibrations. As the size requirement of the contemporary devices is lowered this wasted energy is even more considerable making heat, or waste, management a good idea in solids. This is the main idea behind the prospective field of phononics. This nascent prospects is looking in creating functional devices based on the behavior of phonons instead of photonic or electronic behaviors. The field can be very advantageous in every aspect when combined with electronics and photonic devices. Strides have already been taken in developing the so-called heat diode [49], similar to the electronic diode, which, instead of carriers, allows heat to flow only in one direction by carefully tuning the phonon structures of the interfaced materials. Concepts of a thermal transistor [49], akin to its electronic counterpart, with heat applied at the gate would result in an amplified heat flow between the source and drain. Similarly, concepts of structures exhibiting heat and sound invisibility has been devised[50] where such structures direct sound and heat waves around a designated region of space. FE materials can be of potential use for the nascent field of phononics. For instance in the development of an acoustic or thermal diodes the requirement is an elements with preferably a sizable phonon band gap (PBG) interfaced with another material with a PBG offset with respect to the former. In fact Choudhury et al. demonstrated that perovskite oxides such $SrTiO_3$ have such properties with a PBG nearly 40 meV ($\sim$ 322 cm^{-1}). [51]

1.5 Vacancies and their effects on ferroelectric materials

The working assumption for crystals is that a given structure is perfectly repeated over an infinite range. However such a perfect periodic arrangement is an idealization to render the problem tractable. Realistically imperfections, called defects, are scattered within the system. These defects can be native (intrinsic) or foreign (extrinsic) to the system and they can be intentionally inserted or accidentally present in the system. Vacancy is one type of defects and it is defined by the absence of a given atom from its expected position within the crystal. Vacancies can exist in different type according to the species of the vacant element and in different charge character according to the charge of the vacant ion.

1.5.1 Importance of vacancies in FE

Vacancies, as well as other defects, affect the electronic structure of the material as it introduces an acceptor or a donor level within the band gap of the material. The promotion of an electron onto that energy level from the valence band or from the energy level onto the conduction band leads to a hole or electron conduction, respectively. In the study of materials where insulating property is key, the knowledge of when vacancies may appear is therefore crucial. Indeed conductivity has been shown to exist in $BaTiO_3$ with O-vacancy [52]. Additionally the acceptor or donor levels introduced by vacancies in the band gap may lead to absorption of light and an electron-hole recombination at a particular frequency hence affecting the optical properties of FEs, possibly leading to a coloration of an otherwise transparent material.

Another possible effect of vacancy concerns the very origin of ferroelectricity. As discussed earlier FE stems from the delicate balance between short and long-range interactions between the constituent atoms. However, the presence of vacancies may disrupt this delicate balance and can possibly affect the Ti-O chains, which is paramount to FE [48]. For instance a Ti vacancy, as well as O vacancy, may affect the Ti-O chain and the softening at the vacancy site may also lead to a relaxation that can suppress ferroelectricity.

Vacancies are also detrimental to FE behaviors because at high enough concentration they form a configuration that can pin polarization [9] or domain wall motion thus hampering ferroelectricity. Vacancies and defects are known contributors to fatigues in materials, and in an application where fidelity of memory is paramount, fatigues, which result in possible loss of information, is undesirable. On another note vacancies are nonetheless instrumental to the polarization switching mechanism in ferroelectrics. At low concentration they act as nuclei for the formation of antiphase domain. [39]

Vacancies can exist in different charge character leading to a different number of electrons within the solid. Since electron magnetic moment originates quantum mechanically from the Dirac treatment of electrons, and magnetic properties of materials come mainly from the electron magnetic moments; charged vacancies, which affect the electronic structure can alter the magnetic properties of a given material. For instance the magnetic properties of $PbTiO_3$ have been investigated from first-pinciples by Takahiro Shimada et al. [53] and it indeed shows that vacancies alter the diamagnetic $PbTiO_3$ into a ferromagnetic one. As such, vacancies are a blessing in disguise for FE materials. The multiferroicity of BTO has been demonstrated by Mangalam et al. [54]. It offers the possibility of multiferroicity without diluting foreign magnetic ions in the system, or interfacing with FM materials. In [54], FE are still present in the bulk of the thin BTO film while vacancies on its surface induced magnetization as demonstrated by the presence of both magnetic and electric hysteresis curve.

In summary the attention on vacancies in the studies of FE materials is warranted by the three ways vacancies may affect ferroelectricity: a) Introduction of conduction, hence suppressing the dielectric properties of FEs; b) Disruption of the delicate balance between the short and long-range interactions in perovskite oxides; c) Curbing the polarization switching mechanism by inducing fatigues.

2 Theoretical methods

2.1 Density Functional Theory

In the few years following the establishment of Schrödinger wave equation L. H. Thomas [55] and E. Fermi [56] independently attempted to apply the nascent theory of Quantum Mechanics (QM) to practical situations. Theoretical calculations were made to predict and determine the electronic structure of heavy ions. In doing so, it was realized that the effective potential felt by the electrons depends on their wave functions, which in turn are solutions of the governing Schrödinger equation. To prevent this "chicken-and-egg problem", the system was studied in phase space and it was particularly assumed that the effective potential is determined by the electronic distribution. This assumption, Thomas' fourth assumption [55], makes intuitive sense when viewing the problem from a classical electrostatic perspective. The ensuing *Thomas-Fermi* theory is the precursor of Density Functional Theory (DFT), and it has a practical advantage over the normal quantum mechanical approach because of the reduced dimension required by the density (3-D) as opposed to that required by the wave functions'.

On the other hand, solid is composed of many ions and electrons with a particle density of the order of $\sim 10^{23} cm^{-3}$. It is well known that the discipline of statistical mechanics is better suited to handle systems of such size. Because of the nature of the elements of interest: electrons and ions, a quantum treatment of statistical mechanics is desirable for accuracy of calculations, and further because there are well documented instances where quantum mechanical treatment are required to explain some phenomena among which the most well-known example is the departure from the Dulong-Petit law of heat capacity C_V at constant volume of a solid at low temperature, magnetism (para-, dia- and ferromagnetism) in solids which is essentially a quantum mechanical problem according to the *Bohr-van Leeuwen* theorem. In the particular discipline of Quantum statistics the central quantity or function is the **density operator** $\hat{\rho}(r)$. It is therefore evident that $\rho(r)$ is an indispensable quantity either from a practical (Thomas-Fermi model), or a rigorous (quantum statistics) standpoint.

2.1.1 Hohenberg and Kohn theorems

A breakthrough occurred in the year 1964 when P. Hohenberg and W. Kohn derived the theorems which now bear their names in the work entitled " *Inhomogeneous Electron Gas*". [4]

Theorem I: *For a system of interacting particles in its ground state, under an external potential* $\hat{V}_{ext}$*, we have the following bijective correspondence:* $\hat{V}_{ext} \Longleftrightarrow n(\mathbf{r})$*, where* $n(\mathbf{r})$ *is the density.*

Proof:

To prove this first theorem we start by noting that as a result of the Schrödinger equation, the knowledge of $\hat{V}_{ext}$ implies knowledge of $n(\mathbf{r}) \equiv \langle \psi | \psi \rangle$, where $|\psi\rangle$ represents the many-body wave function, solution of the Schrödinger equation whose potential is V_{ext}.

For the second part of the proof we shall use *Reductio ad absurdum* to prove that $n(\mathbf{r}) = \langle \psi | \psi \rangle \Longrightarrow \hat{V}_{ext}$.

Let us now assume that we have 2 different wave functions $|\psi\rangle$, and $|\psi'\rangle$, both describing the ground state, such that:

$$\hat{H}\left|\psi\right\rangle = (\hat{T}+\hat{V})\left|\psi\right\rangle = E\left|\psi\right\rangle, \tag{2.1}$$

$$\hat{H}'\left|\psi'\right\rangle = (\hat{T}+\hat{V}')\left|\psi'\right\rangle = E'\left|\psi'\right\rangle, \tag{2.2}$$

and $\hat{V} \neq \hat{V}'$. Because $\left|\psi\right\rangle$, and $\left|\psi'\right\rangle$ describe ground state we have:

$$E = \left\langle\psi\right|\hat{H}\left|\psi\right\rangle < \left\langle\psi\right|\hat{H}'\left|\psi\right\rangle, \tag{2.3}$$

$$E' = \left\langle\psi'\right|\hat{H}'\left|\psi'\right\rangle < \left\langle\psi'\right|\hat{H}\left|\psi'\right\rangle. \tag{2.4}$$

We can rewrite the above equations as: $E < \left\langle\psi\right|\hat{T}'+\hat{V}'\left|\psi\right\rangle$ and $E' < \left\langle\psi'\right|\hat{T}+\hat{V}\left|\psi'\right\rangle$ respectively. Knowing that $\hat{T}' = \hat{T} = \hat{H}-\hat{V} = \hat{H}'-\hat{V}'$ we rewrite Eq.2.3 and Eq.2.4 as:

$$E < \left\langle\psi\right|\hat{H}-\hat{V}+\hat{V}'\left|\psi\right\rangle, \tag{2.5}$$

$$E' < \left\langle\psi'\right|\hat{H}'-\hat{V}'+\hat{V}\left|\psi'\right\rangle, \tag{2.6}$$

which when simplified results in

$$E < E - V + V', \tag{2.7}$$

$$E' < E' - V' + V. \tag{2.8}$$

Finally, combining Eq.2.7 and Eq.2.8 yields:

$$E + E' < E + E'. \tag{2.9}$$

This absurd result demonstrates the fallacy of our original assumption. This essentially implies that $n(\mathbf{r})$ uniquely determines the external potential V_{ext}, which completes our proof of how $n_{gs}(\mathbf{r}) \Longleftrightarrow V_{ext}$, for a system of interacting electrons in an external potential and in its *non-degenerate* ground state.

Theorem II: *There exists a universal functional* $F[n(\boldsymbol{r})]$, *independent of* $\hat{V}_{ext}$ *such that the total energy functional:* $E[n(\boldsymbol{r})] = \int v_{ext} n(\boldsymbol{r}) \; d\boldsymbol{r} + F[n(\boldsymbol{r})]$ *has its minimum at the correct ground state density* n_{gs}.

Proof:

The Schrödinger equation for a system of interacting electrons can be written as:

$$\hat{H}\left|\psi\right\rangle = \left(\hat{T} + \hat{V}_{e-e} + \hat{V}_{ext}\right)\left|\psi\right\rangle = E\left|\psi\right\rangle, \tag{2.10}$$

where all the electron-electron interactions are grouped under $\hat{V}_{e-e}$ and the remaining interactions are given by $\hat{V}_{ext}$. If we define by:

$$F[n(\mathbf{r})] = \left\langle\psi\right|\hat{T} + \hat{V}_{e-e}\left|\psi\right\rangle \tag{2.11}$$

It is clear using the formalism of quantum statistics on the one hand, and the proven theorem above on the other, that the quantity $F[n(\mathbf{r})]$ is indeed a functional of the density as given by:

$$F[n(\mathbf{r})] = Tr\left[-\frac{\hat{\nabla}^2}{2}\hat{\rho}\right] + V_{e-e}[n(\mathbf{r})] = Tr\left[-\frac{\hat{\nabla}^2}{2}\hat{\rho}\right] + \int v_{e-e}(\mathbf{r}) n(\mathbf{r}) \; d\mathbf{r}, \tag{2.12}$$

where the quantity $v_{e-e}(\mathbf{r})$ is the potential per particle. By virtue of the variational principle:

$$E_0 \leqslant \langle \psi \,|\, \hat{T} + \hat{V}_{e-e} + \hat{V}_{ext} \,|\, \psi \rangle = F[n(\mathbf{r})] + \langle \psi \,|\, \hat{V}_{ext} \,|\, \psi \rangle, \tag{2.13}$$

for arbitrary state functions $|\psi\rangle$. The equality is attained only when $|\psi\rangle = |\psi_{gs}\rangle$, i.e. $n(\mathbf{r}) = n_{gs}(\mathbf{r})$.

The first Hohenberg-Kohn theorem validates the point raised by Thomas and Fermi, which is the key role of the electron density in the ground state properties of a given quantum system. Contrary to the well established notion in QM that wave functions, hence the densities, are determined as solutions of the Schrödinger differential equation, the theorem implies that the converse is true for ground state, i.e. two different wave functions (different by more than a phase factor) lead to two different environments for the electrons. The first theorem requires that the system have non-degenerate ground state which is a stringent caveat. In fact it is possible for a system to have the same internal energy yet different ground state densities, hence different external potential. This degeneracy problem of Hohenberg-Kohn theorem can be circumvented by using the N-representable densities as first suggested by Levy [57] and Lieb [58]. A density is said to be N-representable when it is derived from arbitrary fermion (antisymmetric) wave functions, whereas the density used in the first Hohenberg-Kohn theorem is known as V-representable due to the fact that it is derived from a given external potential. The idea is to minimize the energy by going through the wave functions that correspond to a particular density n($\mathbf{r}$), and then minimize the energy by changing the density n as summarized in the following equations:

$$\min_{\psi \to n} \langle \psi \,|\, H \,|\, \psi \rangle = \min_{\psi \to n} \langle \psi \,|\, \hat{T} + V_{ee} \,|\, \psi \rangle + \int v(\mathbf{r}) n(\mathbf{r}) \; d\mathbf{r}, \tag{2.14}$$

then

$$E = \min_{n} \left[\min_{\psi \to n} \langle \psi \,|\, H \,|\, \psi \rangle \right]. \tag{2.15}$$

The n-representability approach by Levy and Lieb is more general, or universal as it considers all possible, arbitrary wave functions which correspond to the same density n(**r**). The universal functional in this approach has to be redefined as:

$$F[n(\mathbf{r})] = \min_{\psi \to n} \langle \psi \,|\, \hat{T} + V_{ee} \,|\, \psi \rangle. \tag{2.16}$$

In sum, the density is fixed, one searches through a set of antisymmetric wave-functions giving the same density, the potential is subsequently calculated, the energy is minimized with respect to the wave-functions and the densities.

The second Hohenberg-Kohn theorem establishes the Density Functional theory as an exact theory. The true ground state properties can be exactly determined by minimizing the universal functional, but the exact nature of the theory hinges on the complete knowledge of F[n(**r**)]. A closer glance at the universal — the epithet refers to the fact that the energy functional is independent of the environment of the electrons — functional $F[n(\mathbf{r})]$ shows that:

$$F[n(\mathbf{r})] = Tr\left[-\hat{\nabla}^2 \hat{\rho}\right] + \frac{1}{2} \int \int \frac{n(\mathbf{r}) n(\mathbf{r}')}{|\mathbf{r} - \mathbf{r}'|} \, d\mathbf{r}' \, d\mathbf{r} + E_{xc}, \tag{2.17}$$

where the respective terms are: i) the kinetic energy, ii) the long-range U_{LR} Coulomb repulsive interaction between electrons or the Hartree potential, iii) and the short-range exchange-correlation potential, which takes into account all possible electron-electron interactions other than Coulomb interaction, for example the quantum feature of electrons exclusion principle, the indistinguishability, etc. Unfortunately the exact expression of this exchange-correlation term is yet to be determined.

2.1.2 Kohn-Sham equation and the Local Density Approximation

The results derived by Hohenberg and Kohn in the previous section marked the beginning of Density Functional Theory (DFT). However these results do not necessarily exhibit the advantage they were thought to have over many particles Schrödinger equation. Granted that the dimension of the solution is reduced, the task of finding the solution is nonetheless formidable, not to mention the lack of knowledge of the exchange-correlation potential, which hinders the application of the theory to real-world problems. Hohenberg and Kohn were able to demonstrate the power of their seminal theory to a system of electron gas, a system with the simplest form of exchange-correlation. They managed to show that the Thomas-Fermi model can be derived from DFT by making the simplest assumptions for the exchange-correlation. Kohn and Sham [5] took the theory further and contributed to the extent to which the theory is currently used. Using Eq.2.10. By assuming that *n(r)* is varying slowly, the exchange-correlation functional can be approximated as:

$$E_{xc} = \int n(\mathbf{r})\epsilon\left[n(\mathbf{r})\right]\, d\mathbf{r}, \tag{2.18}$$

where $\epsilon\left[n(\mathbf{r})\right]$ is the exchange-correlation energy per particle (electron) of a uniform gas of density n($\mathbf{r}$), which can be determined from the theory of homogeneous electron gas or Monte Carlo simulations. and Eq.2.17, the energy functional can be written as:

$$\begin{aligned} E[n(\mathbf{r})] \quad &= T[n(\mathbf{r})] + \int v_{ext}(\mathbf{r})n(\mathbf{r})\, d\mathbf{r} + \frac{1}{2}\int\int \frac{n(\mathbf{r})n(\mathbf{r}')}{|\mathbf{r}-\mathbf{r}'|}\, d\mathbf{r}'\, d\mathbf{r} \\ &+ E_{xc}[n(\mathbf{r})], \end{aligned} \tag{2.19}$$

which can be minimized with respect to the density under the constraint of a constant total particle number, namely: $\int n(\mathbf{r})\, d\mathbf{r} = N_{tot}$. The optimization procedure requires the computation of a functional derivatives defined as:

$$\delta F \equiv \int \left(\frac{\delta F}{\delta n(\mathbf{r})}\right) \delta n(\mathbf{r})\, d\mathbf{r} \tag{2.20}$$

with the integrand $\left(\frac{\delta F}{\delta n(\mathbf{r})}\right)$ obtained from the computation of the Fréchet derivative:

$$\frac{\delta F}{\delta n(\mathbf{r})} = \lim_{\delta n(\mathbf{r})\to 0} \frac{F[n(\mathbf{r}) + \delta n(\mathbf{r})] - F[n(\mathbf{r})]}{\delta n(\mathbf{r})}. \tag{2.21}$$

To compute $\delta E[n(\mathbf{r})]$ we start by computing E$[n(\mathbf{r}) + \delta n(\mathbf{r})]$:

$$\begin{aligned} E\left[n(\mathbf{r}) + \delta n(\mathbf{r})\right] \quad &= T\left[n(\mathbf{r}) + \delta n(\mathbf{r})\right] + E_{xc}\left[n(\mathbf{r}) + \delta n(\mathbf{r})\right] + \int v_{ext}(\mathbf{r})(n(\mathbf{r}) + \delta n(\mathbf{r}))\, d\mathbf{r} \\ &+ \frac{1}{2}\int\int \frac{(n(\mathbf{r}) + \delta n(\mathbf{r}))\left(n(\mathbf{r}') + \delta n(\mathbf{r}')\right)}{|\mathbf{r}-\mathbf{r}'|}\, d\mathbf{r}'\, d\mathbf{r}. \end{aligned} \tag{2.22}$$

The third term can be written as:

$$\mathrm{II} = \int v_{ext}(\mathbf{r})(n(\mathbf{r}))\, d\mathbf{r} + \int v_{ext}(\mathbf{r})(\delta n(\mathbf{r}))\, d\mathbf{r}, \tag{2.23}$$

and the last term in Eq.2.22 can be developed as:

$$\begin{aligned} \text{IV} \quad &= \frac{1}{2}\int\int \frac{\left(n(\mathbf{r})n(\mathbf{r}')\right)}{|\mathbf{r}-\mathbf{r}'|}\, d\mathbf{r}'\, d\mathbf{r} + \frac{1}{2}\int\int \frac{\left(\delta n(\mathbf{r})\delta n(\mathbf{r}')\right)}{|\mathbf{r}-\mathbf{r}'|}\, d\mathbf{r}'\, d\mathbf{r} \\ &+ \frac{1}{2}\int\int \frac{\left(\delta n(\mathbf{r})n(\mathbf{r}')\right)}{|\mathbf{r}-\mathbf{r}'|}\, d\mathbf{r}'\, d\mathbf{r} + \frac{1}{2}\int\int \frac{\left(n(\mathbf{r})\delta n(\mathbf{r}')\right)}{|\mathbf{r}-\mathbf{r}'|}\, d\mathbf{r}'\, d\mathbf{r}. \end{aligned} \tag{2.24}$$

Considering the limit $\delta n(\mathbf{r}) \rightarrow 0$, the second term of Eq.2.24, namely the term with $\delta n(\mathbf{r})\delta n(\mathbf{r}')$, tends to 0. Additionally, after realizing that $\mathbf{r}$ and $\mathbf{r}'$ are dummy variables, we end up with:

$$\text{IV} \quad = \frac{1}{2}\int\int \frac{\left(n(\mathbf{r})n(\mathbf{r}')\right)}{|\mathbf{r}-\mathbf{r}'|}\, d\mathbf{r}'\, d\mathbf{r} + \frac{1}{2}\int\int \frac{\left(2\delta n(\mathbf{r})n(\mathbf{r}')\right)}{|\mathbf{r}-\mathbf{r}'|}\, d\mathbf{r}'\, d\mathbf{r}. \tag{2.25}$$

$$\text{IV} \quad = \frac{1}{2}\int\int \frac{\left(n(\mathbf{r})n(\mathbf{r}')\right)}{|\mathbf{r}-\mathbf{r}'|}\, d\mathbf{r}'\, d\mathbf{r} + \int\int \frac{\left(\delta n(\mathbf{r})n(\mathbf{r}')\right)}{|\mathbf{r}-\mathbf{r}'|}\, d\mathbf{r}'\, d\mathbf{r}. \tag{2.26}$$

Now, subtracting E[n($\mathbf{r}$)] from Eq.2.22, and using the results of Eq.2.23 and Eq.2.24 yields:

$$\begin{aligned} \delta E \equiv E[n(\mathbf{r}) + \delta n(\mathbf{r})] - E[n(\mathbf{r})] \quad &= \delta T[n(\mathbf{r})] + \delta E_{xc}[n(\mathbf{r})] + \int v_{ext}(\mathbf{r})\delta n(\mathbf{r})\, d\mathbf{r} \\ &+ \int\int \frac{n(\mathbf{r}')\delta n(\mathbf{r})}{|\mathbf{r}-\mathbf{r}'|}\, d\mathbf{r}'\, d\mathbf{r}, \end{aligned} \tag{2.27}$$

which can be rewritten as:

$$\begin{aligned} \delta E[n(\mathbf{r})] \quad &= \int \frac{\delta T[n(\mathbf{r})]}{\delta n(\mathbf{r})}\delta n(\mathbf{r})\, d\mathbf{r} + \int \frac{\delta E_{xc}[n(\mathbf{r})]}{\delta n(\mathbf{r})}\delta n(\mathbf{r})\, d\mathbf{r} + \int v_{ext}(\mathbf{r})\delta n(\mathbf{r})\, d\mathbf{r} \\ &+ \int\int \frac{n(\mathbf{r}')}{|\mathbf{r}-\mathbf{r}'|}\delta n(\mathbf{r})\, d\mathbf{r}'\, d\mathbf{r}, \end{aligned} \tag{2.28}$$

by grouping the terms in Eq.2.28 together we have:

$$\delta E = \int \delta n(\mathbf{r}) \left\{ \frac{\delta T[n(\mathbf{r})]}{\delta n(\mathbf{r})} + v_{ext} + \int \frac{n(\mathbf{r}')}{|\mathbf{r}-\mathbf{r}'|}\, d\mathbf{r}' + \mu_{xc}[n(\mathbf{r})] \right\} d\mathbf{r}, \tag{2.29}$$

from which $\frac{\delta E}{\delta n(\mathbf{r})}$ can be identified as:

$$\frac{\delta E}{\delta n(\mathbf{r})} = \frac{\delta T[n(\mathbf{r})]}{\delta n(\mathbf{r})} + v_{ext} + \int \frac{n(\mathbf{r}')}{|\mathbf{r}-\mathbf{r}'|}\, d\mathbf{r}' + \mu_{xc}[n(\mathbf{r})], \tag{2.30}$$

where $\mu_{xc}[n(\mathbf{r})] = \frac{\delta E_{xc}}{\delta n(\mathbf{r})}$. The optimization condition $\frac{\delta E}{\delta n(\mathbf{r})} = 0$ leads to:

$$\frac{\delta T[n(\mathbf{r})]}{\delta n(\mathbf{r})} + v_{ext} + \int \frac{n(\mathbf{r}')}{|\mathbf{r}-\mathbf{r}'|}\, d\mathbf{r}' + \mu_{xc}[n(\mathbf{r})] = 0. \tag{2.31}$$

If we define by $\varphi \equiv v_{ext}(\mathbf{r}) + \int \frac{n(\mathbf{r}')}{|\mathbf{r}-\mathbf{r}'|}\, d\mathbf{r}'$, the optimization equation Eq.2.31 in conjunction with the the assumption that the electron density n(**r**)can be constructed using independent, non-interacting electron wave functions (i.e. $n(\mathbf{r}) = \sum |\psi(\mathbf{r})|^2$), gives us the **K**ohn-Sham equation:

$$\left\{ -\frac{1}{2}\hat{\nabla}^2 + \hat{\varphi} + \hat{\mu}_{xc} \right\} |\psi_i\rangle = \varepsilon_i |\psi_i\rangle, \tag{2.32}$$

where ε_i is the Lagrange undetermined multiplier, which has unit of energy per particle.

One noteworthy fact about the Kohn-Sham approach is the assumption of independent, hence non-interacting, electrons. This assumption is needed in order to break the differential equation of the many-body problem into individual Schrödinger-like equations as in Eq.2.32. Thus the problem is solved in the space of non-interacting particles and the result is mapped back to the real system. It is evident that a system of electrons in solids should be interacting hence making the

Kohn-Sham approach dubious but the scheme is validated by Hohenberg-Kohn theorems (within n-representability consideration), stipulating that as long as one is able to construct a given density out of antisymmetric wave functions (be it real or fictitious), the ground state density and energy of the system can be approached from above variationally and the equality holds only for the true ground state density. Therefore the only link between the real versus fabricated depiction of the system is the ground state electronic density. One can also notice that the Kohn-Sham equations form a set of one-particle Schrödinger-like equations with an effective potential of $\hat{V}_{eff} = \hat{\varphi} + \hat{\mu}_{ext}$ that treats the interactions felt by each *i-th* electron, from the other electrons, as a mean field. Hence despite the approach being unrealistic and treats the electrons independently, the potential within which the electrons are embedded effectively describes their interaction.

Each Kohn-Sham equation has to be solved self-consistently, with the steps of the self-consistent approach depicted in the diagram below. One starts with an initial guess for the wave function from which the density is constructed. The effective potential and the Hamiltonian is subsequently constructed and solved to produce a new set eigenfunctions $\left|\psi^{(n)}_{new,i}\right\rangle$. From the resulting new density $n^{(n)}_{new,i}(\mathbf{r})$, the new energy $\mathrm{E}_{new}\left[n^{(n)}_{new,i}(\mathbf{r})\right]$ is evaluated and one defines ΔE as:

$$|\Delta E| \equiv \left|E_{new}\left[n^{(n)}_{new,i}(\mathbf{r})\right] - E\left[n^{(n)}_{i}(\mathbf{r})\right]\right|. \tag{2.33}$$

A new density is constructed from both the old one and the new solution $n^{(n+1)}_{i} = \alpha n^{(n)}_{new,i} + (1-\alpha) n^{(n+1)}_{i}$, and it constitutes a new starting point for the subsequent steps until convergence is achieved, i.e. the condition $\Delta E < \delta_{tol}$ is satisfied, where $\delta_{tol} \in \mathbb{R}_{+}$.

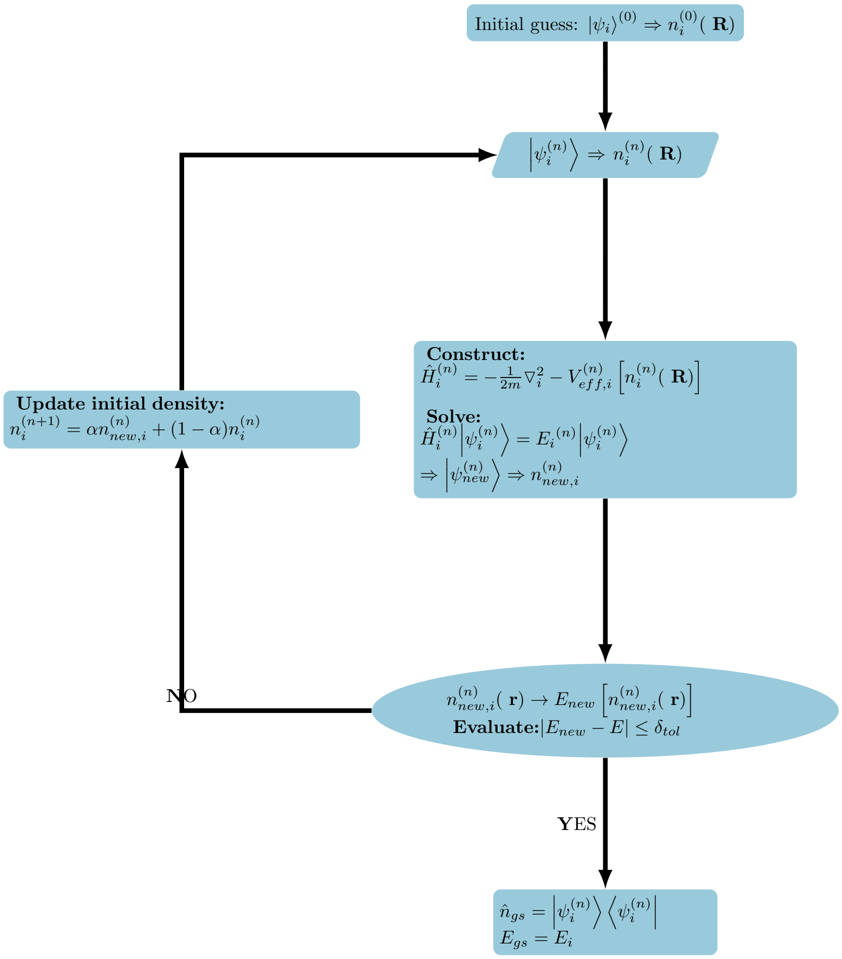

Figure 2.1: Diagram describing the pseudo algorithm for solving the Kohn-Sham equation.

2.1.3 Approximate exchange-correlation

We reiterate that the theory derived by Hohenberg and Kohn is in principle exact, and it has been demonstrated to be so for only two particular cases, namely: a near constant, and slowly varying electron gas densities. However these cases are far from the reality in materials where variations in the electronic densities are evident. It was realized very early in its development that the hindrance to the full fledged use of the exactness of DFT is due to the fact that the remaining possible electronic interactions, apart from the LR Coulomb interaction, were all lumped in on the term E$_{xc}$, and an exact functional form of this term remains elusive. Notwithstanding this limitation, practical calculations and near accurate predictions of electronic properties are obtained with DFT using approximate form of E$_{xc}$. Two such main approximations are:

1. Local Density Approximation (**L**DA),
2. Generalized Gradient Approximation (**G**GA).

LDA

The major assumption of the LDA is that locally, in a neighborhood $\delta\mathbf{r}$ of $\mathbf{r}$, the electrons behave like a homogeneous electron gas (non-interacting). Although electrons in solids do not behave like electron gases, the approximation is sensible in some region and it maps the problem to a solvable one. In the LDA approximation $E_{xc}[n(\mathbf{r})] = \int \epsilon_{xc}\delta n(\mathbf{r})\, d\mathbf{r}$, and the exchange and correlation effects are usually separated as $\epsilon_{xc} = \epsilon_x + \epsilon_c$.

Exchange The exchange functional has initially been investigated by Dirac [59] in 1930, right after Thomas and Fermi derived their models [55, 56]. In the Hartree-Fock theory, in order to correct for some unphysical results of the Hartree self-consistent equation, Fock considered the antisymmetric wave functions in the form of Slater determinant, which generates the exchange term E_x:

$$E_x = -\int\int \frac{\psi_1^*(\mathbf{r}_1)\psi_2^*(\mathbf{r}_2)\psi_1(\mathbf{r}_2)\psi_2(\mathbf{r}_1)}{|\mathbf{r}_1 - \mathbf{r}_2|}\, d\mathbf{r}'\, d\mathbf{r}. \tag{2.34}$$

This correction leads to the Hartree-Fock equation. E_x effectively lowers the Coulomb interaction between electrons of same spin as opposed to the electrons of different spin. Following the derivation of Ref. [60] the functional form of E_x stems from antisymmetric nature of fermions. Central to the derivation is the assumption of an "exchange hole" density of radius $\mathbf{r}_h = \left[\frac{4\pi}{3}n(\mathbf{r})\right]^{-\frac{1}{3}}$ surrounding an electron. This exchange hole prevents any other electron to occupy the sphere of radius r_h, thereby enforcing Pauli exclusion principle. Calculating the difference between the Coulomb potential of a homogeneously distributed electrons and the one resulting from the exchange hole yields:

$$\begin{aligned} \Delta E \quad &\approx n(\mathbf{r})^2 \left[\int_{r_h}^{\infty} d\mathbf{r}\frac{1}{r} - \int_{0}^{\infty} d\mathbf{r}\frac{1}{r}\right] = -n(\mathbf{r})^2 \left[\int_{0}^{r_h} 4\pi r^2 dr \frac{1}{r}\right] \\ &\approx -n(\mathbf{r})^2 \left[\int_{0}^{r_h} 4\pi r\, dr\right] = -2\pi n(\mathbf{r})^2 {r_h}^2. \end{aligned} \tag{2.35}$$

Using the expression of the exchange hole radius in term of density, and simplifying Eq.2.35 result in the so-called Dirac or Slater exchange:

$$\epsilon_x[n(\mathbf{r})] = A\int [n(\mathbf{r})]^{\frac{4}{3}}\, d\mathbf{r}, \tag{2.36}$$

where A is a real, proportionality constant.

Correlation The extent of correlation between electrons has been investigated by Ceperley and Alder [61] from Monte Carlo simulations of homogeneous electron gases, which determined the electronic distribution of non-interacting electrons. The correlation between two electrons obtained from the ensuing charge distribution. Ceperley and Alder's calculations were later parametrized by Perdew and Zunger [62] to yield the following approximation for correlation of unpolarized electronic gases [62]:

$$\epsilon_c = \begin{cases} \frac{-0.1432}{1+1.0529\sqrt{r_s}+0.3333r_s} & for\ r_s \geq 1 \\ -0.048 - 0.0116r_s + (0.0311 + 0.0020r_s)\ln(r_s) & for\ r_s < 1, \end{cases}$$

where the unit is atomic unit (a.u), r$_s$ is the Seitz radius, the radius of the sphere whose volume corresponds to the mean volume per atom in solid, and the functional form can be derived by using the identity $n(\mathbf{r}) = \left(\frac{4\pi}{3}r^3\right)^{-1}$.

Limitations of LDA

The LDA is the simplest of all the approximations of ϵ_{xc}, and in spite of this simplicity it is able to reproduce many experimental results to a good accuracy, with one example of this success being the reproduction of the phase transition of Si by Yin and Cohen [63, 64] with LDA reproducing volumes that are at most 1.1% different from the experimentally measured ones. Owing to this simplicity, computations are faster and tractable, which is one of the reasons why we have chosen LDA for all the calculations performed in this work.

However DFT within the LDA are not without blemish. *Ab initio* calculations using LDA often tend to underestimate the equilibrium lattice constant a_0 by about 1% [65], the energy band gap by about 50%. These shortcomings were thought to be related with the order of expansion, so attempts at next order correction lead to the GGA, an approximation that considers the dependence of the functional not only on the local density but also on its change or gradient.

$$E_{xc} = \int f\,[n(\mathbf{r}), \nabla n(\mathbf{r})]\; d\mathbf{r} \tag{2.37}$$

In doing so, the GGA corrects for the underestimation of lattice constant by the LDA and seems to yield lower prediction error. But GGA also has its problems as it is known to overestimate lattice constants instead. LDA and GGA's are known to suffer systematic problems associated with approximations of ϵ_{xc}. This is the non-vanishing electron self-interaction. In DFT there are energies associated with electrons interacting with itself, dubbed self-interaction energy, as a result of the mean-field approach to the electron-electron interaction. This result is inevitable when one intends to write the Coulomb interaction in a simple density functional form, for example. In general this self interaction should exactly cancel with the exchange term, in Hartree-Fock approach it does, but in DFT within LDA it does not, as pointed out by Perdew and Zunger. [62] Though the approach of Perdew and Zunger intended to write ϵ_{xc} in such a way that the exchange self-interaction cancels the self-interaction coming from the Hartree term, they do no exactly cancel each other.

There are several approximations of ϵ_{xc}, which are more sophisticated such as the meta-GGA (includes Laplacian of the density), hyper-GGA (includes an additional gradient of n($\mathbf{r}$) as compared to meta-GGA) or the hybrid functional (mixed LDA+exact exchange). Let us note that only few of these plethora of functional approximations are first-principles in nature. Many of the more sophisticated approximations: meta-GGA, or hybrid functional approximations require fitting to empirical data, hence strictly and pedantically speaking not first-principles.

In summary the DFT is a theory developed in an attempt to perform calculations of real materials properties out of quantum mechanics. The idea is that it would need a minimal set of inputs, only depending on the nature of the constituents of a given solid, and be able to predict the most stable phases or states depending on these inputs. The difficulty in getting the exact functional form of the exchange-correlation interactions between electrons seemingly stymied the full use of the theory but appropriate approximations gave rather good predictions within satisfactory accuracy. This success of LDA stems from the fortuitous fact that errors compensate one another.

2.2 Pseudopotential

2.2.1 Validity, and conditions for pseudopotential construction

In principle *ab initio* calculations take for only inputs the atomic number of the constituent atoms of a given material. This entails a possible consideration of a large number of electrons within one unit cell or supercell. However, considering all these electrons in our calculations is not computationally advantageous. It is known that the chemistry of a given material is dictated by only a group of electrons loosely bound to the nucleus, called "valence" electrons. The other group of electrons, the one tightly bound to the nucleus, are called "core" electrons and they interact less with the environment of the atoms and are considered chemically inert. This distinction between core and valence electrons should abate the complexity of the problem. The main idea behind the *pseudopotential* approach is to save computational effort by replacing the true all-electron potential V^{AE} with a potential V^{PP}, which is constructed in such a way to reproduce the same scattering properties.

The pseudopotential constructed has to meet the following conditions:

1. **E**xact valence condition:$|\psi^{PP}\rangle = |\psi^{AE}\rangle$ for $r > r_c$, which ensures that the pseudopotential V^{PP} (resp. ψ^{PP}) reproduce the exact valence as V^{AE} (resp. ψ^{AE}).

2. **N**odelessness condition: The pseudo wave function needs to be *nodeless* inside r_c. This condition enables us expand the pseudo wave function using less plane-wave bases.

3. **N**orm conservation condition: $\int_0^{r_c} |\psi^{PP}|^2 r^2 dr = \int_0^{r_c} |\psi^{AE}|^2 r^2 dr$. This condition guarantees the conservation of charge within the core region ($r < r_c(r_<)$).

4. **E**qual eigenvalue condition: $\varepsilon_l^{PP} = \varepsilon_l^{AE}$. This condition is self explanatory since it makes sure that both potential give the same eigenvalue.

The constructed potential fulfilling the 4 conditions above is called "*norm-conserving*" pseudopotential, first introduced by Hamann, Schlüter, and Chiang (HSC) [66]. The pseudopotential in question should describe the free atom very well. However, atoms in a solid are not free thus prompting a query of how to construct a potential such that it could be used in different environment. This leads to the so-called " **transferability condition**" given by:

$$2\pi \left[r\psi^2 \frac{d^2 \ln\psi}{d\varepsilon dr} \right]\Bigg|_{r=r_c} = 4\pi \int_0^{r_c} \psi^2 r^2 dr. \tag{2.38}$$

Eq.2.38 is the so-called Friedel sum rule which in scattering theory means that the scattering phase shift is constant up to a linear variation of the energy eigenvalue ε. The scattering phase shift being related to the scattering cross section, this reasoning entails that Eq.2.38 ensure that the scattering properties of V^{PP} are identical to those of V^{AE} when transferred to a new environment, at least to first order of the change of energy $\delta\varepsilon$. Another way to understand Eq.2.38 uses the well-known boundary condition from Quantum Mechanics treatment of finite well problems, where instead of using two conditions on ψ and $\frac{d\psi}{dr}$ one equates the logarithmic derivative $\frac{d\ln\psi}{dr} = \frac{\psi'}{\psi}$ to a constant. However one can argue that this constant should depend on the potential-well depth hence on the energy. Eq.2.38 in this regard implies that when the environment of the system is changed, the condition $\frac{d\ln\psi^{PP}}{dr} = \frac{d\ln\psi^{AE}}{dr}$, at r=r$_c$ holds to first order of $\delta\varepsilon$.

Pseudopotential Construction

The starting point of a pseudopotential construction is the radial Schrödinger equation or equivalently the radial Kohn-Sham equation, given by:

$$\left(-\frac{1}{2}\frac{d^2}{dr^2} + \frac{l(l+1)}{2r^2} + V^{AE}_{scr,l}[\rho, r]\right) r\psi^{AE}_l(r) = \varepsilon_l r\psi^{AE}_l(r). \tag{2.39}$$

The centrifugal barrier implies a dependence of the potential on the angular momentum l. The screened $V^{AE}_{scr,l}$ encompasses the electron-ion Coulomb interaction, the Hartree and the exchange correlation potential. Assuming a pseudo wave function $\psi^{PP}_l(r)$, resulting from a pseudo potential V^{PP}, fulfilling the conditions mentioned in the previous section, we can invert the radial Schrödinger equation:

$$V^{PP}_{scr,l}[\rho, r] = \varepsilon - \frac{l(l+1)}{2r^2} + \frac{1}{2(r\psi^{PP}_l(r))}\frac{d^2(r\psi^{PP}_l(r))}{dr^2}. \tag{2.40}$$

Note that the nodelessness condition guarantees that this inversion is well defined. The task of constructing a pseudopotential is then reduced to finding wavefunctions satisfying the aforementioned conditions. Right away it can be noticed that there are many functions which can be chosen to construct V^{PP} hinting to the variety of pseudopotential.

Troullier and Martins [67] employed Kerker's method [68] and started the construction by expressing $\psi^{PP}(r)$ as:

$$\psi_l^{PP}(r) = \begin{cases} r^l e^{p(r)} & r < r_c \\ \psi^{AE}(r) & r \geq r_c \end{cases}$$

where l is the angular momentum quantum number, and $p(r)$ is a polynomial. Kerker introduced the choice of either a polynomial or the exponential of a polynomial to express the core-region wave function, but because only the $e^{p(r)}$ guarantees a nodeless core wave function the latter expression is retained. The polynomial is given by the expression $p(r) = c_0 + \sum\limits_{i=2}^{n} c_i r^i$ where the first degree is skipped to reinforce nodelessness, and the coefficients c_i are generated in such a way to enforce all 4 conditions of a norm-conserving pseudopotential, as well as the transferability condition. Using the definition of $\psi_l^{PP}(r)$ and the inversion result of Eq.2.40 we can straightforwardly derive (See App.A.1):

$$V_{scr,l}^{PP} = \varepsilon + l(l+1)\left(\sum_{i=2}^{n} i c_i r^i\right) + \frac{1}{2}\left\{\sum_{i=2}^{n}\left(\sum_{j=2}^{n} j c_i c_j r^j + \sum_{i=2}^{n}(i-1)c_i\right) i r^{i-2}\right\}. \tag{2.41}$$

In a similar manner Bachelet, Hamann, and Schlüter [69] constructed a pseudo wave function that cuts off at the cutoff radius and gives the all-electron valence wave function at $r > r_c$. This cutoff is described by the function $f\left(\frac{r}{r_c}\right) = e^{-\left(\frac{r}{r_c}\right)^{\lambda}}$, where the parameter $\lambda = 3.5$ has been found to yield optimal result [69]. The BHS pseudopotential is given by (See App. A.2):

$$
\begin{aligned}
\hat{V}_{2j}(r) \quad &= \hat{V}_{1j}(r) + \frac{\delta_j r^{l+1} f\left(\frac{r}{r_c}\right)}{2w_{2j}(r)} \left[\frac{\lambda^2 \left(\frac{r}{r_c}\right)^{2\lambda} - [2l\lambda + \lambda(\lambda+1)] \left(\frac{r}{r_c}\right)^{2\lambda}}{r^2} \right] \\
&+ \frac{\delta_j r^{l+1} f\left(\frac{r}{r_c}\right)}{w_{2j}(r)} \left(\varepsilon_j - \hat{V}_{1j}(r)\right), \qquad (2.42)
\end{aligned}
$$

with $j = l \pm \frac{1}{2}$ indicates the total angular momentum, the pseudo wave function $w_{2j} = \gamma_j \left(w_{1j}(r) + \delta_j r^{l+1} f\left(\frac{r}{r_c}\right) \right)$ and $w_{1j}(r)$ the far range $(r_>)$ pseudo wave function which is identified to the major wave function solution of the Dirac equation. Once this screened potential is obtained, the bare ionic pseudopotential can be computed by subtracting the Hartree and the exchange correlation:

$$
V_{bare,l}^{PP} = V_{scr,l}^{PP} - \int \frac{\rho_l^{PP}(r')}{|r - r'|} dr' - \frac{\delta E_{xc}[\rho_l^{PP}]}{\delta \rho_l^{PP}}, \qquad (2.43)
$$

with $\rho_l^{PP}(r) = \sum_{occ} 4\pi r^2 \left(\psi_l^{PP}\right)^* (r) \psi_l^{PP}(r)$.

The BHS pseudopotential construction slightly differ from that of Troullier and Matins. The former describes the pseudopotential using Gaussian functions as basis with the short-range core given by:

$$
\hat{V}_{core} = -\frac{Z_v}{r} \left\{ c_i^{core} erf \left[\sum_{i=1}^{2} r \left(\alpha_i^{core}\right)^{\frac{1}{2}} \right] \right\}, \qquad (2.44)
$$

and the long-range potential by:

$$
\Delta\hat{V}_l = \sum_{i=1}^{3} A_i + r^2 A_{i+3} e^{-(\alpha_i r)^2}, \qquad (2.45)
$$

where Z$_v$ is the valence charge and $\{\alpha_i, c_i^{core}, A_i\}$ form a set of parameters to be determined. Troullier and Martins' construction however uses polynomial as seen in Eq.2.41.

Computationally it is useful to express the wave functions in solids in terms of plane wave basis, one of the main reason is that Bloch wave functions describing valence electrons are plane wave-like, and in atoms its expansion in terms of Spherical harmonics is quite natural. In the procedure just described for one angular momentum l one needs to compute mn^2 integrals, where m, and n indicate Brillouin zone (BZ) points and number of plane waves in the basis to be used in the computation. Because of symmetry only half of the matrix is calculated yielding $\frac{mn(n+1)}{2}$ operations. This is still a considerable computational effort but fortunately Kleinman and Bylander [70] showed that the number of integrals to be computed can be reduced to just mn by separating the bare pseudopotential into local and nonlocal. By nonlocal it should be understood that the pseudopotential depends on the angular coordinates in a nonlocal manner, i.e. admixing of both azimuthal and polar coordinates. The nonlocal part of the pseudopotential is obtained by projecting $V_{bare,l}^{PP}$ onto the space spanned by angular momentum wave function following:

$$\hat{V}_{l\pm\frac{1}{2}}^{NL}(r) = \frac{\left|V_l^{NL}\Psi_l^{PP}\right\rangle\left\langle V_l^{NL}\Psi_l^{PP}\right|}{\left\langle\Psi_l^{PP}\middle|V_l^{NL}\middle|\Psi_l^{PP}\right\rangle}, \tag{2.46}$$

with $\Psi_l^{PP} = \psi_l^{PP}(r)Y_m^l(\phi,\theta)$, is the total pseudo wave function. The approach by Kleinman and Bylander takes advantage of the property of the spherical harmonics Y_m^l, effectively reducing the calculations to only mn integrals (only the diagonal terms yield non zero integrals).

Relativistic consideration It is not hard to extend the norm-conserving pseudopotential to include the relativistic effect. Although the approach we described starts from the Kohn-Sham or Schrödinger equation , to second order of the fine structure constant α the description of the valence electrons from the Dirac equation involving the major wave function is Schrödinger-like, which means to a second order approximation our pseudopotential construction is correct. The relativistic correction of pseudopotential therefore needs to take into effect the intrinsic spin angular momentum of the electron, a natural consequence of Dirac equation. In fact, in some calculations spin-polarization is required and this can only be approached from relativistic consideration. The spin-orbit coupling is determined by the difference between both bare pseudopotentials V_j^{PP} for different values of spin $\pm\frac{1}{2}$ at the same l given by:

$$\hat{V}_l^{SO}(r) = \frac{2}{2l+1}\left(\hat{V}^{ion}_{l+\frac{1}{2}} - \hat{V}^{ion}_{l-\frac{1}{2}}\right). \tag{2.47}$$

The definition in Eq.2.47 enables us to determine the pseudopotential from relativistic calculation as:

$$\hat{V}^{ion}(r) = \sum_l |l\rangle \left[\hat{V}_l^{ion}(r) + \hat{V}_l^{SO}(r)\mathbf{L}\cdot\mathbf{S}\right]\langle l|, \tag{2.48}$$

where the average bare ion potential for relativistic calculation is determined by:

$$\hat{V}_l^{ion}(r) = \frac{1}{2l+1}\left(l\hat{V}^{ion}_{l-\frac{1}{2}} + (l+1)\hat{V}^{ion}_{l+\frac{1}{2}}\right). \tag{2.49}$$

There is no unique way to determine a given pseudopotential. Some pseudopotentials might have an advantage over others with respect to a given condition but are in fact doing worse on the other conditions. Say a smooth pseudopotential, a pseudopotential that converges rapidly, is desired. This requires a large cutoff radius r_c making it hard for the pseudopotential to be transferable. Another example can be the desire for a better accuracy, hence a better fidelity with respect to the all-electron potential through a smaller r_c. This means one should truncate the potential closer to the core. Although the result might reproduce the all-electron calculations very well, the computation time however hugely suffers from this treatment. So there seems to be a *quid pro quo* at work with each implementation of pseudopotential, and the choice of working with a given pseudopotential seems to be much determined by the limitations of the hardware, or the ease of implementation of the code to other calculations, and the use of some preferred bases.

2.3 Modern Theory of polarization

Polarization is a central thermodynamical quantity in FEs. Since its realization in Rochelle salt by Valasek in 1921, ferroelectricity of a given material has been routinely confirmed experimentally through the determination of **P-E** hysteretic behavior. Nonetheless meaningful theoretical calculations of **P** from first-principles have to wait 3 decades after the development of DFT to come into existence. This predicament is not an artifact of DFT but rather stems from a long-standing misconception about polarization in solid. In this chapter we are going to point out that the textbook definition of macroscopic polarization is inadequate, and incompatible for first-principles computation for crystalline solids, thereby prompting a redefinition in terms of quantum geometric phase. We are then going to visit how this modern theory molds with DFT.

2.3.1 Preamble: Failure of classical viewpoint and paradigm shift

Electric polarization is classically understood as the dipole per unit volume of a given solid. This thermodynamical quantity, can in principle be measured and it is an intensive quantity, which means that simply extending the sample doesn't increase its value. Martin[71] also convincingly showed that **P** is a bulk quantity[71], i.e. a quantity which depends on properties of the bulk not the surface, which in the case of thick materials are relatively far from the bulk region that the depolarization effect is negligible. The macroscopic **P** does not change whatever the surface properties are.

From textbooks on Electricity and Magnetism [72, 73], electric polarization is defined as the dipole moment per unit volume of a given material:

$$\mathbf{P} = \frac{1}{V}\sum_i q_i \mathbf{r}_i, \tag{2.50}$$

where $\mathbf{r}_i$ is the position vector of a charge q_i and V the volume of the material under consideration. In Eq.2.50, the summation runs over all the dipole moments present in the volume V, using the superposition principle, in the well-known *Clausius-Mossotti* (CM) model. The extension of Eq.2.50 to the continuum case is not too difficult:

$$\mathbf{P} = \frac{1}{V}\int \mathbf{r}\rho(\mathbf{r})\ d\mathbf{r}, \tag{2.51}$$

where $\rho(\mathbf{r})$ is the charge density distribution. Because the main results of DFT are the ground state energy and the ground state density, the calculation of P using the CM model in DFT should be a straightforward matter. Nevertheless this is not the case since the CM presumes well-defined dipole centers, which are only unequivocal in the case of extreme ionic bonding between ions in materials such as NaCl. In crystalline materials such as the perovskite oxides, we generally encounter a mixture of covalent and ionic bonding hence the ambiguity in defining dipole centers since different choices of dipole center may lead to different values of **P**.

Other approaches at defining **P** are also found inconsistent with electronic behavior in solids, namely:

1. $\mathbf{P}=\frac{1}{V}\sum_{\mu}\mathbf{P}_\mu$, with microscopic polarization $\mathbf{P}_\mu$ given by the differential form of Gauss' law,

$\nabla \cdot \mathbf{P}_\mu = -\rho(\mathbf{r})$, is not unique because $\mathbf{P}_\mu + f$, where f is a divergenceless function, will yield the same density ρ.

2. $\mathbf{P} = \int_{sample} \mathbf{r}\rho(\mathbf{r})\, d\mathbf{r}$ can be split into bulk and surface contribution. Any change in surface preparations leaving the bulk property intact, such as surface termination should change the contribution from the surface, thereby changing **P**, yet **P** is a bulk quantity so its value should not change.

Moreover, experimentally one does not have direct access to the value of polarization. In fact, the value of absolute polarization is indirectly extracted from measurements involving change of **P** such as: the (E-P) hysteresis curves where $P = \frac{\Delta P(E=0)}{2}$, the primary pyroelectric coefficients $\gamma_p^k = \frac{\partial P^k}{\partial T}\Big|_{E,\sigma}$, or the piezoelectric coefficients $e_\alpha^{\beta\gamma} = \frac{\partial P_\alpha}{\partial \eta_{\beta\gamma}}$.

The realization that the value of **P** cannot be accessed directly either from experimental measurements, or from theoretical calculations triggered the reevaluation of which quantity is more fundamental: Δ**P** or **P**. In fact Resta [74] has proven that $\frac{dP}{d\lambda}$, where λ corresponds to thermodynamically controllable parameters, is theoretically a well-defined quantity. This puts forth the argument that the quantity being experimentally measured, Δ**P** is indeed a fundamental quantity, rather than just a convenient mean to an end. Soon after Resta's paper, King-Smith and Vanderbilt [75] outlined the first successful ab-initio approach to calculate P in crystalline polar materials. Resta, King-Smith and Vanderbilt have thenceforth defined the *Modern Theory of Polarization* (MTP).

2.3.2 Modern Theory of Polarization

To construct the result of the MTP we are going to assume that during a measurement the system starts at a state $P(\lambda_0)$ and ends up at a state $P(\lambda_f)$, where λ is a parameter. The fundamental quantity ΔP is therefore given by:

$$\Delta P = P(\lambda_f) - P(\lambda_0) = \int_{\lambda_0}^{\lambda_f} \frac{dP}{d\lambda} d\lambda. \tag{2.52}$$

We are further considering that the process undergone by the system, $P(\lambda_0) \to P(\lambda_f)$, is adiabatic. Theoretically this means the time τ between measurements of $P(\lambda_0)$, and $P(\lambda_f)$ tends to infinity ($\tau \to \infty$). Practically, as long as $\tau \gg t_c$, where t_c is a pertinent characteristic time of the polar material, for instance the dielectric relaxation time, the adiabatic approximation [76] can be applied.

Adiabatic Theorem

Suppose that we have a system whose Hamiltonian $\hat{H}$ *adiabatically changes from* $\hat{H}^i$ *to* $\hat{H}^f$ *such that* $\hat{H}^i \left|\psi_n^i\right\rangle = E_n^i \left|\psi_n^i\right\rangle$, *and* $\hat{H}^f \left|\psi_n^f\right\rangle = E_n^f \left|\psi_n^f\right\rangle$. *Then we have the bijective relation:* $\left|\psi_n^i\right\rangle \longrightarrow \left|\psi_n^f\right\rangle = e^{i\theta(t)} e^{\gamma(t)} \left|\psi_n^i\right\rangle$, *with*

$$\theta(t) \equiv -\frac{1}{\hbar} \int_0^t E_n(t')\, dt', \tag{2.53}$$

and

$$\gamma(t) \equiv i \int_0^t \left\langle \psi_m \middle| \frac{\partial \psi_m}{\partial t'} \right\rangle dt'. \tag{2.54}$$

What the adiabatic theorem entails is that even though the Hamiltonian of the system changes ($\hat{H}^i \rightarrow \hat{H}^f$), the change is slow enough that the order of the states are left unchanged, and the initial and final states only differ by a phase factor. The phase factor can be split into two phases: a **dynamic** phase given by $\theta(t)$ in Eq. 2.53, and a **geometric** phase given by $\gamma(t)$ in Eq. 2.54.

Berry Phase

Focusing on the geometric phase, let us rewrite $\gamma(t)$ as :

$$\gamma(t) = i\int_0^t \left\langle \psi_m \middle| \frac{\partial \psi_m}{\partial t'} \right\rangle dt' = i\int_{\lambda_0}^{\lambda_f} \left\langle \psi_m \middle| \frac{\partial \psi_m}{\partial \lambda} \right\rangle \frac{d\lambda}{dt'}\, dt', \tag{2.55}$$

for any parameter λ. Now if we assume we have n independent parameters λ_n. We can rewrite γ as:

$$\gamma(\lambda) = i\int_{\lambda_0}^{\lambda_f} \langle \psi_m | \nabla_\lambda | \psi_m \rangle\, d\lambda. \tag{2.56}$$

The integrand in Eq.2.56 $\chi(\lambda) = i\langle \psi_m | \nabla_\lambda | \psi_m \rangle$ is called Berry's connection and the quantity $\gamma(\lambda)$ is known as the Berry phase. Let us note that the path in the parameter space can be open or closed. The Berry's connection depends on the path taken in the parameter space implying gauge dependence, however the Berry phase is path or gauge invariant. There are many manifestations of Berry phase such as the Pancharatnam phase in optics, the Aharonov-Bohm effect, etc. that were discovered prior to Berry's work [77]. One phase of particular interest to us is that which is pertinent to Bloch electrons dubbed Zak's phase [78], first derived by Zak [79].

According to Bloch theorem, electrons in solids, subject to periodic boundary condition

$\hat{H}(\mathbf{r}+\mathbf{R}) = \hat{H}(\mathbf{r})$ for any lattice vector $\mathbf{R}$, is described by:

$$\psi_{n,\mathbf{k}}(\mathbf{r}) = e^{i\mathbf{k}\cdot\mathbf{r}} u_{n,\mathbf{k}}(\mathbf{r}), \tag{2.57}$$

where $u_{n,\mathbf{k}}(\mathbf{r}) = u_{n,\mathbf{k}}(\mathbf{r}+\mathbf{R})$ is translationally invariant, and obeys:

$$H_{\mathbf{k}}^{(\lambda)} = \frac{1}{2m_e}(\mathbf{p} + \hbar\mathbf{k})^2 + V^{(\lambda)}(\mathbf{r}). \tag{2.58}$$

Using the transformation Eq. 2.57 along with the periodic boundary condition Eq. 2.56 can be rewritten as:

$$\chi(\mathbf{k}) = i\sum_n \langle u_{n,\mathbf{k}} | \nabla_k u_{n,\mathbf{k}} \rangle, \tag{2.59}$$

where $u_{n,\mathbf{k}}$ is the periodic part of the Bloch function in Eq. 2.57, the reciprocal vector $\mathbf{k}$ is chosen as the parameter.

Berry phase and modern theory of polarization

A heurestic connection between Zak's phase and $\mathbf{P}$ in FE materials may be useful. Our approach follow the same line as that presented in Ref. [31]. We begin with the postulate of modern theory of polarization, using the classical definition of polarization, that is:

$$\Delta\mathbf{P} = \mathbf{P}(\lambda_f) - \mathbf{P}(\lambda_0) = \int_{\lambda_0}^{\lambda_f} \frac{dP}{d\lambda}\, d\lambda. \tag{2.60}$$

Using the chain rule $\frac{dP}{d\lambda}\frac{d\lambda}{dt} = \frac{dP}{d\lambda}\dot{\lambda} = \frac{dP}{dt}$, we can rewrite Eq.2.60 as follow:

$$\Delta\mathbf{P} = \int_{\lambda_0}^{\lambda_f} \frac{1}{\dot{\lambda}}\frac{dP}{dt}\, d\lambda. \tag{2.61}$$

Eq.2.60 is rewritten in this manner to take advantage of the identity: $\mathbf{j} = \frac{dP}{dt}$. So Eq.2.61 becomes:

$$\Delta\mathbf{P} = \int_{\lambda_0}^{\lambda_f} \frac{1}{\dot{\lambda}}\langle\mathbf{j}\rangle\, d\lambda. \tag{2.62}$$

The adiabatic perturbation theory gives us the first-order correction [31, 78]

$$\left|\delta\psi^{(\lambda)}_{n,\mathbf{k}}\right\rangle = -i\hbar\dot{\lambda}\sum_{m\neq n}\frac{\left\langle\psi^{(\lambda)}_{m,\mathbf{k}}\middle|\partial_\lambda\psi^{(\lambda)}_{n,\mathbf{k}}\right\rangle\left|\psi^{(\lambda)}_{m,\mathbf{k}}\right\rangle}{\varepsilon^{(\lambda)}_{n,\mathbf{k}} - \varepsilon^{(\lambda)}_{m,\mathbf{k}}}, \tag{2.63}$$

with $\partial_\lambda = \frac{\partial}{\partial\lambda}$ The polarization current $\mathbf{j}$ is obtained from:

$$\left\langle\mathbf{j}_n\right\rangle = -fe\langle\hat{\mathbf{v}}\rangle, \tag{2.64}$$

where f is the occupation of the electronic band n, e the charge of the electron and $\hat{\mathbf{v}}$ the velocity operator, which can be written in term of the momentum operator $\hat{\mathbf{p}}$ as $\hat{\mathbf{v}} = \frac{\hat{\mathbf{p}}}{m} = \frac{-i\hbar\nabla_{\mathbf{r}}}{m}$.

In the adiabatic process we can compute the expectation value of the polarization current as:

$$\left\langle\mathbf{j}_n\right\rangle = -fe\left\langle\psi^{(\lambda)}_{n,\mathbf{k}} + \delta\psi^{(\lambda)}_{n,\mathbf{k}}\middle|\hat{\mathbf{v}}\middle|\psi^{(\lambda)}_{n,\mathbf{k}} + \delta\psi^{(\lambda)}_{n,\mathbf{k}}\right\rangle. \tag{2.65}$$

By grouping the first-order terms in the perturbation we have:

$$\left\langle \mathbf{j}_n \right\rangle = -fe \left\langle \delta\psi_{n,\mathbf{k}}^{(\lambda)} \middle| \hat{\mathbf{v}} \middle| \psi_{n,\mathbf{k}}^{(\lambda)} \right\rangle + \left\langle \psi_{n,\mathbf{k}}^{(\lambda)} \middle| \hat{\mathbf{v}} \middle| \delta\psi_{n,\mathbf{k}}^{(\lambda)} \right\rangle. \tag{2.66}$$

Summing over the Brillouin zone and using the momentum operator instead of $\hat{\mathbf{v}}$, Eq.2.66 becomes:

$$\left\langle \mathbf{j}_n \right\rangle = \frac{-fe}{(2\pi)^3} \int \left\{ \left\langle \psi_{n,\mathbf{k}}^{(\lambda)} \middle| \frac{\hat{\mathbf{p}}}{m} \middle| \delta\psi_{n,\mathbf{k}} \right\rangle + c.c \right\} d\mathbf{k}, \tag{2.67}$$

where c.c. indicates complex conjugate. When we plug Eq.2.63 in Eq.2.67, we have:

$$\left\langle \mathbf{j}_n \right\rangle = \frac{-fe}{(2\pi)^3} \int \left\{ \left\langle \psi_{n,\mathbf{k}}^{(\lambda)} \middle| \frac{\hat{\mathbf{p}}}{m} \middle| -i\hbar\dot{\lambda} \sum_{m\neq n} \frac{\left\langle \psi_{m,\mathbf{k}}^{(\lambda)} \middle| \partial_\lambda \psi_{n,\mathbf{k}}^{(\lambda)} \right\rangle \left| \psi_{m,\mathbf{k}}^{(\lambda)} \right\rangle}{\varepsilon_{n,\mathbf{k}}^{(\lambda)} - \varepsilon_{m,\mathbf{k}}^{(\lambda)}} \right\rangle + c.c \right\} d\mathbf{k}, \tag{2.68}$$

which can be rearranged as [31]:

$$\left\langle \mathbf{j}_n \right\rangle = \frac{i\hbar fe\dot{\lambda}}{(2\pi)^3 m} \sum_{m\neq n} \int \left\{ \frac{\left\langle \psi_{n,\mathbf{k}}^{(\lambda)} \middle| \hat{\mathbf{p}} \middle| \psi_{m,\mathbf{k}}^{(\lambda)} \right\rangle \left\langle \psi_{m,\mathbf{k}} \middle| \partial_\lambda \psi_{n,\mathbf{k}}^{(\lambda)} \right\rangle}{\varepsilon_{n,\mathbf{k}}^{(\lambda)} - \varepsilon_{m,\mathbf{k}}^{(\lambda)}} + c.c. \right\} d\mathbf{k}. \tag{2.69}$$

Now, the change in polarization in Eq.2.62 becomes:

$$\Delta\mathbf{P} = \frac{i\hbar fe}{(2\pi)^3 m} \int_{\lambda_0}^{\lambda_f} \sum_{m\neq n} \int \left\{ \frac{\left\langle \psi_{n,\mathbf{k}}^{(\lambda)} \middle| \hat{\mathbf{p}} \middle| \psi_{m,\mathbf{k}}^{(\lambda)} \right\rangle \left\langle \psi_{m,\mathbf{k}}^{(\lambda)} \middle| \partial_\lambda \psi_{n,\mathbf{k}}^{(\lambda)} \right\rangle}{\varepsilon_{n,\mathbf{k}}^{(\lambda)} - \varepsilon_{m,\mathbf{k}}^{(\lambda)}} + c.c. \right\} d\mathbf{k}\, d\lambda. \tag{2.70}$$

Therefore, for any adiabatic perturbation λ, $\frac{d\mathbf{P}}{d\lambda}$ is given by:

$$\frac{d\mathbf{P}}{d\lambda} = \frac{i\hbar fe}{(2\pi)^3 m} \sum_{m\neq n} \int \left\{ \frac{\left\langle \psi_{n,\mathbf{k}}^{(\lambda)} \middle| \hat{\mathbf{p}} \middle| \psi_{m,\mathbf{k}}^{(\lambda)} \right\rangle \left\langle \psi_{m,\mathbf{k}}^{(\lambda)} \middle| \partial_\lambda \psi_{n,\mathbf{k}}^{(\lambda)} \right\rangle}{\varepsilon_{n,\mathbf{k}}^{(\lambda)} - \varepsilon_{m,\mathbf{k}}^{(\lambda)}} + c.c. \right\} d\mathbf{k} \tag{2.71}$$

If we use the result of perturbation theory on $\left|\partial_\lambda \psi^{(\lambda)}_{n,\mathbf{k}}\right\rangle$, we have:

$$\frac{d\mathbf{P}}{d\lambda} = \frac{i\hbar f e}{(2\pi)^3 m} \sum_{m\neq n} \int \left\{ \frac{\left\langle \psi^{(\lambda)}_{n,\mathbf{k}} \middle| \hat{\mathbf{p}} \middle| \psi^{(\lambda)}_{m,\mathbf{k}} \right\rangle \left\langle \psi^{(\lambda)}_{m,\mathbf{k}} \middle| \frac{\partial V^\lambda}{\partial\lambda} \middle| \psi^{(\lambda)}_{n,\mathbf{k}} \right\rangle}{\left(\varepsilon^{(\lambda)}_{n,\mathbf{k}} - \varepsilon^{(\lambda)}_{m,\mathbf{k}}\right)^2} + c.c. \right\} d\mathbf{k} \tag{2.72}$$

Using the identity:

$$\frac{\hbar\nabla}{i}\left|\psi^{(\lambda)}_{n,\mathbf{k}}\right\rangle = e^{i\mathbf{k}\cdot\mathbf{r}}\left(\hbar\mathbf{k} + \frac{\hbar}{i}\nabla\right)\left|u^{(\lambda)}_{n,\mathbf{k}}\right\rangle = e^{i\mathbf{k}\frac{m}{\hbar}\cdot\mathbf{r}}\nabla_{\mathbf{k}}\hat{H}^{(\lambda)}_{\mathbf{k}}\left|u^{(\lambda)}_{n,\mathbf{k}}\right\rangle, \tag{2.73}$$

with the Hamiltonian $\hat{H}^{(\lambda)}_{\mathbf{k}}$ defined by in Eq.2.58, we can rewrite Eq.2.71:

$$\frac{d\mathbf{P}}{d\lambda} = \frac{i f e}{(2\pi)^3} \sum_{m\neq n} \int \left\{ \frac{\left\langle u^{(\lambda)}_{n,\mathbf{k}} \middle| \nabla_{\mathbf{k}}\hat{H}^{(\lambda)}_{\mathbf{k}} \middle| u^{(\lambda)}_{m,\mathbf{k}} \right\rangle \left\langle u^{(\lambda)}_{m,\mathbf{k}} \middle| \partial_\lambda u^{(\lambda)}_{n,\mathbf{k}} \right\rangle}{\varepsilon^{(\lambda)}_{n,\mathbf{k}} - \varepsilon^{(\lambda)}_{m,\mathbf{k}}} + c.c. \right\} d\mathbf{k}. \tag{2.74}$$

After writing the expression of $\nabla_{\mathbf{k}} u^{(\lambda)}_{n,\mathbf{k}}$ from first order perturbation theory, we have:

$$\left|u^{(\lambda)}_{n,\mathbf{k}+\Delta\mathbf{k}}\right\rangle \approx \left|u^{(\lambda)}_{n,\mathbf{k}}\right\rangle + \sum_{m\neq n} \frac{\left\langle u^{(\lambda)}_{n,\mathbf{k}} \middle| \Delta H \middle| u^{(\lambda)}_{m,\mathbf{k}} \right\rangle}{\varepsilon^{(\lambda)}_{n,\mathbf{k}} - \varepsilon^{(\lambda)}_{m,\mathbf{k}}} \left|u^{(\lambda)}_{m,\mathbf{k}}\right\rangle, \tag{2.75}$$

where $\Delta H = \nabla_{\mathbf{k}} H^{(\lambda)}_{\mathbf{k}} \cdot d\mathbf{k}$ is the perturbing potential. We then get the expression of $\nabla_{\mathbf{k}} u^{(\lambda)}_{n,\mathbf{k}}$ from Eq.2.75:

$$\left|\nabla_{\mathbf{k}} u^{(\lambda)}_{n,\mathbf{k}}\right\rangle = \sum_{m\neq n} \frac{\left\langle u^{(\lambda)}_{n,\mathbf{k}} \middle| \nabla_{\mathbf{k}} H \middle| u^{(\lambda)}_{m,\mathbf{k}} \right\rangle}{\varepsilon^{(\lambda)}_{n} - \varepsilon^{(\lambda)}_{m}} \left|u^{(\lambda)}_{m,\mathbf{k}}\right\rangle. \tag{2.76}$$

Using Eq.2.76, the simplification of Eq.2.74 straightforwardly gives:

$$\frac{d\mathbf{P}}{d\lambda} = \frac{i f e}{(2\pi)^3} \sum_{n} \int \left\{ \left\langle \nabla_{\mathbf{k}} u^{(\lambda)}_{n,\mathbf{k}} \middle| \frac{\partial}{\partial\lambda} u^{(\lambda)}_{n,\mathbf{k}} \right\rangle + c.c. \right\} d\mathbf{k}. \tag{2.77}$$

It is relatively simple to show that:

$$\left(\nabla\times\chi\right)_{\alpha,\beta}=\nabla\times\left\langle u_{n,\mathbf{k}}^{(\lambda)}\middle|\nabla_{\mathbf{k}}u_{n,\mathbf{k}}^{(\lambda)}\right\rangle=\left\langle\frac{\partial u_{n,\mathbf{k}}^{(\lambda)}}{\partial\xi_\alpha}\middle|\frac{\partial u_{n,\mathbf{k}}^{(\lambda)}}{\partial\xi_\beta}\right\rangle. \tag{2.78}$$

By noting that the three vector **k** and λ constitute our parameters, we have:

$$\Delta\mathbf{P}=-\frac{fe}{(2\pi)^3}\Im\sum_n\int_\sigma\nabla_{\mathbf{k}}\times\left\langle u_{n,\mathbf{k}}^{(\lambda)}\middle|\nabla_{\mathbf{k}}u_{n,\mathbf{k}}^{(\lambda)}\right\rangle\,d\sigma. \tag{2.79}$$

Replacing part of the integrand using result from Eq.2.59 yields the expression of the electronic polarization in terms of the gauge invariant Berry curvature $\gamma(\lambda)$, which is given by:

$$\gamma(\lambda)=-\Im\sum_n\oint d\mathbf{k}\left\langle u_{n,\mathbf{k}}^{(\lambda)}\middle|\nabla_{\mathbf{k}}u_{n,\mathbf{k}}^{(\lambda)}\right\rangle=-\Im\sum_n\oint d\mathbf{k}\times\chi(\mathbf{k}). \tag{2.80}$$

Hence

$$\Delta\mathbf{P}=\frac{fe}{(2\pi)^3}\gamma(\lambda). \tag{2.81}$$

We can from Eq.2.81 that the electronic polarization is indeed related with Berry Phase.

2.3.3 First-principles implementation

The idea behind the modern theory of polarization is to calculate the contribution of electrons to the polarization of a given FE phase corresponding to parameter λ_f with respect to a reference phase, which corresponds to λ_0. One usually takes the centrosymmetric atomic configuration (P(λ_0)=0) as the reference phase, so that the result effectively gives the desired polarization of the FE system at the required configuration λ_f. The parameter λ in this case is associated with adiabatic shift of atomic positions, which implies that $\frac{\partial V}{\partial \lambda}$ amounts to the deformation potential as the atomic positions $\mathbf{R}_i^{\lambda_0} \longrightarrow \mathbf{R}_i^{\lambda_0} + \frac{n}{N}\Delta\mathbf{R}_i$, where $\Delta\mathbf{R}_i = \mathbf{R}_i^{\lambda_f} - \mathbf{R}_i^{\lambda_0}$. The quantity n and N, respectively determine the incremental and total number of steps taken in moving the atoms from the centrosymmetric to the optimal, polar geometry. The electric polarization of a polar material can therefore be calculated from Eq.2.72 under the condition that the system remains insulating throughout its path in parameter space.

It can be seen that a first-principles implementation of Eq.2.72 is straightforward since the quantities: $u_{m,\mathbf{k}}$, $\hat{p}^{\alpha}$, and $\frac{\partial V}{\partial \lambda}$ can easily be obtained from DFT. By defining the overlap matrices S:

$$S_{mn}(\xi_s, \xi_{s+1}) = \left\langle u_{m,\xi_s} \middle| u_{n,\xi_{s+1}} \right\rangle, \tag{2.82}$$

It can be shown (see App.B.1), that the Berry's phase can be calculated straightforwardly from:

$$d\varphi(\xi_{,s}\xi_{s+1}) = \Im \ln \det S(\xi_s, \xi_{s+1}), \tag{2.83}$$

whence the closed loop Berry phase:

$$\oint d\varphi \approx \sum_s \Delta\varphi_s = \Im \ln \prod_s \det S(\xi_s, \xi_{s+1}). \tag{2.84}$$

The discrete approach to Berry phase calculation (BPC) is natural in DFT since Monkhorst and Pack [80] showed that a discrete summation over a judiciously chosen finite set of k-points in the 1BZ is representative of a 1BZ integration, which provides significant computational edge in DFT in general. The phase is consequently calculated as follow:

1. Determine the number of Brillouin zone k-points over which to perform the Berry phase

computation.

2. Fix a surface Σ_{BP} in the 1BZ and define $\mathbf{k}_\perp$ such that $\mathbf{k}_\perp \in \Sigma_{BP}$.

3. For each $\mathbf{k}_\perp \in \Sigma_{BP}$, compute $S(\mathbf{k}_{\parallel,s}, \mathbf{k}_{\parallel,s+1}) \longrightarrow \varphi_\parallel(\mathbf{k}_\perp) = \sum_s \Im \ln \det S$.

4. $\varphi_{tot} = \sum_{\mathbf{k}_\perp} \varphi_\parallel(\mathbf{k}_\perp) w(\mathbf{k}_\perp)$, where $w(\mathbf{k}_\perp)$ is the weight.

With our knowledge of the electronic contribution ΔP_{el}, the total polarization of the system is consequently written as:

$$\mathbf{P}_{tot} = \sum_i Z_i \left(\mathbf{r}_i^f - \mathbf{r}_i^0 \right) + \Delta \mathbf{P}_{el}, \tag{2.85}$$

where $\mathbf{r}_i$ indicate the ionic coordinate and Z_i the charge of the ion i. Ideally this is the bare nucleonic charge, but because of the pseudopotential and the idea of the inert core, Z_i becomes the effective nucleonic charge seen by the valence electrons, i.e. core electronic charge in addition to the bare ionic charge.

Finally, it should be mentioned that the electric polarization derived from the quantum geometric phase is not single-valued. This is a consequence of the choice of the parallel transport gauge: $u_{n,\mathbf{k}}^\lambda = e^{i\mathbf{G}\cdot\mathbf{r}} u_{n,\,\mathbf{k}+\mathbf{G}}^\lambda$, [75] where $\mathbf{G}$ is a reciprocal lattice vector. With this gauge choice we can calculate $\Delta\mathbf{P} = P^{\lambda_f} - P^{\lambda_0}$. We can write ΔP^α as:

$$\Delta P^\alpha = \frac{fe}{(2\pi)^3} \sum_n \int_{1BZ} \left\langle u_{n,\mathbf{k}}^{(\lambda_f)} \middle| \frac{\partial}{\partial k_\alpha} \middle| u_{n,\mathbf{k}}^{(\lambda_f)} \right\rangle - \left\langle u_{n,\mathbf{k}}^{(\lambda_0)} \middle| \frac{\partial}{\partial k_\alpha} \middle| u_{n,\mathbf{k}}^{(\lambda_0)} \right\rangle d\mathbf{k}. \tag{2.86}$$

Knowing that we have the gauge choice $u_{n,\mathbf{k}}^{\lambda_f} = e^{i\theta_{n,\mathbf{k}}} u_{n,\mathbf{k}}^{\lambda_0}$, Eq.2.86 simplifies to:

$$\Delta P^\alpha = \frac{fe}{(2\pi)^3} \sum_n \int_{1BZ} \left\langle u_{n,\mathbf{k}}^{(\lambda_0)} \middle| u_{n,\mathbf{k}}^{(\lambda_0)} \right\rangle \frac{\partial \theta_{n,\mathbf{k}}}{\partial k_\alpha} d\mathbf{k} = \frac{fe}{(2\pi)^3} \sum_n \int_{1BZ} \frac{\partial \theta_{n,\mathbf{k}}}{\partial k_\alpha} d\mathbf{k}, \tag{2.87}$$

with $\left\langle u_{n,\mathbf{k}}^{(\lambda_0)} \middle| u_{n,\mathbf{k}}^{(\lambda_0)} \right\rangle$ is the identity operator, and the phase $\theta_{n,\mathbf{k}}$ can be generally expressed as[75]:

$$\theta_{n,\mathbf{k}} = \beta_{n,\mathbf{k}} + \mathbf{k} \cdot \mathbf{R}_i, \tag{2.88}$$

with $\beta_{n,\mathbf{k}}$ periodic in $\mathbf{k}$. Because of its periodicity $\int\limits_{1BZ} \nabla_{\mathbf{k}} \beta_{n,\mathbf{k}} \; d\mathbf{k} = 0$ and Eq.2.87 then reduces to:

$$\Delta \mathbf{P} = \frac{fe}{(2\pi)^3} \sum_n \int\limits_{1BZ} \mathbf{R}_i \; d\mathbf{k} = \frac{fe}{(2\pi)^3} \frac{\mathbf{R}_i (2\pi)^3}{\Omega} = \frac{fe}{\Omega} \mathbf{R}_i. \tag{2.89}$$

Eq.2.89 defines what is called the “quantum of polarization”. In fact, Berry phase calculations of polar material are well-defined up to P_{quan}. This multi-valuedness of $\mathbf{P}$ can be simply understood by considering Fig.2.2, which depicts a polar material with the polarization described by the arrows. $\mathbf{P}_1$ and $\mathbf{P}_2$ have different magnitudes but it is obvious to see that they describe the same ionic displacement, thus effectively the same local dipole moment. Indistinguishability and translational invariance of a given electronic environment validate the fact that the resulting computation of a given geometric phase may give us phases viewed with respect to different references, but which belong to the same congruence class nonetheless. If the reference for $\mathbf{P}_2$ is translated exactly one lattice vector upward, to give $\mathbf{P}_2'$, then $\mathbf{P}_2'$=$\mathbf{P}_1$. This can be generalized to any translation $\mathbf{t} = \alpha^i \mathbf{R}_i$, where $\alpha^i \in \mathbb{Z}$, and $\mathbf{R}_i$ are lattice vectors. This is the essential idea behind “branching” in MTP, i.e. the shifting of the phase by multiples of $\mathbf{P}_{quan}$. This problem does not arise often for simple Berry phase calculations since there is usually an order of magnitude difference between $\mathbf{P}$ and $\mathbf{P}_{quan}$ ($\Delta P \ll P_{quan}$). However in supercell calculations both quantities become commensurate and the calculated phase can often switch between polarization branches.

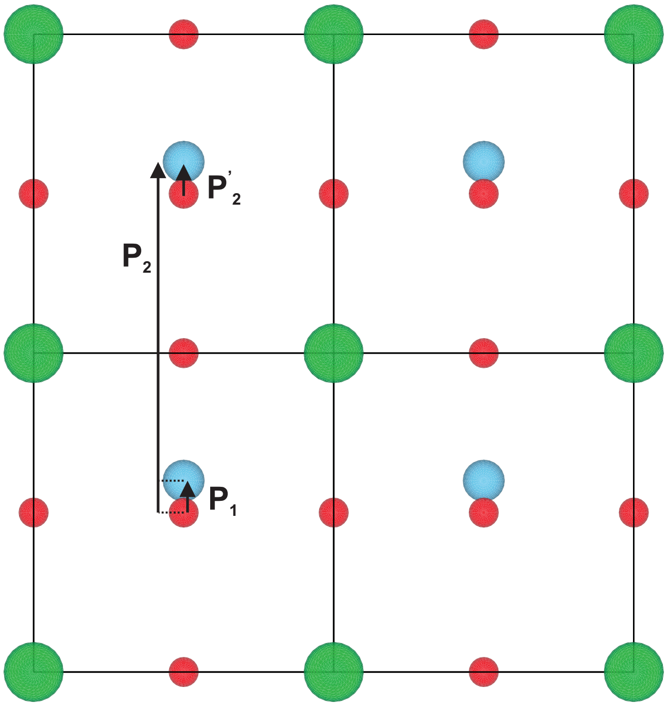

Figure 2.2: Figure elucidating the meaning of P_{quan}

2.3.4 Polarization for charged system

Let us note that a result akin to that of the CM model can be recovered in the MTP by considering Wannier functions which is a Fourier transform of the Bloch wave function:

$$w_{n,\mathbf{R}}(\mathbf{r}\text{-}\mathbf{R}) = \frac{V}{(2\pi)^3} \int\limits_{1BZ} e^{i\mathbf{k}\cdot R} \psi_{n,\mathbf{k}}(\mathbf{r})\, d\mathbf{k}. \tag{2.90}$$

The center of the Wannier functions, in this approach, act as the charge centers and the ensuing definition of polarization has the familiar form as the classically defined **P**, that is:

$$\mathbf{P} = \frac{1}{\Omega} \sum_i q_i \mathbf{r}_i \,, \tag{2.91}$$

where $\mathbf{r}_i$ is the location of either an ion (in which q_i is the point charge of the ion) or the center of a Wannier function (in which q_i is the charge of the Wannier function), and Ω the volume of one cell. The approach to compute $\mathbf{P}$ prescribed thus far by MTP concerns neutral systems. In solids, defects such as vacancies can occur and they are known to exist most likely with a non-zero charge character [81], and they can also simultaneously exhibit insulating behavior. Fundamentally, the existence of charged defects induces a loss of translation invariance of $\mathbf{P}$, therefore loss of its physical meaning. However, in line with the paradigm of MTP we can again prove that, $\Delta\mathbf{P}$ is indeed physically meaningful contrary to the $\mathbf{P}$.

If the solid is translated by a constant vector $\mathbf{t}$ as $\mathbf{r}'_i = \mathbf{r}_i + \mathbf{t}$, the polarization, according to Eq.2.91 will then become $\mathbf{P}' = \mathbf{P} + \frac{1}{\Omega}\sum_i q_i\mathbf{t}$. For charged systems, the second term in $\mathbf{P}'$ does not vanish, and the magnitude of polarization is thus not translation invariant.

However, even for charged systems, the change in polarization is unique. To see this, let the ion or the Wannier functions' centers change from initial position $\mathbf{r}_i^s$ to final position $\mathbf{r}_i^f$ by a displacement $\mathbf{d}_i$ (which is ion dependent, but does *not* depend on the choice of the vector $\mathbf{t}$) as $\mathbf{r}_i^f = \mathbf{r}_i^s + \mathbf{d}_i$. Then, although both the initial polarization $\mathbf{P}^s$ and the final polarization $\mathbf{P}^f$ are not translation invariant as $\mathbf{P}'^s = \mathbf{P}^s + \frac{1}{\Omega}\sum_i q_i\mathbf{t}$ and $\mathbf{P}'^f = \mathbf{P}^f + \frac{1}{\Omega}\sum_i q_i\mathbf{t}$, the change in polarization $\mathbf{P}'^f - \mathbf{P}'^s = \mathbf{P}^f - \mathbf{P}^s = \frac{1}{\Omega}\sum_i q_i\mathbf{d}_i$ nevertheless does not depend on $\mathbf{t}$ and is physically meaningful. More specifically, DFT calculations are performed to determine the atomic locations (denoted as $\{\mathbf{r}_i^f\}$) when a charged vacancy is present. Then, the change in polarization is calculated with respect to the centrosymmetric configuration (denoted as $\{\mathbf{r}_i^s\}$), using multiple steps connecting the starting and final configurations as $\mathbf{r}_i = \mathbf{r}_i^s + \lambda(\mathbf{r}_i^f - \mathbf{r}_i^s)$ with $0 \leq \lambda \leq 1$. Berry phase calculations are performed at each step.

2.4 Density Functional Perturbation Theory

The variational approach in the search for ground state gives us insight into the electronic structure of a given material. Although electronic properties are important, lattice vibration of solid is important too. Studies of the latter are important for several quantities such as: ionic vibration frequencies, dielectric constant, electric susceptibility, specific heat, etc. are all related to lattice properties. The main idea is to consider the change in the system's Hamiltonian, say $\Delta\mathbf{r}_i, E$, to be minute, which warrants a treatment of the problem with perturbation theory. In the perturbation theory, we are primarily concerned with the leading correction term to the electronic density, and Kohn-Sham eigenvalues. The use of perturbation theory within DFT leads to what is called Density Functional Perturbation Theory (DFPT).

2.4.1 Linear response theory

Let us start with the full Hamiltonian of the system:

$$\begin{aligned} H = \quad & \sum_{i=1}^{N} \frac{1}{2m_e}\hat{p}_i^2 + \sum_{n=1}^{K} \frac{1}{2M_n}\hat{P}_n^2 + \frac{e^2}{4\pi\epsilon_0}\left\{\frac{1}{2}\sum_{i\neq j=1}^{N}\frac{1}{|\mathbf{r}_i - \mathbf{r}_j|}\right\} \\ & -\frac{e^2}{4\pi\epsilon_0}\left\{\sum_{n=1}^{K}\sum_{i=1}^{N}\frac{Z_n}{|\mathbf{r}_i - \mathbf{R}_n|} - \frac{1}{2}\sum_{n\neq n'=1}^{K}\frac{Z_n Z_{n'}}{|\mathbf{R}_n - \mathbf{R}_{n'}|}\right\}, \end{aligned} \tag{2.92}$$

where e, Z_n, m_e, M_n is are the electronic, ionic charges and masses respectively; p_i and P_N the electronic and ionic momentum operators respectively; $\mathbf{r}_i$ and $\mathbf{R}_n$ are the respective electronic and ionic positions. In the Born-Oppenheimer (B-O) approximation, the ionic Kinetic energy (2^{nd} term) is approximately zero because of its large mass relative to that of the electrons. Furthermore the ion-ion interaction can be cast as a reference level. The resulting Born-Oppenheimer

Hamiltonian for the electron system is therefore:

$$H_{BO} = \sum_{i=1}^{N} \frac{1}{2m_e}\hat{p}_i^2 + \frac{e^2}{4\pi\epsilon_0}\left\{\frac{1}{2}\sum_{i\neq j=1}^{N}\frac{1}{\left|\mathbf{r}_i-\mathbf{r}_j\right|} - \sum_{n=1}^{K}\sum_{i=1}^{N}\frac{Z_n}{|\mathbf{r}_i-\mathbf{R}_n|}\right\}. \tag{2.93}$$

This equation is similar to the starting equation of the DFT with the definition that

$$\hat{V}_{ext} = -\frac{e^2}{4\pi\epsilon_0}\sum_{n=1}^{K}\sum_{i=1}^{N}\frac{Z_n}{|\mathbf{r}_i-\mathbf{R}_n|}. \tag{2.94}$$

The Kohn-Sham equations within the B-O approximation is a static nuclei treatment. But we know from thermodynamics that at non zero temperature motion is induced. In order to incorporate the ionic motion into our solution we need to realize that the interatomic interaction leads to an oscillation of the nucleus around its equilibrium position. This oscillation is what is called lattice vibration. The lattice vibrations are small deviations from the equilibrium position thereby warranting a treatment of the problem with perturbation. The frequencies of the vibration is solved from the Hessian of the BO energy $\frac{d^2E_{BO}}{d\mathbf{R}_I d\mathbf{R}_J}$.

In regular perturbation theory, the Hamiltonian is assumed to only differ from a known Hamiltonian $H^{(0)}$ by small deviations parametrized as λ. It is assumed that the ensuing wave functions and Kohn-Sham eigenvalues follow suit, namely:

$$H = H^{(0)} + \sum_n \lambda^n H^{(n)}; \tag{2.95}$$

$$\epsilon = \epsilon^{(0)} + \sum_n \lambda^n \epsilon^{(n)}; \tag{2.96}$$

$$|\psi\rangle = |\psi^{(0)}\rangle + \sum_n \lambda^n |\psi^{(n)}\rangle, \tag{2.97}$$

where superscripts indicate the order of the correction to the unperturbed states, which are : $H^{(0)}, \epsilon^{(0)}_{m,\mathbf{k}}, \left|\psi^{(0)}_{m,\mathbf{k}}\right\rangle$. Therefore by developing the Schrödinger equation and collecting the equations corresponding to the same order of the perturbing parameter λ, we arrive quite straightforwardly, at the results of regular perturbation theory:

Zeroth order:

$$\hat{H}^{(0)} \left|\psi^{(0)}\right\rangle = \epsilon^{(0)} \left|\psi^{(0)}\right\rangle, \tag{2.98}$$

First order:

$$\left(\hat{H}^{(0)} - \epsilon^{(0)}\right) \left|\psi^{(1)}\right\rangle = -\left(H^{(1)} - \epsilon^{(1)}\right) \left|\psi^{(0)}\right\rangle, \tag{2.99}$$

N-th order:

$$\left(\hat{H}^{(0)} - \epsilon^{(0)}\right) \left|\psi^{(n)}\right\rangle = \sum_{i=1}^{n} -\left(\hat{H}^{(i)} - \epsilon^{(i)}\right) \left|\psi^{(n-i)}\right\rangle. \tag{2.100}$$

In the above set of equations, Eq.2.98 is just the unperturbed Schrödinger equation, or Kohn-Sham equation, and the first order equation is the so-called **S**ternheimer equation. The Sternheimer equation gives the first order response of the wave function, hence the electronic density, to the perturbation.

The idea in the DFPT approach is to reproduce the results of DFT in the presence of certain perturbation to the ground state Hamiltonian. The difficulty lies in the fact the Hamiltonian is a functional of the density, hence the perturbed wave function, and in principles it is also perturbed. Two theorems aid us in unveiling the interdependence of the Hamiltonian and the wave functions:

Hellmann-Feynman theorem:

Assume that the Hamiltonian $\hat{H}$ is parametrized by λ. Let $\left|\psi_n^{(\lambda)}\right\rangle$, and $E_n(\lambda)$ be the normalized eigenstates and eigenvalues of $\hat{H}(\lambda)$ respectively. We then have:

$$\frac{dE_n}{d\lambda} = \left\langle \psi_n^{(\lambda)} \middle| \frac{d\hat{H}(\lambda)}{d\lambda} \middle| \psi_n^{(\lambda)} \right\rangle. \tag{2.101}$$

Proof:

$$\begin{aligned}
\frac{dE_n}{d\lambda} &= \frac{d}{d\lambda}\left\{\left\langle \psi_n^{(\lambda)} \middle| \hat{H}(\lambda) \middle| \psi_n^{(\lambda)} \right\rangle\right\}, \\
&= \left\langle \frac{d\psi_n^{(\lambda)}}{d\lambda} \middle| \hat{H}(\lambda) \middle| \psi_n^{(\lambda)} \right\rangle + \left\langle \psi_n^{(\lambda)} \middle| \hat{H}(\lambda) \middle| \frac{d\psi_n^{(\lambda)}}{d\lambda} \right\rangle \\
&+ \left\langle \psi_n^{(\lambda)} \middle| \frac{d\hat{H}(\lambda)}{d\lambda} \middle| \psi_n^{(\lambda)} \right\rangle, \\
&= E_n(\lambda)\left(\left\langle \frac{d\psi_n^{(\lambda)}}{d\lambda} \middle| \psi_n^{(\lambda)} \right\rangle + \left\langle \psi_n^{(\lambda)} \middle| \frac{d\psi_n^{(\lambda)}}{d\lambda} \right\rangle\right) \\
&+ \left\langle \psi_n^{(\lambda)} \middle| \frac{d\hat{H}(\lambda)}{d\lambda} \middle| \psi_n^{(\lambda)} \right\rangle \\
&= E_n(\lambda)\frac{d\left\langle \psi_n^{(\lambda)} \middle| \psi_n^{(\lambda)} \right\rangle}{d\lambda} + \left\langle \psi_n^{(\lambda)} \middle| \frac{d\hat{H}(\lambda)}{d\lambda} \middle| \psi_n^{(\lambda)} \right\rangle, \\
\therefore \frac{dE_n}{d\lambda} &= \left\langle \psi_n^{(\lambda)} \middle| \frac{d\hat{H}(\lambda)}{d\lambda} \middle| \psi_n^{(\lambda)} \right\rangle.
\end{aligned} \tag{2.102}$$

In the above proof we have made use of the Hermitian property of $\hat{H}$, the eigenvalue equation $\hat{H}\left|\psi_n^{(\lambda)}\right\rangle = E_n(\lambda)\left|\psi_n^{(\lambda)}\right\rangle$, and the fact that $\left|\psi_n^{(\lambda)}\right\rangle$ are normalized. The Hellmann-Feynman theorem implies that although the electronic density can vary with the perturbation, to linear order only the perturbation of the Hamiltonian is important.

Wigner's $(2n+1)$ theorem:

The computation of $\frac{d^{2n+1}E}{d\lambda^{2n+1}}$ requires only knowledge of $\psi_n(\lambda)$ up to n-th order perturbation.

The $(2n+1)$ theorem was proven by X. Gonze [82] to work for a system, not necessarily quantum-mechanical one, obeying variational principle, and under which one is considering to apply a generic perturbation theory. The proof relies on a Taylor expansion of the Hamiltonian bounded above by an error term expressed as the difference between generic wave functions. One immediate implications of Wigner's $(2n+1)$ theorem is that one needs only the linear change in electronic density in order to determine the Hessian of the Born-Oppenheimer energy $\frac{d^2E(\mathbf{R})}{d\mathbf{R}_I d\mathbf{R}_J}$, a quantity which is known to be pivotal to vibration frequency calculations.

Once the atomic positions and the cell parameters of the ground state are known, Density Functional Perturbation Theory (DFPT) is used to determine phonon frequencies and phonon eigendisplacements. Lattice vibrations lead to the deformation potential:

$$\Delta V = \sum_I [V(\mathbf{R}_I + \mathbf{u}_I) - V(\mathbf{R}_I)], \tag{2.103}$$

where $\mathbf{R}_I$ and $\mathbf{u}_I$ indicates the equilibrium ionic positions and atomic displacements respectively. These ionic displacements about their equilibrium positions due to thermal energy are usually small, the deformation potential can be treated as a perturbation term in the Hamiltonian of the system, which can be written as $H = T + V_0 + \Delta V$ where T is the kinetic energy, V_0 is the potential of the system subject to no vibration. The DFPT calculates in a straightforward way the response of the system to the perturbation. Under these considerations then, $H_0 = T + V_0$ and $H^{(1)} = \Delta V$.

The first order response of the charge density n($\mathbf{r}$) is given by:

$$\Delta n(\mathbf{r}) = 2\sum_{n=1}^{N/2}\left(\psi_n^*(\mathbf{r})\Delta\psi_n(\mathbf{r}) + \Delta\psi_n^*(\mathbf{r})\psi_n(\mathbf{r})\right), \tag{2.104}$$

where the summation is assumed over doubly occupied band. The latter equation can be simplified as:

$$\Delta n(\mathbf{r}) = 4\Re\left(\sum_{n=1}^{N/2}\psi_n^*(\mathbf{r})\Delta\psi_n(\mathbf{r})\right), \tag{2.105}$$

with $\Re(z)$ is the real part of the complex number z. $\Delta\psi_n(\mathbf{r})$ in Eq.2.105 is simply given by the Sternheimer equation:

$$(H_{SCF} - \epsilon_n)\left|\Delta\psi_n\right\rangle = -(\Delta V_{SCF} - \Delta\varepsilon_n)\left|\psi_n\right\rangle, \tag{2.106}$$

with H$_{SCF}$ and V$_{SCF}$ being the Kohn-Sham Hamiltonian and perturbing self-consistent potential respectively, and ϵ_n the eigenvalue of H$_{SCF}$. The resulting first order correction is given by:

$$\Delta\psi_n(\mathbf{r}) = \sum_{m\neq n}\psi_m(\mathbf{r})\frac{\left\langle\psi_m\middle|\Delta V_{SCF}\middle|\psi_n\right\rangle}{\varepsilon_n - \varepsilon_m}, \tag{2.107}$$

where the summation runs over all bands (occupied or not). Because the perturbation term ΔV_{SCF} depends on the correction to the electronic density $\Delta n(\mathbf{r})$ we have [83]:

$$\Delta V_{SCF(\mathbf{r})} = \Delta V(\mathbf{r}) + e^2\int\frac{\Delta n(\mathbf{r}\prime)}{|\mathbf{r}-\mathbf{r}'|}\,d\mathbf{r}' + \left.\frac{dv_{xc}(n)}{dn}\right|_{n=n(\mathbf{r})}\Delta n(\mathbf{r}). \tag{2.108}$$

Plugging Eq.2.107 into Eq.2.105 yields:

$$\Delta n(\mathbf{r}) = 4\sum_{n=1}^{N/2}\sum_{m\neq n}\psi_n^*(\mathbf{r})\psi_m(\mathbf{r})\frac{\left\langle\psi_m\middle|\Delta V_{SCF}\middle|\psi_n\right\rangle}{\varepsilon_n - \varepsilon_m}. \tag{2.109}$$

We can see from Eq.2.105, Eq.4.1, Eq.2.108, and Eq.2.109 that the calculations of the response is done in a self consistent manner indeed, and they constitute the core steps of DFPT.

The summation over the Kohn-Sham states in principles requires large basis sets since m in principle includes non-occupied orbitals. However, given the domain of definition of the unperturbed wave function, namely valence states, and their orthogonality the Sternheimer equation can be rewritten as:

$$(H_{SCF} - \varepsilon_n)\,\mathbb{P}_c \Delta\psi_n(\mathbf{r}) = -\mathbb{P}_c \Delta V_{SCF} \psi_n(\mathbf{r}), \tag{2.110}$$

where $\mathbb{P}_c = 1 - \mathbb{P}_v = 1 - \sum_{n_{occ}} |\psi_n\rangle\langle\psi_n|$, is the projector onto the unoccupied electronic states. We can thus focus only on the valence states and their responses as shown by [83]:

$$(H_{SCF} + \alpha\mathbb{P}_v - \varepsilon_n)\,\Delta\psi_{n,v}(\mathbf{r}) = -\,(1 - \mathbb{P}_v)\,\Delta V_{SCF}\psi_{n,v}(\mathbf{r}). \tag{2.111}$$

The advantage of DFPT over other methods that calculate lattice vibration such as the well-known frozen phonon, is that the computational workload in the former method is lower than in the latter method and it also allows computation of the response at any wave vector **q**. This is evident when one Fourier transforms the summands in Eq.2.111, the resulting first principles response becomes [83]:

$$\Delta n^{\mathbf{q}}_{n,v}(r) = 4\sum_{\mathbf{k},v} \left(u^{\mathbf{k}}_v(\mathbf{r})\right)^{*} \Delta u^{\mathbf{k}+\mathbf{q}}_v(\mathbf{r}), \tag{2.112}$$

where **k** runs over points in the 1BZ defined by the Monkhorst-Pack [80] procedure.

2.4.2 Homogeneous electric field

In the presence of electric field $\mathbf{E}^0$, any materials respond according to [72, 73]:

$$\mathbf{D} = \mathbf{E}^0 + 4\pi\mathbf{P}, \tag{2.113}$$

where **P** includes both the frozen-in polarization, if the material is FE, and P_{ind} induced by the E^0. E^0 affects charge density n(**r**), which in turn affects P of a given system. In addition to this effect on polarization, there is an effect on V_{SCF} due to Hohenberg and Kohn theorem, since the potential now acquires a perturbing term $e\mathbf{E}^0 \cdot r$. This leads to the following perturbation:

$$\Delta V^{lf}(n(\mathbf{r})) = e^2 \int \frac{\Delta^E n(\mathbf{r}')}{|\mathbf{r}-\mathbf{r}'|}\, d\mathbf{r}' + \frac{dv_{xc}}{dn}\Delta^E n(\mathbf{r}). \tag{2.114}$$

$$V^{pert} = -e\mathbf{r}\cdot E + \Delta V^{lf}, \tag{2.115}$$

with the local field potential defined as:

$$\Delta V^{lf}(n(\mathbf{r})) = e^2 \int \frac{\Delta^E n(\mathbf{r}')}{|\mathbf{r}-\mathbf{r}'|}\, d\mathbf{r}' + \frac{dv_{xc}}{dn}\Delta^E n(\mathbf{r}). \tag{2.116}$$

In crystalline solids, the ill-defined quantity **r** can be rewritten as:

$$r_\alpha \left|\psi\right\rangle = \left|\overline{\psi}_{n,\alpha}\right\rangle = \sum_{m\neq n} |\Psi_m\rangle \frac{\left\langle\psi_m\right|[H, r_\alpha]\left|\psi_n\right\rangle}{\epsilon_m - \epsilon_n}, \tag{2.117}$$

and the Sternheimer equation becomes:

$$(H_{SCF} - \epsilon_n)\left|\Delta^E \psi_n\right\rangle = -eE^\alpha \left|\overline{\psi}_{n,\alpha}\right\rangle - \mathbb{P}_c \Delta V^{lf}, \tag{2.118}$$

with the assumption of Einstein notation. With the first order response of the wave function, and the charge density known, the induced polarization is given by:

$$\begin{aligned} P_\alpha &= \frac{-4e}{V}\sum_{n=1}^{N/2}\langle\psi_n|\,r_\alpha\,|\Delta^E\psi_n\rangle, && (2.119)\\ &= \frac{-4e}{V}\sum_{n=1}^{N/2}\sum_{m\neq n}\langle\Psi_m|\Delta^E\psi_n\rangle\frac{\langle\psi_m|\,[H,\mathbf{r}]\,|\psi_n\rangle}{\epsilon_m-\epsilon_n} && (2.120)\\ P_\alpha &= \frac{-4e}{V}\sum_{n=1}^{N/2}\langle\overline{\psi}_{n,\alpha}|\Delta^E\psi_n\rangle. && (2.121)\end{aligned}$$

With the knowledge of the Δn and $\Delta\psi$, the calculation of important quantities such as: the electronic polarization (**P**), the Born effective charges ($\mathbf{Z}^*$) and the dielectric tensors (ϵ) follow because these are first or higher order derivatives of the energy with respect to various perturbations: [83]

$$\begin{aligned} &\mathbf{P} = -\frac{e}{V}\int_V \mathbf{r}\Delta n(\mathbf{r})\,d\mathbf{r}. && (2.122)\\ &Z_s^{*\alpha\beta} = \frac{\Omega}{e}\left.\frac{\partial P_\alpha}{\partial u_s^\beta(\mathbf{q}=0)}\right|_{\mathbf{E}=0}, && (2.123)\\ &\epsilon_\infty^{\alpha\beta} = \delta_{\alpha\beta} + 4\pi\left.\frac{\partial P_\alpha}{\partial E_\beta}\right|_{\mathbf{u}_s(\mathbf{q}=0)} = \delta_{\alpha\beta} - \frac{16\pi e}{\Omega E_\beta}\sum_n\langle\overline{\psi}_{n,\alpha}|\Delta^E\psi_n\rangle. && (2.124)\end{aligned}$$

2.4.3 Phonon

In the BO approximation above the ions are considered at rest. If we relax this approximation and consider their motion, two assumptions are paramount:

1. The ionic motion is a vibration, confined within a small, immediate neighborhood of the equilibrium position τ_0, $|\mathbf{u}| \ll |\mathbf{R}_0|$.
2. The vibration in question is assumed to have harmonic time dependence, i.e. $\mathbf{u}(\mathbf{r}, t) = \mathbf{u}(\mathbf{r})e^{i\omega t}$.

The potential is given by:

$$U = \frac{1}{2}\sum_{\mathbf{R}_I}\sum_{\mathbf{R}_J}\phi\left(\mathbf{R}_I - \mathbf{R}_J\right), \tag{2.125}$$

where $\mathbf{R}_I$ and $\mathbf{R}_I$ are ionic coordinates that can be written in the general expression:

$$\mathbf{R}_I = \mathbf{R}_l + \tau_s, \tag{2.126}$$

where $\mathbf{R}_l,$ and τ_s quantify the position of the *l-th* Bravais Lattice point and the equilibrium position of the ion s, respectively. Note that the Roman, and Greek indices mark ionic type, and Cartesian components respectively. The upper case lumps two indices together, unit cell l and ion type s. Knowing that the ions vibrate in the vicinity of the equilibrium τ_s, we can expand the potential U in Eq.2.125 in powers of the displacements $\mathbf{u}_s$ as:

$$U = \frac{1}{2}\sum_{\mathbf{R}_I}\sum_{\mathbf{R}_J}\left\{\phi(\mathbf{R}_I - \mathbf{R}_J) + \frac{1}{n!}\left((\mathbf{u}_s(\mathbf{R}_I) - \mathbf{u}_s(\mathbf{R}_J)) \cdot \triangledown\right)^n \phi(\mathbf{R}_I - \mathbf{R}_J)\right\}. \tag{2.127}$$

By using the equilibrium condition and halting the Taylor series at the second order yields the so-called *Harmonic* potential we have:

$$U_{harm} = \frac{1}{4}\sum_{\mathbf{R}_I}\sum_{\mathbf{R}_J}\left((\mathbf{u}_s(\mathbf{R}_I) - \mathbf{u}_s(\mathbf{R}_J)) \cdot \triangledown\right)^2 \phi\left(\mathbf{R}_I - \mathbf{R}_J\right), \tag{2.128}$$

which can be reduced to: [84]

$$U_{harm} = \frac{1}{2}\sum_{\mathbf{R}_I}\sum_{\mathbf{R}_J}\left\{u^s_\alpha(\mathbf{R}_I)C^{\alpha\beta}_{st}(\mathbf{R}_I - \mathbf{R}_J)u^t_\beta(\mathbf{R}_J)\right\}, \tag{2.129}$$

with the Interatomic Force Constant (IFC) matrix $C^{\alpha\beta}_{st}(\mathbf{R}_I - \mathbf{R}_J)$ defined as:

$$C^{\alpha\beta}_{st}(\mathbf{R}_I - \mathbf{R}_J) = \frac{\partial^2\phi}{\partial u^s_\alpha \partial u^t_\beta}. \tag{2.130}$$

Using the second assumption of lattice vibration, i.e. harmomic time dependence of the ionic displacement, we can write the equation of motion (EOM):

$$M_s\frac{\partial^2 u^s_\alpha}{\partial t^2} = -\omega^2 M_s u^s_\alpha = -\nabla U_{harm}. \tag{2.131}$$

The right-hand side of Eq.2.131 gives:

$$\begin{aligned}\frac{\partial U_{harm}}{\partial u^s_\alpha} \quad &= \frac{1}{2}\sum_{\mathbf{R}_I}\sum_{\mathbf{R}_J}\left\{\delta_{\mathbf{R}_I,\mathbf{R}_1}\delta_{a,s}\delta_{\mu,\nu}C^{\mu\beta}_{ab}(\mathbf{R}_I - \mathbf{R}_J)u^b_\beta(\mathbf{R}_J)\right\} \\ &+ \frac{1}{2}\sum_{\mathbf{R}_I}\sum_{\mathbf{R}_J}\left\{\delta_{\mathbf{R}_J,\mathbf{R}_1}u^a_\alpha(\mathbf{R}_I)C^{\mu\nu}_{ab}(\mathbf{R}_I - \mathbf{R}_J)\delta_{b,t}\delta_{\nu,\beta}\right\}.\end{aligned} \tag{2.132}$$

Because we have dummy variables and indices, we end up with:

$$\frac{\partial U_{harm}}{\partial u^s_\alpha} = \sum_t\sum_{\mathbf{R}_J}C^{\alpha\beta}_{st}(\mathbf{R}_I - \mathbf{R}_J)u^t_\beta(\mathbf{R}_J), \tag{2.133}$$

and the EOM Eq.2.131 has the simplified form:

$$\omega^2 M_s u_\alpha^s = \sum_t \sum_{\mathbf{R}_J} C_{st}^{\alpha\beta}(\mathbf{R}_I - \mathbf{R}_J) u_\beta^t(\mathbf{R}_J). \tag{2.134}$$

If we define phonon eigenvectors $\overline{\mathbf{u}}$ as: $u_\alpha^s = \frac{1}{\sqrt{M_s}} \overline{u}_\alpha^s$, then Eq.2.134 becomes:

$$\omega^2 \overline{u}_\alpha^s = \frac{1}{\sqrt{M_s M_t}} \sum_t \sum_{\mathbf{R}_J} C_{st}^{\alpha\beta}(\mathbf{R}_I - \mathbf{R}_J) \overline{u}_\beta^t(\mathbf{R}_J). \tag{2.135}$$

Taking into account the wave vector dependence of the eigenvector $\overline{\mathbf{u}}(\mathbf{R})$

$$\overline{\mathbf{u}}(\mathbf{R}_I) = \overline{\mathbf{u}} e^{i\mathbf{q}\cdot\mathbf{R}_I}, \tag{2.136}$$

we recover from Eq.2.135, after some algebra and using Fourier transformation, the secular equation:

$$\det \left| \tilde{D}_{st}^{\alpha\beta}(\mathbf{q}) - \omega(\mathbf{q}) \right| = 0, \tag{2.137}$$

where the Dynamical matrix is defined using the Fourier transform of the IFC matrix $C_{st}^{\alpha\beta}(\mathbf{R}_I - \mathbf{R}_J)$ as:

$$\tilde{D}_{st}^{\alpha\beta}(\mathbf{q}) = \frac{1}{\sqrt{M_s M_t}} \tilde{C}_{st}^{\alpha\beta}(\mathbf{q}). \tag{2.138}$$

The solutions of the secular equation are the eigenvectors $\mathbf{e}_n(\mathbf{q})$, and the eigenvalues $\omega_n^2(\mathbf{q})$ of the phonon $\{n, \mathbf{q}\}$. Let us note the dependence of $\tilde{D}_{st}^{\alpha\beta}$ on $\mathbf{q}$, which enables us to compute the phonon structure at any wave vector belonging to the 1BZ.

Long-wavelength phonons and LO-TO splitting

When dealing with long wavelength phonons, or phonons at the Brillouin zone center $\mathbf{q} = (0,0,0)$, one has to be careful. The IFC matrix has terms that involve $\frac{1}{\mathbf{q}}$. This can be seen explicitly in the first 2 expressions of $\tilde{C}_{ion}$ contribution in Appendix B of [83]. The IFC matrix can then be divided into analytic and non-analytic contributions according to Born and Huang [85]:

$$\tilde{C}_{st}^{\alpha\beta} = \tilde{C}_{st}^{an,\alpha\beta} + \tilde{C}_{st}^{na,\alpha\beta}, \tag{2.139}$$

The nonanalytic part has the form [86]:

$$\tilde{C}^{na} = \frac{4\pi}{\Omega} e^2 \sum_s \frac{1}{M_s} \frac{(\mathbf{q}.\mathbf{Z}_s^*)(\mathbf{q}.\mathbf{Z}_s^*)}{\mathbf{q}.\epsilon^{\infty}.\mathbf{q}}, \tag{2.140}$$

where ϵ^{∞} is the high frequency dielectric constant, Ω is the unit cell volume. When $\mathbf{q} = (0,0,0)$, $\tilde{C}^{na}$ is undetermined. To thwart this problem, the value of the nonanalytic contribution can be calculated by taking the limit as $\mathbf{q}$ approaches the Brillouin zone center from a chosen direction. This results in what is known as the LO-TO splitting. The frequencies of Longitudinal Optic (LO) phonons ($\mathbf{u} \| \mathbf{q}$) and Transverse Optic (TO) phonons ($\mathbf{u} \perp \mathbf{q}$), indistinguishable before calculating $\tilde{C}^{na}$, interact differently with electric field resulting from atomic displacements $\mathbf{u}$ [87]:

$$\mathbf{E} = \frac{\mathbf{P}}{\epsilon_0 \chi} = \frac{1}{\Omega} \sum_s e Z_s^* \mathbf{u}_s, \tag{2.141}$$

where s indicates the ions within the unit cell, $\mathbf{u}_s$ their displacements.

In the literature, LO-TO splitting is usually given by [88]:

$$\omega^2(\mathbf{q} \to 0) = \omega^2(\mathbf{q} = 0) + \frac{4\pi}{\Omega} e^2 \frac{(\mathbf{q}.\mathbf{Z}_s^*)(\mathbf{q}.\mathbf{Z}_s^*)}{\mathbf{q}.\epsilon^{\infty}.\mathbf{q}} \tag{2.142}$$

The calculation of $\tilde{C}(\mathbf{q} \to 0)$ comes about when a correction on the diagonalization of $\tilde{C}^{an}(\mathbf{q} = 0)$ is made, as the so-called Acoustic Sum Rule (ASR) is enforced. This particular sum rule imposes on the eigenvalue of $\tilde{C}$ the fact that translation of the whole cell should not change the total energy, meaning acoustic phonons should yield zero frequencies.

3 Various evidences for the unusual polarization behaviors in epitaxially strained (111) BaTiO$_3$

3.1 Introduction

Ferroelectric (FE) perovskites grown epitaxially along the (111) direction are technologically important, since by possessing $R3m$ symmetry they can, as experimentally demonstrated, form interfaces with topological insulators such as (Bi$_{1-x}$Sb$_x$)Te,[6] semiconductors ZnO or AlN,[2, 3] colossal magnetoresistance manganite (LaSr)MnO$_3$,[4] as well as (with) other ferroelectrics Pb(ZrTi)O$_3$[5]. The strong spontaneous polarization in ferroelectrics can be utilized to change and control the material properties in topological insulators, semiconductors, and manganites. Therefore, determining the ferroelectric behaviors in (111)-oriented FE films and understanding how to tune these behaviors is thus a topic of technological relevance. Strong interest in epitaxially grown (111) FEs has been further encouraged by the recent advance that high-quality atomically flat (111) surfaces of perovskite oxides have been made possible in experiments.[6]

Furthermore, the (111)-oriented epitaxially strained ABO$_3$ perovskites are also of fundamental relevance. In (001)-oriented films, atoms are alternated by BO$_2$ and AO planes. But, in (111)-oriented films, atoms are alternated by B and AO$_3$ planes, with completely different chemical and physical interactions. The profound differences in terms of interactions in two oriented films make it interesting to study the ferroelectric properties in (111)-oriented FEs since these properties are known to depend critically on the delicate balance of different interactions.[7]

Compared to the (001)-oriented FEs where effects of epitaxial strain have been amply studied and many new phenomena have been reported,[2, 8, 10, 11, 12, 13, 14, 15, 26, 30, 18, 19, 20, 21, 22, 23] the (111)-oriented FEs and their polarization properties under external strain are, however, much less understood [7, 25].

In this study, we present various evidences for the unusual ferroelectric behaviors in (111)-oriented $BaTiO_3$ caused by the in-plane strain, provided by first-principles density functional calculations and modern theory of polarization. In (001)-oriented FEs, different studies have yielded two widely accepted conclusions: (i) Compressive in-plane strain tends to enhance the out-of-plane polarization, and (ii) The enlarged out-of-plane strain (or c/a tetragonality) strongly correlates with the enhanced out-of-plane polarization. Here we find that the strain effects are very different in the (111)-oriented $BaTiO_3$. Both conclusions should be revisited.

More specifically, we find that the magnitude of the out-of-plane polarization in (111)-oriented $BaTiO_3$, instead of being enhanced, is weakened by the compressive in-plane strains. This leads to an unusual and positive e_{31} piezoelectric coefficient. Furthermore, with the increasing compressive in-plane strain, the out-of-plane strain is shown to increase despite polarization decreases, revealing that the strain-polarization coupling between the out-of-plane strain and the out-of-plane polarization is also unusual in (111)-oriented $BaTiO_3$. Various evidences are examined in this paper to confirm these uncommon polarization behaviors, including ferroelectric instability, strain-dependence of the polarization, and the phonon dispersion across the Brillouin zone. In addition to the rhombohedral $R3m$ phase, we also consider the lower-symmetry Cm phase, showing that the conclusion remains. The significant differences between the (001)-oriented and (111)-oriented FEs may provide an effective and previously less emphasized strategy of using the interactions caused by orientation to modify the ferroelectric behaviors.

3.2 Theoretical methods

Three complementary theoretical techniques are employed to calculate various physical quantities that are relevant to the strain-dependent ferroelectric behaviors in (111)-oriented FEs. More specifically, (i) we use density functional theory (DFT) within the local density approximation [34] to determine the optimized structure and total energy under a given strain; (ii) The electric polarization is computed using the Berry phase approach as described in the modern theory of polarization [39, 40]; (iii) Density functional perturbation theory (DFPT) [29] is used to compute the force constants and phonon dispersion across the Brillouin zone, as implemented in Quantum-Espresso [18].

We consider the rhombohedral (111)-oriented $BaTiO_3$ of $R3m$ symmetry, with polarization pointing at the [111] direction which is defined as the z-axis in this study, for the following reason. For many technological applications (e.g., interfaces between ferroelectric and topological insulator), the most important polarization component is the out-of-plane polarization. In the rhombohedral phase of (111)-oriented $BaTiO_3$, the polarization is along the out-of-plane direction, and furthermore, can be effectively controlled by the in-plane strain. The lattice vectors of the rhombohedral phase are $\mathbf{a}_1 = a(\sin\frac{\alpha}{2}, -\frac{1}{\sqrt{3}}\sin\frac{\alpha}{2}, \sqrt{\cos^2\frac{\alpha}{2} - \frac{1}{3}\sin^2\frac{\alpha}{2}})$, $\mathbf{a}_2 = a(0, \frac{2}{\sqrt{3}}\sin\frac{\alpha}{2}, \sqrt{\cos^2\frac{\alpha}{2} - \frac{1}{3}\sin^2\frac{\alpha}{2}})$, and $\mathbf{a}_3 = a(-\sin\frac{\alpha}{2}, -\frac{1}{\sqrt{3}}\sin\frac{\alpha}{2}, \sqrt{\cos^2\frac{\alpha}{2} - \frac{1}{3}\sin^2\frac{\alpha}{2}})$, where a is the length of a lattice vector and α is the angle between $\mathbf{a}_i$ and $\mathbf{a}_j$ that satisfies $\mathbf{a}_i \cdot \mathbf{a}_j = a^2 \cos\alpha$ for $i \neq j$. The pair of parameters (a, α) thus determine the cell structure; under zero strain, the optimization of the global-minimum crystal structure is performed with respect to both α and a parameters as well as atomic positions. The biaxial in-plane strain is applied on the xy plane. Following the common approach,[20, 21, 26] we study the effects of epitaxial strain by considering bulk samples rather than thin-film samples. This approach allows us to separate strain effects from surface effects. Epitaxial strain is imposed by changing the in-plane lattice constant a_{in}, and strain is defined as $\eta_{in} = \frac{a_{in}-a_{in}^0}{a_{in}^0}$, with $\eta_{in} < 0$ ($\eta_{in} > 0$) for compressive (tensile) strains. When the system is under in-plane strain, the cell structure and atomic positions are fully optimized by constraining $a_{in} = a\sin(\frac{\alpha}{2})$ for a given in-plane a_{in}. We study the (111)-oriented $BaTiO_3$ under both compressive and tensile in-plane strains ranging from $\eta_{in} = -3\%$ to $\eta_{in} = +3\%$.

The interactions between the inert core electrons and the valence electrons are described using pseudopotentials. We use norm-conserving Trouiller-Martins pseudopotentials.[34] Electron wave functions are expanded using plane-wave bases with an energy cutoff of 90 Ry which is checked to be sufficient, and the force threshold of atomic optimization is less than 10^{-5} Ry/ Bohr.

In the linear-response density functional perturbation calculations for phonon spectrum, a $4 \times 4 \times 4$ grid inside the first Brillouin zone is used to obtain the interatomic force constants; use of $8 \times 8 \times 8$ grid does not change the results appreciably. The phonon dispersion in the Brillouin zone is presented along the $\Gamma - X - M - \Gamma - R - M$ path using the notation of pseudo-cubic Bravais lattice. This choice of notation is made to avoid the cumbersome definition of high-symmetry points in the trigonal symmetry, and the same coordinates as the pseudo-cubic can be used provided that the primitive reciprocal lattice vectors $\{\mathbf{b}_1, \mathbf{b}_2, \mathbf{b}_3\}$ are used instead of the cartesian ones.

3.3 Results and discussions

Ferroelectric instability: The instability is examined by total energy and the depth of ferroelectric potential well. Let us first define the following displacements,

$$\boldsymbol{\xi}_i = \mathbf{R}_i - \mathbf{R}_i^0, \tag{3.1}$$

where $\mathbf{R}_i$ and $\mathbf{R}_i^0$ are the position of atom i in the DFT-optimized structure and in the non-polar centrosymmetric structure, respectively. The cell structure is the same for configurations $\{\mathbf{R}_i\}$ and $\{\mathbf{R}_i^0\}$. The depth of ferroelectric potential well is calculated by displacing atoms from their centrosymmetric locations according to

$$\mathbf{R}_i(\lambda) = \mathbf{R}_i^0 + \lambda \boldsymbol{\xi}_i, \tag{3.2}$$

where λ specifies the magnitude of displacements and is chosen to be between 0.0 and 1.6. Denote the total energy of the system, calculated self-consistently for a given $\mathbf{R}_i(\lambda)$, as E(λ). Fig.3.1 shows the relative energy

$$\Delta E(\lambda) = E(\lambda) - E(\lambda = 0), \tag{3.3}$$

as a function of λ for zero-strain and for a tensile strain η_{in} = +2.5% as well as a compressive strain $\eta_{in} = -2.5\%$.

Figure 3.1 shows that at η_{in} = 0% the off-centered structure (λ=1) is more stable than the centrosymmetric structure (λ=0) as it should be, since the ferroelectric rhombohedral structure is the ground state of unstrained $BaTiO_3$. The depth of potential well $\Delta E(\lambda = 1)$ at η_{in} = 0% is merely 4.55 meV with respect to the centrosymmetric structure of rhombohedral lattice. One notable result in Fig.3.1 is that, when a tensile (not compressive) in-plane strain η_{in} = 2.5% is applied, $\Delta E(\lambda = 1)$ is drastically increased to 35.5 meV, 700% larger than the zero-strain case. It demonstrates that a moderate tensile in-plane strain considerably increases the ferroelectric instability in (111)-oriented $BaTiO_3$. Here one may naively think that the applied tensile strain enhances the ferroelectricity along the *in-plane* directions. But surprisingly, as will be shown later, the ferro-

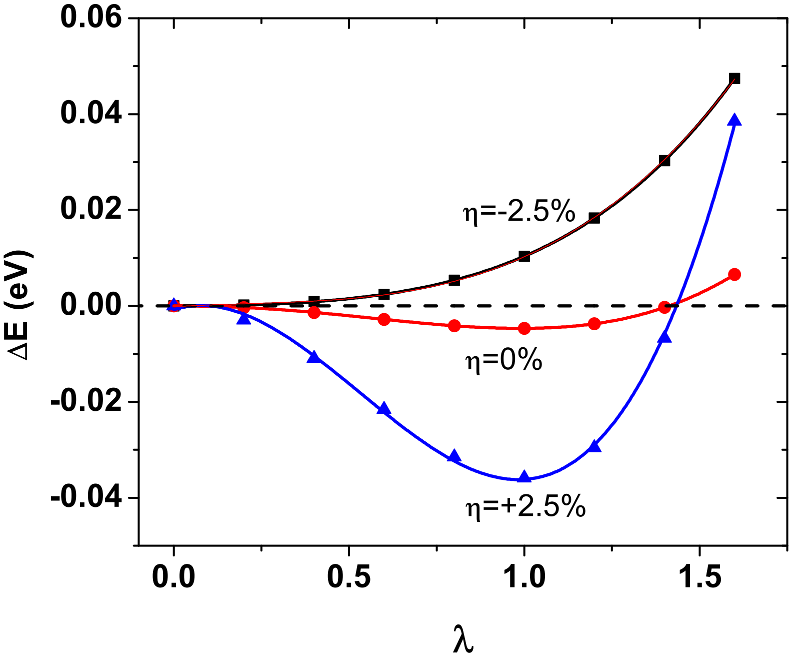

Figure 3.1: Energy difference ΔE between the shifted atomic configuration and the centrosymmetric configuration as a function of λ, for different in-plane η_{in} strains.

electricity is not within the in-plane directions.

While the transition temperature for the rhombohedral $BaTiO_3$ at *zero* strain is low[32] (~183 K), this temperature can nevertheless be significantly increased by tensile strain, which is corroborated by the drastically increased well-depth of the ferroelectric instability under $\eta_{in} = +2.5\%$ in Fig.3.1. Therefore, the temperature range of the rhombohedral $BaTiO_3$ and its applications can be considerably increased.

Another interesting result in (111)-oriented $BaTiO_3$ is that no ferroelectric instability is found at a compressive strain $\eta_{in} = -2.5\%$, and our DFT-optimized atomic positions have centrosymmetry although the cell structure is rhombohedral. This is rather unexpected, because it is well known in (001)-oriented $BaTiO_3$ that a compressive strain enhances the out-of-plane ferroelectricity. Since the system is not ferroelectric, $\{\xi_i\}$ vanish at $\eta_{in} = -2.5\%$. To illustrate the total-energy change caused by atomic displacements for $\eta_{in} = -2.5\%$, we use $\{\boldsymbol{\xi}_i\}$ of the zero-strain case to obtain the $\eta_{in} = -2.5\%$ curve in Fig.3.1. We see that the $\eta_{in} = -2.5\%$ curve indeed shows no ferroelectric instability, consistent with the centrosymmetric atomic positions.

Also note that the ΔE-vs-λ curvature is steep near the minimum for the $\eta_{in} = +2.5\%$ curve, and in contrast, flat near the minimum for the $\eta_{in} = -2.5\%$ curve. This may have implication on the electromechanical response, since a flat energy surface tends to generate a large electromechanical response.[12, 38] From Fig.3.1, an enhanced electromechanical response is anticipated between $\eta_{in} = 0$ and $\eta_{in} = -2.5\%$.

Strain-dependent polarization: Polarizations in (111)-oriented $BaTiO_3$, calculated using the geometric Berry phase approach [39, 40], are shown in Fig.3.2a for different magnitudes of in-plane strains. Polarizations in Fig.3.2a all point along the out-of-plane direction. At zero strain, the calculated polarization in the present study is 0.263 Cm^{-2}, which is close to the theoretical value 0.28 Cm^{-2} by Choudhury *et al.*[35] and the experimental value 0.225 Cm^{-2} reported in Ref.[36].

Upon *compressive* strains ($\eta_{in} < 0$), Fig.3.2a reveals that the polarization in (111)-oriented $BaTiO_3$ behaves anomalously. More specifically, the magnitude of polarization is found to decrease drastically under compressive strains. Furthermore, when η_{in} is below the threshold value $\eta_{in}^c = -1.75\%$, polarization utterly disappears. The system undergoes a ferroelectric-to-paraelectric phase transition and becomes nonpolar with $R\bar{3}m$ symmetry. The existence of phase transition in Fig.3.2a further confirms the lack of ferroelectric instability exhibited by the total energy at $\eta_{in} = -2.5\%$ in Fig.3.1. The compressive-strain induced phase transition in Fig.3.2a is second order, which will lead to large dielectric and piezoelectric responses near the critical η_{in}^c strain.[29]

The tensile-strain result in Fig.3.2a is also less intuitive. It is well established that, for (001)-oriented FEs, a tensile strain tends to increase the ferroelectric instability along the in-plane

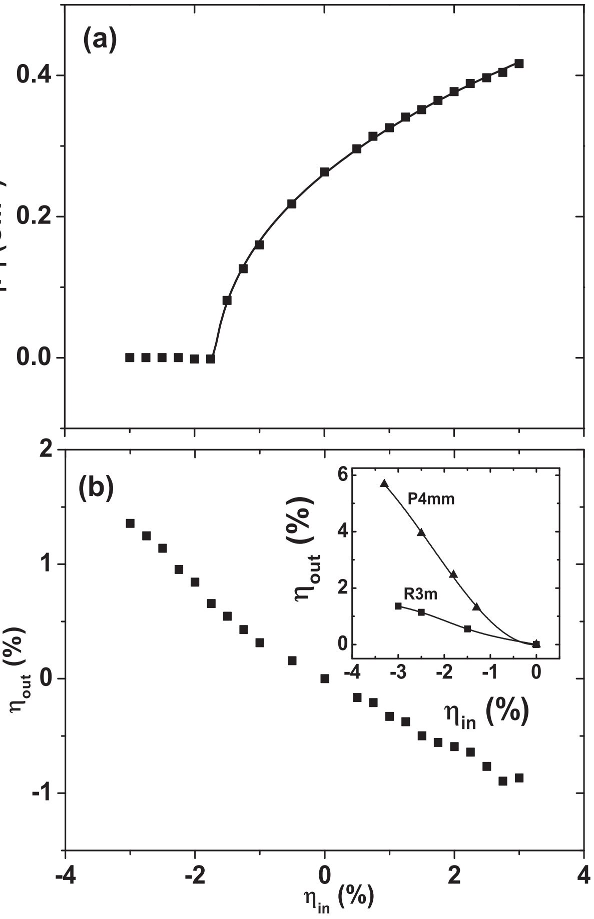

Figure 3.2: The dependencies of the following quantities as a function of in-plane strain η_{in} in the (111)-oriented BaTiO$_3$: (a) the magnitude of polarization, and (b) the out-of-plane strain η_{out}. The solid line in (a) is the result obtained by the analytic scaling law in the text. The inset of (b) shows the comparison of the out-of-plane strain η_{out} in the (111)-oriented BaTiO$_3$ with $R3m$ symmetry and in the (001)-oriented BaTiO$_3$ with $P4mm$ symmetry, where η_{out} is fairly linear in $R3m$ but not in $P4mm$.

directions,[2, 22, 20] because the strain enlarges atom-atom in-plane distance and allows atoms to move off-center more easily within the plane. But for the (111)-oriented BaTiO$_3$, Fig.3.2a tells us that a tensile strain enlarges and thus favors the out-of-plane (not in-plane) polarization.

The polarization behaviors in Fig.3.2a for (111)-oriented BaTiO$_3$ are in sharp difference from those for (001)-oriented BaTiO$_3$. In the (001)-oriented BaTiO$_3$, studies revealed that compressive strains increase the out-of-plane component of polarization[20, 21, 26], a conclusion that has been widely accepted. Calculation results in Fig.3.2a show that the above conclusion cannot be generalized to the (111)-oriented FEs. Since ferroelectricity and polarization is governed by the delicate balance of different interactions, the profound differences in polarization between two oriented FEs must result from important differences in terms of interaction at the microscopic level.

The calculated polarization-vs-strain relation at $\eta_{in} > -1.75\%$ in Fig.3.2a can be well described by an analytic scaling law $P = \alpha(100\eta_{in} + 1.75)^t$, where the fitting parameters α and t are found to be $\alpha = 0.2$ Cm^{-2} and $t = 0.4741$. Under the mean-field Landau theory, the $\eta \sim P^2$ relation (or, equivalently the $P \sim \eta^{1/2}$ relation) can be derived by minimizing the free energy with respect to the strain and by noticing that the lowest strain-polarization coupling term is ηP^2 by symmetry in uniaxial ferroelectrics.[38] The critical power t obtained in our study deviates only slightly from the mean-field value 0.5, which implies to some extent that the present calculation is trackable. The above scaling law yields an improper effective piezoelectric coefficient e_{31} = 7.06 Cm^{-2} at zero strain, where e_{31} is defined as $\Delta P_3 = e_{31}\eta_1$ [21]. Notice that e_{31} is positive in (111)-oriented BaTiO$_3$. However, the e_{31} coefficient in most of (001)-oriented FEs is negative, for instance, e_{31} was reported to be -9.71 Cm^{-2} in BaTiO$_3$, -8.04 Cm^{-2} in PbTiO$_3$, and -2.33 Cm^{-2} in LiNbO$_3$[21]. In another study for (001)-oriented PbTiO$_3$,[39] e_{31} is also negative. The sign change in e_{31} reveals that the polarizations ΔP_3 in two oriented FEs respond to in-plane strain in qualitatively different manner. Using the scaling law, the e_{31} coefficient in (111)-oriented BaTiO$_3$ at moderate $\eta_{in} = -1.70\%$ reaches, as it should be, a phenomenal value of 45.83 Cm^{-2}, an eight-fold increase with respect to the zero-strain case.

Results in Fig.3.2a are also technologically relevant. First, if (111)-oriented FEs is used in capacitors where large dielectric response is desirable, a moderate *compressive* strain is needed to enlarge their dielectric susceptibility by driving the system close to the ferroelectric-to-paraelectric phase transition. On the other hand, if one intends to enhance the effects caused by ferroelectric polarization in, for instance, heterostructures between the (111)-oriented $BaTiO_3$ and other technological materials such as semiconductors[2, 3] or topological insulators[6], we then have to apply *tensile* strains.

Another issue of interest concerns the correlation between the out-of-plane strain and out-of-plane polarization. In (001)-oriented FEs, the out-of-plane strain (which is also related to the tetragonality) has been known to closely correlate with polarization, namely an enhanced out-of-plane polarization is often associated with a stretched lattice length along the same direction.[2, 26] By the same principle one may wonder whether the decline of the polarization in (111)-oriented $BaTiO_3$ under compressive strain in Fig.3.2a is caused by the shrink of the out-of-plane lattice length. This turns out to be untrue. In Fig.3.2b the out-of-plane $\eta_{out} = \frac{c-c_0}{c_0}$ strain is depicted as a function of the in-plane η_{in} strain, showing that under compressive strain, η_{out} increases although polarization declines, again unlike (001)-oriented FEs. This anti-correlation between η_{out} and polarization demonstrates that the polarization-strain coupling is also unusual in (111)-oriented $BaTiO_3$.

Phonon dispersion: To provide more compelling evidence for the disappearance of ferroelectricity at compressive strains, we calculate the full-zone phonon dispersion of the (111)-oriented $BaTiO_3$ at $\eta_{in} = -2.5\%$, using the optimized cell structure and atomic positions. The phonon dispersion is depicted in Fig.3.3. In cubic $BaTiO_3$, phonon instability (or so-called soft mode) is known to occur at zone-center Γ and zone boundary X and M.[40, 41] When phase transitions take place in $BaTiO_3$, these soft phonons are frozen as temperature is lowered, and are responsible for the off-center displacements and structural phase transition. If such a phonon instability exists in (111)-oriented $BaTiO_3$ under $\eta_{in} = -2.5\%$ (where the LDA-optimized atomic positions possess an inversion symmetry in Fig.3.1), we would also expect a softening of some phonon modes that is signaled by imaginary phonon frequencies.[48, 14, 4]

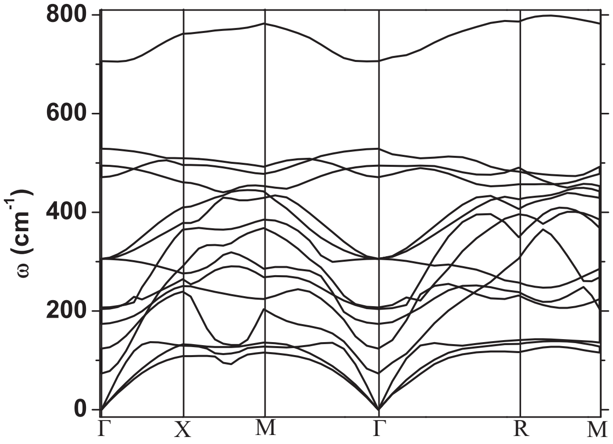

Figure 3.3: Phonon dispersion of the (111)-oriented $BaTiO_3$ under a compressive η_{in}=-2.5% strain, showing non-existence of soft modes.

Fig.3.3 reveals that there are no soft modes at the zone-center Γ. Furthermore, there are no rotational and other instabilities at the zone boundary. The non-existence of soft modes excludes potentially complicated structures as the most stable phase. It also rules out the possibility that polarization may point along the in-plane directions. The phonon dispersion thus gives a strong evidence that the centrosymmetric paraelectric structure found at $\eta_{in} = -2.5\%$ in our calculations is indeed a stable structure. It shows that the disappearance of polarization caused by sufficient compressive strains in (111)-oriented $BaTiO_3$ is valid.

Discussions and implications: Our theoretical results explain some interesting observations in experiment.[44] In Ref.[44], various (111)-oriented $BaTiO_3$(111)/$SrTiO_3$(111) multilayer superlattices, with the period of stacking layers ranging from 0.45nm/0.45nm to 10nm/10nm, were epitaxially grown on SrTiO(111) substrates, where the $BaTiO_3$ component is under compressive strain. The spontaneous polarizations in the superlattices were reported to be exceptionally small but nonzero, with an observable hysteresis loop.[44] More specifically, the polarization in

$BaTiO_3(111)/SrTiO_3(111)$ with a 2nm/2nm stacking period is about 1.35 μC/cm^2.[44] Note that this polarization is nearly twenty times smaller than the value of 23 μC/cm^2 in the (001)-oriented $BaTiO_3(001)/SrTiO_3(001)$ superlattices of similar period length.[44, 45] The reason for the very small polarization in (111)-oriented $BaTiO_3/SrTiO_3$ superlattices was not previously clear.[44] Now, according to the calculation results in Fig.3.2a, when $BaTiO_3(111)$ is epitaxially strained to $SrTiO_3(111)$, namely when $BaTiO_3(111)$ is subjected to a compressive strain of $\eta_{in} = -1.5\%$, the polarization is about 0.02 Cm^{-2} (i.e., 2.0 μC/cm^2), agreeing with the magnitude (~1.35 μC/cm^2) measured in experiment [44]. Our theory thus provides a feasible explanation for the abnormal polarization observed in the (111)-oriented $BaTiO_3/SrTiO_3$ superlattices. To further confirm that the (111)-oriented $BaTiO_3$ under $\eta_{in} = -1.5\%$ is indeed polar, we also examine the phonon dispersion at this compressive strain. At $\eta_{in} = -1.5\%$, our calculations first show that the nonpolar $R\bar{3}m$ phase is not stable, and atoms like to move off-center to form a ferroelectric phase. After atoms are relaxed to form the ferroelectric $R3m$ phase, we then calculate again the phonon dispersion across the Brillouin zone, showing that the optimized ferroelectric $R3m$ phase displays no soft modes of imaginary frequency. The combined results on phonon dispersion and ferroelectric instability thus demonstrate that the polar $R3m$ phase is locally stable at $\eta_{in} = -1.5\%$, in agreement with the existence of hysteresis observed in experiment[44].

The physical reason for the unusual ferroelectric behaviors in (111)-oriented $BaTiO_3$ is simple. In (001)-oriented $BaTiO_3$, Ti and O atoms belong to the same atomic layer along the in-plane directions of biaxial strain (see Fig.3.4a). Under compressive in-plane strains, the Ti atom tends to be pushed off-center by surrounding four oxygen atoms, leading to an enlarged c-axis polarization. However, this is not the case in (111)-oriented $BaTiO_3$ (Fig.3.4b), where two oxygen (111) planes are separated from the Ti atom. At zero strain, the Ti-atom is closer to one of the

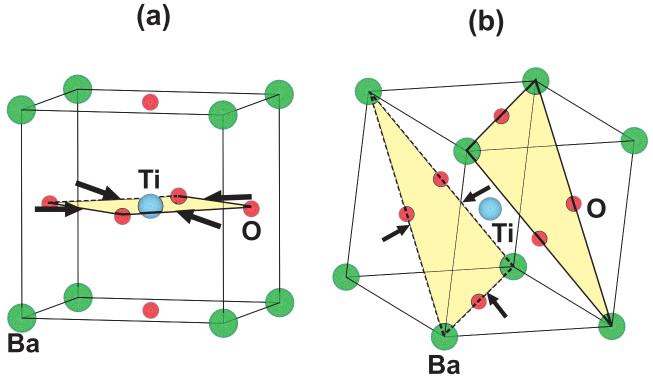

Figure 3.4: Schematic in-plane atomic configurations of (a) (001)-oriented $BaTiO_3$ with TiO_2 plane and (b) (111)-oriented $BaTiO_3$ with two BaO_3 planes. The thick arrows represent the directions of the compressive epitaxial strain.

two planes, causing ferroelectricity. As the solid is under a compressive in-plane strain, the three oxygen atoms in each plane move toward each other and fill the hollow space at the center of the oxygen triangle. Subsequently the Ti atom is pushed back toward the centrosymmetric position, giving rise to the decline of polarization. Furthermore, under compressive strains, the out-of-plane strain η_{out} in the (111)-oriented $BaTiO_3$ is much smaller than the value in the (001)-oriented $BaTiO_3$ (see the inset of Fig.3.2b). This also inhibits the off-center instability.

Although the main focus of this paper is on the ferroelectric properties and polarization behaviors of the rhombohedral phase in (111)-oriented $BaTiO_3$, we nevertheless have further considered other structural phases of lower symmetry than the rhombohedral phase by lifting the symmetry constraint. We find that, for all compressive strains considered in this paper, as well as for tensile strains below $\eta_{in} < 0.375\%$, the rhombohedral phase is the most stable structure in (111)-oriented $BaTiO_3$, and therefore, the polarization results in Fig.3.2(a) remain unchanged after symmetry constraint is lifted. For tensile strains $\eta_{in} > 0.375\%$, our calculations show that the lower-symmetry Cm phase has a slightly lower energy than the $R3m$ phase and becomes more stable after symmetry constraint is lifted, as shown in Fig.3.5(a). Nevertheless, the energy differences between the $R3m$ and Cm phases are small, being ~2.4 meV at η_{in} = 1%, which indicates that electric fields can be used to drive the system from one phase to another. The magnitude of polarization ($|\mathbf{P}|$) of the Cm phase, also depicted in Fig.3.5(a), is larger than that of the $R3m$ phase for the same strain. The calculation result of $|\mathbf{P}|(Cm) \neq |\mathbf{P}|(R3m)$ at a given strain reveals that the strain effect is not a simple polarization rotation process in which the polarization magnitudes are nearly equal in two phases[38]. To gain more insight into the polarization behavior, we plot in Fig.3.5(b) the three polarization components of the lowest-energy structure phase before and after the transition strain η_{in} = 0.375%. Two key outcomes can be seen in Fig.3.5(b): (i) When $BaTiO_3$ transitions from $R3m$ to Cm phase at η_{in} = 0.375%, the P_y polarization component undergoes a sudden and drastic change, which behaves like a first-order phase transition. (ii) In (001)-oriented $BaTiO_3$, polarization tends to lie completely within the inplane directions when tensile strain is larger than 1.5%.[46] However, and interestingly, this is not the case in (111)-oriented $BaTiO_3$ in Fig.3.5(b), where, even at a tensile strain as large as η_{in} = 3.0%, the Cm phase still has a significant out-of-plane polarization component. This unusual (and technologically useful) out-of-plane polarization at large tensile strains in (111)-oriented $BaTiO_3$ is due to the fact that under large tensile strains the three oxygen atoms in Fig.3.4(b) move away from each other and open an empty space at the center of the oxygen triangle, which allows Ti atom to move off-center. Also interestingly, the out-of-plane P_z component of the Cm phase in Fig.3.5b slightly increases (not decreases) with the tensile strain.

3.4 Summary

Different physical quantities—ferroelectric instability, strain-dependent polarization, out-of-plane strain response, and Brillouin-zone phonon dispersion—were examined to investigate the

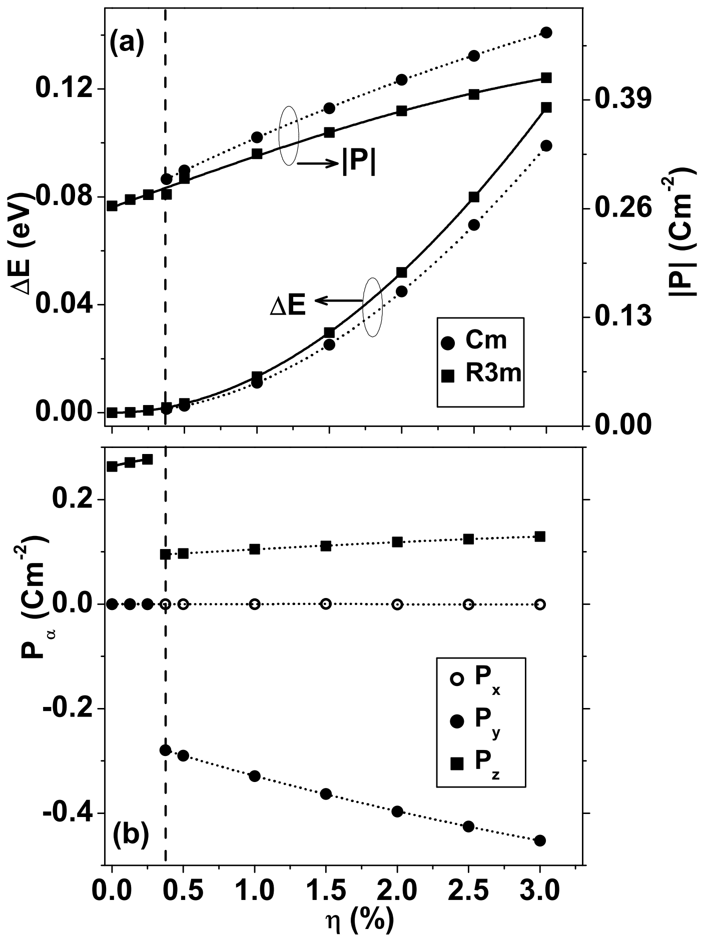

Figure 3.5: (a) Total energies $\Delta E(\eta_{in}) = E(\eta_{in}) - E_0$ (using the left vertical axis, where E_0 is the energy of the $R3m$ phase at $\eta_{in} = 0$) and the magnitudes |**P**| of polarization (using the right vertical axis) of the $R3m$ and Cm phases at different tensile strains; (b) Three polarization components of the lowest-energy structural phase in (111)-oriented $BaTiO_3$ under different tensile strains. The lowest-energy structure phase is the $R3m$ phase (when $0 < \eta_{in} < 0.375\%$) and the Cm phase (when $\eta_{in} \geq 0.375\%$). The y and z axes are along the pseudocubic $[\bar{1}2\bar{1}]$ and [111] directions, respectively.

ferroelectric and polarization properties in (111)-oriented $BaTiO_3$. These properties are found to be rather unusual and in significant differences from those of (001)-oriented $BaTiO_3$.

More specifically, we found that in (111)-oriented $BaTiO_3$, polarization declines when compressive strain is applied. This leads to a positive piezoelectric e_{31} coefficient, unlike in the (001) case where e_{31} is negative. A ferroelectric-to-paraelectric phase transition occurs at a compressive strain of η_{in}=-1.75%. This phase transition is independently confirmed by the lack of ferroelectric instability in potential well and by the lack of soft modes in phonon dispersion at $\eta_{in} = -2.5\%$. When the phase transition occurs, large piezoelectric e_{31} coefficients and dielectric response can be obtained. In contrast, polarization in the epitaxially strained (001)-oriented $BaTiO_3$ may rotate between in-plane and out-of-plane, but never vanish at low temperatures.[47] Furthermore, we showed that under increasing compressive strains, η_{out} in (111)-oriented $BaTiO_3$ increases despite polarization decreases, revealing that the strain-polarization coupling between out-of-plane strain and out-of-plane polarization is also unusual.

When (111)-oriented $BaTiO_3$ forms heterostructure and/or interface with topological insulators, semiconductors, magnetic manganites or other technological materials, our calculations reveal that one needs to apply epitaxial tensile strains to enhance the polarization effects. Under the increase of tensile strains, the out-of-plane component of the polarization was shown to increase for both the $R3m$ and Cm phases in (111)-oriented $BaTiO_3$. Interestingly, even under very large tensile strains (~3%), the polarization in (111)-oriented $BaTiO_3$ still possesses a significant (and technologically useful) out-of-plane component and does not fully lie within the inplane directions.

The different ferroelectric behaviors between two oriented $BaTiO_3$ can be explained by the atomic configurations and short-range interactions caused by orientations. The results also demonstrate a feasibility of using different orientations to control the ferroelectric properties. Considering that high-quality atomically flat $SrTiO_3$(111) substrates are now available [6], we hope that the unusual polarization properties revealed in the current study will generate further theoretical and experimental interest in (111)-oriented ferroelectrics.

Bibliography

[1] X.Y. He, T. Guan, X.X. Wang, B.J. Feng, P. Cheng, L. Chen, Y.Q. Li, and K.H. Wu, Appl. Phys. Lett. **101**, 123111 (2012).

[2] X.H. Wei, Y.R. Li, J. Zhu, W. Huang, Y. Zhang, W.B. Luo, and H. Ji, Appl. Phys. Lett. **90**, 151918 (2007).

[3] J.L. Wang, G. Tang, X.S. Wu, and M.Q. Gu, J. Crystal Growth, **353**, 134 (2012).

[4] L. Yan, K.R. Balasubramaniam, S.L. Wang, H. Du, and P.A. Salvador, Solid State Ionics, **194**, 9 (2011).

[5] Q. Yu, J.F. Li, Z.X. Zhu, Y. Xu, and Q.M. Wang, J. Appl. Phys. **112**, 014102 (2012).

[6] J. Chang, Y.-S. Park, and S.-K. Kim, Appl. Phys. Lett. **92**, 152910 (2008).

[7] R.E. Cohen, Nature (London) **358**, 136 (1992); R.E. Cohen and H. Krakauer, Phys. Rev. B **42**, 6416 (1990).

[8] J. Sinsheimer, S.J. Callori, B. Bein, Y. Benkara, J. Daley, J. Coraor, D. Su, P.W. Stephens, and M. Dawber, Phys. Rev. Lett. **109**, 167601 (2012).

[9] Y. Yang, W. Ren, M. Stengel, X.H. Yan, and L. Bellaiche, Phys. Rev. Lett. **109**, 057602 (2012).

[10] T. Gunter, E. Bousquet, A. David, Ph. Boullay, Ph. Ghosez, W. Prellier, and M. Fiebig, Phys. Rev. B **85**, 214120 (2012).

[11] P. Aguado-Puente, P. Garcia-Fernandez, and J. Junquera, Phys. Rev. Lett. **107**, 217601 (2011).

[12] X. Wu, K.M. Rabe, and D. Vanderbilt, Phys. Rev. B **83**, 020104 (2011).

[13] J.H. Lee and K.M. Rabe, Phys. Rev. Lett. **104**, 207204 (2010).

[14] S.M. Nakhmanson and I. Naumov, Phys. Rev. Lett. **104**, 097601 (2010).

[15] Y. Yao and H. Fu, Phys. Rev. B **82**, 174119 (2010).

[16] Y. Yao and H. Fu, Phys. Rev. B **80**, 035126 (2009).

[17] Q.Y. Liu, V. Nagarajan, and S.P. Alpay, Phys. Rev. B **78**, 064117 (2008).

[18] H.N. Lee, S.M. Nakhmanson, M.F. Chisholm, H.M. Christen, K.M. Rabe, and D. Vanderbilt, Phys. Rev. Lett. **98**, 217602 (2007).

[19] C.J. Fennie and K.M. Rabe, Phys. Rev. B **71**, 100102 (2005).

[20] A. Antons, J.B. Neaton, K.M. Rabe, and D. Vanderbilt, Phys. Rev. B **71**, 024102 (2005).

[21] C. Ederer and N. Spaldin, Phys. Rev. Lett. **95**, 257601 (2005).

[22] K.J. Choi *et al.*, Science **306**, 1005 (2004).

[23] J.H. Haeni *et al.*, Nature (London) **430**, 758 (2004).

[24] R. Kagimura and D.J. Singh, Phys. Rev. B **77**, 104113 (2008).

[25] R. Oja, K. Johnston, J. Frantti, and R. Nieminen, Phys. Rev. B **78**, 094102 (2008).

[26] P. Hohenberg and W. Kohn, Phys. Rev. **136**, B864 (1964); W. Kohn and L.J. Sham, Phys. Rev. **140**, A1133 (1965).

[27] R.D. King-Smith and D. Vanderbilt, Phys. Rev. B **47**, 1651 (1993).

[28] R. Resta, Rev. Mod. Phys. **66**, 899 (1994).

[29] S. Baroni, S. de Gironcoli, A. Dal Corso, and P. Giannozzi, Rev. Mod. Phys. **73**, 515 (2001).

[30] P. Giannozzi *et al.*, J. Phys. C **21**, 395502 (2009); P. Giannozi *et al.*, http://www.quantum-espresso.org.

[31] N. Troullier and J. L. Martins, Phys. Rev. B **43**, 1993 (1991).

[32] T. Mitsui *et al.*, *Landolt-Bornstein Numerical Data and Functional Relationships in Science and Technology* (Springer-Verlag, 1981), New Series, III/16.

[33] A. Garcia and D. Vanderbilt, Appl. Phys. Lett. **72**, 2981 (1998).

[34] H. Fu and R.E. Cohen, Nature (London) **403**, 281 (2000).

[35] N. Choudhury, E. J. Walter, A. I. Kolesnikov, and C-K Loong, Phys. Rev. B **77**, 134111 (2008).

[36] G. H. Kwei, A. C. Lawson, S.J.L. Billinge, and S. W. Cheong, J. Phys. Chem. **97**, 2368 (1993).

[37] L.D. Landau and E.M. Lifshitz, *Statistical Physics* (Pergamon, NY 1980), Part I.

[38] K.M. Rabe, C.H. Ahn, and J.-M. Triscone, *Physics of Ferroelectrics*, (Springer-Verlag, Berlin, 2007), Page 79.

[39] G. Saghi-Szabo, R.E. Cohen, and H. Krakauer, Phys. Rev. Lett. **80**, 4321 (1998).

[40] Ph. Ghosez, E. Cockayne, U.V. Waghmare, and K.M. Rabe, Phys. Rev. B **60**, 836 (1999).

[41] A.I. Lebedev, Physics of the Solid State **51**, 362 (2009).

[42] A. Garcia and D. Vanderbilt, Phys. Rev. B **54**, 3817 (1996).

[43] R. Yu and H. Krakauer, Phys. Rev. Lett. **74**, 4067 (1995).

[44] O. Nakagawara, T. Shimuta, T. Makino, S. Arai, H. Tabata, and T. Kawai, Appl. Phys. Lett. **77**, 3257 (2000).

[45] H. Tabata, H. Tanaka, and T. Kawai, Appl. Phys. Lett. **65**, 1970 (1994).

[46] O. Dieguez, S. Tinte, A. Antons, C. Bungaro, J.B. Neaton, K.M. Rabe, and D. Vanderbilt, Phys. Rev. B **69**, 212101 (2004).

[47] N.A. Pertsev, A.G. Zembilgotov, and A.K. Tagantsev, Phys. Rev. Lett. **80**, 1988 (1998).

4 Mode sequence, frequency change of non-soft phonons, and LO-TO splitting in strained tetragonal $BaTiO_3$

4.1 Introduction

A breakthrough was made in probing the lattice dynamics in nanoscale ferroelectrics (FE),[1, 2, 3] by using *ultraviolet* (UV) Raman spectroscopy rather than conventional Raman spectroscopy. Conventional Raman spectroscopy uses *visible* light as the probing source,[4] and works poorly for FE thin films since visible light, with its energy much smaller than the band gaps of FE oxides, is weakly absorbed by thin films and will penetrate deeply into substrates, leading to large unwanted signals from substrates and thus a low resolution. In fact, signal of visible-light Raman spectroscopy largely comes from the vibrations of the substrate, not from FE thin films. In contrast, the UV-Raman, utilizing UV-light with an energy larger than the band gaps of oxides, can be absorbed strongly by the FE thin films and thus can reveal the phonon structure of thin films with high resolution. Indeed, using UV-Raman, multiple sharp peaks were clearly observed in $BaTiO_3$/$SrTiO_3$ superlattices epitaxially grown on a $SrTiO_3$ substrate.[1, 2]

Furthermore, interesting phonon physics was revealed.[1] For instance, a new and pronounced Raman peak was observed at frequency 540 cm^{-1}, and was assigned as the transverse TO_4 mode originated from the strained $BaTiO_3$.[1] However, in bulk $BaTiO_3$, the frequency of the TO_4 mode is merely 486 cm^{-1} (Ref.[5]). Whereas it is known that strain may cause a large frequency shift to the soft mode, note that TO_4 is not a soft mode, however. A very large strain-induced frequency shift that occurs to a non-soft mode is interesting itself. It further raises other intriguing questions: (i) What is the origin of the drastic frequency shift? (ii) Are there other non-soft modes that may also exhibit large frequency shifts, but have not been detected in experiments?

Previously there were many important works on the lattice dynamics in ferroelectrics, yielding critical understanding on the structural instability,[6, 7] characteristic difference in phonon dispersion among different materials,[8] phonon in composition-modulated FE superlattices,[9] and finite electric-field induced phonon hardening in incipient ferroelectrics.[10, 11] Most of these studies paid attention to the behaviors of soft modes in the high-symmetry *non-polar* phase, namely the phase before ferroelectric transition occurs. In contrast, relatively less attention is given to the *polar* phase[12] and to the non-soft phonon modes.

The experimental advance[1, 2, 3] also brings another issue of broad interest, namely how the sequence of phonon modes is altered by external conditions. Sequencing of phonon modes, namely the ordering of vibration modes according to frequencies, is of fundamental relevance for unveiling the interatomic interaction in solids,[13] because the sequence is determined by the microscopic nuclei-nuclei, nuclei-electron, and electron-electron interactions. In contrast to a *single* mode, the mode sequencing reflects collectively the behaviors of a *group* of modes. Since different modes respond to the external conditions (such as pressure, strain, and electric field) in different manners, it is nontrivial to determine how the mode sequence alters with external conditions. Determination of mode sequencing is also of practical importance, since in infrared or Raman experiments this sequence is much needed in order to correctly assign phonon modes to individual peaks and to determine the origin of these peaks.[4] This knowledge is particularly relevant when the mode sequence under the ambient condition is, after the external condition has changed, no longer valid.

Owing to the facts that (i) ferroelectric properties are sensitive to lattice dynamics[6, 7, 8, 9, 14] and (ii) ferroelectrics possess a myriad of technological applications in dielectric capacitors,[16, 2] field-effect transistors,[17] electrical-caloric energy conversion,[3] piezoelectric devices and transducers,[13, 20, 21, 36, 23] and non-volatile ferroelectric random access memory,[12] studying phonon properties in ferroelectrics is thus very important. Interest in ferroelectrics also arises from the fundamental concepts these materials can bring to attention, such as the origin of ferroelectricity,[25, 5] the modern theory of polarization,[48, 40] theory of phase transitions,[29, 30] etc.

Another subject of profound interest in FEs is the LO-TO splitting. Transverse optic (TO) modes interact with light, which is a key process that determines optical properties.[13] On the other hand, longitudinal optic (LO) modes interplay with electric fields, determining the dielectric responses of solids.[13] The LO and TO modes are thus of key importance both in optical and dielectric properties. Further, the LO and TO modes are also critical in testing the fundamental 2n-1 sum rule.[31] Moreover, the LO-TO splitting arises from the long-range Coulomb interaction, manifesting the influence of this interaction on the lattice dynamics and the origin of anomalous Born effective charge.[32, 33]

A long-standing problem inhibits the *quantitative* study of the LO-TO splitting, however. That is, the splitting has not been fundamentally well defined. As have been realized by Zhong and Vanderbilt in a seminal work,[32] it is generally *not* possible to find a one-to-one correspondence between a LO mode and a TO mode. In fact, when lattice vibrations interact with electric fields via the long-range Coulomb interaction, more than one TO mode may contribute simultaneously—and all of them, significantly—to form a single LO mode as a result of the strong mode mixing caused by the Coulomb interaction. Here we give a concrete example to illustrate this spread mode mixing. We consider $BaTiO_3$ at a compressive strain of -2.5%. By quantitative mode projection, our first-principles calculations show that the E(LO_4) mode at frequency ω =735 cm^{-1} has contributions from five TO modes with the contribution weights at 7%, 23%, 21%, 8%, and 40%, respectively, revealing that the contributions are indeed widespread and there is no dominating one. This mode mixing is fundamental and cannot be avoided. As a consequence, attempt to define the LO-TO splitting as the frequency difference between one LO mode and one TO mode cannot be justified. The lack of quantitative study of the LO-TO splitting hampers the efforts in obtaining insight knowledge about this important quantity. It also prevents us from investigating how the splitting may be quantitatively tuned by external conditions such as epitaxial strain and electric field.

The purposes of this paper are fourfold: (i) to explain the origin of the large frequency shift of the non-soft TO_4 mode observed in the UV Raman experiments, and one step further, to determine which modes are susceptible, and which modes react less, to the epitaxial strain; (ii) to reveal how the sequencing of phonon modes can be significantly changed by strain, thereby the mode sequence at ambient condition should not be used to assign the peaks observed in strained FEs; (iii) to show that the LO-TO splitting can be rigorously defined, which paves a way to quantitatively study this important quantity; and (iv) to determine whether there are any other modes that exhibit large LO-TO splittings besides the soft TO mode.

This paper is organized as follow. In Sec.6.2 we will describe the calculation methods and theories pertinent to the vibrations in solids, and then in Sec.6.3 we will present the calculation results along with some key theoretical formulations for analysis. A summary in Sec.IV concludes the paper. Other useful results on the phonon displacements and infrared (IR) intensities are given in the Appendix.

4.2 Theoretical methods

Structural optimization: We consider tetragonal $BaTiO_3$ with the $P4mm$ symmetry. Total energy, atomic forces, and structural optimization are determined using the density functional theory (DFT) within the local density approximation[34] (LDA) via Quantum-ESPRESSO.[35, 36] Troullier-Martins pseudopotentials[34] are used to mimic the interaction between valence electrons and inert core electrons. Ti $3s$ and $3p$ semi-core states are treated as valence states.[38] The energy cutoff for wave function expansions is 95 Ry. Both cell parameters and atomic positions are optimized for a given inplane strain, with the force threshold set below 10^{-5} Ry/Bohr. The biaxial η strain is enforced by changing the in-plane lattice constant a as $\eta = \frac{a-a_0}{a_0}$, where a_0 is the in-plane lattice constant of $BaTiO_3$ at equilibrium. A negative η means that the strain is compressive. We find for unstrained $BaTiO_3$ a_0=3.93Å and $c/a = 1.007$, which are close to the values in other calculations (for instance, $a_0 = 3.945$Å and $c/a = 1.009$ in Ref.[19]).

Phonon structure: Phonon frequencies and eigenvectors are determined by the density functional perturbation theory (DFPT).[40, 41, 42] Vibration of atoms leads to the deformation potential $\Delta V(\mathbf{r}) = \sum_{l,i}[V(\mathbf{r}-\mathbf{R}_l-\mathbf{t}_i-\mathbf{u}_i) - V(\mathbf{r}-\mathbf{R}_l-\mathbf{t}_i)]$, where $\mathbf{t}_i$ and $\mathbf{u}_i$ are the equilibrium ionic position and atomic displacement of atom i, respectively; $\mathbf{R}_l$ is the lattice vector for cell l. By treating ΔV as perturbation, the response of electron density $\Delta n(\mathbf{r}) = 4\Re \sum_{n}^{N/2} \psi_n^*(\mathbf{r})\Delta\psi_n(\mathbf{r})$ is determined by solving the Sternheimer equation,[40]

$$(H_{scf} - \varepsilon_n)|\Delta\psi_n\rangle = -(\Delta V_{scf} - \Delta\varepsilon_n)|\psi_n\rangle\ , \tag{4.1}$$

where H_{scf} is the Kohn-Sham Hamiltonian, ε_n the single-particle eigenvalue of H_{scf}, and $\Delta V_{scf}(\mathbf{r}) =$

$\Delta V(\mathbf{r}) + e\int \frac{\Delta n(\mathbf{r}\prime)}{|\mathbf{r}-\mathbf{r}\prime|}\mathrm{d}r\prime + \frac{dv_{xc}(n)}{dn}\Big|_{n=n(\mathbf{r})}\Delta n(\mathbf{r})$ the self-consistent perturbation potential.

With Δn and $\Delta\psi$, other important quantities such as the change in the electric polarization ($\Delta\mathbf{P}$), the Born effective charges ($\mathbf{Z}^*$), and the dielectric tensor (ϵ) can be calculated, respectively, as $\Delta\mathbf{P} = \sum_i z_i e\,\mathbf{u}_i - \frac{e}{V}\int_V \mathbf{r}\Delta n(\mathbf{r})\,\mathrm{d}\mathbf{r}$, $(Z_i^*)_{\alpha\beta} = \frac{\Omega}{e}\frac{\partial P_\alpha}{\partial u_i^\beta(\mathbf{q}=0)}\Big|_{\mathbf{E}=0}$, and $\epsilon^\infty_{\alpha\beta} = \delta_{\alpha\beta} + 4\pi\frac{\partial P_\alpha}{\partial E_\beta}\Big|_{\mathbf{u}_i(\mathbf{q}=0)}$, where α and β are the direction indices, and Ω is the unit-cell volume.

*Nonanalytic contribution at **q**=0:* When dealing with the long wavelength phonons with wave vector **q** at the zone center, the interatomic force constant (IFC) matrix can be divided into analytic and nonanalytic contributions $C_{ij}^{\alpha\beta} = C_{ij}^{a,\alpha\beta} + C_{ij}^{na,\alpha\beta}$, where i and j are atomic indices. The nonanalytic part takes the form [43] $C_{ij}^{na,\alpha\beta} = \frac{4\pi}{\Omega}e^2\frac{(\mathbf{q}\cdot\mathbf{Z}_i^*)_\alpha(\mathbf{q}\cdot\mathbf{Z}_j^*)_\beta}{\mathbf{q}\cdot\epsilon^\infty\cdot\mathbf{q}}$. Note that C^{na} is not diagonal and will often cause strong mixings among different modes. At **q**=0, the nonanalytic contribution can be calculated by allowing **q** to approach the Brillouin zone center from a chosen direction. This nonanalytic contribution leads to the difference in frequency between LO phonon ($\mathbf{u}\|\mathbf{q}$) and TO phonon ($\mathbf{u}\perp\mathbf{q}$), due to the strong interaction between ions and displacement-induced electric field.[13, 4]

4.3 Results and discussions

Before we present our main results for strained $BaTiO_3$, it is important to examine the dielectric and phonon properties at zero strain since they are used as reference for the strained cases. The Born effective charges Z^* and high-frequency dielectric constant ϵ^∞ are given in Table 4.1, and the phonon frequencies of the zone-center modes are in Table 4.2. We see that Z^* and ϵ^∞ obtained in our calculations are in good agreement with others,[44] so are the phonon frequencies.[5, 45] The slight difference between our results and those of Ref.[44] in Table 4.1 is because the authors of Ref.[44] performed their calculations using the experimental value of lattice constant.

Table 4.1: Born effective charges and high-frequency dielectric constants for unstrained $BaTiO_3$. O2 is the apical oxygen atom beneath Ti along the tetragonal *c*-axis.

Quantity	Present work	Other work (Ref.[44])
Z^*_{xx}(Ba)	2.77	2.73
Z^*_{zz}(Ba)	2.81	2.81
Z^*_{xx}(Ti)	7.11	7.04
Z^*_{zz}(Ti)	6.54	5.97
Z^*_{xx}(O1)	-5.56	-5.60
Z^*_{zz}(O1)	-2.05	-2.15
Z^*_{xx}(O2)	-2.09	-2.02
Z^*_{zz}(O2)	-5.07	-4.84
ϵ^{∞}_{xx}	6.54	6.48
ϵ^{∞}_{zz}	6.07	5.84

Table 4.2: Frequencies of the phonon modes at the zone center in zero-strained $BaTiO_3$.

ω(cm^{-1})	Present work	Other theory (Ref.[45])	Experiments (Ref.[5])
E(TO_1)	-78	-79	36
A_1(TO_1)	178	190	170
E(LO_1)	180	188	180
E(TO_2)	183	192	180
A_1(LO_1)	186	195	185
A_1(TO_2)	211	237	270
B_1	296	301	305
E(LO_2)	300	302	305
E(TO_3)	300	302	305
E(LO_3)	462	462	463
A_1(LO_2)	465	465	475
E(TO_4)	480	487	486
A_1(TO_3)	497	507	520
E(LO_4)	678	701	715
A_1(LO_3)	697	721	720

The normal modes in tetragonal $BaTiO_3$ are $5E\bigoplus 4A_1\bigoplus B_1$, labelled according to the irreducible representations of the crystallographic space group $P4mm$. E modes are doubly degenerate; these modes vibrate along the ab plane on which the biaxial strain is applied. A_1 and B_1 modes are singly degenerate and vibrate along the c axis perpendicular to the directions of applied biaxial strain. Since the tetragonal phase is not the most stable phase for $BaTiO_3$ (the rhombohedral phase is), obviously there is one soft mode, $E(TO_1)$, in Table 4.2, as it should be. The atomic vibration directions and amplitudes are shown in the Appendix for each mode.

According to their vibration patterns in the Appendix, the modes can be categorized as (i) Slater modes, in which Ti and O atoms vibrate oppositely to each other without involving significantly Ba, such as $E(TO_1)$, $E(LO_4)$, $A_1(TO_2)$, and $A_1(LO_3)$; (ii) Last modes, where Ti and O vibrate in the same direction but opposite to Ba, such as $E(TO_2)$, $E(LO_1)$, $A_1(TO_1)$, and $A_1(LO_1)$; (iii) Axe mode, where the O atoms on one plane (not necessarily the base plane) vibrate oppositely to that of the O atom out of the plane, e.g., $E(TO_4)$ and $A_1(TO_3)$; (iv) Axe+Ti mode, where its vibration pattern resembles the Axe mode but involving Ti, e.g., $E(LO_3)$ and $A_1(LO_2)$; (v) O-plane distortion mode, where the O atoms on one plane move in opposite directions, e.g., $E(TO_3)$, $E(LO_2)$, and B_1.

4.3.1 Mode sequence in strained $BaTiO_3$

Phonon frequencies at Γ in $BaTiO_3$ under six different inplane strains are shown in the inset of Fig.4.1. Note that only discrete symbols as those in the inset of Fig.4.1 are the results directly obtained from calculations. With these discrete symbols alone, it is hard to figure out which mode at η=-2.5% corresponds to which mode at η=0, since strain often gives rise to frequency crossings due to strong mixing between different modes. Furthermore, in the inset of Fig.4.1, many modes have nearly the same frequency, and keeping track of the strain-induced evolution for these modes is nontrivial. As a consequence, the important knowledge of how individual phonon modes evolve with strain—and how the mode sequence changes by strain—is unclear.

To solve this problem and to obtain valuable insight into the phonon evolution with strain, we use an approach based on mode projection. Let $|\epsilon_n^{i\alpha}(\eta)\rangle$ be the phonon eigenvector of the nth mode at strain η, and $|\epsilon_n^{i\alpha}(\eta)\rangle$ is related to the phonon displacement $|u_n^{i\alpha}(\eta)\rangle$ by $|\epsilon_n^{i\alpha}(\eta)\rangle = \sqrt{M_i}|u_n^{i\alpha}(\eta)\rangle$, where i is the atom index, α the direction index, and M_i the mass of atom i. The eigenvectors satisfy the orthonormality condition $\sum\limits_{i\alpha}\langle\epsilon_m^{i\alpha}(\eta)|\epsilon_n^{i\alpha}(\eta)\rangle = \delta_{mn}$. Using the vibration eigenvectors at η_1 as bases, one can expand the eigenvectors at η_2 as

$$\epsilon_n^{i\alpha}(\eta_2) = \sum_m p_{mn}\epsilon_m^{i\alpha}(\eta_1)\,, \tag{4.2}$$

where $p_{mn} = \sum\limits_{i\alpha}\langle\epsilon_m^{i\alpha}(\eta_1)|\epsilon_n^{i\alpha}(\eta_2)\rangle$ describes the degree of correlation between mode m at strain η_1 and mode n at strain η_2. We expect $\sum\limits_m |p_{mn}|^2$=1, which is indeed confirmed by our numerical calculations. From the quantity p_{mn}, one can identify the correspondences and evolutions between modes at different strains. The correspondences are depicted by the connecting lines in Fig.4.1. Furthermore, p_{mn} is also very useful in examining the strain-induced inter-mode mixing when it does occur.

Fig.4.1 reveals that the mode sequence in strained $BaTiO_3$ drastically differs from the unstrained case. This drastic difference occurs even for a moderate strain at $\eta = -2.5\%$. The key distinctions between mode sequences at $\eta = -2.5\%$ and at $\eta = 0$ are: (i) At $\eta = -2.5\%$, the frequency of $A_1(TO_2)$ is notably above those of $E(TO_3)$, $E(LO_2)$, and B_1. This clearly is not the case at $\eta = 0\%$, where the former mode is well below the latter three modes. (ii) $A_1(LO_3)$ and $E(LO_4)$

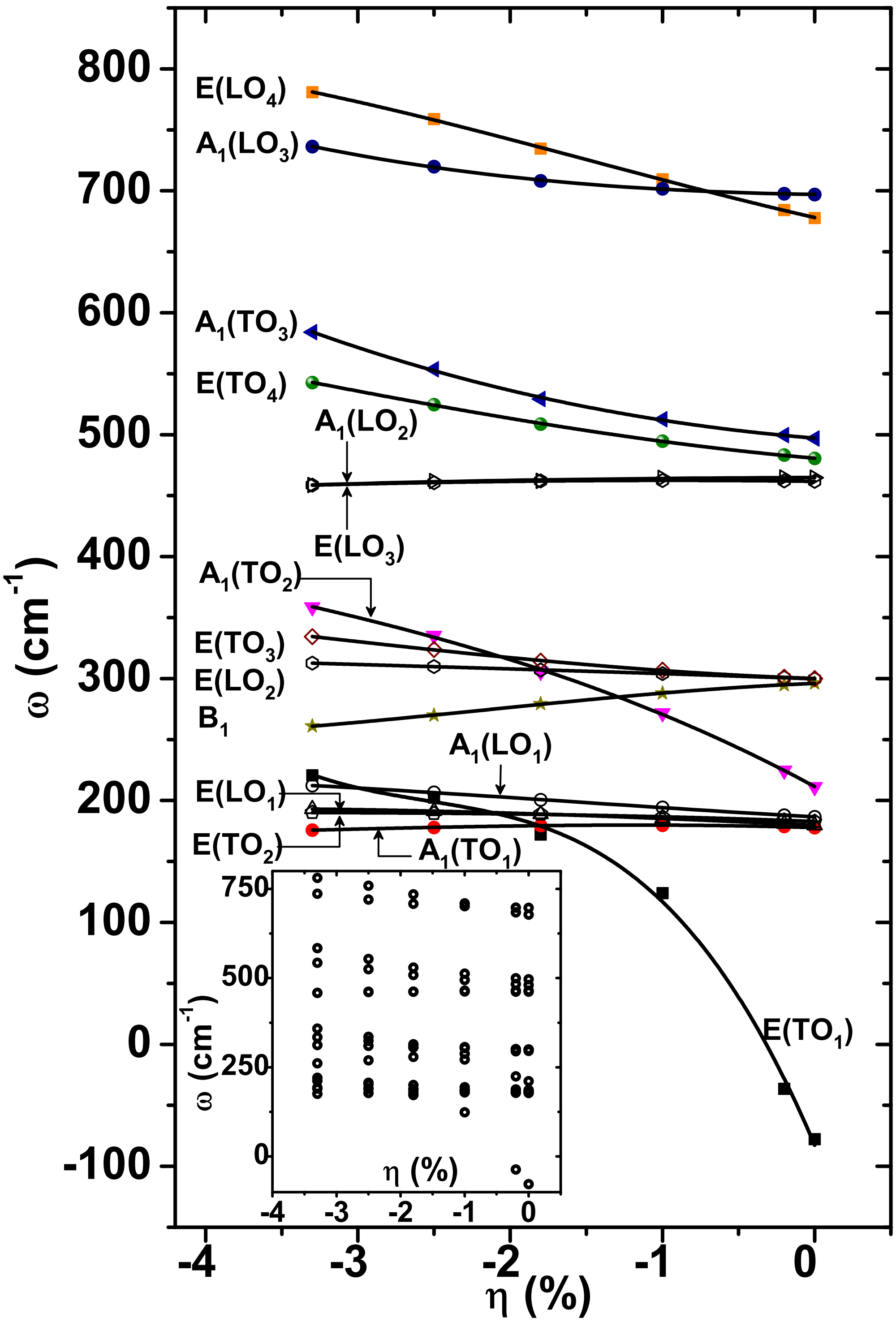

Figure 4.1: Phonon frequencies at Γ as a function of epitaxial strain. The acoustic phonons at Γ are trivial and hence omitted from this plot. Nonanalytic C^{na} matrix is calculated with q→ [001] for A$_1$(LO) modes, and with q→ [100] for E(LO) modes. The inset shows the mode frequencies directly obtained from the DFPT calculations, without applying the mode projection.

undergo a crossover in frequency as strain varies. At $\eta = 0$, $A_1(LO_3)$ is the mode with the highest frequency. However, at $\eta = -2.5\%$, $E(LO_4)$ exhibits the highest frequency. (iii) Interestingly, $E(TO_3)$, $E(LO_2)$ and B_1 modes are very close in frequency at $\eta = 0$, but they are well separated in sequence at $\eta = -2.5\%$. (iv) Obviously, the hardening of the soft mode $E(TO_1)$, which crosses with $A_1(TO_1)$, $E(TO_2)$, $E(LO_1)$, and $A_1(LO_1)$, also contributes substantially to the change in mode sequence. Furthermore, as pointed out by Choudhury *et al.*, the zone-center phonons in unstrained perovskites exhibit interesting frequency gaps.[46] These phonon gaps may have innovative applications in sound and heat revolutions.[47] The phonon-frequency gaps are confirmed by the η=0 calculations in Fig.4.1 in the frequency ranges of 200–300, 300–450, and 500–670 cm^{-1}. These phonon gaps largely disappear, or are significantly reduced, at strain $\eta = -3.3\%$, however.

The theoretical results have important implication for experiments. They reveal that, in Raman and/or infrared experiments, using the mode sequence of unstrained $BaTiO_3$ to index the spectroscopy peaks observed in epitaxially strained $BaTiO_3$ may lead to significant errors. Specifically, when $BaTiO_3$ is strained to $SrTiO_3$ substrate (with about 2.5% compressive strain), the mode sequence is very different from that in unstrained $BaTiO_3$, as shown in Fig.4.1. We instead need to use the correct mode sequence (e.g., the one in Fig.4.1) to assign experimentally measured peaks.

4.3.2 Strain-induced large frequency shifts for non-soft modes

Strain-dependent frequency shift, defined as $\Delta\omega_n(\eta) = \omega_n(\eta) - \omega_n(\eta = 0)$ for a given mode n, is depicted in Fig.4.2. Note that determination of $\Delta\omega_n(\eta)$ is possible only after the correspondences between modes at different strains have been mapped out. According to the magnitude and sign of $\Delta\omega$, the frequency responses in Fig.4.2 can be categorized into three groups: large increase ($\Delta\omega > 50$ cm^{-1}), moderate increase ($0 < \Delta\omega < 50$ cm^{-1}), and frequency decrease $\Delta\omega < 0$, when η

varies in the considered strain range from 0 to -3.3%.

Interestingly, $A_1(TO_2)$, $E(LO_4)$, $A_1(TO_3)$, and $E(TO_4)$ in Fig.4.2 all display a large strain-induced frequency shift, with $\Delta\omega > 50$ cm^{-1} at η=-3.3%. Particularly, $A_1(TO_2)$ increases its frequency by more than 140 cm^{-1} at η=-3.3% with respect to η=0, which is rather phenomenal. Note that none of the above modes are soft modes. Also notably, unlike most other modes, B_1 shows an unusual frequency decrease in Fig.4.2.

Results in Fig.4.2 defy the common wisdom. According to symmetry, vibrations in perovskites of tetragonal structure can be either along the in-plane directions (e.g., the E modes) with frequency to be denoted as $\omega_{\parallel}$, or along the out-of-plane direction (e.g., the A_1 modes) with frequency to be denoted as $\omega_{\perp}$. When a compressive strain is applied, one would think that $\omega_{\parallel}$ should increase, since along the in-plane directions atomic interaction is strengthened by the strain. Meanwhile, along the out-of-plane direction, interatomic interaction is weakened, and hence a decrease in $\omega_{\perp}$ is expected. However, the calculation results in Fig.4.2 reveal different conclusions. In fact, upon the impose of strain, $A_1(TO_2)$, $A_1(TO_3)$, and $A_1(LO_3)$ in Fig.4.2 all increase their $\omega_{\perp}$ frequencies very substantially, in sharp contrast to the common belief. Furthermore, note the subtle decrease in the $\omega_{\parallel}$ frequency for $E(LO_3)$, which also deviates from the above common thinking. The direct first-principles calculations suggest a different mechanism that dictates the mode's frequency response.

Our calculations are consistent with, and provide explanation for, experimental observations. In the UV-Raman experiments, when $(BaTiO_3)_5/(SrTiO_3)_4$ ×25 superlattice is epitaxially strained to a $SrTiO_3$ substrate, the non-soft TO_4 mode of $BaTiO_3$ is shifted from 486 cm^{-1} in bulk to 540 cm^{-1} in strained superlattice.[1] According to Fig.4.2, when $BaTiO_3$ is strained to $SrTiO_3$ at $\eta = -2.5\%$, the $E(TO_4)$ frequency increases by 45 cm^{-1}. This is in good agreement with the

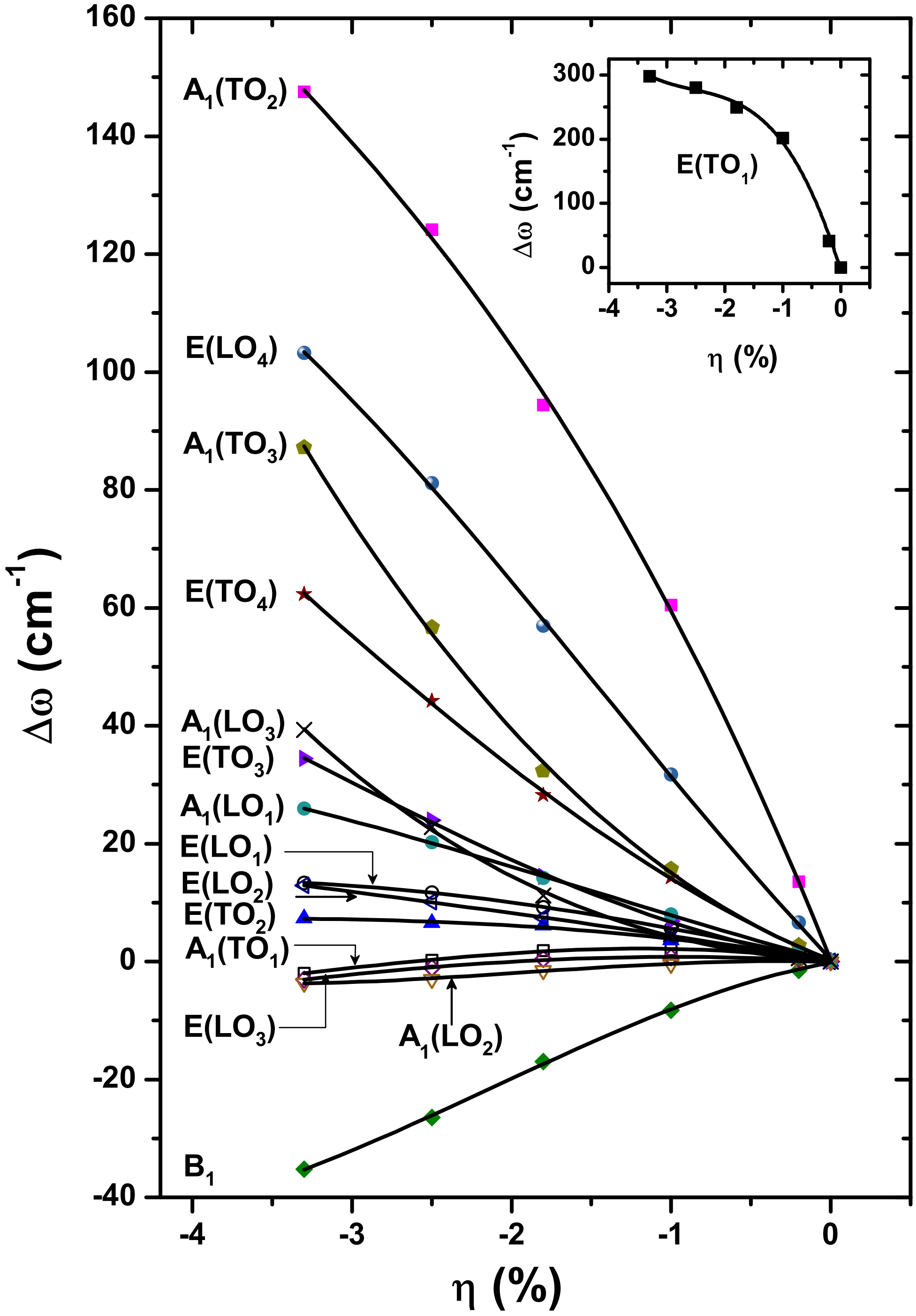

Figure 4.2: Frequency shift ($\Delta\omega$) as a function of strain. In the inset, the frequency shift for soft mode E(TO$_1$) is shown.

experiment where a shift of 54 cm^{-1} was observed.[1] Moreover, our theory predicts that there are other non-soft modes such as $A_1(TO_2)$, $E(LO_4)$, and $A_1(TO_3)$ that are subjected to even larger shifts (see Fig.4.2).

The physical origin underlying the mode behaviors in Fig.4.2 is rather simple and can be explained by the relative motion between Ti and O along the direction of vibration. When Ti and O vibrate oppositely, or when Ti does not vibrate but O vibrates toward Ti, the frequency increases with strain, which is indeed the case for the Slater modes $A_1(TO_2)$ and $E(LO_4)$, and for the Axe modes $A_1(TO_3)$ and $E(TO_4)$ (The displacement patterns of these modes are given in the Appendix). On the other hand, for modes in which Ti and O atoms vibrate in the same direction, the frequencies moderately change, such as the Last modes $E(TO_2)$ and $E(LO_1)$. For the B_1 mode, the vibration largely weakens the atomic interaction along the out-of-plane direction, leading to a frequency decrease.

Another interesting observation in Fig.4.2 is that $\Delta\omega$ is nonlinear as a function of strain for $A_1(TO_2)$, $A_1(TO_3)$, and $A_1(LO_3)$, while for other modes it is fairly linear. The nonlinearity has important consequence for the strain-mode coupling. To see this, we start with a simple model and write the energy as $E = \frac{1}{2}m\omega^2(\eta)Q^2$, where Q is the normal mode and $\omega(\eta)$ is strain-dependent. Consider the strain dependence of ω as $\omega(\eta) = \omega_0 + \alpha_1\eta + \alpha_2\eta^2$. It is straightforward to prove that, if ω depends linearly on η, i.e., α_2=0, the strain-coupling terms include only ηQ^2 and $\eta^2 Q^2$. But when the nonlinear effect is important, i.e., α_2 cannot be neglected, the strain-mode coupling should also include the $\eta^3 Q^2$ term. To explain the nonlinear strain-dependence of $\Delta\omega$, we give in Table 4.3 the phonon eigenvectors at different strains for some selected modes. We find that, for $A_1(TO_3)$, its eigenvector (particularly the Ti component) changes substantially with strain, which leads to the strong nonlinearity.

Table 4.3: Evolution of selected phonon eigenvectors with the η strain in tetragonal BaTiO$_3$. The selected modes possess noticeable change in the individual components at higher strains. The vibration direction is indicated in the first column, by an italic letter inside a parenthesis below the mode name. O2 is the apical oxygen atom beneath Ti along the tetragonal c-axis.

Modes	Atoms	Eigenvector components		
		$\eta = 0$	$\eta = -1.8\%$	$\eta = -3.3\%$
E(TO$_1$)	Ba	0.020	0.081	-0.078
(*y*)	Ti	0.677	0.611	0.694
	O1	-0.358	-0.584	-0.661
	O2	-0.308	-0.244	-0.040
	O3	-0.564	-0.468	-0.271
A$_1$(TO$_2$)	Ba	-0.190	-0.089	-0.085
(*z*)	Ti	0.835	0.766	0.715
	O1	-0.270	-0.422	-0.491
	O2	-0.348	-0.223	-0.007
	O3	-0.270	-0.422	-0.491
E(TO$_4$)	Ba	-0.011	-0.002	0.001
(*y*)	Ti	0.142	0.025	-0.091
	O1	-0.478	-0.456	-0.431
	O2	-0.467	-0.384	-0.269
	O3	0.730	0.803	0.856
A$_1$(TO$_3$)	Ba	-0.009	-0.002	0.008
(*z*)	Ti	0.052	-0.115	-0.288
	O1	-0.429	-0.335	-0.216
	O2	0.794	0.874	0.908
	O3	-0.429	-0.335	-0.216

4.3.3 LO-TO splitting

We begin by rigorously defining the LO-TO splitting, which will serve as the foundation for the present study of this important quantity. Let $\{|\epsilon\prime_n\rangle,\ \omega\prime_n(\mathbf{q}\to 0)\}$ be the mode eigenvectors and eigenvalues obtained from the diagonalization of the total dynamic matrix $D = D^a(\mathbf{q}=0) + D^{na}(\mathbf{q}\to 0)$, which $D_{ij}^{\alpha\beta} = \frac{1}{\sqrt{M_i M_j}} C_{ij}^{\alpha\beta}$ includes both the analytic and non-analytic contributions, thereby the LO-TO splitting. Let $\{|\epsilon_n\rangle,\ \omega_n(\mathbf{q}=0)\}$ be the eigenvectors and eigenvalues obtained from the analytic $D^a(\mathbf{q}=0)$ only, and therefore the displacement-induced electric field and the LO-TO splitting are not accounted for. Since $\{|\epsilon_m\rangle\}$ form a complete basis for any mode at **q=0**, it is hence always possible to write $|\epsilon\prime_n\rangle = \sum_m \alpha_{mn}|\epsilon_m\rangle$. Due to the strong mixing among different modes caused by the displacement-induced electric field, there are more than one dominant contributions in the above summation over m. In other words, α_{mn} are often large and significant for multiple m modes. One can define new frequencies as

$$\widetilde{\omega}_n^2 = \sum_m \mid \alpha_{mn} \mid^2 \omega_m^2, \tag{4.3}$$

bearing in mind that the dynamic eigenstate equation is $D|\epsilon_m\rangle = \omega_m^2|\epsilon_m\rangle$, not $D|\epsilon_m\rangle = \omega_m|\epsilon_m\rangle$. $\widetilde{\omega}_n$ in Eq.(4.3) properly accounts for the mode mixing when multiple TO modes contribute to form a LO phonon, and meanwhile, all frequencies in this equation are without LO-TO splittings. The LO-TO splitting $\Delta\omega_n^{LT}$ is then defined as

$$\Delta\omega_n^{LT} = \omega\prime_n(\mathbf{q} \to 0) - \widetilde{\omega}_n(\mathbf{q} = 0), \tag{4.4}$$

by which one can calculate $\Delta\omega_n^{LT}$ for any mode $|\epsilon\prime_n\rangle$. Eq.(4.3) and Eq.(4.4) provide a rigorous approach to determine and quantitatively study LO-TO splittings.

Using the above approach and formulas, we numerically find that $\Delta\omega_n^{LT}$ is significant only for the LO modes as it should be. To gain more insight, Fig.4.3 depicts the LO-TO splittings for the LO modes with significant $\Delta\omega^{LT}$. In Fig.4.3, $\mathbf{q}$ approaches the zone center along the [001] direction for A(LO) modes, and along the [100] direction for E(LO) modes.

While soft mode in ferroelectrics, such as E(TO$_1$) in BaTiO$_3$, is known to interact strongly with the displacement-induced electric field and generate a giant LO-TO splitting in forming the E(LO$_4$) mode, the quantitative understanding of LO-TO splitting for *other modes* is virtually

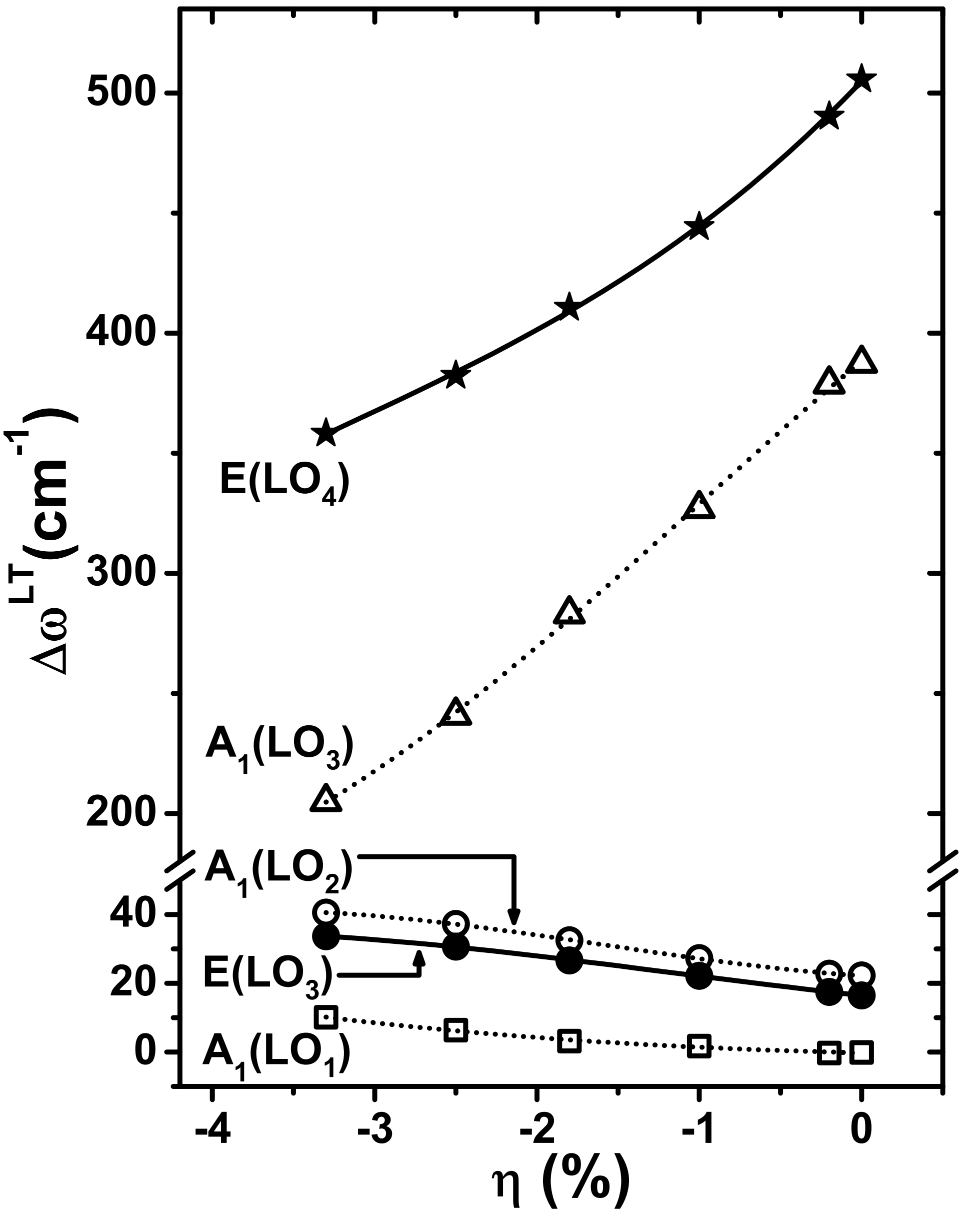

Figure 4.3: The LO-TO splittings $\Delta\omega^{LT}$ as a function of strain, for those modes with sizable splittings.

unknown. Interestingly, Fig.4.3 reveals that E(LO$_4$) is not the only mode that displays a large LO/TO splitting. Rather remarkably, $\Delta\omega_n^{LT}$ of A$_1$(LO$_3$) is nearly as large as that of E(LO$_4$). This is phenomenal since, unlike E(LO$_4$), A$_1$(LO$_3$) does not originate from a soft mode.

Furthermore, Fig.4.3 shows quantitatively for the first time (to our knowledge) that the

LO/TO splittings in ferroelectric BaTiO$_3$ change in an approximately linear manner with the strain. More specifically, with the increase of compressive strain, $\Delta\omega_n^{LT}$ decreases sharply for E(LO$_4$) and A$_1$(LO$_3$) modes.

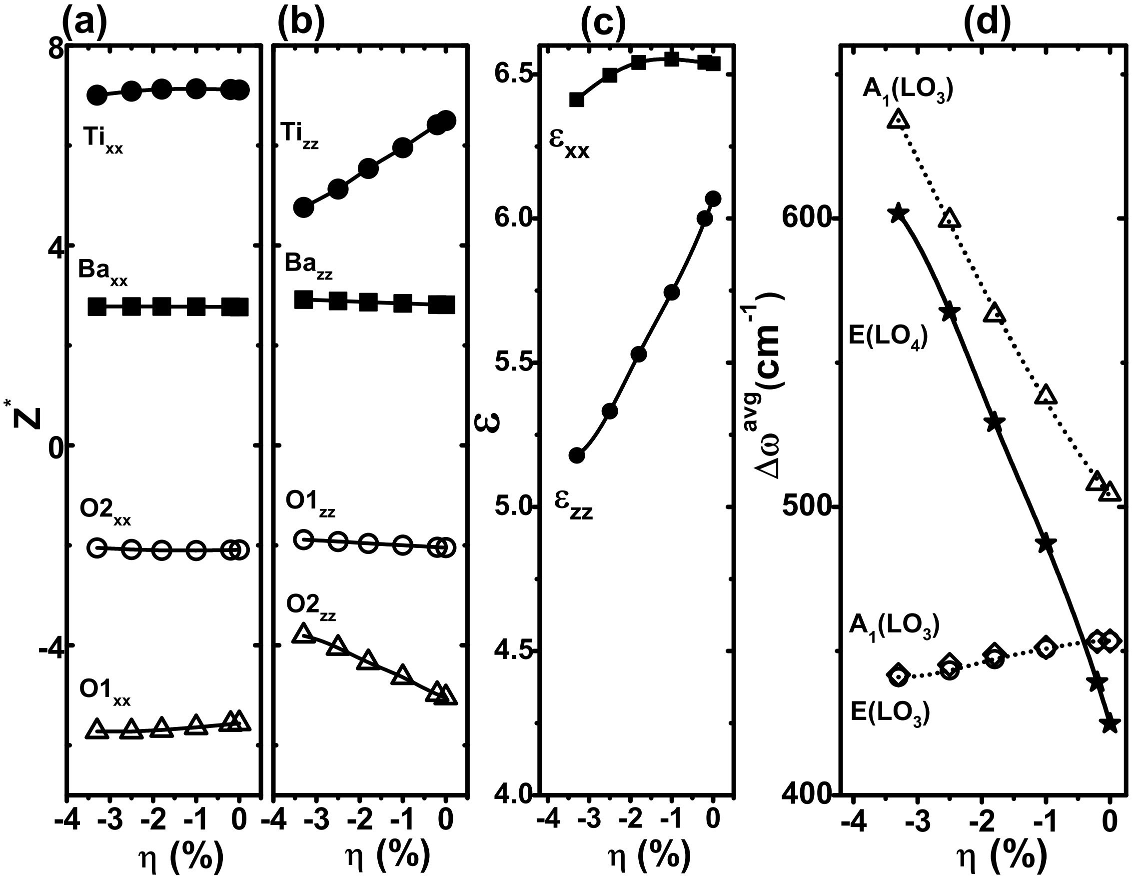

Figure 4.4: Changes of the following quantities as a function of strain in BaTiO$_3$: (a) the Z^*_{xx} component of the Born effective charge, (b) the Z^*_{zz} component of the Born effective charge, (c) the high-frequency dielectric constants ϵ^∞_{xx} and ϵ^∞_{zz}, and (d) the average ω^{avg} for E(LO$_4$) and A$_1$(LO$_3$) modes.

The dramatic decrease of the LO-TO splitting with strain for E(LO$_4$) and A$_1$(LO$_3$) cannot be naively explained by the Born effective charge (Z^*) and the dielectric constant ϵ^∞; the latter two quantities are shown in Fig.4.4(a)-(c). Take E(LO$_4$) as an example. The E(LO$_4$) modes vibrate along the inplane directions. However, the inplane component Z^*_{xx} almost does not change for all atoms (Fig.4.4a), and ϵ^∞_{xx} does not change much either (Fig.4.4c). Consequently, the non-analytic

$D_{ij}^{\alpha\beta,na}$ contribution is nearly a constant independent of strain for the E(LO$_4$) mode, which cannot explain the drastic decrease of the LO-TO splitting for this mode. We find that the declining $\Delta\omega^{LT}$ is due to the increase of the average frequency, defined as

$$\omega_n^{\mathrm{a}vg} = \frac{\omega\prime_n(\mathbf{q} \rightarrow 0) + \widetilde{\omega}_n(\mathbf{q} = 0)}{2}. \tag{4.5}$$

Using $\omega_n^{\mathrm{a}vg}$, the LO-TO splitting can be written as $\Delta\omega_n^{LT} = \frac{1}{2\omega_n^{\mathrm{a}vg}} \sum_i \frac{4\pi}{\Omega M_i} e^2 \frac{(\mathbf{q}\cdot\mathbf{Z}_i^*)(\mathbf{q}\cdot\mathbf{Z}_i^*)}{\mathbf{q}\cdot\epsilon^{\infty}\cdot\mathbf{q}}$, i.e., $\Delta\omega_n^{LT}$ is inversely proportional to $\omega_n^{\mathrm{a}vg}$. Fig.4.4(d) shows the average frequency $\omega_n^{\mathrm{a}vg}$ for E(LO$_4$) and A$_1$(LO$_3$). We see that, when η varies from 0 to -3.3%, $\omega_n^{\mathrm{a}vg}$ increases considerably for both modes, leading to the significant decrease of the LO-TO splitting. Therefore, it is $\omega_n^{\mathrm{a}vg}$ that governs the strain dependence of the LO-TO splitting in perovskite ferroelectrics.

4.4 Summary

Mode sequence is of key relevance in properly assigning spectroscopic peaks. In this study, several interesting changes in mode sequence were determined and revealed in strained BaTiO$_3$ by density functional perturbation calculations; these changes are caused by the intrinsic strain-induced mode crossing and inter-mode mixing. Furthermore, the frequency shifts of individual zero-center phonons were mapped out and compared to experiments, with particular attention to those non-soft modes. A group of non-soft modes with a sensitive strain-dependent frequency were identified. Moreover, the LO-TO splitting is rigorously defined, which allows this important physical quantity to be quantitatively studied. We further revealed which mode other than E(LO$_4$) displays strong LO-TO splitting and how the splitting depends on the epitaxial strain. Our specific findings are summarized in the following.

(i) The mode sequence is widely different at $\eta = -2.5\%$ than at zero strain. The changes in mode sequence stem from multiple mode crossings. At η =-2.5%, the highest mode is E(LO_4), not A_1(LO_3). Also, unlike the unstrained $BaTiO_3$ in which A_1(TO_2) is well below E(TO_3), E(LO_2) and B_1, at high strain A_1(TO_2) surpasses all of them. Furthermore, the characteristic phonon gaps at zero strain largely disappear at high strains. Our calculations quantitatively predict the magnitude of strain at which one mode crosses the others (see Fig.4.1).

(ii) Large strain-induced frequency shifts were shown to occur, even for non-soft phonons. As shown in Fig.4.2, these non-soft modes include A_1(TO_2), E(LO_4), A_1(TO_3), and E(TO_4). Indeed, large shift has been observed in experiments using the new UV-Raman spectroscopy.[1] At η =-2.5%, the theoretical shift of 45 cm^{-1} for E(TO_4) is in good agreement with the measured value of 54 cm^{-1} in experiment. Note that our theory predicts that E(TO_4) is only one of the non-soft modes displaying large strain-induced frequency change; the frequency shifts of other three non-soft modes are even larger (see Fig.4.2).

Our calculations in Fig.4.2 further reveal that, while frequency shift $\Delta\omega$ linearly depends on strain for most modes, there are interesting exceptions, that is, strong nonlinear dependency is found for modes A_1(TO_3) and A_1(LO_3), caused by considerable changes in the phonon eigenstates. This nonlinear dependence implies that the $\eta^3 Q^2$ term cannot be neglected in the formulation of the strain-mode coupling.

(iii) The rigorous definition of the LO-TO splitting enables the discovery of new physics. A markedly large LO-TO splitting is found for the A_1(LO_3) mode, in addition to the well-known E(LO_4). We further showed that the LO-TO splittings of A_1(LO_3) and E(LO_4) decrease sharply with the increasing compressive strain, showing a rather linear dependence. The decline of the LO-TO splitting cannot be explained by the effective charge and high-frequency dielectric constant, and is instead due to the large change in the average frequency ω_n^{avg}.

Considering that ultraviolet Raman spectroscopy is now available in experiments,[1, 2, 3] and considering that non-soft modes may play a pivotal role in determining the structure properties in ferroelectrics as demonstrated in Ref.[48], we hope that our study will stimulate further theoretical and experimental interest in mode sequence, the behaviors of non-soft modes, and the quantitative understanding of LO-TO splitting.

4.5 Appendix

This appendix provides additional results that include the vibration displacements and infrared (IR) intensities of the zone-center modes. Vibration displacements are of key relevance in terms of understanding the behaviors of individual modes, and are given in Fig.4.5 for all E modes and in Fig.4.6 for all A_1 modes in unstrained $BaTiO_3$. We choose the top view (i.e., view from the - **c** axis) for the E modes since they vibrate on the **ab** plane. Meanwhile, we choose the side view (i.e., view from the **b** axis) for the A_1 modes since these modes vibrate along the **c** axis.

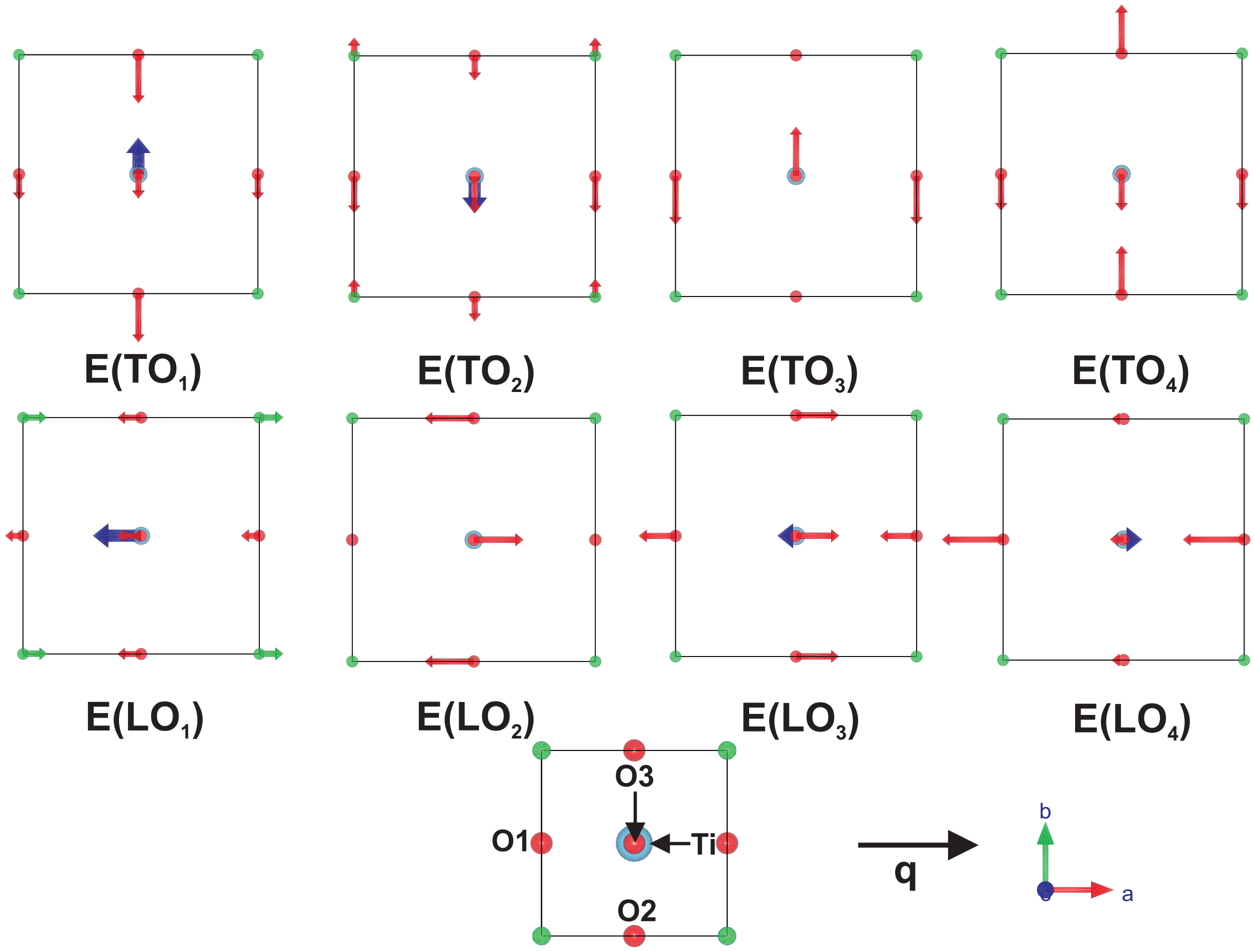

Figure 4.5: (Color online) Top view (i.e., from the - **c** axis) of phonon displacements of the E modes in unstrained BaTiO$_3$. The axes at the bottom-right corner refer to the crystallographic axes {**a**, **b**, **c**}, coinciding with the cartesian {**x**, **y**, **z**} directions, respectively. **q** approaches the zone center along the [100] direction for E(LO) modes. The green, light blue, and red spheres represent Ba, Ti, and O atoms, respectively. Atoms are labeled at the bottom of the figure. The arrows on atoms represent the magnitude of displacement; the dark-blue arrow is for Ti atom, to differentiate its displacement from that of the O2 atom along the same line of view.

Infrared (IR) spectroscopy is an important technique that probes the change in the dipole moment due to lattice vibration, namely the infrared intensity $I \propto \left|\frac{\partial \mathbf{P}}{\partial \mathbf{Q}}\right|^2$, where **Q** is the normal mode amplitude. This results in[49]

$$I = \sum_{\alpha} \left| \sum_{s\beta} Z_s^{*\,\alpha\beta} u_s^{\beta} \right|^2 , \tag{4.6}$$

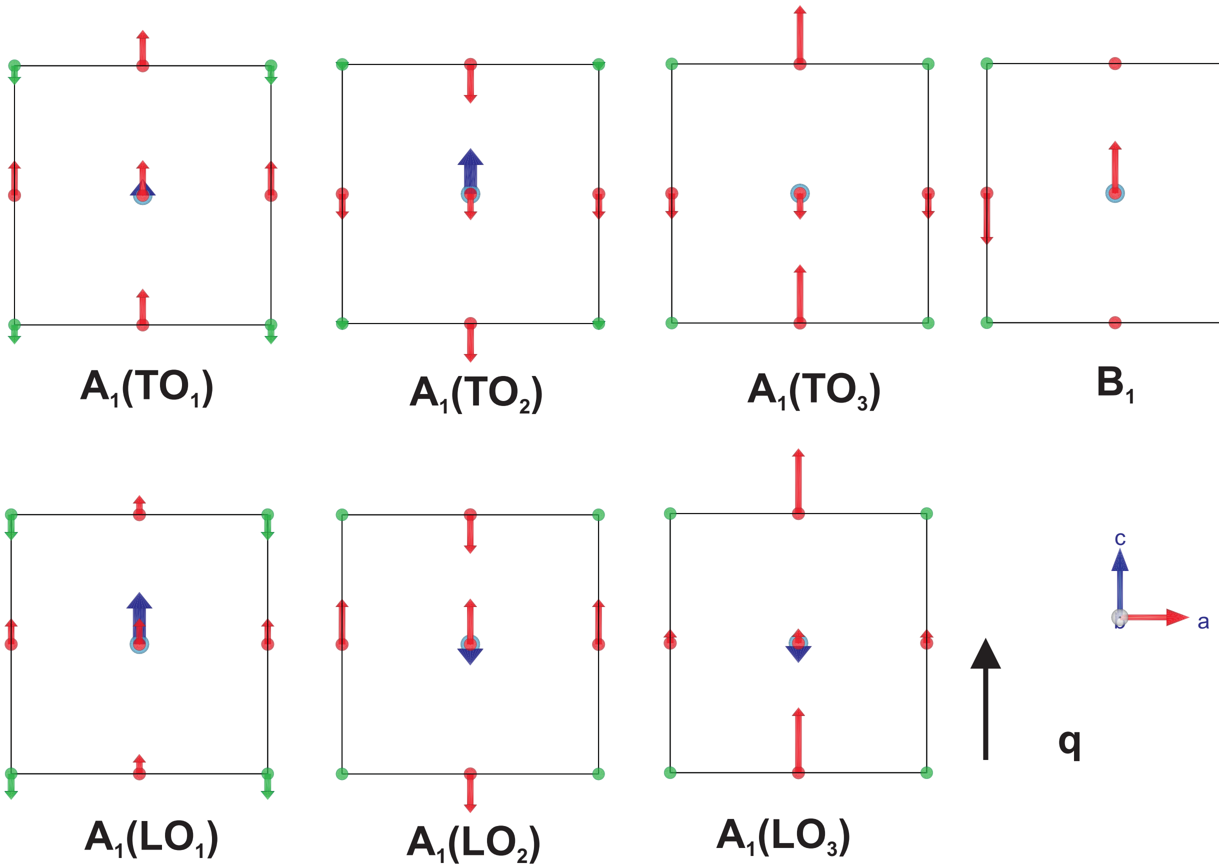

Figure 4.6: (Color online) Side view (i.e., from the **b** axis) of phonon displacements of A_1 and B_1 modes in unstrained $BaTiO_3$. The axes at the lower-right corner refer to the crystallographic axes. **q** approaches the zone center along the [001] direction for A_1(LO) modes.

where u_s^β is the displacement of atom s in the β direction. When normal modes alter with strain, the change in IR intensity may also be detected.

From the group-theory analysis, all modes except B_1 in $BaTiO_3$ of $P4mm$ symmetry are {IR+R} active while the B_1 mode is only Raman active. The change in IR intensity, $\Delta I_n(\eta) = I_n(\eta) - I_n(\eta = 0)$, is depicted in Fig.4.7 for different modes as a function of strain. Intensities of E(TO_1) and A_1(TO_2) decrease with strain while those of A_1(LO_3), A_1(LO_1), and E(TO_4) increase. The behaviors of the IR intensities in Fig.4.7 can be largely explained by the strain dependence of the effective charges (Fig.4.4a-b) and displacements (Table 4.3) according to Eq.(4.6). For A_1(TO_2) which vibrates along the c-axis, $|Z^*_{zz}|$ decreases for both Ti and O2 (Fig.4.4b), and displacements of these two atoms also decrease, leading to the declining IR intensity. For E(TO) modes, since Z_{xx}^* does not change much upon the strain (Fig.4.4a), the change in IR intensity is mainly due to the displacement change. For instance, for E(TO_4) mode, the increase of its IR intensity comes largely from the increase of the O3 displacement (Table 4.3).

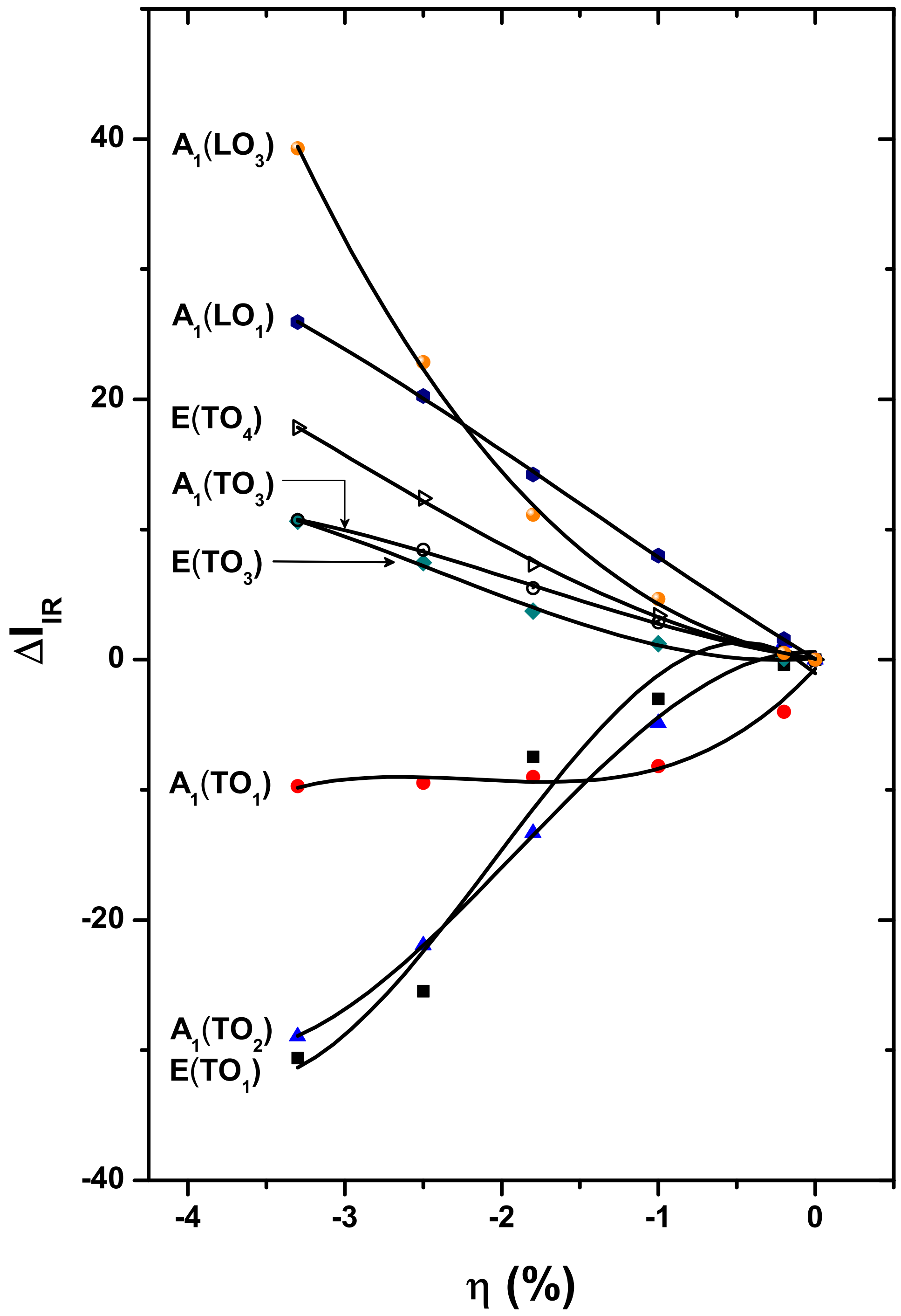

Figure 4.7: Changes in infrared intensity as a function of strain for those modes that display noticeable intensity variation.

Bibliography

[1] D. Tenne, A. Bruchhausen, N.D. Lanzillotti-Kimura, A. Fainstein, R.S. Katiyar, A. Cantarero, A. Soukiassian, V. Vaithyanathan, J.H. Haeni, W. Tian, D.G. Schlom, K.J. Choi, D.M. Kim, C.B. Eom, H.P. Sun, X.Q. Pan, Y.L. Li, L.Q. Chen, Q.X. Jia, S.M. Nakhmanson, K.M. Rabe, and X.X. Xi, Science **313**, 1614 (2006).

[2] D. A. Tenne, P. Turner, J. D. Schmidt, M. Biegalski, Y. L. Li, L. Q. Chen, A. Soukiassian, S. Trolier-McKinstry, D. G. Schlom, X. X. Xi, D. D. Fong, P. H. Fuoss, J. A. Eastman, G. B. Stephenson, C. Thompson, and S. K. Streiffer, Phys. Rev. Lett. **103**, 177601 (2009).

[3] D. A. Tenne, A. K. Farrar, C. M. Brooks, T. Heeg, J. Schubert, H. W. Jang, C. W. Bark, C. M. Folkman, C. B. Eom, and D. G. Schlom, Appl. Phys. Lett. **97**, 142901 (2010).

[4] P.Y. Yu and M. Cardona, *Fundamentals of Semiconductors Physics and Materials Properties* (Springer, Berlin, 2001).

[5] U. D. Venkateswaran, V. M. Naik, and R. Naik, Phys. Rev. B **58**, 14256 (1998), and references therein.

[6] R. Yu and H. Krakauer, Phys. Rev. Lett. **74**, 4067 (1995).

[7] D. J. Singh, Phys. Rev. B **53**, 176 (1996).

[8] Ph. Ghosez, E. Cockayne, U. V. Waghmare, and K. M. Rabe, Phys. Rev. B **60**, 836 (1999).

[9] C. Bungaro and K.M. Rabe, Phys. Rev. B **65**, 224106 (2004).

[10] I.I. Naumov and H. Fu, Phys. Rev. B **72**, 012304 (2005).

[11] X. Wang and D. Vanderbilt, Phys. Rev. B **74**, 054304 (2006).

[12] A. Garcia and D. Vanderbilt, Phys. Rev. B **54**, 3817 (1996).

[13] M. Born and K. Huang, *Dynamical Theory of Crystal lattices* (Oxford University Press, Oxford, 1954).

[14] R.A. Cowley, Adv. Phys. **29**, 1 (1980).

[15] M.E. Lines and A.M. Glass, *Principles and Applications of Ferroelectrics and Related Materials* (Clarendon, Oxford, 1979).

[16] M. Dawber, K.M. Rabe, and J.F. Scott, Rev. Mod. Phys. **77**, 1083 (2005).

[17] C.H. Ahn, K.M. Rabe, and J.M. Triscone, Science **303**, 488 (2004).

[18] A.S. Mischenko, Q. Zhang, J.F. Scott, R.W. Whatmore, and N.D. Mathur, Science **311**, 1270 (3006); J.F. Scott, Annu. Rev. Mater. Res. **41**, 229 (2011).

[19] K. Uchino, *Piezoelectric Actuators and Ultrasonic Motors* (Kluwer Academic, Boston, 1996).

[20] S.-E. Park and T.R. Shrout, J. Appl. Phys. **82**, 1804 (1997).

[21] A. Garcia and D. Vanderbilt, Appl. Phys. Lett. **72**, 2981 (1998).

[22] H. Fu and R.E. Cohen, Nature **403**, 281 (2000).

[23] X. Fu, I.I. Naumov, and H. Fu, Nano. Lett. **13**, 491 (2013).

[24] J.F. Scott, *Ferroelectric Memories* (Springer, Berlin, 2000).

[25] R.E. Cohen, Nature (London) **358**, 136 (1992).

[26] R.E. Cohen and H. Krakauer, Phys. Rev. B **42**, 6416 (1990).

[27] R.D. King-Smith and D. Vanderbilt, Phys. Rev. B **47**, 1651 (1993).

[28] R. Resta, Rev. Mod. Phys. **66**, 899 (1994).

[29] L.D. Landau and E.M. Lifshitz, *Statistical Physics* (Pergamon, New York, 1980), Part 1.

[30] I.I. Naumov, L. Bellaiche, and H. Fu, Nature (London) **432**, 737 (2004); I. Naumov and H. Fu, Phys. Rev. Lett. **98**, 077603 (2007).

[31] A.S. Barker Jr., Phys. Rev. **136**, A1290 (1964).

[32] W. Zhong, R. D. King-smith, and D. Vanderbilt, Phys. Rev. Lett. **72**, 3618 (1994).

[33] Ph. Ghosez, J.-P. Michenaud, and X. Gonze Phys. Rev. B **58**, 6224 (1998).

[34] P. Hohenberg and W. Kohn, Phys. Rev. **136**, B864 (1964); W. Kohn and L.J. Sham, Phys. Rev. **140**, A1133 (1965).

[35] P. Giannozzi *et al.*, J. Phys. C **21**, 395502 (2009).

[36] P. Giannozzi *et al.*, http://www.quantum-espresso.org.

[37] N. Troullier and J. L. Martins, Phys. Rev. B **43**, 1993 (1991).

[38] H. Fu and O. Gulseren, Phys. Rev. B **66**, 214114 (2002); A. Raeliarijaona and H. Fu, J. Appl. Phys. **115**, 054105 (2014).

[39] R. Whal, D. Vogtenhuber, and G. Kresse, Phys. Rev. B **78**, 104116 (2008).

[40] S. Baroni, S. de Gironcoli, A. Dal Corso, and P. Giannozzi, Rev. Mod. Phys. **73**, 515 (2001).

[41] S. Baroni, P. Giannozzi, and A. Testa, Phys. Rev. Lett. **58**, 1861 (1987).

[42] X. Gonze, Phys. Rev. A **52**, 1096 (1995).

[43] X. Gonze and C. Lee, Phys. Rev. B **55**, 10355 (1997).

[44] P. Hermet, M. Veithen, and Ph. Ghosez, J. Phys. C **21**, 215901 (2009).

[45] R. A. Evarestov and A. V. Bandura, Journal of Computational Chemistry **33**, 1123 (2012).

[46] N. Choudhury, E.J. Walter, A.I. Kolesnikov, and C.-K. Loong, Phys. Rev. B **77**, 134111 (2008).

[47] M. Maldovan, Nature (London) **503**, 209 (2013).

[48] J.M. Perez-Mato, M. Aroyo, A. Garcia, P. Blaha, K. Schwarz, J. Schweifer, and K. Parlinski, Phys. Rev. B **70**, 214111 (2004).

[49] D. Porezag and M.R. Pederson, Phys. Rev. B **54**, 7830 (1996).

5 Unsuppressed polarization and new polarization switching mechanism in ferroelectrics with vacancies

5.1 Introduction

Vacancies in ferroelectrics (FE), one key class of defects, are of considerable importance both fundamentally and technologically.[16, 2, 3] Fundamentally, vacancies disrupt the interaction among atoms on the microscopic scale, and break the delicate balance[4, 5] between long-range and short-range interactions in FEs, which profoundly affects the polarization and electrical properties.[16, 2] Technologically, vacancies in FEs have been linked to fatigues;[3, 6, 8, 7] they also lead to the pinning of polarization near domain wall,[6] the reduction of polarization magnitude, and the increase of coercive field. [10, 11] Consequently, vacancies hamper the vital applications of FEs in ferroelectric memories and piezoelectric devices. [12, 13, 14] On the other hand, vacancies can be beneficial. In fact, vacancies are pivotal in polarization switching by acting as the nucleation centers of antiphase domains, [2, 15, 16] in the Kolomogorov-Avrami model [17, 18] of polarization reversal or its variants [19, 20]. Vacancies were also demonstrated to induce large electromechanical response in aged $BaTiO_3$ crystals,[21] and the V_{Pb}-V_O di-vacancy complex was shown to enhance local polarization in $PbTiO_3$. [22] In ferroelectric tunnel junctions, the control of polarization switching in terms of nucleation and domain growth is instrumental in the realization of FE memristors. [23, 24] Furthermore, it was shown that even under the optimal chemical potentials of electron and atomic reservoirs, vacancies can still appear and they are hard to avoid.[26]

There are reasons that vacancies are detrimental to the polarization in FEs. It is known that

Ti $3d$ and O $2p$ hybridization is important for ferroelectric instability.[4, 5, 26] The Ti-O chain is widely believed to be critical in the formation of ferroelectricity.[7, 27] Creation of Ti or O vacancy disrupts the Ti-O chain, thereby significantly affecting the polarization properties. Furthermore, since polarization switching depends on the local structure and local interaction near the defect, existence of vacancy drastically alters the chemical bonding in the neighborhood of the vacancy site and is thus expected to impact the polarization switching.

However, the above belief and anticipation regarding the impact of vacancy and broken Ti-O chain on polarization have not been firmly confirmed since there are long-standing fundamental problems that prevent us from obtaining microscopic understanding on how vacancies *quantitatively* change the polarization and polarization properties. First, the stable state of a vacancy is often charged,[29, 28] and indeed, the most stable O vacancy[26] in $PbTiO_3$ is the positively charged V_O^{2+}. Here we use the notation V_X^q to denote a vacancy of species X carrying an amount of charge q. For a *charged* vacancy in a periodic solid, it is a fundamental question whether polarization is well-defined and physically meaningful. Second, when vacancy is present, there is a possibility that the system could be metallic, in which conducting electrons will screen the polarization, if any. It thus remains unclear whether it is possible to quantitatively determine the magnitude of polarization when vacancy occurs in FEs. As a consequence of these problems, a quantitative and accurate understanding of the influence of vacancies on ferroelectric polarization, which goes beyond the qualitative argument based on the Ti-O chain, is lacking. This hampers the important effort toward the design of FEs by controlling vacancies.

Another subject of equal importance is the mechanism of polarization switching. In various models [17, 18, 19, 20] that describe the polarization switching in FEs, the consensus is that switching is initiated by nucleation of antiphase domain. However, little is understood on how the antiphase domain forms in the first place. In other words, how the polarization is reversed near the defects to form an antiphase domain at the key stage of nucleation is microscopically unknown. In studies of ideal *bulk* FEs without defects, polarization reversal is realized by shifting the atoms from one of the degenerate potential wells, say the state with $\mathbf{P} > 0$, going through the centrosymmetric configuration, and ending at the enantiomorphic state with $\mathbf{P} < 0$.[30, 31] This, to our knowledge, is the only approach employed by first-principles calculations in studying the energetics of polarization switching. Since nucleation often occurs near vacancies, we therefore need to account for the presence of vacancies in polarization switching. Specifically we must consider how polarization is switched in the nearby of the vacancies, which is in fact the nucleation process. Nevertheless, with charged vacancies, it is unclear whether polarization is well defined, and it is even less clear by what mechanism the polarization is switched.

The purpose of this paper is threefold: (i) to show that polarization can be meaningfully defined even when charged vacancies exist, and furthermore, can be accurately calculated provided that a correct procedure is undertaken. (ii) To reveal that, unlike the commonly accepted belief, the break of the Ti-O chain surprisingly does not significantly reduce the magnitude of polarization. In fact, we find that, regardless of the vacancy species (V_{Ba}, V_{Ti}, or V_O), the polarization is interestingly similar. (iii) To demonstrate that the polarization reversal mechanism in FEs with vacancy differs from that in ideal bulk, in that the system need not undergo the centrosymmetric configuration in order to switch its polarization. Concurrently, these studies suggest that there are interesting physics to be learnt on FEs with vacancies.

5.2 Methodology

We perform first-principles calculations using the density functional theory (DFT) within the spin-polarized local density approximation (LDA) [16] to investigate the vacancy properties of tetragonal $BaTiO_3$, a phase stable near room temperature. Spin-polarized calculations are needed since charged vacancies may introduce magnetism.[33] Norm-conserving pseudopotentials [34] are used to describe the interaction between core and valence electrons. Ti $3s$ and $3p$ semi-core orbitals are treated as valence states; qualities of our pseudopotentials were very good by comparing with the full-potential LAPW calculations.[35, 36]. The energy cutoff for plane-wave expansion of wavefunctions is 90 Ry, which is checked to be sufficient. All calculations are performed using the Quantum-espresso package. [18] The calculated lattice constant a=3.93Å and tetragonality c/a=1.007 for bulk $BaTiO_3$ are in good agreement with other calculations in the literature (for example, a =3.945Å and c/a=1.009 in Ref.[38]). Polarization is calculated using the modern theory of polarization via the Berry phase approach.[39, 40] To reduce the interaction between vacancies, we use 3×3×3 supercells of 135 atoms with a vacancy located at the cell center.

5.3 Results and Discussions

5.3.1 Vacancy charge state and the insulating nature

We first calculate the vacancy formation energy ΔH using the chemical-potential approach[29, 28], namely

$$\Delta H = E[\mathrm{V}_X^q] + (E_\mathrm{X} + \mu_\mathrm{X}) + q(\varepsilon_{\mathrm{V}BM} + \Delta\bar{V} + \mu_e) - E_0(\mathrm{B}TO)\,, \tag{5.1}$$

where $E[\mathrm{V}_X^q]$ is the total energy of $\mathrm{BaTiO_3}$ with vacancy V_X^q, E_X the total energy of the elemental solid of species X (for oxygen, E_X is the energy per atom in an O_2 molecule), μ_X the chemical potential of the atomic reservoir of species X, $\varepsilon_{\mathrm{V}BM}$ the Kohn-Sham orbital energy of the valence band maximum (VBM) of the perfect $\mathrm{BaTiO_3}$ crystal, $\Delta\bar{V}$ the difference in the average potential between a perfect crystal and a crystal with vacancy, μ_e the chemical potential of the electron reservoir, and $E_0(\mathrm{B}TO)$ the total energy of perfect $\mathrm{BaTiO_3}$. The rationale for each term in Eq.(5.1) was given in Ref.[26].

The chemical potentials (μ_X) of atomic reservoirs are constrained by using the thermodynamical conditions and the requirement of no appearance of secondary unwanted phases. The details were previously described in Ref.[41]. From the thermodynamical constraints, μ_O needs to satisfy $-5.7 \le \mu_O \le 0$ eV.[42] The maximally allowed $\mu_O = 0$ eV corresponds to the O-rich condition, and the minimally allowed $\mu_O = -5.7$ eV corresponds to the O-poor condition. For a given μ_O, μ_{Ba} and μ_{Ti} can vary within the ranges $-7.39 \le \mu_{Ba}+\mu_O \le -5.70$ eV and $-12.13 \le \mu_{Ti}+2\mu_O \le -10.44$ eV. We choose the middle point of each allowed range, namely $\mu_{Ba}+\mu_O = -6.545$ eV and $\mu_{Ti}+2\mu_O = -11.285$ eV, to determine μ_{Ba} and μ_{Ti}.

For a given vacancy species X, we compute ΔH for different charge states q. More specifically, we consider the charge states q=0, 1−, 2− for V_{Ba}^q, q=0, 1−, 2−, 3−, 4− for V_{Ti}^q, and q=0, 1+, 2+ for V_O^q. The formation energies and relative stabilities of different charge states for each vacancy species are determined according to Eq.(5.1),[43] from which we identify the optimal charge state that has the lowest formation energy under a given chemical potential μ_e of the electron reservoir. The optimal charge states are given in Fig.5.1(a) for the oxygen-rich condition (μ_O=0 eV). Note in Fig.5.1(a) that, for a given vacancy species, only the optimal charge state with the lowest formation energy is presented. Other charge states with higher formation energies (and thus being less stable) are not shown for clarity. Since in experiments the chemical potential μ_O of the oxygen reservoir is often used to control the growth of perovskite FEs, we simulate this situation by also determining the vacancy formation energy under different chemical potentials of $\mu_{\rm O}$, shown in Fig.5.1(b) and (c). μ_O=-4 eV in Fig.5.1(c) is close to the oxygen-poor condition.

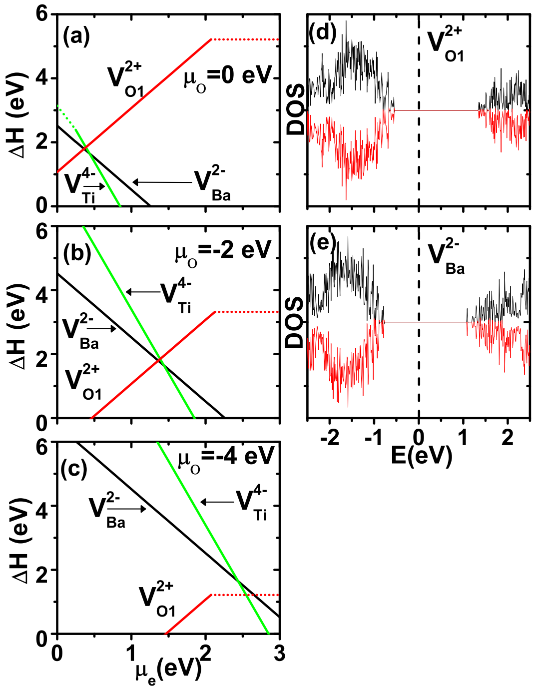

Figure 5.1: (Color online) (a)-(c): Vacancy formation energy ΔH of the optimal charge state as a function of the chemical potential μ_e of the electron reservoir, under different chemical potential $\mu_{\rm O}$ of the atomic reservoir of oxygen: (a) $\mu_{\rm O}$=0 eV, (b) $\mu_{\rm O}$=-2 eV, and (c) $\mu_{\rm O}$=-4 eV. (d) and (e): Spin-polarized density of states (DOS) of $BaTiO_3$ with vacancy V_{O1}^{2+} and V_{Ba}^{2-}, respectively. The minority DOS component is plotted as negative values. The spin majority and minority DOS are identical, with no ferromagnetism, for V_{O1}^{2+} and V_{Ba}^{2-} vacancies. The vertical dashed line in (d) and (e) marks the Fermi energy.

In $BaTiO_3$ of the P4mm symmetry, there are two inequivalent O atoms, one directly beneath the Ti atom along the c-axis (labeled as apical O1), the other on the base plane of TiO_2 (labeled as O2). We have computed the vacancy formation and polarization for both types of O vacancies, and we found that they are very similar due to the small c/a ratio in $BaTiO_3$. We will thus present only the results of V_{O1} for apical O1.

Calculation results in Fig.5.1(a)-(c) show that the most stable charge state is largely V_{Ba}^{2-} for Ba vacancy, V_{Ti}^{4-} for Ti vacancy, and V_{O1}^{2+} for O vacancy when μ_e is below 2 eV, regardless of whether the system is under the oxygen-rich condition (μ_O=0eV, Fig.5.1a), or oxygen-poor condition (μ_O=-4eV, Fig.5.1c), or in between (μ_O=-2eV, Fig.5.1b). In other words, charged vacancies are energetically favorable in $BaTiO_3$. The three charged vacancies (V_{Ba}^{2-}, V_{Ti}^{4-}, and V_{O1}^{2+}) are the most encountered ones under different oxygen chemical potentials.

We next determine whether the vacancy of the most stable charge state is metallic or insulator. This question seems trivial, but is of important relevance since defects often introduce partially occupied states inside the band gap and make the system metallic, in which the conducting electrons will lead to the screening of ferroelectricity. The metallic nature occurs so often that many believe that vacancies in FEs always make the system metallic and thus inhibit ferroelectricity. However, it is a misconception. Although metallic behavior may occur for some charge states [2, 45], it by no means occurs for all charged vacancies. We calculate the density of states (DOS) for the optimal charge states (V_{Ba}^{2-}, V_{Ti}^{4-}, V_{O1}^{2+}), and the DOS is depicted in Fig.5.1(d) for V_{O1}^{2+} and in Fig.5.1(e) for V_{Ba}^{2-}.

Fig.5.1(d) and (e) reveal that $BaTiO_3$ with vacancy of optimal charge state is an insulator since there are no partially occupied states inside the band gap, thereby there are no conducting electrons to screen the ferroelectricity if ferroelectricity does exist. The insulating nature is not surprising, because no free charge is available for the above three optimal charged vacancies, resembling the perfect crystal.[46] Take V_O^{2+} as an example. In a prefect $BaTiO_3$, due to charge transfer from cations, there are two additional electrons surrounding an O atom. When one oxygen atom is removed from the perfect crystal to create a vacancy, this O atom prefers to take the two additional electrons with it owing to the strong electron negativity of oxygen atom. As a result, no free electrons are left in the solid, and $BaTiO_3$ with V_O^{2+} is thus an insulator.

For isolated or closed systems, the initial state is charge neutral, and the Fermi level is determined by the charge-neutrality condition. However, in the polarization measurements, ferroelectric material is connected to electrodes and is an open system. In an open system, the FE solid with vacancy may not be charge neutral. Take $BaTiO_3$ with oxygen vacancy V_O as an example. Let us temporarily assume that the vacancy is initially charge neutral, i.e., V_O^0 with $q = 0$, rather than the most stable charge state V_O^{2+} with $q = 2+$. Note that $BaTiO_3$ with neutral V_O^0 is metallic, and possesses two unbounded (conducting) electrons per supercell as compared to $BaTiO_3$ with V_O^{2+}. When $BaTiO_3$ with V_O^0 is connected to electrodes during the polarization measurement, the two unbounded electrons will flow out of the solid, leaving the vacancy to be charged as V_O^{2+}. With the charged V_O^{2+}, $BaTiO_3$ becomes an insulator that could host polarization, and no more current will flow in the FE solid.

5.3.2 Polarization in FEs with charged vacancy

For charge *neutral* systems, it is known that polarization can be computed by the modern theory of polarization.[39, 40] However, the stable vacancies V_{Ba}^{2-}, V_{Ti}^{4-}, V_O^{2+} are all charged. A fundamental problem arises when dealing with the polarization in a charged system, that is, the polarization itself is not translation invariant and not physically meaningful. In the following, we show that even in charged systems, change in polarization can still be rigorously determined. First we point out that, although the absolute polarization is not definite in charged systems, the polarization *change* is nevertheless well defined, which coincides with the key requirement in the modern theory of polarization. For electrons in solids, it is well known that their wave functions are extended and cannot be treated as point charges.[47] Here, we begin by using the centers of

Wannier functions[48] (WanF), and write the polarization in a solid as

$$\mathbf{P} = \frac{1}{\Omega}\sum_i q_i \mathbf{r}_i\,, \tag{5.2}$$

where $\mathbf{r}_i$ is the location of either an ion (in which q_i is the point charge of the ion) or the center of a Wannier function (in which q_i is the charge of the Wannier function), and Ω the volume of one cell. If the solid is translated by a constant vector $\mathbf{t}$ as $\mathbf{r}'_i = \mathbf{r}_i + \mathbf{t}$, the polarization will then become $\mathbf{P}' = \mathbf{P} + \frac{1}{\Omega}\sum_i q_i \mathbf{t}$. For charged systems, the second term in $\mathbf{P}'$ does not vanish, and the magnitude of polarization is thus not translation invariant.

However, even for charged systems, the change in polarization is unique. To see this, let the ion or the WanF center change from initial position $\mathbf{r}^s_i$ to final position $\mathbf{r}^f_i$ by a displacement $\mathbf{d}_i$ (which is ion dependent, but does *not* depend on the choice of the vector $\mathbf{t}$) as $\mathbf{r}^f_i = \mathbf{r}^s_i + \mathbf{d}_i$. Then, although both the initial polarization $\mathbf{P}^s$ and the final polarization $\mathbf{P}^f$ are not translation invariant as $\mathbf{P}'^s = \mathbf{P}^s + \frac{1}{\Omega}\sum_i q_i \mathbf{t}$ and $\mathbf{P}'^f = \mathbf{P}^f + \frac{1}{\Omega}\sum_i q_i \mathbf{t}$, the change in polarization $\mathbf{P}'^f - \mathbf{P}'^s = \mathbf{P}^f - \mathbf{P}^s = \frac{1}{\Omega}\sum_i q_i \mathbf{d}_i$ nevertheless does not depend on $\mathbf{t}$ and is physically meaningful.

The uniquely defined polarization change for charged defects in extended solids, along with the insulator nature demonstrated in previous section, establishes firmly that ferroelectricity exists for BaTiO$_3$ with V^{2-}_{Ba}, V^{4-}_{Ti}, or V^{2+}_{O1} vacancy. We next determine the magnitude of polarization associated with these charged vacancies, following the modern theory of polarization.[39, 40] More specifically, DFT calculations are performed to determine the atomic locations (denoted as $\{\mathbf{r}^f_i\}$) when a charged vacancy is present. Then, change in polarization is calculated with respect to the centrosymmetric configuration (denoted as $\{\mathbf{r}^s_i\}$), using multiple steps connecting the starting and final configurations as $\mathbf{r}_i = \mathbf{r}^s_i + \lambda(\mathbf{r}^f_i - \mathbf{r}^s_i)$ with $0 \le \lambda \le 1$. Berry phase calculations are performed at each step. The results of calculations are shown in Fig.5.2, in which the polarization value at $\lambda = 1$ is what we will focus on. Furthermore, the change in polarization does not depend on the structural relaxation algorithm (see Appendix).

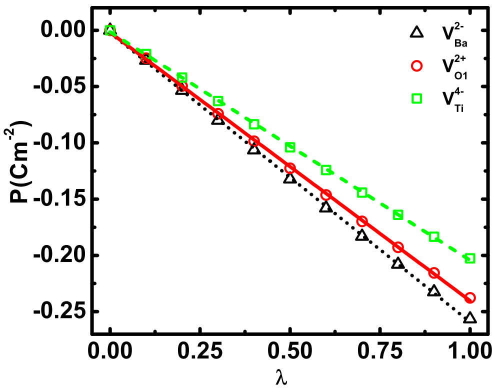

Figure 5.2: (Color online) Polarization as a function of atomic shifts from the centrosymmetric configuration ($\lambda = 0$) to the DFT-relaxed configuration ($\lambda = 1$) in BaTiO$_3$ with V^{2-}_{Ba}, V^{4-}_{Ti}, or V^{2+}_{O1} vacancy. For perfect bulk BaTiO$_3$, the first-principles calculated polarization is -0.21 C·m^{-2}.

Two key outcomes are revealed by Fig.5.2. First, the polarization turns out to be interestingly similar for three vacancies. More specifically, the magnitude of polarization at λ=1 is 0.24, 0.20, and 0.26 C·m^{-2} for V^{2+}_{O1}, V^{4-}_{Ti}, and V^{2-}_{Ba}, respectively. Note that different vacancies have drastically different environments, for instance, a Ti atom interacts with six oxygen atoms and contributes strongly toward forming the ferroelectricity, whereas a Ba atom plays a much less role in developing the ferroelectricity and is largely a spectator.[4, 5] The close polarizations in Fig.5.2 show that taking a pivotal Ti atom away from the solid generates nearly the same effect on polarization as taking a less-significant Ba atom away, which is indeed rather striking. Second, the polarization in BaTiO$_3$ with vacancy is comparable to the value of a perfect bulk (which is P=0.21 C·m^{-2} from our calculation and P=0.18 C·m^{-2} from Ref.[49]). Contrary to the common belief that breaking the Ti-O chain shall drastically change the ferroelectric polarization, the current first-principles calculations reveal that individual vacancies do not substantially alter the polarization.

In fact, the polarization of V_{Ba}^{2-} is even slightly larger than that in perfect bulk $BaTiO_3$. The enhancement of polarization was also shown[22] to be possible in $PbTiO_3$ by di-vacancy, namely the defect complex containing the coexistence of V_{Pb} and V_O.

The unsuppressed polarization, despite the appearance of vacancy, may be explained by the fact that the off-center displacements are mainly caused by long-range Coulomb interaction. The existence of vacancy does not dramatically change this long-range Coulomb interaction, although it significantly alters the local environment.

5.3.3 Polarization switching in FEs with vacancy

We start this section by describing a correct pathway for polarization switching in FEs when vacancy is present. Fig.5.3(a) illustrates schematically the initial polar configuration, where only B-site atoms (B_1 and B_2) and vacancy V_X^q are shown for the sake of clarity. Atoms B_1 and B_2 in Fig.5.3(a) are not symmetric from the vacancy V_X^q due to the occurrence of ferroelectricity, and the centrosymmetric position of each B_i atom in the bulk unit cell of this atom is indicated by the dash line. Note that B_1 and B_2 are not both above (or both below) the centrosymmetric positions because of the atomic relaxation caused by the Coulomb interaction of the charged vacancy. In perfect perovskites without vacancy, B-site atoms need to pass the centrosymmetry positions in order to reverse the polarization, which is termed as the centrosymmetric switching pathway.

When vacancy is present, a correct polarization-switching pathway is described in Fig.5.3(b), in which B_1 does not cross the centrosymmetric position, but instead moves toward the mirror-reflected position of B_2, with the mirror plane located at the vacancy site and perpendicular to the polarization direction. Similarly B_2 moves toward the mirror-reflected position of B_1. Since each atom moves toward the mirror-reflected position of its corresponding atom, the polarization

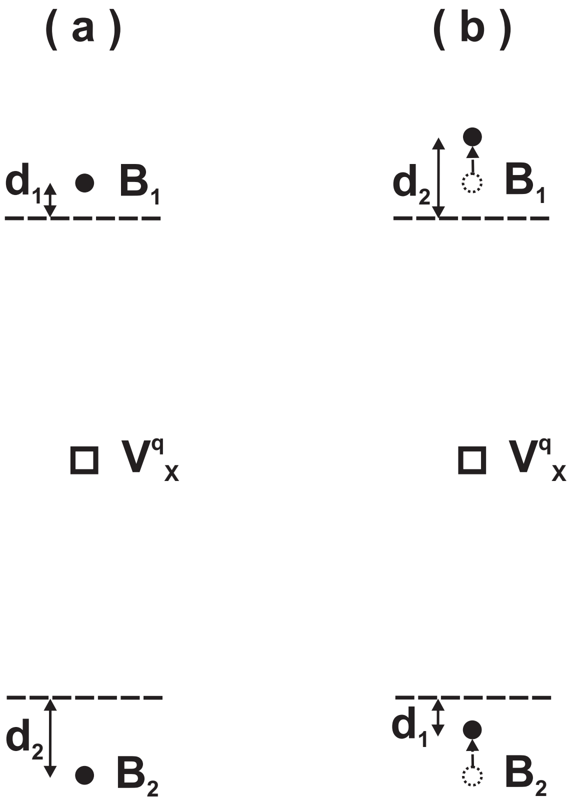

Figure 5.3: Schematic illustration of the polarization-switching pathway in the presence of vacancy: (a) the initial configuration with an asymmetric structure, where B_1 and B_2 are B-site atoms, the dash lines indicate the centrosymmetric planes of the bulk 5-atoms cell for these two atoms, and V_x^q is the vacancy; (b) Polarization switching in which atoms do not cross the centrosymmetric positions, where empty circles indicate initial positions and solid circles the final positions.

switching is guaranteed.

Caution should be taken to investigate the polarization switching when defects are present in FEs. To demonstrate this, we switch the polarization in $BaTiO_3$ with V_{O1}^{2+} vacancy using the pathway in Fig.5.3(b) according to $\mathbf{r}_i = \mathbf{r}_i^s + \eta(\mathbf{r}_i^f - \mathbf{r}_i^s)$, where $\mathbf{r}_i^s$ ($\mathbf{r}_i^f$) are the atomic positions of the initial (final) configuration. η is the parameter specifying a configuration during the switching. The solid symbols in Fig.5.4(a) depict the polarizations directly obtained from the Berry-phase calculations during the polarization switching. We see that the calculated polarization data fluctuate wildly between positive and negative values, which makes it hard to determine whether or not the polarization is switched. We find that this radically fluctuating polarization is not an artifact, and in fact it originates from the polarization quantum. Calculations of electric polarization in systems with vacancies are often carried out using supercells, which makes the polarization quantum very small. The polarization quantum is defined[39, 40] as $\mathbf{P}_{quan} = \frac{2e\mathbf{R}}{\Omega}$, where $\mathbf{R}$ is the lattice vector along the polarization direction, and e the electron charge. An increase in the cell volume by using supercell leads to a drastic reduction of $\mathbf{P}_{quan}$. Therefore, during the switching, the polarization changes branch several times, and the polarization switching becomes difficult to track. Shifting the polarization by an integer number of polarization quanta yields a polarization that is continuously changing as shown by the empty circles in Fig.5.4(a), showing that the polarization indeed is switched from -0.24 C·m^{-2} at η=0 to +0.24 C·m^{-2} at η=1.

The energy barrier, calculated by DFT and shown in Fig.5.4(b) for V_{O1}^{2+}, reveals key information on polarization switching when vacancy is present. For the switching pathway in Fig.5.3(b), the energy barrier is 0.224 eV for one supercell with 27 bulk cells. The ferroelectricity considered here is a single domain, and the ferroelectric state is polarized over the entire supercell. The polarization-switching barrier is the energy to switch the polarization of the whole supercell. To compare with the polarization switching in bulk, we convert the energy barrier of one supercell into one bulk cell, and the barrier is 8.3 meV per bulk cell, which is small. The reversed polarization in Fig.5.4(a) and the small energy barrier in Fig.5.4(b) thus demonstrate that, even in the presence of vacancy, the electric polarization can be switched in $\mathrm{BaTiO_3}$.

It is worth to estimate the magnitude of correction due to the use of finite-size supercell in our calculations.[50, 51] Using the formula of finite-supercell image-charge correction[50] and the dielectric constant of tetragonal $\mathrm{BaTiO_3}$, we calculate that the finite-supercell correction on the formation energy of V_{O1}^{2+} is on the order of 1.6 meV. This correction is much smaller than the switching barrier of 224 meV for V_{O1}^{2+}. The small finite supercell correction in $\mathrm{BaTiO_3}$ is due to its

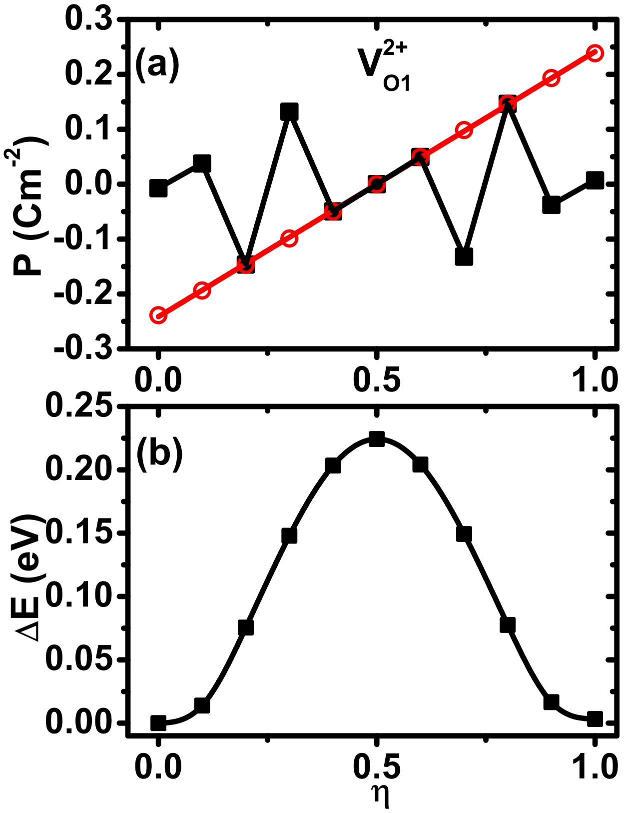

Figure 5.4: (Color online) (a) Polarization as a function of parameter η during the switching for BaTiO$_3$ with V_{O1}^{2+} vacancy. Square symbols and black lines are the raw data directly obtained from the Berry phase calculations. Empty circles and red line are the results after shifting the polarization across different branches using $\mathbf{P}_{quan}$, showing a continuous change of $\mathbf{P}$ with respect to η. (b) Change in energy $\Delta E(\eta) = E(\eta) - E(\eta = 0)$ as a function of η during polarization switching for BaTiO$_3$ with V_{O1}^{2+} vacancy, using the proposed switching pathway in Fig.5.3(b).

large static dielectric constant. Therefore the finite-size correction does not significantly alter our conclusions. Furthermore, since the correction is similar for different intermediate configurations during the polarization switching, the error will be largely offset.

We further calculate and compare the switching barriers for different vacancies, using the non-centrosymmetric pathway. The results are shown in Fig.5.5. Interestingly, despite that V_{Ba}^{2-}, V_{Ti}^{4-} and V_{O1}^{2+} have very different local environments, Fig.5.5 reveals that the polarization-switching barriers are similar. The barriers are found to be 0.252, 0.132, 0.224 eV per supercell—or equivalently, 9.3, 4.9, 8.3 meV per bulk cell—for V_{Ba}^{2-}, V_{Ti}^{4-} and V_{O1}^{2+}, respectively. Calculation results in Fig.5.5 thus tell that polarization can be reversed in the presence of all three types of vacancies (V_{Ba}^{2-}, V_{Ti}^{4-}, and V_{O1}^{2+}) that maintain ferroelectricity in the system. We also compute the switching barrier for perfect bulk $BaTiO_3$, which is found to be 4.5 meV per bulk cell. The switching barriers in the presence of vacancies are therefore comparable to that in a perfect bulk.

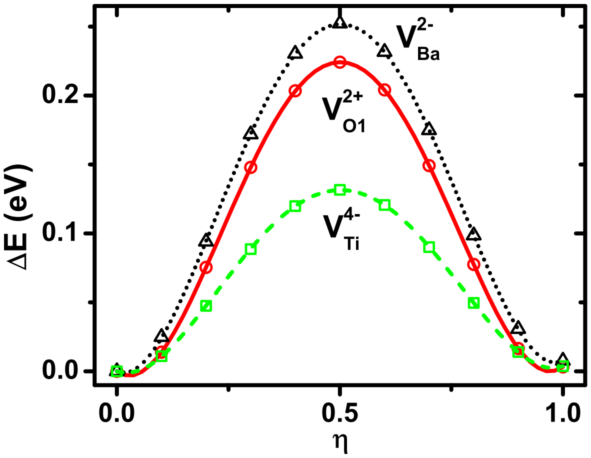

Figure 5.5: (Color online) Polarization-switching energy barriers for V_{Ba}^{2-} (dotted curve), V_{O1}^{2+} (solid curve), and V_{Ti}^{4-} (dashed curve). All switchings are performed using the non-centrosymmetric pathway.

The theoretical results are consistent with, and are able to explain, experimental observations. In experiments, it was shown that oxygen-deficient $Ba_4Nd_2Fe_2Nb_8O_{30}$ (Ref.[52]) and $Bi_{3.25}La_{0.75}Ti_3O_{12}$ (Ref.[53]) both have significant ferroelectric remnant polarizations, despite the existence of oxygen vacancies. This is in agreement with our result that there is ferroelectricity for vacancies of optimal charge states (Fig.5.2). Furthermore, in different ferroelectric materials with oxygen vacancies (such as $Ba_4Nd_2Fe_2Nb_8O_{30}$ in Ref.[52], $Bi_{3.25}La_{0.75}Ti_3O_{12}$ in Ref.[53], and $BaTiO_3$ in Ref.[54]), polarization switching was clearly demonstrated by the hysteresis loops.[52, 53, 54] These experiments provide strong support to the theoretical result that polarization in FEs with vacancies is switchable.

Although we consider only the $BaTiO_3$ compound, we nevertheless investigate different vacancies (V_{Ba}, V_{Ti}, and V_O). Our conclusions—namely polarizations are unsuppressed by the vacancies, and the polarizations are switchable with low switching barriers—apply to all vacancies and are thus rather general. Furthermore, in different ferroelectric compounds such as $BaTiO_3$ and $PbTiO_3$, the Ti-O bonds are similar, and it is thus reasonable that the conclusions may also apply to other FE compounds.

The finding that the switching barriers are comparable for different vacancies is interesting and meanwhile puzzling. It also suggests that the local environments of different vacancies play only a minor role in influencing the polarization switching. We now provide a microscopic origin responsible for the above intriguing result. For this purpose, we calculate the mechanical work that is needed to move atoms during the switching. More specifically, we calculate adiabatically the work $W = -\sum_i \int \mathbf{F}_i \cdot d\mathbf{r}_i$ between the initial configuration $\eta = 0$ and the configuration of $\eta = 0.2$ for each considered vacancy, where $\mathbf{F}_i$ is the force on atom i. To demonstrate the contribution of the local environment, we separate the summation over atoms into two groups: those atoms within a chosen cutoff radius (r_{cut}) from the vacancy (termed as group I), and those outside the cutoff radius (termed as group II). We choose r_{cut} so that atoms of the nearest species are included in group I. The contribution of group I thus reveals the influence of local environment on switching.

Fig.5.6 depicts the mechanical works to move atoms in groups I and II. We see that, for each vacancy, the work W_I used for moving atoms in group I is small. In fact, nearly 90% of the mechanical work of switching comes from moving atoms in group II (not group I), which demonstrates that the local environment near vacancy indeed is insignificant in the polarization switching.

Our calculation result has another important implication for polarization imprinting. In experiments, it is known that polarization often becomes hard to switch after a great number of

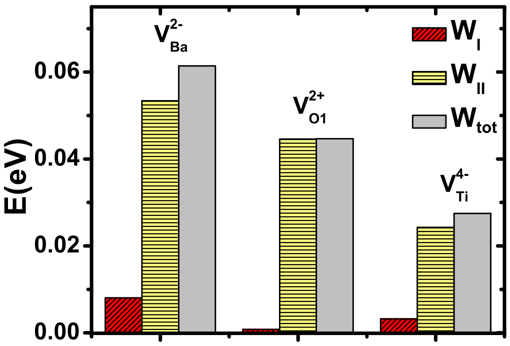

Figure 5.6: (Color online) Mechanical works done to move atoms in group I (W_I) and in group II (W_{II}), and total work (W_{tot}), during the polarization switching process between the initial configuration (η=0) and the configuration of η =0.2, for different vacancies. For V^{2+}_{O1}, the contribution W_I is too small to be seen in the graph.

cycles, a phenomenon called imprinting. Since individual vacancy does not considerably change the switching barrier as shown in this study, the imprinting must have originated from the *extended* defects (for instance, defect lines and defect clusters) that develop after individual defects migrate to form an aggregate.

5.4 Conclusion

It was shown that (i) in FEs with charged defects, change in polarization can be meaningfully defined, and (ii) the system is insulating for $BaTiO_3$ with V^{2-}_{Ba}, V^{4-}_{Ti}, or V^{2+}_{O1} vacancy. By these conclusions, we established rigorously that ferroelectricity persists in $BaTiO_3$ in the presence of the above three vacancies. Our Berry-phase calculations further revealed that the polarization in $BaTiO_3$ with isolated vacancy is similar to, or even larger than, that in a perfect crystal. Therefore, polarization in $BaTiO_3$ is not suppressed by the existence of the considered vacancies. Moreover, we described a new microscopic polarization-switching mechanism when vacancy occurs in FEs, which yields one order of magnitude less energy barrier than the centrosymmetric switching. The polarization in $BaTiO_3$ with vacancy was demonstrated to be easily switchable, with a switching barrier comparable to that in perfect bulk. The mechanism further reveals that the local environment near vacancy plays a surprisingly minor role in polarization switching.

5.5 Appendix

In this appendix we first show in an intuitive and easily visualized way that for charged systems the polarization difference can be uniquely computed. To demonstrate this, let us consider a simple one-dimensional model system with two point charges (A and B) as shown in Fig.5.7a, where A carries a charge amount of $+2q$ while B carries $-q$ so that the system is net charged. More complicated systems such as solids can be similarly handled by using the centers of Wannier functions. Now let A displaced by a distance Δ_1 and B by a distance Δ_2 (Fig.5.7b). The change in dipole moment (directly related to polarization by a volume factor) for the configuration (b) with respect to configuration (a), $\Delta\tau = 2q\Delta_1 - q\Delta_2$, is well defined, despite the system is charged.

Furthermore, the computed polarization difference will not depend on the structural relaxation algorithm in density-functional calculations. Here it is useful to realize that, when calculating the polarization change, we must use the same origin of the coordinate system as properly done in Fig.5.7a and Fig.5.7b, since polarization is a quantity related to the position operator. In other words, we need to fix the origin of coordinate. This is what we have done in the calculations. More specifically, for a given LDA-determined final configuration ($\{\mathbf{r}_i^f\}$), we construct a centrosymmetric configuration ($\{\mathbf{r}_i^s\}$) with the same origin of coordinate, and then use multiple intermediate configurations according to $\mathbf{r}_i = \mathbf{r}_i^s + \lambda(\mathbf{r}_i^f - \mathbf{r}_i^s)$ (in which $0 \le \lambda \le 1$) to reach the final configuration ($\{\mathbf{r}_i^f\}$), where the same origin of coordinate is guaranteed by design and no structural relaxation is allowed for the intermediate configurations as it should be. Only the polarization value of the final configuration is needed. Now that we need to fix the origin, we cannot simultaneously fix another position by fixing a sublattice in solids. In structural relaxation, one can fix a sublattice since the energy is translation invariant. But the absolute value of polarization is not.

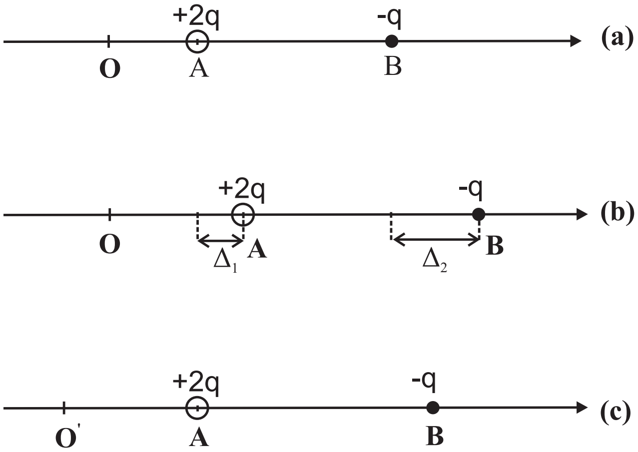

Figure 5.7: Schematic illustration of displacements of two point charges in the determination of polarization: (a) Initial positions of charges A and B, and the origin O of the coordinate system; (b) Final positions of A and B after they are displaced; (c) Shifting the charges in (b) so that the position of A is fixed at the same location as the initial position in (a).

If we insist to fix one sublattice when we calculate the polarization change, e.g., fixing the position of charge A as shown in Fig.5.7c, we must also move the origin from O to O′, namely we translate the whole system (charges A, B, and the origin). Then, the dipole-moment change of the configuration (c) with respect to the configuration (a) is $\Delta\tau' = 2q\Delta_1 - q\Delta_2$, which is the same as $\Delta\tau$.

Bibliography

[1] M. E. Lines and A. M. Glass *Principles and applications of ferroelectrics and related materials* (Clarendon Press, Oxford, 1977).

[2] M. Dawber, K. M. Rabe, and J. F. Scott, Rev. Mod. Phys. **77**, 1083 (2005).

[3] J. F. Scott and M. Dawber, Appl. Phys. Lett. **76**, 3801 (2000).

[4] R. E. Cohen, Nature (London) **358**, 136 (1992).

[5] R. E. Cohen and H. Krakauer, Phys. Rev. B **42**, 6416 (1990).

[6] M. Brazier, S. Mansour, and M. McElfresh, Appl. Phys. Lett. **74**, 4032 (1999).

[7] S. Pöykkö and D. J. Chadi, Phys. Rev. Lett. **83**, 1231 (1999).

[8] F. Yang, M. H. Tang, Y. C. Zhou, Fen Liu, Y. Ma, X. J. Zheng, J. X. Tang, H. Y. Xu, W. F. Zhao, and Z. H. Sun, Appl. Phys. Lett. **92**, 022908 (2008).

[9] L. He and D. Vanderbilt, Phys. Rev. B **68**, 134103 (2003).

[10] Y. Zhang, J. Li, and D. Fang, Phys. Rev. B **82**, 064103 (2010).

[11] V.-C. Lo, W. W.-Y. Chung, H. Cao, and X. Dai, J. Appl. Phys. **104**, 064105 (2008).

[12] J. F. Scott, *Ferroelectric memories* (Springer, Berlin, 2000).

[13] K. Uchino, *Piezoelectric Actuators and Ultrasonic Motors* (Kluwer Academic, Boston, 1996).

[14] J. F. Scott, Science **315**, 954 (2007).

[15] S. Jesse, B. J. Rodriguez, S. Choudhury, A. P. Baddrof, I. Vrejoiu, D. Hesse, M. Alexe, E. A. Eliseev, A. N. Morozovska, J. Zhang, L.-Q. Chen, and S. V. Kalinin, Nat. Mater. **7**, 209 (2008).

[16] S. V. Kalinin, S. Jesse, B. J. Rodriguez, Y. H. Chu, R. Ramesh, E. A. Eliseev, and A. N. Morozovska, Phys. Rev. Lett. **100**, 155703 (2008).

[17] A. N. Kolmogorov, Izv. Akad. Nauk SSSR, Ser. Math **3**, 355 (1937).

[18] M. Avrami, J. Chem. Phys. **8**, 212 (1940).

[19] H. Orihara, S. Hashimoto, and Y. Ishibashi, J. Phys. Soc. Jpn. **63**, 1031 (1994).

[20] A. K. Tagantsev, I. Stolichnov, N. Setter, J. S. Cross, and M. Tsukada, Phys. Rev. B **66**, 214109 (2002).

[21] X. Ren, Nat. Mater. **3**, 91 (2004).

[22] E. Cockayne and B. P. Burton, Phys. Rev. B **69**, 144116 (2004).

[23] A. Chanthbouala *et al.*, Nat. Mater. **11**, 860 (2012).

[24] V. Garcia and M. Bibes, Nat. Commun. **5**, 4289 (2014).

[25] Y. Yao and H. Fu, Phys. Rev. B **84**, 064112 (2011).

[26] Ph. Ghosez, X. Gonze and J.-P. Michenaud, Ferroelectrics **206**, 205 (1998).

[27] C.H. Park and D.J. Chadi, Phys. Rev. B **57**, R13961 (1998).

[28] A. Garcia and J.E. Northrup, Phys. Rev. Lett. **74**, 1131 (1995).

[29] S.-H. Wei and S.B. Zhang, Phys. Rev. B **66**, 155211 (2002).

[30] X. Liu, Y. Wang, P. V. Lukashev, J. D. Burton, and E. Y. Tsymbal, Phys. Rev. B **85**, 125407 (2012).

[31] K. McCash, A. Srikanth, and I. Ponomareva, Phys. Rev. B **86**, 214108 (2012).

[32] W. Kohn and L. J. Sham, Phys. Rev. **140**, A1133 (1965).

[33] A. Raeliarijaona and H. Fu, unpublished.

[34] N. Troullier and J. L. Martins, Phys. Rev. B **43**, 1993 (1991).

[35] H. Fu and O. Gulseren, Phys. Rev. B **66**, 214114 (2002).

[36] H. Fu and R.E. Cohen, Nature **403**, 281 (2000).

[37] P. Giannozzi *et al.*, J. Phys. C **21**, 395502 (2009); P. Giannozi *et al.*, http://www.quantum-espresso.org.

[38] R. Wahl, D. Vogtenhuber, and G. Kresse, Phys. Rev. B **78**, 104116 (2008).

[39] R.D. King-Smith and D. Vanderbilt, Phys. Rev. B **47**, 1651 (1993).

[40] R. Resta, Rev. Mod. Phys. **66**, 899 (1994).

[41] Z. Alahmed and H. Fu, Phys. Rev. B **76**, 224101 (2007).

[42] The chemical potentials of atomic reservoirs differ slightly from those in Ref.[41] because of different computational packages.

[43] The formation energies of different charge states are given at http://comp.uark.edu/~hfu/DH_BaTiO3.pdf for each vacancy species.

[44] C. N. Berglund and W. S. Baer, Phys. Rev. **157**, 358 (1966).

[45] D. Mahgerefteh, D. Kirillov, R. S. Cudney, G. D. Bacher, R. M. Pierce, and J. Feinberg, Phys. Rev. B **53**, 7094 (1996).

[46] Our calculations show that other charge states with higher formation energies are metallic.

[47] R. Resta, J. Phys. C **22**, 123201 (2010).

[48] D. Vanderbilt and R.D. King-Smith, Phys. Rev. B **48**, 4442 (1993).

[49] G. H. Kwei, A. C. Lawson, S.J.L. Billinge, and S. W. Cheong, J. Phys. Chem. **97**, 2368 (1993).

[50] G. Makov and M. C. Payne, Phys. Rev. B **51**, 4014 (1995).

[51] S. Lany and A. Zunger, Phys. Rev. B **78**, 235104 (2008).

[52] S.F. Liu, Y.J. Wu, J. Li, and X.M. Chen, Appl. Phys. Lett. **104**, 082912 (2014).

[53] S.-T. Zhang, G.-L. Yuan, J. Wang, Y.-F. Chen, G.-X. Cheng, and Z.-G. Liu, Solid State Commun. **132**, 315 (2004).

[54] W.L. Warren, D. Dimos, B.A. Tuttle, G.E. Pike, and H.N. AlShareef, Integrated Ferroelectrics **16**, 77 (1997).

6 Ferromagnetism induced by vacancies in ferroelectric BaTiO$_3$: sensitive dependence on charge state, origin of magnetism, and allowed temperature range

6.1 Introduction

Vacancies in ferroelectric (FE) materials have been of fundamental and technological interest for decades.[16] Fundamentally, the existence of vacancy breaks the delicate balance between the long-range and short-range interactions, thus affecting the polarization and dielectric properties. Furthermore, vacancies also influence conductivity, [2] optical absorption, [3], and the photorefractive effects [4], indicating a long-lasting interest that span across different fields from material science to nonlinear optics. Technologically it is known that vacancies play a critical role in polarization switching, and are one of the main causes for fatigue. Interestingly, apart from the detrimental effects, vacancies may nevertheless bring favorable properties, for example, vacancies may drastically enhance the piezoelectric responses.[6] The strong interest in studying vacancies thus stems from both the need to fundamentally understand new effects caused by these vacancies and the technological demand of better materials with better control of vacancies either to suppress their detrimental effects or to enhance the desirable properties.

Recently, another fundamental interest in vacancies in FEs emerges because of the possibility of vacancy-induced ferromagnetism (FM) (BTO [5, 7, 8, 9, 10, 11] or PbTiO$_3$ [12]), aimed at understanding the coexistence of multiferroic properties and the creation of room-temperature multiferroics. Indeed, there is experimental evidence showing hysteretic behavior of magnetization in BTO annealed at various temperature and oxygen pressure. [5] Meanwhile, experimental investigation of nonstoichiometric thin-film reported the evidence of FM on the film's *surface* with ferroelectricity persisting in the bulk. [8]

Nevertheless, there is considerable misconception and misunderstanding regarding vacancy-induced magnetism in FEs. First, experiments often assumed that only oxygen vacancy (V_O) may induce FM. What if samples are grown under the oxygen rich condition and V_O is unlikely to form? Will FM exist? Nowadays, with the contemporary progress of Molecular Beam Epitaxy (MBE), there is a much better control of crystal growth, which allows the tuning of the growth conditions for a particular vacancy to appear and hence the possibility of controlling the induced magnetism in FEs. Second, it is fundamentally unclear how the charge state of vacancy influence the magnetism. With the change of the electron Fermi energy, the same vacancy but with different charge states could have very different formation energies and therefore, different magnetic properties. Another incorrect assumption related to this subject is that people tend to assume that unpaired electrons will induce FM. With this assumption, oxygen vacancy with charge state $q = 1+$ is to be FM, which, as will be shown below, is not true. Third, it is not clear what temperature range the FM is allowed, if vacancy indeed introduces FM. Room-temperature FM and FE may have technological implications. Last but not least, there is an outstanding issue regarding the origin of vacancy-induced magnetism. As pointed out by T. Moryia [14], there are two starting points in the study of ferromagnetism: the local moment theory and the itinerant electron theory. The former starts with a consideration of a spin polarization localized in the real-space representation, while the latter starts from the localization in reciprocal space, which is equivalent to an extended state in real space. It remains unclear whether the vacancy-induced spin moments are to be localized near the vacancy, or to be extended over a considerable region in real space.

The purpose of this paper is three-fold: (i) to determine what vacancy and what charge state can induce FM in bulk $BaTiO_3$? We also point out the growth conditions in which one expects a particular vacancy to occur. (ii) to reveal the origin of the vacancy-induced FM and the nature of the spin-polarization moments; (iii) to find the temperature range within which the FM can sustain for different vacancies.

We use the first-principles density-functional theory (DFT) to study the different charged vacancies and their effects on the magnetic properties of $BaTiO_3$. We show that FM can be generated by the vacancy of all three species (V_{Ba}, V_{Ti}, and V_O), not by V_O alone. Meanwhile, for a given vacancy specie, the charge state of the vacancy is found to be critical for determining whether FM exists or not. For instance, while V_O^0 is FM, V_O^{1+} is not. Further, it is shown that despite one's effort to reduce vacancies by choosing the Fermi energy within its optimal range, vacancies can still form and they can possibly induce ferromagnetism with a magnetization that may be as high as 1.33 emu/g. Furthermore, we reveal the origins of vacancy-induced FM in BTO, demonstrating that both itinerant electron and itinerant hole can induce magnetization. Magnetism due to V_O^0 is caused by spin-polarization of itinerant electrons at Ti $3d$ orbitals, while magnetism due to V_{Ti}^{3-} originates from the the itinerant *hole* at O $2p$ orbitals. The temperature range that magnetic moment can sustain is found to be drastically different for different vacancies. In particular, FM induced by V_{Ti}^{3-} can sustain at room temperature.

The paper is organized as follows. In Sec. 6.2 we describe the calculation methods and theories used in this study. We will then present in Sec. 6.3 the calculation results and relevant discussions. In Sec.IV, a summary is given to conclude the paper. In Appendix, the formation energies and the growth conditions for different vacancies are presented.

6.2 Theoretical methods

Let us begin by defining notations to be used in this paper. Vacancy of specie X with the charge state q is denoted as V_X^q, where q is a number followed by a sign. For instance, V_{Ba}^{1-} stands for a Ba vacancy with a charge 1-. In tetragonal $BaTiO_3$, there are two symmetry inequivalent oxygen sites, and to distinguish them, we use O1 to denote an oxygen atom at the apex of the pyramid, and O2 to denote an oxygen on the TiO_2 base plane.

Calculations of the total energy and structural optimization were performed using DFT within the local density approximation (**LDA**). [16] Effects of core electrons are described via norm-conserving Trouiller-Martins pseudopotentials, with semicore states Ti $3s$ and $3p$ treated as valence states for a better accuracy. [17] An energy cutoff of 80Ryd is used for the plane-wave expansion of electron wavefunctions, which was checked to provide a sufficient convergence. Optimization of the atomic positions was done by setting a force threshold of 10^{-4} Ryd/Bohr. All calculations were performed using Quantum Espresso, [18] and atomic positions were optimized for each charge state of a given vacancy specie.

We choose to study the tetragonal (P4mm) structure of $BaTiO_3$, since it was previously found that different ferroelectric phases have negligible effects on the vacancy-induced properties such as vacancy formation energy.[28] Our calculated bulk BTO has an in-plane lattice constant $a = 3.928$ Å and a c/a ratio of 1.007, which are close to the values from other calculations (such as $a = 3.945$Å, c/a=1.009 in Ref.[19]) and also to the experimental values [20] ($a = 3.9945$Å, $c/a = 1.0098$).

To simulate $BaTiO_3$ with vacancy, a 3×3×3 supercell with 135 atoms is used, and the vacancy is seated at the center of the supercell. The 3×3×3 supercell is sufficient and gives converged results. To handle the metallic states introduced by the vacancies, the smearing technique of Marzari and Vanderbilt [21, 22] was used. A typical smearing parameter $\sigma = 0.02Ry$ is used in total-energy calculations and structural optimization. For the supercell calculations, a well-converged 4×4×4 Monkhorst-Pack **k**-points sampling grid is used.

6.3 Results and discussions

6.3.1 Dependence of ferromagnetism on vacancy specie and charge state

The stability of ferromagnetic state caused by vacancy is determined by comparing the energy difference $\Delta E = E_{\mathrm{M}} - E_{\mathrm{N}M}$ between the spin-polarized magnetic state, E_{M}, and the non-magnetic state, $E_{\mathrm{N}M}$. We perform both spin polarized and spin non-polarized calculations for a given vacancy specie and a given charge state, which, when the magnetic state is more stable, will yield both E_{M} and $E_{\mathrm{N}M}$. However, when the non-magnetic state is more stable, the *unconstrained* magnetic moment calculations will find only the NM ground state, not the high-energy magnetic state. As a result, E_{M} cannot be determined because it is a meta-stable state, and we put $\Delta E = 0$.

Table 6.1 lists the value of ΔE and the magnitude of magnetism for all three vacancy species of different charge states in $\mathrm{BaTiO_3}$. One key outcome in Table 6.1 is that FM can be induced by all three vacancies. More specifically, ΔE is all negative for V^0_{Ba}, V^q_{Ti} $(q = 0, 1-, 2-, 3-)$, V^0_{O1} and V^0_{O2}, showing that FM is stable for these vacancies. Furthermore, the V^{3-}_{Ti}-induced FM state is found to be very stable (ΔE=-6.9 meV) and with a large magnetic moment of 1 μ_B per vacancy. In contrast, the energy gain of the V^0_O-induced FM state is considerably less (ΔE=-0.5 meV), and the magnetic moment is only 0.25 μ_B per vacancy. We thus see that FM caused by different vacancies behave markedly differently.

Table 6.1: Energy difference $\Delta E = E_{\mathrm{M}} - E_{\mathrm{N}M}$ and the magnitude of magnetization (M) for all vacancy species of different charge states in $BaTiO_3$.

Vacancy	charge q	ΔE (meV)	$\|\mathbf{M}\|$ ($\mu_B/Cell$)	$\|\mathbf{M}\|$ (emu/g)
V^q_{O1}	0	-0.5	0.25	0.22
	1+	0.0	0.01	0.00
	2+	0.0	0.00	0.00
V^q_{O2}	0	-0.5	0.25	0.22
	1+	0.0	0.02	0.00
	2+	0.0	0.00	0.00
V^q_{Ti}	0	-20.5	3.50	3.10
	1-	-10.4	1.70	1.51
	2-	-17.2	1.52	1.33
	3-	-6.9	1.00	0.89
	4-	0.0	0.00	0.00
V^q_{Ba}	0	-2.1	1.00	0.89
	1-	0.0	0.00	0.00
	2-	0.0	0.00	0.00

Obviously, whether or not the above vacancies—that are able to induce FM—occur in solids depend on their formation energies. In Appendix, we determine the formation energies of various vacancies, and it were found that V^0_{Ba}, V^{3-}_{Ti} (even V^{2-}_{Ti}), V^0_{O1}, and V^0_{O2} are all likely to occur depending on the choice of the oxygen atomic reservoir and the Fermi energy of electron reservoir. Consequently, the magnetism in $BaTiO_3$ can be caused by the vacancies of all three species, rather than V_O as commonly assumed. This is important since, if FM is caused by V^{3-}_{Ti}, artificially assuming that it is caused by V^0_O will lead to an incorrect interpretation and wrong understanding of the origin of the magnetism.

Another notable result of Table 6.1 is that the induced magnetism depends critically on the charge state of the vacancy. For instance, V^q_O can induce magnetism only when q=0, and in contrast, V^q_O is diamagnetic when $q = 2+$ or $q = 1+$. Also, for Ti vacancy, the magnetic moments vary significantly for different charge states q, ranging from 3.50μ_B for q=0 to only 1.0μ_B for q=3-.

In addition, two interesting and generally applicable observations can be made in Table 6.1.

First, V_{O1}^{1+}, V_{O2}^{1+}, and V_{Ba}^{1-} have an odd number of electrons, but these vacancies are diamagnetic. Traditionally it is often assumed that systems with an odd number of electrons tend to be spin-polarized. This is not the case for vacancy-induced magnetism in Table 6.1. The result also tells that, for a given charge state, one should not rely on counting the number of electrons to determine whether there is magnetism. Second, and interestingly, the nominal charge states of all three vacancy species (i.e., V_{Ba}^{2-}, V_{Ti}^{4-}, and V_{O}^{2+}) do not induce any magnetism. Here, the nominal charge state means that the vacancy carries an opposite charge as the ion in the perfect solid does. The nominal charge state is the charge state commonly expected for a vacancy. For instance, in perfect bulk $\mathrm{BaTiO_3}$, an O ion is 2- with two additional electrons surrounding the ion. When one creates an oxygen vacancy by taking one O atom away from the bulk solid into the oxygen reservoir, these two additional electrons would like to follow the O atom because of its strong electron affinity (rather than staying in the solid), which will lead to an oxygen vacancy carrying an opposite q=2+ charge state (i.e., V_{O}^{2+}). The reason that the nominal charge state is diamagnetic is due to the fact that this charge state resembles closely the perfect BTO. Again, take V_{O}^{2+} as an example. In BTO with V_{O}^{2+}, since two additional electrons are take away from the solid with an oxygen atom, the shells of all neighboring Ti and Ba atoms remain full as in the perfect solid, leaving no possibility for spin polarization.

To make sure that the magnetic states found in Table 6.1 are not meta-stable states, we have further performed constrained-moment calculations for each vacancy. The constrained moment calculations confirm that all the magnetic states in Table 6.1 are indeed the ground state. Take V_{O1}^{0} and V_{Ba}^{0} as example, and the constrained-moment calculation results are given in Fig. 6.1, showing that the magnetic moment $|M|$ is indeed $0.25\mu_B$ for V_{O1}^{0}. For V_{Ba}^{0}, there are two local energy minima, one at $|M| = 0.25\mu_B$ and the other at $|M| = 1.0\mu_B$. The latter is the global minimum by having a slightly lower energy. Fig.6.1 also reveals that the magnetic switching barrier is small for V_{O1}^{0} (0.5meV) and for V_{Ba}^{0} (~2meV).

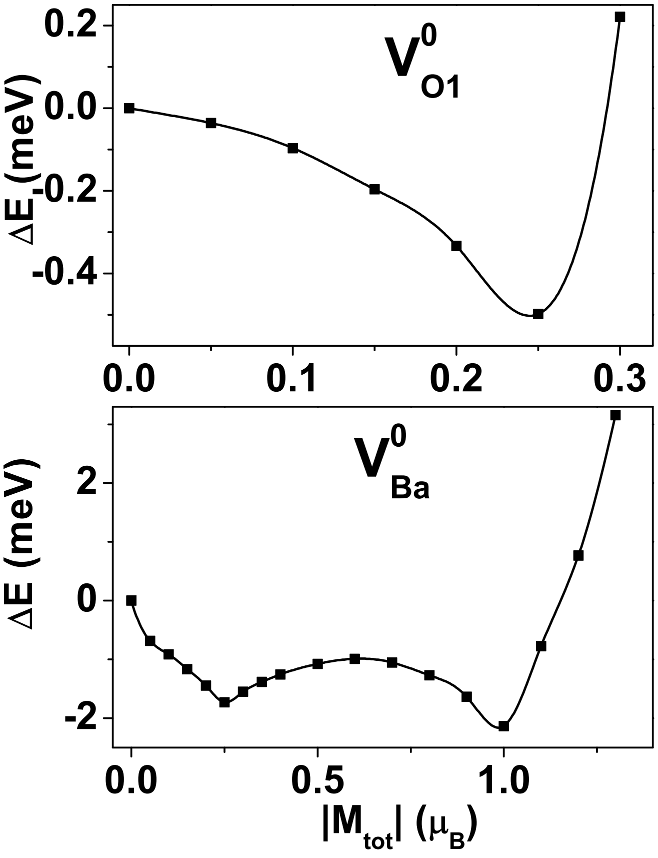

Figure 6.1: Constrained search of spin-polarized ground state.

6.3.2 Origin of ferromagnetism

The density of states (DOS) near the Fermi energy E_F is plotted in Fig.6.2 for the spin-up and spin-down components of different vacancies that induce magnetism. When system is diamagnetic such as V_{Ba}^{2-}, V_{Ti}^{4-}, and V_{O1}^{2+}, the up and down DOS components (not shown) are identical. For cation vacancies with magnetism—namely V_{Ba}^{0}, V_{Ti}^{2-}, and V_{Ti}^{3-}, Fig.6.2 shows that (i) their E_F all are located inside the valence states, revealing that with these vacancies we are dealing with acceptors in which carriers are holes; (ii) For *valence* states, the spin-up DOS component subjects to an evident downshift as compared to the spin-down component [see, e.g., Fig.6.2(c)], namely, the valence states are clearly spin polarized; (iii) However, and interestingly, this is not the case for the conduction states, in which the up and down DOS components remain nearly identical and are spin non-polarized. We thus see that the spin polarization in V_{Ba}^0, V_{Ti}^{2-}, and V_{Ti}^{3-} occurs only to the valence states, not the conduction states. The above results (i)-(iii) convincingly demonstrate that the FM induced by the cation vacancies is caused by the spin polarization of holes.

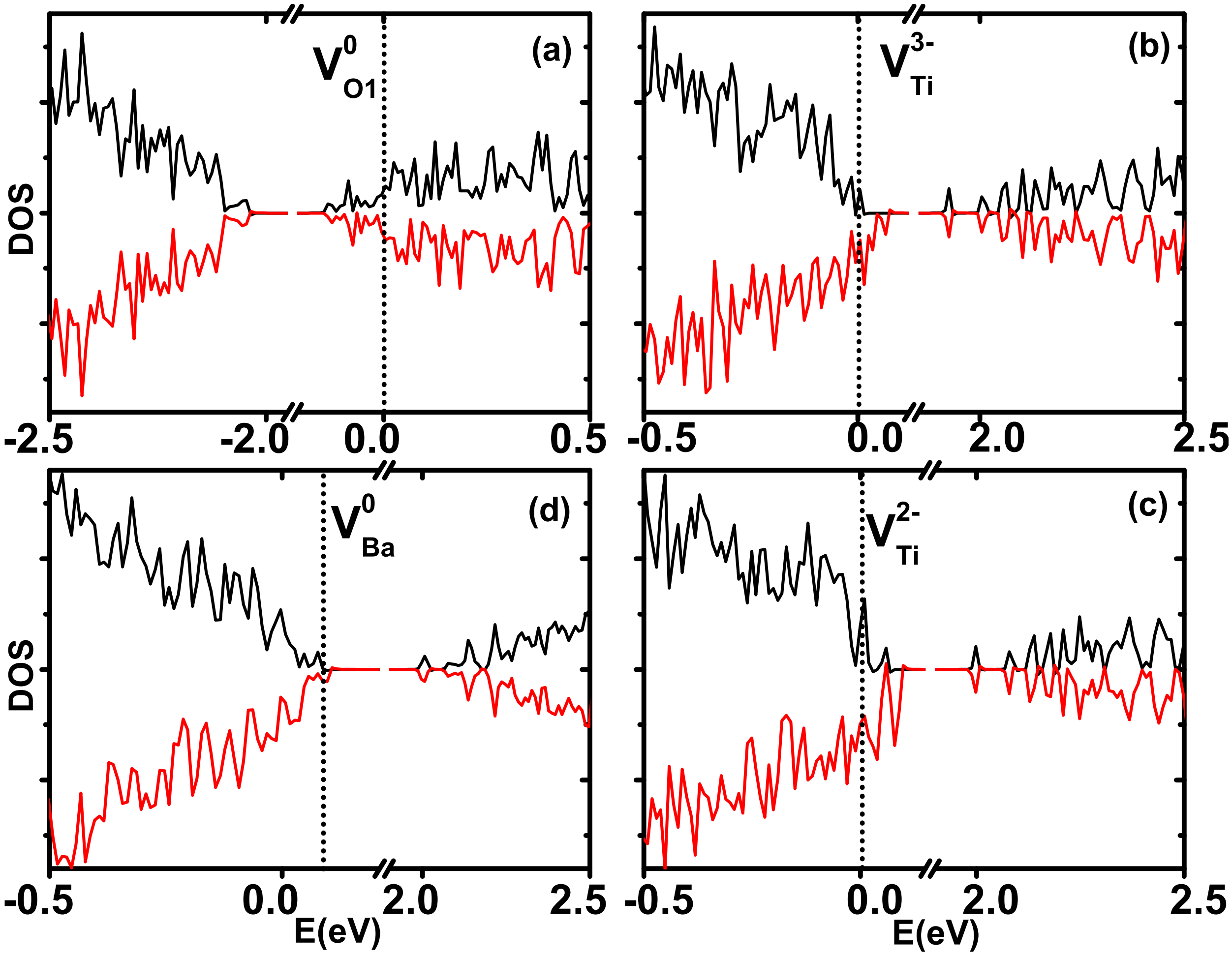

Figure 6.2: (Color online) Density of states (DOS) near E_F for V_{Ba}^0, V_{Ti}^{2-}, V_{Ti}^{3-}, and V_{O1}^0. Black and red lines are spin-up and spin-down components, respectively. E_F is chosen to be the zero reference.

Meanwhile, for anion vacancy V_O^0, Fig.6.2(d) shows an entirely different behavior. E_F is now located inside the conduction states, and the conduction states are spin polarized while the valence states are nearly not. Therefore, with the O vacancy we are dealing with a donor with carriers being electrons, and the FM is caused by the spin polarization of electrons. Also note in V_O^0 that the energy shift of the spin-up DOS component with respect to the spin-down component is barely perceptible and much smaller as compared to V_{Ti}^{3-}, which explains the better stability and larger magnitude of the magnetization of V_{Ti}^{3-} than those of the O vacancy in Table 6.1.

To obtain more microscopic insight that is responsible for the magnetism, we depict in Fig.6.3(a)-(d) the contour plots of the real-space spin density $\Delta\rho(\mathbf{r}) = \rho_\uparrow(\mathbf{r}) - \rho_\downarrow(\mathbf{r})$, on the XZ plane that contains the vacancy. The XZ plane is the ac plane in tetragonal $BaTiO_3$. For V_{O1}^0, two key conclusions can be drawn from Fig. 6.3(a). First, the spin density is distributed mainly on the Ti atoms, and is contributed by the unbalanced spin-up and spin-down occupations on the t_{2g} orbitals. This can be explained by the fact that V_{O1}^0 has an excess of two electrons compared to V_{O1}^{2+}, and these additional electrons have to be placed on the low-energy conduction states that are mainly the Ti $3d$ orbitals, hence the shape of the spin-polarized densities in Fig 6.3. Second, the spin density is not localized near the vacancy, instead it spread out in the supercell. This delocalized nature of the spin density reveals that V_O^0-induced ferromagnetism in $BaTiO_3$ is due to the itinerant electrons. It is worth pointing out that a $3 \times 3 \times 3$ supercell is necessary to obtain the correct spreading-out spatial distribution of $\Delta\rho(\mathbf{r})$. Using a smaller $2 \times 2 \times 2$ supercell, we found that $\Delta\rho(\mathbf{r})$ instead is rather localized near the vacancy, much like the one shown by Shimada *et al.* for the oxygen vacancy in $PbTiO_3$.

For cation vacancies (V_{Ti}^{3-}, V_{Ti}^{2-}, and V_{Ba}^0), Fig.6.3(b)-(d) show that spin polarization occurs on the O atoms, and once again $\Delta\rho(\mathbf{r})$ spreads out in the supercell. The shape of $\Delta\rho(\mathbf{r})$ manifests that mainly the O $2p$ orbitals are spin-polarized. This makes sense if we start from the nominal

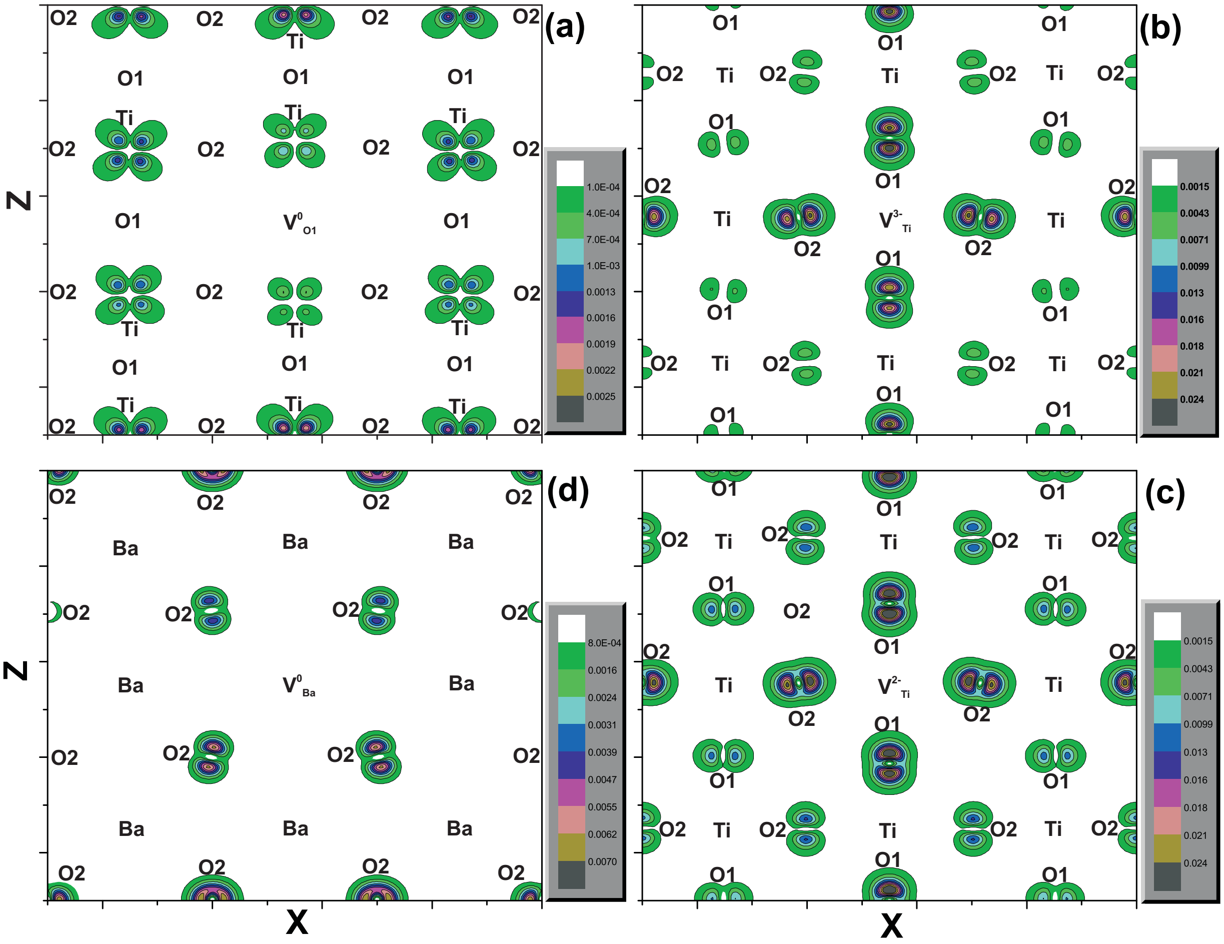

Figure 6.3: (Color online) Contour plots of $\Delta\rho(\mathbf{r})$ on the XZ plane that contains the site of vacancy for (a) V^0_{O1}, (b) V^{3-}_{Ti}, (c) V^{2-}_{Ti}, and (d) V^0_{Ba}. The XZ plane is the ac plane in the tetragonal $BaTiO_3$.

charge state that resembles the perfect BTO, namely V^{4-}_{Ti} or V^{2-}_{Ba}, in which the shells of all atoms are filled, hence the O $2p$ orbitals. Now with charge states V^{3-}_{Ti} or V^0_{Ba}, less electrons are in the systems, thereby creating holes near the top of valence states which are mainly the $2p$ states of the O atoms. Another notable feature about V^{3-}_{Ti} in Fig.6.3(b) is that the p-like shape of $\Delta\rho(\mathbf{r})$ on the O atoms and vacancy form a 180^0 angle, implying that the 180^0-degree spin exchange in play[29].

Combining Fig.6.2 and Fig.6.3, we thus see that the magnetism of the oxygen vacancy originates from the spin polarization of the itinerant electrons at Ti t_{2g} orbitals. The itinerant theory of magnetism also applies to the cation vacancies, but instead we need to think in term of the non-localized holes. More specifically, the FM induced by V_{Ti}^{3-}, V_{Ti}^{2-}, and V_{Ba}^{0} are attributed to the spin-polarization of itinerant holes at the O $2p$ orbitals.

Magnetism may be caused by (i) localized magnetic moment, where electrons are bound only near the atom to which it belongs and the exchange interaction between electrons, with the help of Pauli's exclusion principle, cause the spin alignment or anti-alignment. This includes direct exchange, superexchange or indirect exchange (RKKY, Zener double exchange). (ii) Delocalized magnetic moment, where the interacting electrons causing the magnetization are the conduction electrons. This is known as the itinerant exchange. This analysis is ultimately expressed by the well known Stoner Criterion, which states that for a system with itinerant electrons to be ferromagnetic the system must satisfy the criterion: $U > \frac{2}{g(E_F)\Omega}$, where U is the on-site Coulomb repulsion, g(E_F) is the density of states at the Fermi energy before spin-polarization, and Ω is the volume of the unit cell.

6.3.3 Allowed temperature range for magnetism

The temperature range that ferromagnetism can sustain is, in terms of potential technological applications, an important quantity. For instance, ferromagnetism existing at room temperature or even higher are desirable. Different vacancy species create very different interactions and new balances around the defect, and it is thus interesting to investigate the magnetic moment of which vacancy may survive at high temperatures. To determine the temperature range that allows the magnetism, we vary the smearing width σ to mimic the effects of temperature in the calculations of spin-polarized band structure and magnetic moments, while the atomic positions are fixed at their optimized locations. The obtained magnetic moments are depicted in Fig.6.4 as a function of σ for V_{O1}^{0}, V_{Ti}^{3-}, and V_{Ba}^{0}.

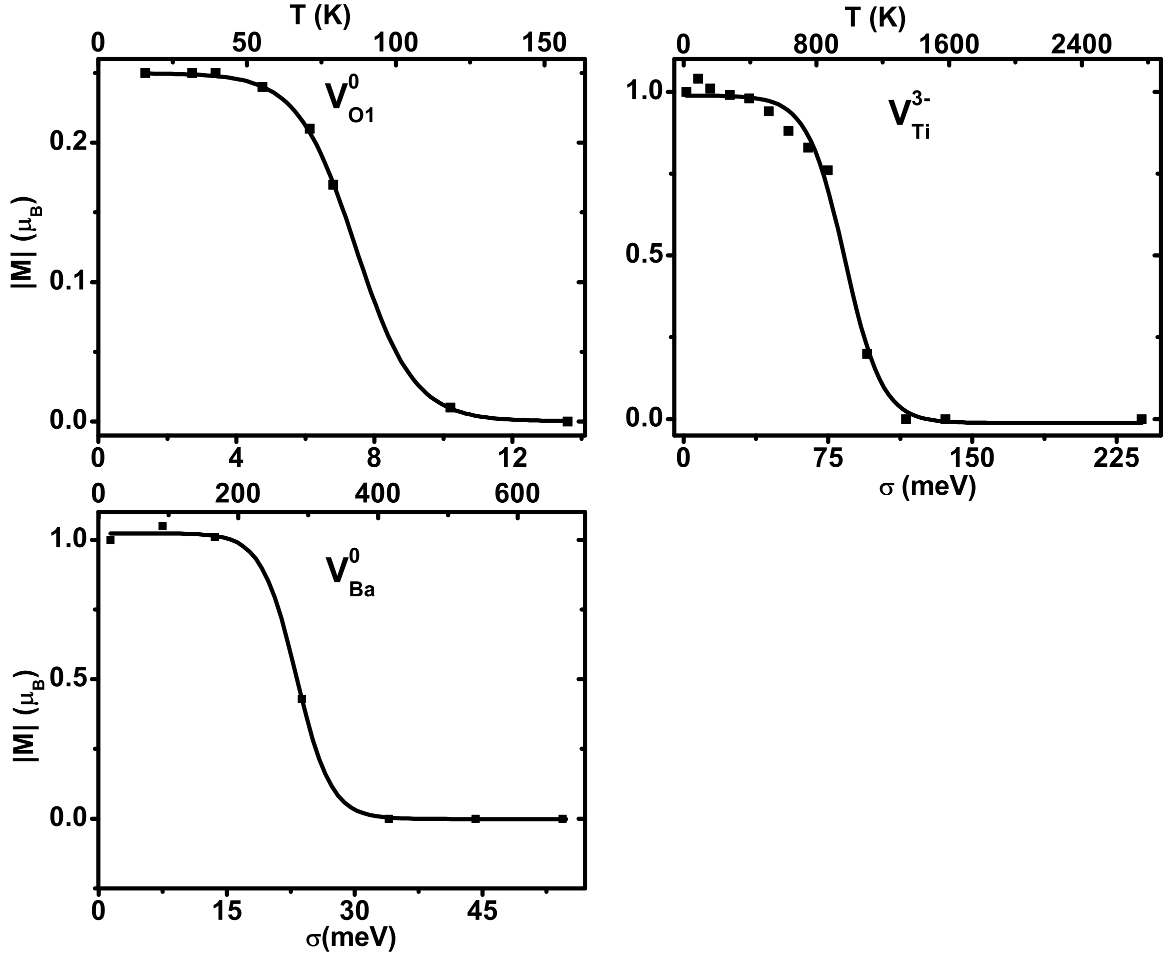

Figure 6.4: Magnetization as a function of the broadening width σ for V_{O1}^{0}, V_{Ti}^{3-}, and V_{Ba}^{0} vacancies.

Interestingly one common feature emerges for all three vacancies in Fig.6.4. That is, the magnetic moment saturates at low temperatures, starts to decline at some transition σ value, and then vanishes at high σ. This behavior can be intuitively explained by one electron in a two-level system and the Fermi-Dirac distribution. The two levels are separated by a energy difference of Δ due to spin polarization. When thermal excitation energy ($k_\mathrm{B}T$) is much smaller than the energy separation (Δ), only one level is occupied, leading to spin polarization and magnetic moment. In the opposite limit of $k_\mathrm{B}T >> \Delta$, thermal excitation will occupy both levels, resulting in a spin non-polarized system.

Furthermore, we numerically find that the shapes of the three $M \sim \sigma$ curves in Fig.6.4 can be well described by

$$M = \frac{M_0}{1 + e^{(\sigma - \sigma_0)/d}} \tag{6.1}$$

where M_0 is the saturated magnitude of magnetic moment at low temperature, σ_0 the characteristic transition point where M decreases to half of the saturated M_0 value, d is the transition width. σ_0 quantitatively indicates the high temperature limit up to which magnetism can sustain. M_0, σ_0, and d are found to be respectively $0.25\mu_B$, 7.46 meV, and 0.84 meV for V_{O1}^{0}, $1.0\mu_B$, 83.7 meV, and 9.68 meV for V_{Ti}^{3-}, and $1.0\mu_B$, 23.1 meV, and 2.03 meV for V_{Ba}^{0}. The saturated M_0 values agree well with the direct first-principle calculation results in Table 6.1.

As another key outcome, Fig.6.4 reveals that magnetism caused by oxygen vacancy can sustain only at small σ; above $\sigma = 10meV$, M due to V_{O1}^{0} becomes practically zero, showing that FM occurs only at low temperatures. In sharp contrast, ferromagnetism due to V_{Ti}^{3-} is capable of existing at much larger σ, up to 90 meV, indicating that FM of Ti vacancy sustains at much higher temperature. This study thus predicts that the temperature range that magnetism can occurs differ drastically for different vacancies.

6.4 Summary

Magnetism caused by intrinsic vacancies in ferroelectric $BaTiO_3$ is a topic of fundamental interest, and was studied using first-principles density functional calculations. We examined which vacancy specie gives rise to magnetism, the influence of charge state on the induced magnetic moment, the microscopic origin responsible for the occurrence of the magnetism, and the temperature range that the induced magnetism can sustain. The present study not only provides the needed and comprehensive understanding for vacancy-induced magnetism in ferroelectrics, it also settles down key issues that are previously unclear. Furthermore, this work is useful to experimentalists in terms of providing knowledge on how to deliberately control the magnetism by controlling which vacancy to appear under a certain growth condition (see Appendix). Our specific findings are summarized in the following.

(i) FM can be induced by all three vacancy species in $BaTiO_3$, and more specifically by V^0_{Ba}, V^q_{Ti} ($q = 3-, 2-, 1-, 0$), and V^0_O. The existence of ferromagnetism is confirmed by both unconstrained and constrained-moment calculations. Furthermore, as shown in the Appendix, by tuning the chemical potential of the atomic and electron reservoirs, V^0_{Ba} and V^q_{Ti} are possible under the O-rich conditions with Fermi energy near the VBM, while V^0_O is abundant under the O-poor condition with $E_F \geq 2$ eV.

(ii) The charge state of vacancy, often neglected previously in the study of vacancy-induced magnetism, is found pivotal in terms of determining the stability of FM phase and the magnetic moment of vacancy. For instance, V^{2+}_O and V^{1+}_O are diamagnetic, whereas V^0_O is ferromagnetic. Also, the magnetic moments of V^0_{Ti} and V^{3-}_{Ti}, two different charge states of the same vacancy specie, drastically differ; M is $3.5\mu_B$ for the former and merely $1.0\mu_B$ for the latter. Furthermore, our calculation results demonstrate that the approach is invalid to judge vacancy-induced ferromagnetism by counting the number of electrons.

(iii) The origin is different for cation- and anion-induced FMs. Ferromagnetism induced by V^0_O originates from the spin polarization of itinerant *electrons* in the conduction states, with spin density predominately located at Ti $3d$ orbitals. Interestingly, for this vacancy, the valence states are nearly spin non-polarized. On the other hand, the magnetism induced by V^{3-}_{Ti} and V^0_{Ba} is caused by the spin polarization of itinerant *holes*, in which the spin density is found to be mainly located at at the $O\,2p$ orbital.

(iv) FM induced by different vacancy species can sustain at very different temperature range. FM of V_O^0 may sustain only at low temperatures, while that of V_{Ti}^{3-} can exist at very high temperatures. V_{Ba}^0 is in between. This allowed temperature range is also consistent with the energy gain ΔE of the FM phase in Table.6.1.

6.5 Appendix

In this Appendix we show how vacancies in $\mathrm{BaTiO_3}$ may be controlled during growth using the chemical potentials of the atomic reservoirs and the Fermi energy of the electron reservoir. The formation energy of a charged vacancy V_X^q determines the vacancy concentration, and is given by [25, 26, 27]

$$\begin{aligned}\Delta H[\mathrm{V}_X^q] &= E(\mathrm{V}_X^q) + \left[\mu_X + E_X^0\right] \\ &\quad + q\left[E_F + \varepsilon_{\mathrm{V}BM}^0 + \Delta\overline{V}\right] - E(\mathrm{A}BO_3),\end{aligned}$$

where $E(\mathrm{V}_X^q)$ is the total energy of solid with vacancy V_X^q, $E(\mathrm{A}BO_3)$ the total energy of perfect solid, E_{X}^0 the total energy of elemental solid of species X, $\varepsilon_{\mathrm{V}BM}^0$ the single-particle energy of the valence band maximum of perfect crystal, $\Delta\overline{V}$ the change in the average potential from perfect crystal to the solid with vacancy, μ_X the relative chemical potential of atomic reservoir with respect to the energy of elemental solid. E_F is the Fermi energy of the solid with respect to the VBM in solid with vacancy so that the chemical potential μ_e of electron reservoir equals $E_F + \varepsilon_{\mathrm{V}BM}^0 + \Delta\overline{V}$, knowing that mu_e and the Fermi level of the system must match at thermal equilibrium. According to the tradition of defect physics,[25, 27] E_X^0 of elemental solid of species X is used as the zero reference energy for chemical potential of atomic reservoir. $\Delta\overline{V}$ is determined by the shift in the energy of the Ti semicore $3s$ orbitals, since this state has very little dispersion. Quantities μ_X and E_F control the probability of vacancy occurrence during an equilibrium growth.

μ_X must satisfy certain constraints to avoid the formation of secondary phases such as BaO, TiO_2 compounds or elemental solids during growth, as shown in Ref.[28]. We calculate these constraints using Quantum Espresso, and the results are very similar to those in Ref.[28] using a different DFT code, for instance, for a given μ_O, the width Δ that μ_{Ti} can vary is $\Delta = 1.69$ eV in current calculation, close to $\Delta = 1.62$ eV in Ref.[28]. In experiments, the chemical potential of oxygen is often used to control the growth. We thus allow μ_O to change, and μ_{Ba} and μ_{Ti} are determined by the constraints accordingly. For $BaTiO_3$, μ_O can vary within $\mu_O \in [-5.7, 0]$ eV. We consider both the O-rich condition and the O-poor condition. Under O-rich condition (μ_O=0, we choose μ_{Ba}=-6.55 eV and μ_{Ti}=-11.29 eV. Under O-poor condition (μ_O=-5.7 eV), we choose μ_{Ba}=0 eV and μ_{Ti}=-0.73 eV. It should be understood that the μ_{Ba} and μ_{Ti} can vary within a width of Δ. The formation energies of different vacancies are shown in Fig.6.5.

Vacancy concentration $N[\mathrm{V}_X^q]$ is related to the formation energy $\Delta H(\mathrm{V}_X^q)$ by $N[\mathrm{V}_X^q] = N_0 e^{-\Delta H(\mathrm{V}_X^q)/k_B T}$, where N_0 us the number of atomic sites per unit volume. Carrier concentration measurements on $BaTiO_3$ with O vacancy gives a common value around[2, 3] 8×10^{18} cm^{-3}. Higher concentrations can reach 4.53×10^{21} (cm^{-3} ([5]) and $\sim 10^{20} - 10^{21}$ cm^{-3} ([24]). Using the common value of V_O concentration, we estimate that the formation energy is about 1 eV using the common annealing temperature around 1000 K. This suggests that vacancy is common and easy to form when the formation energy is less than 1.5 eV. When formation energy is between 1.5 to 4 eV, vacancy is still likely to occur. On the other hand, if formation energy is above 4 eV, vacancy is unlikely.

Fig.6.5 reveals the following: (i) Under the O-poor condition, and when E_f is above 2 eV,

V_{O1}^{0} is the lowest-energy charge state for oxygen vacancy with a low formation energy of xxx eV, and is thus likely to form. As shown in Table 6.1, this V_{O1}^{0} vacancy gives rise to FM. (ii) Under the O-rich condition, the formation energies of V_{Ti}^{4-}, V_{Ti}^{3-}, and even V_{Ti}^{2-} are all quite close when E_F is below 0.8eV (see Fig.6.5e), and all these vacancies may likely occur. Since V_{Ti}^{3-} and V_{Ti}^{2-} are ferromagnetic with strong energy gain (Table 6.1), Fig.6.5e thus demonstrates that it is possible that the magnetism in $BaTiO_3$ is caused by Ti vacancy, not by oxygen vacancy alone. (iii) Similarly, under the O-rich condition and E_F is less then 0.5eV in Fig.6.5(d), V_{Ba}^{0} may also be possible and will cause ferromagnetism. We thus conclude that all three vacancy species (V_{O1}^{0}, V_{Ti}^{3-}, V_{Ti}^{2-}, and V_{Ba}^{0}), which are FM, are likely to occur when the chemical potential μ_O of oxygen reservoir and Fermi energy E_F are properly chosen.

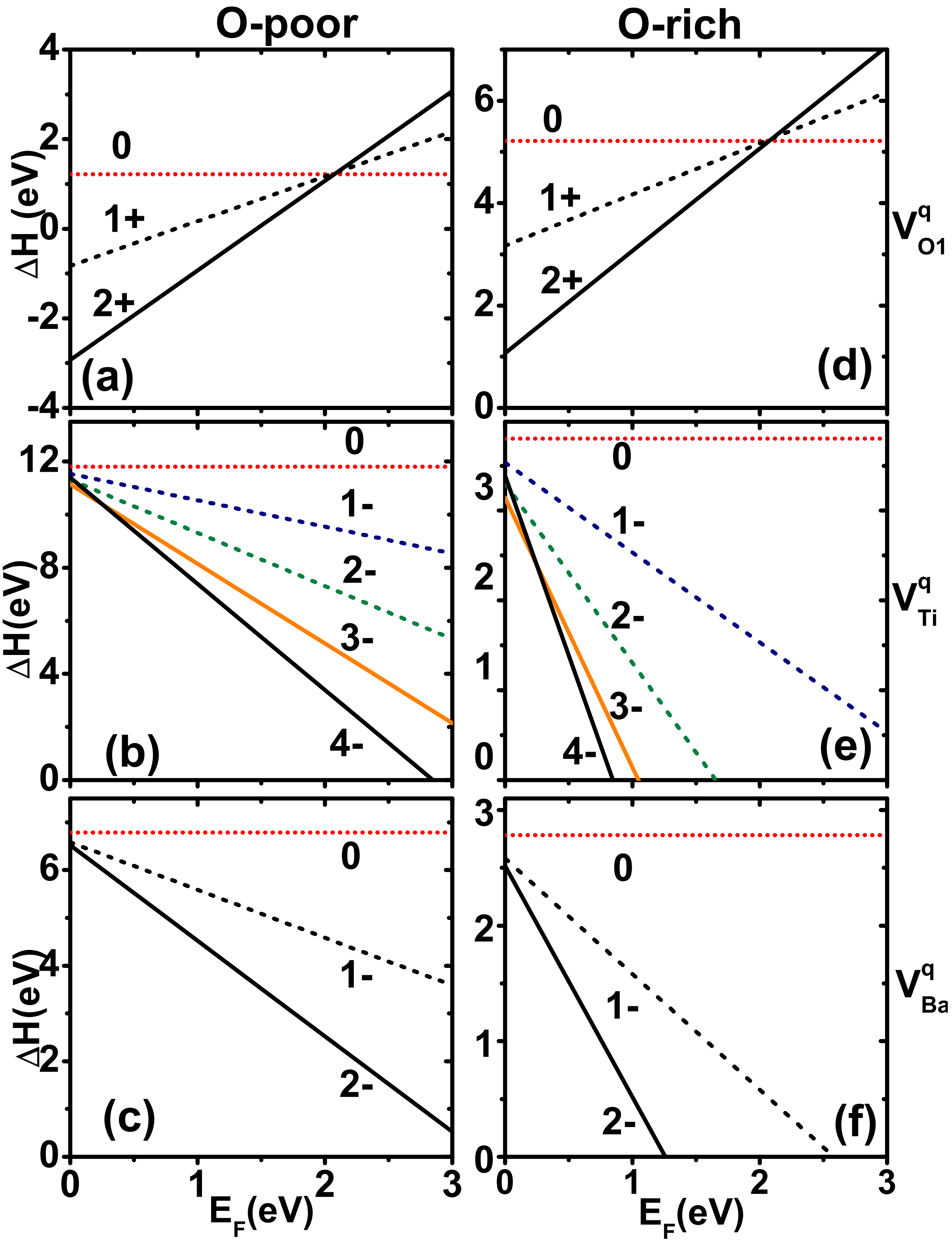

Figure 6.5: Vacancy formation energies as a function of E_F for different vacancies: Left column (a)-(c) under the O-poor condition (μ_O=-5.87 eV); Right column (d)-(e): under the O-rich condition.

Bibliography

[1] M. E. Lines and A. M. Glass *Principles and applications of ferroelectrics and related materials* (Clarendon Press, Oxford, 1977).

[2] C. N. Berglund and W. S. Baer , Phys. Rev. **157**, 358, (1966).

[3] C. N. Berglund and H. J. Braun , Phys. Rev. **164**, 790, (1967).

[4] B. A. Weschler and M. B. Klein , J. Opt. Soc. Am. B **5**, 1711, (1988).

[5] Y. Fang, K. Jin, H. Lu, M. He, C. Wang, J. Wen, G. Yang ,Sci. China Physics, Mechanics and Astronomy **53**, 852-855 (2009).

[6] X. Ren, Nature Materials **3**, 91 (2004).

[7] S. Qin, D. Liu, Z. Zuo, Y. Sang, X. Zhang, F. Zheng, H. Liu, and X.-G. Xu, J. Phys. Chem. Letter **2010**, 238-241 (2009).

[8] R. V. K. Mangalam, N. Ray, U. V. Waghmare, A. Sundaresan, C. N. R. Rao, Solid State Communications **149** , 1-5 (2009).

[9] M. Ishii, D. Ohta, M. Uehara and Y. Kimishima, Procedia Engineering **36**, 578-582 (2012).

[10] D. Cao, M. Q. Cai, Yue Zheng and W. Y. Hu, Phys. Chem. Chem. Phys., **11**, 10934-10938 (2009).

[11] Q.-L. Fang, J.-M. Zhang, K.-W. Xu, Physica B **424**, 79-83 (2013).

[12] Takahiro Shimada, Yoshitaka Uratani, Takayuki Kitamura, App. Phys. Lett. **100**, 162901 (2012).

[13] T. Shimada, Y. Uratani, and T. Kitamura, Acta Materialia, **60**, 6322 (2012).

[14] T. Moriya *Spin fluctuation in Itinerant Electron Magnetism model* (Springer-Verlag, Berlin Heidelberg, 1985).

[15] F. A. Kröger, H. J. Vink, Solid State Phys. **3**, 307-435 (1956).

[16] W. Kohn, L. J. Sham, Phys. Rev. **140**, A1133 (1965).

[17] N. Troullier and J. L. Martins, Phys. Rev. B **43**, 1993 (1991).

[18] P. Giannozzi *et al.*, J. Phys. C **21**, 395502 (2009); P. Giannozi *et al.*, http://www.quantum-espresso.org.

[19] R. Whal, D. Vogtenhuber, G. Kresse, Phys. Rev. B **78**, 104116 (2008).

[20] J. Harada, T. Pedersen, Z. Barnea, Acta Cryst. **A26**, 336 (1970).

[21] N. Marzari and D. Vanderbilt, Phys. Rev. Lett. **79**, 1337 (1997).

[22] N. Marzari, Ph.D. Thesis, University of Cambridge, 1996.

[23] J. D. Pack and H. J. Monckhorst, Phys. Rev. B **16**, 1748 (1977).

[24] S. Banarjee, A. Datta, A. Bhaumik, D. Chakravorty, J. Appl. Phys. **110**, 064316 (2011).

[25] Su-Huai Wei and S. B. Zhang, Phys. Rev. B **66**, 155211 (2002).

[26] Y. Yao and H. Fu, Phys. Rev. B **84**, 064112 (2011).

[27] C. Freysoldt, B. Grabowski, T. Hickel, J. Neugebauer, G. Kresse, A. Janotti, C. G. Van de Walle, Rev. Mod. Phys. **86**, 253 (2014).

[28] Z. Alahmed and H. Fu, Phys. Rev. B **76**, 224101 (2007).

[29] D. Khomskii *Electronic Structure, Exchange and Magnetism in Oxides* (Springer-Verlag, Berlin Heidelberg, 2001).

7 Coupling of the Electromagnetic Angular Momentum Density with Magnetic Moments: Proof and Consequences

The angular moment density associated with an electromagnetic field is defined as [1]:

$$\mathscr{J} = \frac{1}{c^2}\mathbf{r} \times (\mathbf{E} \times \mathbf{H}) \tag{7.1}$$

where $\mathbf{r}$ is the position vector, $\mathbf{E}$ is the electric field, $\mathbf{H}$ is the magnetic field, and c is the speed of light. Interestingly, it was first predicted and then experimentally demonstrated that the angular momentum resulting from the integration of $\mathscr{J}$ over a volume can be *transferred* to microscopic objects, causing these latter to rotate or spin [2, 3, 4]. This transfer occurs because of the conservation of angular momentum between the electromagnetic field and the object, and has been put to use to design original devices such as optical tweezers [5] or spanners [6, 7].

Bearing in mind the spin-orbit effect that couples the angular momentum of a particle with its spin [8], it is legitimate to wonder if the angular moment density associated with an electromagnetic field can *directly couple* with magnetic moments, and therefore produce a physical energy. To our surprise, we are not aware that this fundamental question has ever been resolved or even addressed in the literature! As a result, it is currently unknown if the direct coupling between the electromagnetic angular moment density and magnetic moments can exist, and, if it does, what are the physical consequences of such coupling.

The goal of this Letter is to resolve these questions. In particular, we analytically prove, by studying a specific case involving magnetic vortices, that such direct coupling can indeed occur.

We then demonstrate that this coupling is at the heart of the recently proposed and subtle spin-current model [9] in magnetoelectric materials (for which magnetic properties can be controlled by electric fields, or conversely, electric properties can be varied by magnetic fields [10]). Moreover, the direct coupling between the electromagnetic angular moment density and magnetic moments also allows for the prediction of novel energy terms that can result in new physical effects. An example of such effects is the occurrence of an *antiferroelectricity-driven* magnetic anisotropy.

Let us first demonstrate that the angular momentum density can directly couple with magnetic moments. For that, we start with the definition of the so-called magnetic toroidal moment, **T** [12, 11]:

$$\mathbf{T} = \frac{1}{2}\int (\mathbf{r} \times \mathscr{M})\, d^3 r \quad , \tag{7.2}$$

where **r** is the position vector and $\mathscr{M}(r)$ is the magnetization field (which has the units of a magnetic moment per unit volume).

The magnetic toroidal moment is an important physical quantity, since it is, e.g., the order parameter associated with magnetic vortices (see, e.g., Refs. [13, 14] and references therein). Moreover, it is known [12, 11, 15, 10] that this toroidal moment can directly couple with the cross product between the electric field and the magnetic field. There is therefore an energy of the form:

$$\mathscr{E} = a\mathbf{T} \cdot (\mathbf{E} \times \mathbf{H}) \quad , \tag{7.3}$$

where a is a constant. The existence of such energetic term allows, e.g., magnetic vortices to be manipulated and controlled. For instance, the sense of rotation of the magnetic vortices (i.e., clockwise *versus* counterclockwise) can be switched by changing the direction of $\mathbf{E} \times \mathbf{H}$ – similar to the fact that an electric polarization can be switched by an electric field in ferroelectric materials [16].

Inserting Eq. (7.2) into Eq. (7.3) for homogeneous **E** and **H**, and using associative properties of the mixed product, we get:

$$\mathscr{E} = -\frac{a}{2}\int (\mathbf{r} \times (\mathbf{E} \times \mathbf{H})) \cdot \mathscr{M}(r)\ d^3 r \tag{7.4}$$

Equation (7.4) can be re-written by using the definition of the angular moment density (see Eq. (7.1)) as:

$$\mathscr{E} = -\frac{ac^2}{2}\int \mathscr{J} \cdot \mathscr{M}\ d^3 r, \tag{7.5}$$

The existence of a dot product between $\mathscr{J}$ and $\mathscr{M}$ on the right side of this latter Equation and the fact that the physical quantity on the left-side of Eq. (7.5) is an energy demonstrate that the electromagnetic angular momentum density can indeed directly couple with magnetic moments to provide an energy.

Having proved such important result, let us now use it to illustrate an example of a physical effect that such coupling can induce. More precisely, what we have in mind here is to consider a (multiferroic) material possessing both magnetic and electric dipoles around each lattice site, and to reveal that the aforementioned coupling is at the heart of the so-called and recently proposed spin-current model [9]. Let us denote as $\mathbf{d}_i$ the electric dipole existing on the lattice site i, and $\mathbf{m}_i$ and $\mathbf{m}_j$ the magnetic moments centered around the lattice sites i and j, respectively. Following Eq. (7.1), one can define an angular momentum density produced by site i and acting around site

j as:

$$\mathscr{J} = \frac{1}{c^2}\mathbf{r}_{i\to j} \times \left(\mathbf{E}_{i\to j} \times \mathbf{H}_{i\to j}\right) \quad , \tag{7.6}$$

where $\mathbf{E}_{i\to j}$ and $\mathbf{H}_{i\to j}$ are the electric field and magnetic field produced by site i and acting around site j, respectively. $\mathbf{r}_{i\to j}$ is the vector joining the site i to any position contained in the (ionic) volume, V, centered around the site j. For simplicity, we assume that such volume is a sphere of radius R_{ion} (see Fig. **??**). We can thus write:

$$\mathbf{r}_{i\to j} = \mathbf{R}_{i\to j} + \delta\mathbf{r} \tag{7.7}$$

where $\mathbf{R}_{i\to j}$ is the vector joining site i to site j and $\delta\mathbf{r}$ is the vector joining site j to the tip of $\mathbf{r}_{i\to j}$. Since, within the volume V, one can always find two points with opposite $\delta\mathbf{r}$, the integration of $\mathbf{r}_{i\to j}$ around V gives:

$$\int_V \mathbf{r}_{i\to j}\ d^3r = \int_V \mathbf{R}_{i\to j}\ d^3r + \int_V \delta\mathbf{r}\ d^3r = \frac{4\pi R_{ion}^3}{3}\mathbf{R}_{i\to j} \tag{7.8}$$

since $\mathbf{R}_{i\to j}$ is a constant, $\int_V d^3r = \frac{4\pi R_{ion}^3}{3}$ and $\int_V \delta\mathbf{r}\ d^3r = \mathbf{0}$.

Let us also assume that $\delta\mathbf{r}$ is much smaller in magnitude than $\mathbf{R}_{i\to j}$ (which is usually justified since distances between ions are typically much larger than ionic radius). As a result, $\mathbf{E}_{i\to j}$ and $\mathbf{H}_{i\to j}$ can be taken as constant at any point located inside the volume V and are equal to

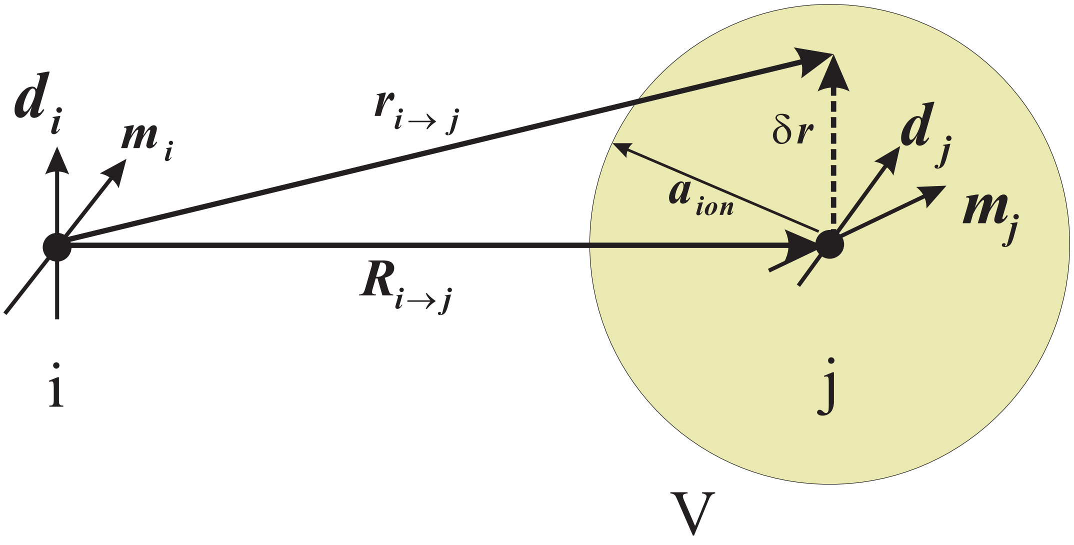

Figure 7.1: Schematic of the quantities involved in the derivation of the formula associated with the spin-current model (see Eq. (7.13) in the text)

[1]:

$$\begin{aligned}\mathbf{E}_{i\to j} &= \frac{1}{4\pi\epsilon_\infty R_{i\to j}^3}\left[3\left(\mathbf{d}_i\cdot\mathbf{e}_{i\to j}\right)\mathbf{e}_{i\to j}-\mathbf{d}_i\right]\\ \mathbf{H}_{i\to j} &= \frac{1}{4\pi R_{i\to j}^3}\left[3\left(\mathbf{m}_i\cdot\mathbf{e}_{i\to j}\right)\mathbf{e}_{i\to j}-\mathbf{m}_i\right]\end{aligned} \tag{7.9}$$

where ϵ_∞ is the electronic dielectric constant, and $\mathbf{e}_{i\to j}$ is the unit vector along $\mathbf{R}_{i\to j}$.

Combining Eqs. (7.6) and Eq. (7.9) gives:

$$\mathscr{J} = \frac{1}{16\pi^2c^2\epsilon_\infty R_{i\to j}^6}\mathbf{r}_{i\to j}\times\left\{\left(\mathbf{d}_i\times\mathbf{m}_i\right)-3\mathbf{e}_{i\to j}\times\left[\left(\mathbf{d}_i\cdot\mathbf{e}_{i\to j}\right)\mathbf{m}_i-\left(\mathbf{m}_i\cdot\mathbf{e}_{i\to j}\right)\mathbf{d}_i\right]\right\} \tag{7.10}$$

According to Eq. (7.5), the coupling between this angular momentum density and the magnetic moment $\mathbf{m}_j$ inside the volume V centered around site j results in the following energy:

$$\mathscr{E}_{i\to j} = -\frac{ac^2}{2}\frac{3}{4\pi R_{ion}^3}\left(\int_V \mathscr{J}\cdot\mathbf{m}_j\, d^3r\right) \quad , \tag{7.11}$$

As detailed in the supplemental material, inserting Eq. (7.10) into Eq. (7.11), realizing that $\mathbf{m}_j$ can be taken as a constant inside V, and using Eq. (7.8), as well as properties associated with cross and mixed products, we get:

$$\begin{aligned}
\mathscr{E}_{i\to j} &= \mathscr{E}_{i\to j,1} + \mathscr{E}_{i\to j,2} + \mathscr{E}_{i\to j,3} \quad with \\
\mathscr{E}_{i\to j,1} &= -\frac{a}{16\pi^2\epsilon_\infty R^5_{i\to j}}\left(\mathbf{d}_i \times \mathbf{e}_{i\to j}\right)\cdot\left(\mathbf{m}_i \times \mathbf{m}_j\right) \quad , \\
\mathscr{E}_{i\to j,2} &= +\frac{a}{16\pi^2\epsilon_\infty R^5_{i\to j}}\left(\mathbf{d}_i \cdot \mathbf{m}_i\right)\left(\mathbf{e}_{i\to j} \cdot \mathbf{m}_j\right) \quad , \\
\mathscr{E}_{i\to j,3} &= -\frac{a}{16\pi^2\epsilon_\infty R^5_{i\to j}}\left(\mathbf{d}_i \cdot \mathbf{e}_{i\to j}\right)\left(\mathbf{m}_i \cdot \mathbf{m}_j\right)
\end{aligned} \tag{7.12}$$

Such energy terms characterize the effect of site i on the magnetic moment at site j, and similar expressions can be derived when considering the (reverse) effect of site j on the magnetic moment at site i. Combining these two effects therefore gives:

$$\begin{aligned}
\mathscr{E}_{ij} = \frac{1}{2}\left(\mathscr{E}_{i\to j} + \mathscr{E}_{j\to i}\right) &= -\frac{a}{32\pi^2\epsilon_\infty R^5_{i\to j}}\left(\left[\mathbf{d}_i + \mathbf{d}_j\right] \times \mathbf{e}_{i\to j}\right)\cdot\left(\mathbf{m}_i \times \mathbf{m}_j\right) \\
&+ \frac{a}{32\pi^2\epsilon_\infty R^5_{i\to j}}\left[\left(\mathbf{d}_i \cdot \mathbf{m}_i\right)\left(\mathbf{e}_{i\to j} \cdot \mathbf{m}_j\right) - \left(\mathbf{d}_j \cdot \mathbf{m}_j\right)\left(\mathbf{e}_{i\to j} \cdot \mathbf{m}_i\right)\right] \\
&- \frac{a}{32\pi^2\epsilon_\infty R^5_{i\to j}}\left(\left[\mathbf{d}_i - \mathbf{d}_j\right] \cdot \mathbf{e}_{i\to j}\right)\left(\mathbf{m}_i \cdot \mathbf{m}_j\right)
\end{aligned} \tag{7.13}$$

Let us now consider the case for which the electric dipoles moments are *homogeneous*, that is $\mathbf{d}_i = \mathbf{d}_j$. In that case, it is trivial to show that the third term of Eq. (7.13) vanishes and that the second term is minus half the first term, which therefore leads to the following energy:

$$\mathscr{E}_{ij} = +b\left(\mathbf{d}_i \times \mathbf{e}_{i\to j}\right)\cdot\left(\mathbf{m}_i \times \mathbf{m}_j\right) \quad , \tag{7.14}$$

where b is a coefficient equal to $\frac{-a}{32\pi^2\epsilon_\infty R_{i\to j}^5}$.

Remarkably, Eq. (7.13) characterizes the so-called spin-current model [9, 17], which is a novel magnetoelectric effect that has been recently proposed to explain why a spiral spin structure can generate an electric polarization [9] or how the existence of an electrical polarization can lead to a magnetic cycloid [17] in multiferroics. In other words, our (straightforward) derivations demonstrate that the direct coupling between the electromagnetic angular momentum density and magnetic moments can be thought as being the origin of the "mysterious" spin-current model [18].

Interestingly, the (general) Eq. (7.13) can also reveal additional novel magneto-electric equations and effects that have never been mentioned in the literature! For instance, let us consider the *antiferroelectric* case for which $\mathbf{d}_i = -\mathbf{d}_j$, with $\mathbf{d}_i$ and $\mathbf{e}_{i\to j}$ perpendicular to each other. Let us also assume that $\mathbf{m}_i$ and $\mathbf{m}_j$ have the same magnitude and both belong to the plane spanned by $\mathbf{d}_i$ and $\mathbf{e}_{i\to j}$. In that case, the first and third terms of Eq. (7.13) vanish, and it is easy to prove (by using equalities from trigonometry) that one has:

$$\mathcal{E}_{ij} = \frac{a|\mathbf{d}_i|m^2}{32\pi^2\epsilon_\infty R_{i\to j}^5}\sin(\alpha+\beta) \tag{7.15}$$

where α is the angle between $\mathbf{d}_i$ and $\mathbf{m}_i$, and β is the angle between $\mathbf{d}_i$ and $\mathbf{m}_j$. This novel energy term therefore desires (through its minization) the sum of α and β to be 90 degrees (270 degrees) if a is negative (positive). As a result, a collinear solution for a *ferromagnetic* material will be to have $\mathbf{m}_i$ and $\mathbf{m}_j$ both making an angle of 45 degrees with respect to $\mathbf{d}_i$, if a is negative. Similarly, a collinear solution for an *antiferromagnetic* material will be to have $\mathbf{m}_i$ and $\mathbf{m}_j$ being antiparallel and $\mathbf{m}_i$ making an angle of 45 degrees with respect to $\mathbf{d}_i$, if a is positive. A a result, Eq. (7.15) should influence the direction of the easy axis in ferromagnetic and antiferroelectric materials, and will also affect the preferred direction of the antiferromagnetic vector in antiferromagnetic and antiferroelectric materials. In other words, Eq. (7.15) can be seen as characterizing an *antiferroelectricity-driven magnetic anisotropy*, which is a novel effect to the best of our knowledge.

In summary, this Letter first proves that the electromagnetic angular momentum density can directly couple with magnetic moments (this proof was done here by considering the magnetic toroidal moment and its interaction with the cross-product of the electric field and magnetic field). Secondly, we also demonstrate an important consequence of such coupling, namely the existence of the so-called spin-current model in multiferroics [9]. Thirdly, we show that this direct coupling also leads to the prediction of novel magnetoelectric features (e.g., an antiferroelectricity-driven magnetic anisotropy). Moreover, the Supplementary Material also reveals (in a simple and straightforward manner) that this coupling can originate from spin-orbit and relativistic effects, and can involve a striking product between spin-orbit interactions and electric potential – that also naturally arises from perturbation theory at the second order. Because electromagnetism is fundamental to many branches of physics, chemistry and engineering, it is likely that this direct coupling will explain other subtle effects or will be useful in discovering other novel phenomena in diverse fields of research such as optics, condensed matter, material science, and device physics. We therefore expect that this work would be of great interest and benefit to the scientific community at large.

Bibliography

[1] J.D. Jackson, *Classical Electrodynamics* (Wiley, New York, 1962).

[2] R. A. Beth, Phys. Rev. **50**, 115125 (1936).

[3] L. Allen, Stephen M. Barnett, Miles J. Padgett, *Optical Angular Momen- tum* (Institute of Physics, Bristol, 2003).

[4] L. Allen, M. J. Padgett and M. Babiker, Prog. Opt. **34**, 291 (1999).

[5] J. E. Molloy, K. Dholakia, M. J. Padgett, J. Mod. Opt. **50**, 1501 (2003).

[6] H. He, M. E. J. Friese, N. R. Heckenberg, and H. Rubinsztein-Dunlop, Phys. Rev. Lett. **75**, 826 (1995).

[7] N. B. Simpson, K. Dholakia, L. Allen, and M. J. Padgett, Opt. Lett. **22**, 52 (1997).

[8] R. Scherrer. *Quantum Mechanics, an accessible introduction* (Pearson, Addison Wesley, San Francisco, 2006).

[9] H. Katsura, N. Nagaosa and A.V. Balatsky, Phys. Rev. Lett. **95**, 057205 (2005).

[10] H. Schmid, Ferroelectrics **252**, 41 (2001).

[11] C. Ederer and N.A. Spaldin, Phys. Rev. B **76**, 214404 (2007).

[12] V. M. Dubovik and V. V. Tugushev, Physics Reports **187**, 145 (1990).

[13] S. Prosandeev, I. Ponomareva, I. Kornev and L. Bellaiche, Phys. Rev. Lett. **100**, 047201 (2008).

[14] S. Prosandeev and L. Bellaiche, Phys. Rev. Lett. **102**, 097205 (2009).

[15] A. A. Gorbatsevich, Yu.V. Kopaev, and V.V. Tugushev, Zh. Eksp. Teor. Fiz. **85**, 1107 (1983) [Sov. Phys. JETP **58**, 643 (1983)].

[16] M.E. Lines and A.M. Glass. *Principles and Applications of Ferroelectrics and Related Materials* (Clarendon Press, Oxford, 1977).

[17] D. Rahmedov, D. Wang, J Iñiguez and L. Bellaiche, , Phys. Rev. Lett. **109**, 037207 (2012).

[18] Note that the pioneering work of Ref. [9] derived the spin-current model by combining several effects, namely a (i) microscopic electronic Hamiltonian, (ii) a three atom model, (iii) a hole picture (in which oxygen orbitals are empty), (iv) second-order perturbation theory and (v) double-exchange interactions [19, 20] or superexchange [21] interactions. We humbly believe that our method is more straightforward, more general, and provides a clear picture of the

origin of the spin-current model (namely, the direct coupling between the electromagnetic angular momentum density and magnetic moments).

[19] P.W. Anderson and H. Hasegawa, Phys. Rev. **100**, 675 (1955).

[20] M. Kataoka *et al.*, J. Phys. Soc. Jpn. **53**, 3624 (1984).

[21] P.W. Anderson, in Solid State Physics, edited by F. Seitz and D. Turnbull (Academic Press, New York, 1963), Vol. 14, p. 99.

8 Conclusion

The first-principles studies of FE materials under strain and in the presence of vacancies reported in this dissertation revealed interesting behavior of polarization P. It was first reported that strained (111)-BTO exhibit a polarization whose behavior is peculiar and unusual with regards to the more familiar polarization behavior of (001)-BTO. The significant differences, namely: (i) the decline of P under compressive epitaxial strain; (ii) the positive piezoelectric coefficient e_{31} in (111)-BTO, as opposed to the negative e_{31} of (001)-BTO lead to a rethinking of the basic intuitions in FE materials, and also the realization of the difference in the microscopic interactions responsible for ferroelectricity in (111)-BTO and (001)-BTO. A strain-induced phase transition, and an accompanying large piezoelectric response, is also shown to occur at $\eta = -1.75\%$. The out-of-plane polarization P_{out} is also shown to increase with tensile strain, and this is technologically advantageous especially when (111)-BTO is interfaced with other functional materials of the same symmetry such as: topological insulators, semiconductors, magnetic manganites, etc. A simple physical explanation was also provided pertaining to the difference in ferroelectric behaviors of the two oriented BTO.

I also reported in this dissertation the theoretical study, using density functional perturbation calculations, of Brillouin zone-center phonon mode sequencing in strained tetragonal (P4mm) BTO. It is evident from the results presented here that strain affect the mode sequencing — the most striking result occurs at $\eta = -2.5\%$ — by causing various phonon modes to mix. Large frequency shifts occur even for modes that are not soft and they are shown to be mostly linearly dependent with strain, except in the case of $A_1(TO_3)$ and $A_1(LO_3)$ where nonlinearity cannot be ignored. The importance of mode mixing has also been determined and shown to greatly influence LO-TO splitting. One immediate area to which these results may pertain is in the assignment of spectroscopic peaks, where FE are usually strained.

In our studies of the factors affecting FE behaviors, in this dissertation we highlighted that defects such as vacancies can be deliberately inserted in FEs by carefully tuning the chemical potential of atomic or electronic reservoirs during growth. They can also occur unintentionally despite the care taken in choosing the most optimal growth conditions. The theoretical calculations reported here demonstrate that various charged vacancies can occur and they can lead to different functional materials. For BTO with V_{Ba}^{2-}, V_{Ti}^{4-}, or V_{O1}^{2+} vacancies, the system remains insulating without major changes in its FE behavior — polarization and polarization switching. Surprisingly, all three type of vacancies have similar polarization and polarization switching energy barrier. We have demonstrated and successfully introduced new calculation methods required in the study of polarization and polarization switching of FE materials in the presence of charged vacancies.

Additionally, we have demonstrated that depending on the charge character, vacancies such V_{Ba}^{0}, V_{Ti}^{q} for q={3-;2-;1-;0}, and V_{O}^{0} can induce ferromagnetism in BTO. We have shown that careful tuning of the chemical potentials of atomic and electron reservoirs can induce different ferroic ordering in FE BTO. Fundamentally, by study of spin resolved charge distribution as well as density of state near the Fermi level, we have pinpointed the microscopic origin of the FM, to be the itinerant carrier (holes, or electrons) introduced by the vacancy. The FM has also been shown to persist at high temperature.

Bibliography

[1] S. B. Lang, “Pyroelectricity: From ancient curiosity to modern imaging tool.,” *Physics Today*, vol. 58, pp. 31–36, 2005.

[2] W. M. Haynes, *CRC Handbook of Chemistry and Physics.* 95th ed., 2014-2015.

[3] J. Valasek, “Piezoelectric and applied phenomena in rochelle salt.,” *Physical Review*, vol. 17, p. 475, 1921.

[4] P. Hohenberg and W. Kohn, “Inhomogeneous electron gas.,” *Physical Review*, vol. 136, p. B864, 1964.

[5] W. Kohn and L. Sham, “Self-consistent equations including exchange and correlation effects.,” *Physical Review*, vol. 140, p. A1133, 1965.

[6] J. C. Slater, “The lorentz correction in barium titanate.,” *Physical Review*, vol. 78, p. 748, 1950.

[7] W. Cochran, “Crystal stability and the theory of ferroelectricity.,” *Adv. Phys.*, vol. 9, p. 387, 1960.

[8] R. E. Cohen, “Origin of ferroelectricity in perovskite oxides.,” *Nature*, vol. 358, p. 136, 1992.

[9] M. Dawber and J. F. Scott, “A model for fatigue in ferroelectric perovskite thin films.,” *App. Phys. Lett.*, vol. 76, p. 1060, 2000.

[10] A. N. Kolmogorov, “On the statistical theory of crystallization of metals.,” *Izv. Akad. Nauk, USSR Ser. Math*, vol. 3, p. 355, 1937.

[11] M. Avrami, “Kinetics of phase change,” *J. Chem. Phys.*, vol. 8, p. 212, 1940.

[12] H. Orihara, S. Hashimoto, and Y. Ishibashi, “A theory of d-e hysteresis loop based on the avrami model.,” *J. of Phys. Soc. Jpn.*, vol. 63, p. 1031, 1994.

[13] M. Itoh, R. Wang, Y. Inaguma, T. Yamaguchi, Y.-J. Shan, and T. Nakamura, “Ferroelectricity induced by oxygen isotope exchange in strontium titanate perovskite.,” *Phys. Rev. Lett.*, vol. 82, p. 3540, 1999.

[14] J. F. Scott, “Soft-mode spectroscopy: Experimental studies of structural phase transitions.,” *Rev. Mod. Phys.*, vol. 46, pp. 83–128, 1974.

[15] W. Zhong, D. Vanderbilt, and K. M. Rabe, “First-principles theory of ferroelectric phase transitions for perovskites: The case of $BaTiO_3$.,” *Phys. Rev. B*, vol. 52, pp. 6301–6312, 1995.

[16] L. D. Landau, "Theory of phase transformations. I," *Zh. Eksp. Teor. Fiz.*, vol. 7, p. 19, 1937.

[17] L. D. Landau, "Theory of phase transformations. II," *Zh. Eksp. Teor. Fiz.*, vol. 7, p. 627, 1937.

[18] G. Morandi, F. Napoli, and E. Ercolessi, *Statistical Mechanics An intermediate Course*. World Scientific, second ed., 2001.

[19] G. H. Kwei, A. C. Lawson, S. J. L. Billinge, and S.-W. Cheong, "Structures of the ferroelectric phases of barium titanate.," *J. Phys. Chem.*, vol. 97, pp. 2368–2377, 1993.

[20] D. J. Amit, D. J. Bergman, and Y. Imry, "The wilson theory and the ginzburg critical region," *J. Phys. Chem. C: Solid State Phys.*, vol. 6, p. 2685, 1973.

[21] G. H. Haertling, "Ferroelectric ceramics: History and technology.," *J. Am. Ceram. Soc.*, vol. 82, pp. 797–818, 1999.

[22] C. Kittel, *Introduction to Solid State Physics.* John Wiley & Sons, Inc., eighth ed., 2005.

[23] T. Karaki, K. Yan, and M. Adachi, "Barium titanate piezoelectric ceramics manufactured by two-step sintering," *Japanese Journal of Applied Physics*, vol. 46, p. 7035, 2007.

[24] C. Ederer and N. Spaldin, "Effect of epitaxial strain on the spontaneous polarization of thin film ferroelectrics," *Phys. Rev. Lett.*, vol. 95, p. 257601, 2005.

[25] H. Savakus, K. Klicker, and R. Newnham, "Pzt-epoxy piezoelectric transducers: A simplified fabrication procedure," *Materials Research Bulletin*, vol. 16, pp. 677 – 680, 1981.

[26] L. Bellaiche and D. Vanderbilt, "Intrinsic piezoelectric response in perovskite alloys: Pmn-pt versus pzt," *Phys. Rev. Lett.*, vol. 83, pp. 1347–1350, 1999.

[27] N. Nakamura, H. Ogi, and M. Hirao, "Elastic, anelastic, and piezoelectric coefficients of gan," *Journal of Applied Physics*, vol. 111, 2012.

[28] R. Bechmann, "Elastic and piezoelectric constants of alpha-quartz," *Phys. Rev.*, vol. 110, pp. 1060–1061, 1958.

[29] C. Shekhar Pandey and J. Schreuer, "Elastic and piezoelectric constants of tourmaline single crystals at non-ambient temperatures determined by resonant ultrasound spectroscopy.," *Journal of Applied Physics*, vol. 111, p. 013516, 2012.

[30] I. Naumov, L. Bellaiche, and H. Fu, "Unusual phase transitions in ferroelectric nanodisks and nanorods," *Nature*, vol. 432, pp. 737–740, 2004.

[31] K. Rabe, M. Dawber, C. Lichtensteiger, C. Ahn, and J.-M. Triscone in *Physics of Ferroelectrics*, vol. 105 of *Topics in Applied Physics*, Springer Berlin Heidelberg, 2007.

[32] I. Naumov and H. Fu, "Vortex-to-polarization phase transformation path in ferroelectric Pb(ZrTi)O_3 nanoparticles," *Phys. Rev. Lett*, vol. 98, 2007.

[33] D. Khomskii, "Classifying multiferroics: Mechanisms and effects.," *Physics*, vol. 2, p. 20, 2009.

[34] T. Kimura, T. Goto, H. Shintani, K. Ishizaka, T. Arima, and Y. Tokura, “Magnetic control of ferroelectric polarization.,” *Nature*, vol. 426, pp. 55–58, 2003.

[35] N. Hur, S. Park, P. A. Sharma, J. S. Ahn, S. Guha, and S.-W. Cheong, “Electric polarization reversal and memory in a multiferroic material induced by magnetic fields.,” *Nature*, vol. 429, pp. 392–395, 2004.

[36] E. Kim, A. SteinbrÃ¼ck, M. T. Buscaglia, V. Buscaglia, T. Pertsch, and R. Grange, “Second-harmonic generation of single batio3 nanoparticles down to 22 nm diameter,” *ACS Nano*, vol. 7, no. 6, pp. 5343–5349, 2013.

[37] P. G. Schunnemann, D. A. Temple, R. S. Hathcock, H. L. Tuller, H. P. Jenssen, D. R. Gabbe, and C. Warde, “Role of iron center in the photorefractive effect in barium titanate,” *J. Opt. Soc. Am. B*, vol. 5, pp. 1685–1696, 1988.

[38] B. A. Wechsler and M. B. Klein, “Thermodynamic point defect model of barium titante and application to the photorefractive effect,” *J. Opt. Soc. Am. B*, vol. 5, pp. 1711–1722, 1988.

[39] S. Kalinin, S. Jesse, B. J. Rodriguez, Y. H. Chu, R. Ramesh, E. A. Eliseev, and A. N. Morozovska, “Probing the role of single defects on the thermodynamics of electric-field induced phase transitions,” *Phys. Rev. Lett.*, vol. 100, p. 155703, 2008.

[40] J. F. Scott, “Applications of modern ferroelectrics,” *Science*, vol. 315, pp. 954–959, 2007.

[41] J. F. Scott, “The physics of ferroelectric memories,” *Physics Today*, pp. 22–27, 1998.

[42] J. Junquera and P. Ghosez, “Critical thickness for ferroelectricity in perovskite ultrathin films,” *Nature*, vol. 422, pp. 506–509, 2003.

[43] A. Chanthbouala, V. Garcia, R. O. Cherifi, K. Bouzehouane, S. Fusil, X. Moya, S. Xavier, H. Yamada, C. Deranlot, N. D. Mathur, M. Bibes, A. Barthélémy, and J. Grollier, “A ferroelectric memristor,” *Nature Materials*, vol. 11, pp. 860–864, 2012.

[44] W. Eerenstein, N. D. Mathur, and J. F. Scott, “Multiferroics and magnetoelectric materials,” *Nature*, vol. 442, pp. 759–765, 2006.

[45] Y. Liu, Y. Zhang, M.-J. Chow, Q. Chen, and J. Li, “Biological ferroelectricity uncovered in aortic walls by piezoresponse force microscopy,” *Phys. Rev. Lett.*, vol. 108, p. 078103, 2012.

[46] X. Z. Liao, A. Serquis, Y. T. Zhu, D. E. Peterson, F. M. Mueller, and H. F. Xu, “Strain effect on the superconducting temperature of MgB_2,” *Superconducting Science and Technology*, vol. 17, pp. 1026–1030, 2004.

[47] M. T. Dove, *Introduction to Lattice Dynamics*. Cambridge University Press, 1993.

[48] P. Ghosez, X. Gonze, and J.-P. Michenaud, “Ab initio phonon dispersion curves and interatomic force constants of barium titanate,” *Ferroelectrics*, vol. 206, pp. 205–217, 1998.

[49] N. Li, J. Ren, L. Wang, G. Zhang, P. Hanggi, and B. Li, “Phononics: Manipulating heat flow with electronics analogs and beyond,” *Rev. Mod. Phys*, vol. 84, pp. 1045–1066, 2012.

[50] M. Maldovan, “Sound and heat revolutions in phononics,” *Nature*, vol. 503, pp. 209–217, 2013.

[51] N. Choudhury, E. J. Walter, A. I. Kolesnikov, and C.-K. Loong, “Large phonon band gap in $SrTiO_3$ and the vibrational signatures of ferroelectricity in $ATiO_3$ perovskites: First-principles lattice dynamics and inelastic neutron scattering.,” *Phys. Rev. B*, vol. 77, p. 134111, 2008.

[52] C. Berglund and W. Baer, “Electron transport in single-domain, ferroelectric barium titanate,” *Phys. Rev.*, vol. 157, pp. 358–366, 1967.

[53] T. Shimada, Y. Uratani, and T. Kitamura, “Vacancy-driven ferromagnetism in ferroelectric pbtio3,” *App. Phys. Lett.*, vol. 100, p. 162901, 2012.

[54] R. Mangalam, N. Ray, U. V. Waghmare, A. Sundaresan, and C. Rao, “Multiferroic properties of nanocrystalline $BaTiO_3$,” *Solid State Communications*, vol. 149, pp. 1–5, 2009.

[55] L. H. Thomas, “The calculation of atomic fields,” *Proc. Camb. Phil. Soc.*, vol. 23, p. 542, 1927.

[56] E. Fermi, “Uno metodo statistico per la determinazione di alcune priopricta dell’atomo,” *Rend. Acad. Naz. Lincei*, vol. 6, p. 602, 1927.

[57] M. Levy, “Universal variational functionals of electron densities, first-order density matrices, and natural spin-orbitals and solution of the v-representability problem,” *Proc. Natl. Acad. Sci.*, vol. 76, p. 6062, 1979.

[58] E. H. Lieb, “Density functional for coulomb systems,” *Int. J. Quant. Chem.*, vol. 24, p. 243, 1983.

[59] P. A. M. Dirac, “Note on exchange phenomena in the thomas atom,” *Mathematical Proceedings of the Cambridge Philosophical Society*, vol. 26, p. 376, 1930.

[60] J. M. Thijssen, *Statistical Mechanics An intermediate Course*. Cambridge Univversity Press, 1999.

[61] D. M. Ceperley and B. J. Alder, “Ground state of the electron gas by a stochastic method,” *Phys. Rev. Lett.*, vol. 45, p. 566, 1980.

[62] J. P. Perdew and A. Zunger, “Self-interaction correction to density-functional approximations for many-electron systems,” *Phys. Rev. B*, vol. 23, p. 5048, 1981.

[63] M. T. Yin and M. L. Cohen, “Microscopic theory of the phase transformation and lattice dynamics of si,” *Phys. Rev. Lett.*, vol. 45, p. 1004, 1980.

[64] S. Kümmel and L. Kronik, “Orbital-dependent density functionals: Theory and applications,” *Rev. Mod. Phys.*, vol. 80, p. 3, 2008.

[65] C. Fiolhais, F. Nogueira, and M. A. L. Marques, *A Primer in Density Functional Theory*. Springer Berlin Heidelberg, 2003.

[66] D. R. Hamann, M. Schlüter, and C. Chiang, "Norm-conserving pseudopotentials," *Phys. Rev. Lett.*, vol. 43, p. 1494, 1979.

[67] N. Troullier and J. L. Martins, "Efficient pseudopotentials for plane-wave calculations," *Phys. Rev. B*, vol. 43, p. 1993, 1991.

[68] G. P. Kerker, "Non-singular atomic pseudopotentials for solid state applications," *Journal of Physics C: Solid State Physics*, vol. 13, p. L189, 1980.

[69] G. B. Bachelet, D. R. Hamann, and M. Schlüter, "Pseudopotentials that work: From h to pu," *Phys. Rev. B*, vol. 26, p. 4199, 1982.

[70] L. Kleinman and D. M. Bylander, "Efficacious form for model pseudopotentials," *Phys. Rev. Lett.*, vol. 48, p. 1425, 1982.

[71] R. M. Martin, "Piezoelectricity," *Phys. Rev. B*, vol. 5, p. 1607, 1972.

[72] J. D. Jackson, *Classical Electrodynamics*. Wiley, third ed., 1998.

[73] D. J. Griffiths, *Introduction to Electrodynamics*. Boston:Pearson, 4th edition ed., 1999.

[74] R. Resta, "Theory of the electric polarization in crystals," *Ferroelectrics*, vol. 136, p. 51, 1992.

[75] R. D. King-Smith and D. Vanderbilt, "Theory of polarization of crystalline solids," *Phys. Rev. B*, vol. 47, p. 1651, 1993.

[76] D. J. Griffiths, *Introduction to Electrodynamics*. Upper Saddle River, NJ : Pearson Prentice Hall, 2nd edition ed., 2005.

[77] M. V. Berry, "Quantal phase factors accompanying adiabatic changes," *Proceedings of the Royal Society of London A: Mathematical, Physical and Engineering Sciences*, vol. 392, p. 45, 1984.

[78] R. Resta, "Manifestations of berry's phase in molecules and condensed matter," *Journal of Physics: Condensed Matter*, vol. 12, p. R107, 2000.

[79] J. Zak, "Berry's geometrical phase for noncyclic hamiltonians," *EPL (Europhysics Letters)*, vol. 9, p. 615, 1989.

[80] H. J. Monkhorst and J. D. Pack, "Special points for brillouin-zone integrations," *Phys. Rev. B*, vol. 13, p. 5188, 1976.

[81] S.-H. Wei and S. B. Zhang, "Chemical trends of defect formation and doping limit in ii-vi semiconductors:the case of cdte," *Phys. Rev. B*, vol. 66, p. 155211, 2002.

[82] X. Gonze, "Perturbation expansion of variational principles at arbitrary order," *Phys. Rev. A*, vol. 52, p. 1086, 1995.

[83] S. Baroni, S. de Gironcoli, A. Dal Corso, and P. Giannozzi, “Phonons and related crystal properties from density-functional perturbation theory,” *Rev. Mod. Phys.*, vol. 73, p. 515, 2001.

[84] N. Ashcroft and N. Mermin, *Solid State Physics*. Saunders College, 1976.

[85] M. Born and K. Huang, *Dynamical Theory of Crystal lattices*. Oxford University Press, Oxford, 1954.

[86] W. Cochran and R. A. Cowley, “Dielectric constants and lattice vibrations,” *J. Phys. Chem. Solids*, vol. 23, p. 447, 1962.

[87] P. Y. Yu and M. Cardona, *Fundamentals of Semiconductors Physics and Materials Properties*. Springer-Verlag, Berlin Heidelberg New York, third ed., 2001.

[88] X. Gonze and C. Lee, “Dynamical matrices, born effective charges, dielectric permittivity tensors, and interatomic force constants from density-functional perturbation theory,” *Phys. Rev. B*, vol. 55, p. 10355, 1997.

A Pseudopotential derivations

A.1 Inversion for Trouiller-Martins construction

Applying Eq.2.40 to Kerker's construction gives:

$$V_{scr,l}^{PP}[\rho,r]=\varepsilon-\frac{l(l+1)}{2r^2}+\frac{1}{2r^{l+1}e^{p(r)}}\frac{d^2\left(r^{l+1}e^{p(r)}\right)}{dr^2} \tag{A.1}$$

We can compute the last term using Leibniz general product rule:

$$(fg)^{(n)}=\sum_{k=0}^{n}\binom{n}{k}f^{(k)}g^{(n-k)}, \tag{A.2}$$

where A$^{(n)}$ means the n-th derivative of A. We have:

$$\begin{aligned}\frac{d^2\left(r^{l+1}e^{p(r)}\right)}{dr^2} &= r^{l+1}\left(p'(r)+p''(r)\right)e^{p(r)}+(l+1)r^l p'(r)e^{p(r)}\\ &+l(l+1)r^{l-1}e^{p(r)}\\ &= r^{l+1}e^{p(r)}\left[\left(p'(r)+p''(r)\right)+\frac{(l+1)}{r}p'(r)+\frac{l(l+1)}{r^2}\right]\end{aligned} \tag{A.3}$$

where $p'(r)=\frac{dp(r)}{dr}$ and $p''(r)=\frac{d^2p(r)}{dr^2}$. Now using $p(r)=c_0+\sum_{i=2}^{n}c_i r^i$, after simplification of the r^{-2} terms and factorization we recover Eq.2.41.

A.2 Inversion for Bachelet-Hammann-Schlüter construction

To demonstrate Eq.2.42 we start with:

$$\hat{V}_{2j} = \varepsilon - \frac{l(l+1)}{2r^2} + \frac{1}{2w_{2j}} \frac{d^2 w_{2j}(r)}{dr^2}. \tag{A.4}$$

We first compute $\frac{d^2 w_{2j}(r)}{dr^2}$ using Leibniz rule, which gives us:

$$\begin{aligned} w''_{2j}(r) \quad &= \gamma_j \left[w''_{1j} + \delta_j \left(r^{l+1} f''\left(\frac{r}{r_c}\right) \right) \right] \\ &+ \gamma_j \delta_j \left[2(l+1) r^l f'\left(\frac{r}{r_c}\right) + l(l+1) r^{l-1} f\left(\frac{r}{r_c}\right) \right]. \end{aligned} \tag{A.5}$$

Using the definition of the cutoff function $f\left(\frac{r}{r_c}\right) = e^{-\left(\frac{r}{r_c}\right)^\lambda}$, we have

$$f'' = \frac{1}{r^2} \left[\lambda^2 \left(\frac{r}{r_c}\right)^{2\lambda} - \lambda(\lambda-1) \left(\frac{r}{r_c}\right)^{\lambda} \right] f\left(\frac{r}{r_c}\right). \tag{A.6}$$

Using Eq.A.6 in Eq.A.5 yields:

$$\begin{aligned} w'' \quad &= \gamma_j w''_{1j} + \gamma_j \delta_j \frac{1}{r^2} \left[\lambda^2 \left(\frac{r}{r_c}\right)^{2\lambda} - \lambda(\lambda-1) \left(\frac{r}{r_c}\right)^{\lambda} \right] f\left(\frac{r}{r_c}\right) \\ &+ \gamma_j \delta_j \left[2(l+1) r^{l+1} \left(-\frac{\lambda}{r^2}\right) \left(\frac{r}{r_c}\right)^{\lambda} f\left(\frac{r}{r_c}\right) + \frac{l(l+1) r^{l+1}}{r^2} f\left(\frac{r}{r_c}\right) \right], \end{aligned} \tag{A.7}$$

which upon further development and calculations yields:

$$\begin{aligned} w''_{2j}(r) \quad &= \gamma_j \left[w''_{1j} + \delta_j \frac{l(l+1) r^{l+1}}{r^2} r^{l+1} f\left(\frac{r}{r_c}\right) \right] \\ &+ \gamma_j \delta_j \left[\frac{r^{l+1}}{r^2} f\left(\frac{r}{r_c}\right) \left(\lambda^2 \left(\frac{r}{r_c}\right)^{2\lambda} - (\lambda(\lambda+1) + 2l\lambda) \left(\frac{r}{r_c}\right)^{\lambda} \right) \right]. \end{aligned} \tag{A.8}$$

So Eq.A.1 becomes:

$$\begin{aligned}\hat{V}_{2j} \quad &= \varepsilon - \frac{l(l+1)}{r^2} + \frac{\gamma_j}{2w_{2j}}\left(w''_{1j} + \delta_j \frac{l(l+1)r^{l+1}}{r^2} f\left(\frac{r}{r_c}\right)\right) \\ &+ \frac{\gamma_j \delta_j}{2w_{2j}} \frac{r^{l+1}}{r^2} f\left(\frac{r}{r_c}\right)\left(\lambda^2\left(\frac{r}{r_c}\right)^{2\lambda} - (\lambda(\lambda+1) + 2l\lambda)\left(\frac{r}{r_c}\right)^{\lambda}\right).\end{aligned} \tag{A.9}$$

Given that $w_{1j}(r)$ obeys the equation:

$$w''_{1j}(r) = \left(\frac{l(l+1)}{r^2} - \varepsilon + V_{1j}\right) 2w_{1j}, \tag{A.10}$$

the third term of Eq.A.9 becomes:

$$\frac{\gamma_j}{2w_{2j}} w''_{1j}(r) = \frac{\gamma_j w_{1j}}{w_{2j}}(V_{1j} - \varepsilon) + \frac{\gamma_j w_{1j}}{w_{2j}} \frac{l(l+1)}{r^2}. \tag{A.11}$$

When results in Eq.A.11 is combined with the fourth term $\frac{\gamma_j \delta_j}{2w_{2j}} \frac{l(l+1) r^{l+1}}{r^2} f\left(\frac{r}{r_c}\right)$, we have:

$$\begin{aligned}\xi \quad &= \frac{\gamma_j w_{1j}}{w_{2j}}(V_{1j} - \varepsilon) + \frac{l(l+1)}{w_{2j} r^2} \gamma_j \left(w_{1j} + \delta_j r^{l+1} f\left(\frac{r}{r_c}\right)\right) \\ &= \frac{\gamma_j w_{1j}}{w_{2j}}(V_{1j} - \varepsilon) + \frac{l(l+1)}{r^2},\end{aligned} \tag{A.12}$$

where the definition of w_{2j} has been used to simplify the expression of ξ. Now using results of Eq.A.12 in Eq.A.9 we end up, after simplification, with:

$$\hat{V}_{2j} = \varepsilon + \frac{\gamma_j w_{1j}}{w_{2j}}(V_{1j} - \varepsilon) + \frac{\gamma_j \delta_j}{2w_{2j}} \frac{r^{l+1}}{r^2} f\left(\frac{r}{r_c}\right)\left(\lambda^2\left(\frac{r}{r_c}\right)^{2\lambda} - (\lambda(\lambda+1) + 2l\lambda)\left(\frac{r}{r_c}\right)^{\lambda}\right). \tag{A.13}$$

Using the identity $\gamma_j w_{1j} = w_{2j} - \gamma_j \delta j r^{l+1} f\left(\frac{r}{r_c}\right)$ and after some simplifications we obtain Eq.2.42.

B Berry phase

B.1 Discrete formulation of Berry phase

Let us consider two wavefunctions $\left|\psi_s\right\rangle$, and $\left|\psi_{s+1}\right\rangle$ that obey the adiabatic approximation. By the adiabatic theorem,

$$\left|\psi_{s+1}\right\rangle = e^{i\Delta\varphi_{s,s+1}}\left|\psi_s\right\rangle, \tag{B.1}$$

from which

$$i\Delta\varphi_{s,s+1} = \ln\left\langle\psi_s\middle|\psi_{s+1}\right\rangle, \tag{B.2}$$

and

$$\Delta\varphi_{s,s+1} = \Im\ln\left\langle\psi_s\middle|\psi_{s+1}\right\rangle. \tag{B.3}$$

If we now consider more than two points in parameter space, that is we assume: $\left|\psi_s\right\rangle,\ldots,\left|\psi_{s+i}\right\rangle,\ldots,\left|\psi_{s+n}\right\rangle$ the resulting phase difference becomes:

$$\Delta\varphi = \sum_{i=1}^{n}\Delta\varphi_{s,s+i} = \Im\sum_{i=1}^{n}\ln\left\langle\psi_s\middle|\psi_{s+i}\right\rangle = \Im\ln\prod_{i=1}^{n}\left\langle\psi_{s+i-1}\middle|\psi_{s+i}\right\rangle. \tag{B.4}$$

Knowing that the fermion many-body wave function $|\Psi\rangle$ is expressed as a Slater determinant of one-body wave functions $\left|\psi_i\right\rangle$, $|\Psi\rangle = \det\left|\psi_i\right\rangle$, where i is an electron index. We can thus express the overlap between the many-body wave function as:

$$S_\Psi = \left\langle\Psi_\xi\middle|\Psi_{\xi'}\right\rangle = \det\left(\left\langle\psi_{i,\xi}\right|\right)\det\left(\left|\psi_{j,\xi'}\right\rangle\right) = \det\left(\prod_{i,j}\left\langle\psi_{i,\xi}\middle|\psi_{j,\xi'}\right\rangle\right). \tag{B.5}$$

By using the one-electron overlap matrix $S_{mn}(\xi,\xi')$ we have:

$$\left\langle \Psi_{\xi} \middle| \Psi_{\xi'} \right\rangle = \prod \det Tr S(\xi,\xi'). \tag{B.6}$$

When used in conjunction with Eq.B.6, Eq.B.4 reproduces the desired discrete formulation of Berry's phase in Eq.2.83.